AD-A132-031   SPACECRAFT CHARGING AT GEOSYNCHRONOUS ORBIT AND LARGE   1/3
                SCALE ELECTRIC FIEL..(U) BOSTON COLL CHESTNUT HILL MA
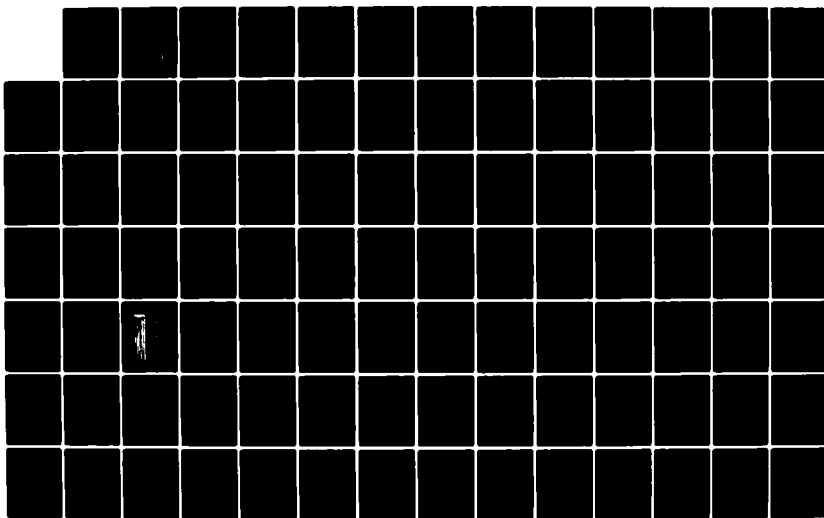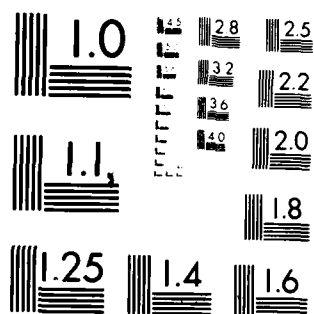   DEPT OF PHYSICS J FEYNMAN ET AL. 30 SEP 81
UNCLASSIFIED   AFGL-TR-82-0032 F19628-79-C-0031   F/G 22/3   NL

MICROCOPY RESOLUTION TEST CHART
NATIONAL BUREAU OF STANDARDS 1963 A

AFGL-TR-82-0032

SPACECRAFT CHARGING AT GEOSYNCHRONOUS
ORBIT AND LARGE SCALE ELECTRIC FIELDS
IN THE HIGH LATITUDE IONOSPHERE

Joan Feynman
William J. Burke

Trustees of Boston College
Department of Physics
Chestnut Hill, Massachusetts 02167

Final Report
1 October 1978 - 30 September 1981

30 September 1981

DTIC
ELECTE
SEP 2   1983

A

83 08 31 009

REPORT DOCUMENTATION PAGE		READ INSTRUCTIONS BEFORE COMPLETING FORM
1. REPORT NUMBER AFGL-TR-82-0032	2. GOVT ACCESSION NO. AD-A132031	3. RECIPIENT'S CATALOG NUMBER
4. TITLE (and Subtitle) SPACECRAFT CHARGING AT GEOSYNCHRONOUS ORBIT AND LARGE SCALE ELECTRIC FIELDS IN THE HIGH LATITUDE IONOSPHERE		5. TYPE OF REPORT & PERIOD COVERED Final Report 10/1/78 - 9/30/81
		6. PERFORMING ORG. REPORT NUMBER
7. AUTHOR(s) Joan Feynman William J. Burke*		8. CONTRACT OR GRANT NUMBER(s) F19628-79-C-0031
9. PERFORMING ORGANIZATION NAME AND ADDRESS Trustees of Boston College Department of Physics Chestnut Hill, Massachusetts 02167		10. PROGRAM ELEMENT, PROJECT, TASK AREA & WORK UNIT NUMBERS 62101 766106AJ
11. CONTROLLING OFFICE NAME AND ADDRESS Air Force Geophysics Laboratory Hanscom AFB, Massachusetts 01731 Monitor/David A. Hardy/PHG		12. REPORT DATE 30 September 1981
		13. NUMBER OF PAGES 211
14. MONITORING AGENCY NAME & ADDRESS(if different from Controlling Office)		15. SECURITY CLASS. (of this report) Unclassified
		15a. DECLASSIFICATION DOWNGRADING SCHEDULE

16. DISTRIBUTION STATEMENT (of this Report)

Approved for public release; distribution unlimited

17. DISTRIBUTION STATEMENT (of the abstract entered in Block 20, if different from Report)

18. SUPPLEMENTARY NOTES

*Currently at AFGL, Hanscom AFB, MA 01731

19. KEY WORDS (Continue on reverse side if necessary and identify by block number)
Spacecraft charging, ionospheric electric fields, geosynchronous environment, high latitude ionosphere.

20. ABSTRACT (Continue on reverse side if necessary and identify by block number)
Problems pertaining to spacecraft charging at near-geosynchronous orbit were investigated using data from P78-2 SCATHA collected in 1979-80. These studies included specification of significant aspects of the near-geosynchronous environment, effectiveness of active control systems and verification of computer modeling of satellite potentials. Environmental specification studies were made of major plasma sheet boundaries, near-geosynchronous particle fluxes and long term prediction of hazardous geomagnetic conditions.
(Continued on back)

DD FORM 1473 1 JAN 73

$X_{xe-e}(+)$

20.
Work was begun on magnetospheric modeling. Unfortunately, the particle beam active control system caused the failure of two instruments. These events were thoroughly studied but some uncertainty remains concerning the causes of the problems. Comparisons of spacecraft discharge techniques indicated the X_e^+ plasma source was the preferred operational mode. Satisfactory agreement with observed charging levels was obtained when the NASCAP/AFGL computer model was used with environmental input derived from observed particle fluxes.

A secondary research effort focused on studies of ionosphere-magnetosphere interactions in the polar cap and auroral zone. Air Force measurements of S3-2 electric and magnetic fields and electron and thermal plasma fluxes were used as well as DMSP auroral imagery.

Scientific Personnel

Principal Investigators

    Joan Feynman   5/79 - 9/81
    Senior Research Physicist, Boston College

    William J. Burke 10/78 - 4/79
    Senior Research Physicist, Boston College

Senior Scientific Investigating Team

    Joan Feynman

    William J. Burke

    M. Susan Gussenhoven

    Michael A. Heinemann

    Nicolas A. Saflekos

Contributing Scientific Investigators

    Jeffrey M. Forbes

    Gabor J. Kalman
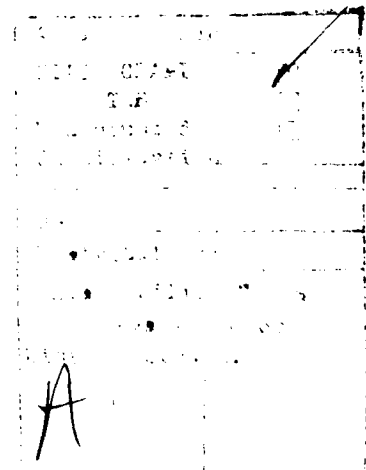
    Walther N. Spjeldvik

    Gordon Wrenn

TABLE OF CONTENTS

CONTRACT OBJECTIVES

The purposes of the studies carried out in fulfillment of this contract were twofold. The major effort was expended on studies pertaining to spacecraft charging at geosynchronous orbit which had as their aims:

1. The specification of the environment at geosynchronous orbit

2. The evaluation of the effectiveness of active control systems as a function of environmental condition

3. Verification and updating of computer code models for satellite potentials.

A secondary effort involved studies of the large scale electric fields in the high latitude ionosphere. The work made extensive use of the Air Force Geophysics Laboratory instrumentation on SCATHA (P78-2), on S3-2 and on the DMSP satellites.

The SCATHA (P78-2) results are given in Section I which is divided into three tasks according to the listed aims; environmental specification, active control systems, and computer code verification. The large scale electric fields results are in Section II. Each of these sections gives a very brief description of the progress made in that area with references to the over 30 papers that have been prepared. The details of the work can be found in the papers which have been published as technical reports or are appended. References to each of these papers are made in the text. These references are not superscripted and the reader should consult the technical reports or the appended papers. References to papers not supported by this contract are superscripted and the appropriate reference appears at the foot of the page.

1

SPACECRAFT CHARGING AT GEOSYNCHRONOUS ORBIT

PARTICLE AND FIELD ENVIRONMENT

Knowledge of the plasma envrionment at near geosynchronous oroit is required for optimal design of satellites intended to operate for long periods of time in that area of space. From the time of ATS 1 it was known that frequently the satellite was immersed in a hot plasma.[1] Experiments on ATS5 and ATS6 showed that the vehicles could attain spacecraft charging potentials of as much as several kilovolts negative with respect to the plasma.[2] Arcing and differential charging also occurred.

One of the purposes of the SCATHA P78-2 satellite was to investigate and describe the environment that caused charging. To this end a complex system of instruments was carried into space, including electric and magnetic field monitors and instruments to observe electron and ion parameters over a broad energy range. It was envisioned that data from the Air Force Geophysics Laboratory Rapid Scan Particle Detector and its Thermal Plasma Analyzer would be used in carrying out the work on this contract. Unfortunately, the Thermal Plasma Analyzer malfunctioned soon after it was turned on. However, the Rapid Scan Particle Detector (SC-5) operated well and data from that instrument were used in several of the studies described in this Section. A brief discussion of the instrument's operation is given in Appendex I and in the papers referenced there.

Because the major threat ot charging occurs when the vehicle is within the plasma sheet, environmental specification focused on that region of the magnetosphere. As described below, investigations were made of the behavior

---

[1]Freeman, J. W. and J. J. Maguire, J. Geophys. Res. _72_, 5257, 1967

[2]De Forest, S. E. and C. F. McIllwain, J. Geophys. Res. _76_, 3587, 1971

of the boundaries of the plasma sheet and of the fluxes observed to occur within it. It was found that the position of the equatorward boundary of the plasma sheet, as implied from the equatorward extent of diffuse auroral electron precipitation was unexpectedly strongly related to the Kp index of the geomagnetic variability. It was also found that at certain positions of SCATHA's orbit the spacecraft routinely probed the boundary of trapping of high energy particles even at low levels of geomagnetic activity. SCATHA is the first satellite to routinely penetrate this region. The description of the fluxes within the plasma sheet was carried forward by a map showing the regions of highest electron fluxes in the energy range 10 to 80 keV which is so important to spacecraft charging, and it was found that the region of 6 to 7 Re is more frequently hazardous than the region between 5 and 6 Re or between 7 and 8 Re. The most severe environment associated with charging was extensively described. A multiple satellite study of plasma injections showed our data was inconsistent with existing models and a new scenario of plasma injections was developed. These studies are described in more detail below.

If the near geosynchronous environment is to be well described and understood so that predictions of hazardous regions can be made, a magnetospheric model based on the operative physical principles must be developed. A status report on our progress in that regard is given.

It is well established that there is a statistical relation between geomagnetically disturbed conditions and spacecraft charging at geosynchronous orbit. We therefore undertook the development of a method of prediction of geomagnetic conditions to be used for spacecraft design. We found that if the yearly average value of one of the geomagnetic activity indices could be predicted the number of disturbed and hence hazardous days in the expected year is easily estimated. We also showed, however, that there is a 90 year

3

cycle in geomagnetic activity and the last minimum was about 1901 and so the level of activity can now be expected to generally decline in the next decade relative to the last two decades. However, activity can be expected to be quite erratic and generally unpredictable, suggesting the spacecraft design should be conservative with respect to charging.

There are several other factors besides the particle and field properties that strongly influence spacecraft charging. The most important of these is the ultraviolet flux that causes secondary electron emmision from satellite surfaces. A model was developed of the attenuation of UV due to the earth's atmosphere and the entry into eclipse. In addition, the fate of ion contaminant clouds from spacecraft effluents was studied.

MAJOR BOUNDARIES OF THE PLASMA SHEET

Equatorial Edge

The position of the equatorward edge of the plasma sheet was investigated indirectly by studying the equatorward edge of electron precipitation in the 50 eV to 20 keV energy range as observed by the Air Force Geophysics Laboratory detector onboard the polar orbiting DMSP/F2 satellite (Gussenhoven et al. 1981a, appended paper 1). The detectors and their operation and calibration are described in Hardy et. al. (1979 AFGL-TR-79-0210). It is widely accepted that diffuse auroral electrons come from the central plasma sheet and thus it is expected that the equatorward boundary is the equatorward edge of the plasma sheet. An extensive study of the position of the equatorward boundary was completed in which the corrected geomagnetic latitude of more than 6000 boundary crossings was determined. The time sectors covered were in the 1600-2300 and 0400-1000 MLT magnetic local time sectors. In the evening the equatorward boundaries could be precisely determined from the rise in the total electron flux. The morningside boundary could not always be

clearly delineated. Data were divided into 1 hour magnetic local time bins with approximatley 400 samples per bin. In each of the MLT bins the position of the equatorward boundary was found to be strongly related to the degree of geomagnetic disturbances as measured by Kp. Typical correlation coefficients were 0.8 to 0.9 in most of the time zones studied. The typical value of the slopes of the regression lines in each bin (latitude $= m$Kp $+ b$) was two. The values of the latitude of the equatorward edge determined from these regression lines were projected to the magnetic equatorial plane using the Mead-Fairfield magnetic field model. The projected boundaries are not in good agreement with the injection boundaries of Mauk and McIllwain but are best fit to boundaries derived using Volland-Stern type electric fields with the axis of symmetry rotated into the evening sector for Kp $<$ 2 and into the afternoon sector for Kp $>$ 2 as shown in figure 12 of Gussenhoven et. al, (1981a). In another paper Gussenhoven et. al. (1980 appended paper 2), suggest that most of the 30% increase that had been reported by Meng[1] (1979) in his study of the diurnal variations of the size of the quiet time auroral oval could be explained as simply a reflection of diurnal shifts in the satellites trajectory in the (magnetic local time)-(magnetic latitude) frame of reference and hence is not physically real.

Boundary of the High Energy Trapping Region

The near geosynchronous orbit of SCATHA, (P78-2) is ideal for extending studies of features earlier detected by geosynchronous satellites. SCATHA, (P78-2) sweeps through the geosynchronous region and samples the magnetospheric environment over a widened range of latitude and distance from the earth. Geosynchronous satellites had earlier experienced sudden disappearances and reappearances of electrons and ions with energies above 50 keV. These events were called dropouts and the major kilovolts charging event

---

[1]Meng, C. -I. Diurnal variation of the auroral oval size, J. Geophys. Res. 84, 5319, 1979.

of March 28, 1979 was caused by a particle return from a dropout. A survey of the nightside particle environment as observed by the AFGL Rapid Scan Particle Detector frequently shows dropouts. A scan of the first 88 days of data in the period from January 20 to August 8 permitted the identification of 39 days on which dropouts occurred. A study of the position and geomagnetic activity dependence of these days is described in Feynman et al. (1981b AFGL-TR-81-0270). It was found that the days grouped themselves into dropout rich and dropout poor periods. This is interpreted as an orbit effect and most dropouts at low geomagnetic activity occur on L shells > 7. There was also a region of latitude about 10 degrees wide in which dropouts did not occur during quiet times. The geomagnetic activity dependence of dropout occurrence also was investigated and it was concluded that at SCATHA's orbit both the orbital position and geomagnetic activity must be taken into account in evaluating the chances of experiencing a dropout.

FLUXES WITHIN THE PLASMA SHEET

Multiple Spacecraft Study of Injections

Three different types of particle flux enhancements associated with the plasma sheet have been distinguished; entry into the plasma sheet by crossing the equatorward boundary of convection, entry by crossing the boundary of high energy trapping (return from "dropouts") and sudden increases (injections) experienced when the satellite is already within the plasma sheet. The first two types of enhancements have been discussed above. The injections were examined in a cooperative study with the University of New Hampshire which has a plasma detector on ATS-6 at geosynchronous orbit (Moore et al, 1981, appended paper 3). Several injection events were identified on three different days during which SCATHA and ATS-6 were in favorable positions for joint studies. These events were studied in detail, using SCATHA SC-5 (Rapid Scan Particle Detector)

6

electron and ion data from the detector looking parallel to the spin axis. In addition to these two major satellites, the studies used data from the AFGL magnetometer chain. This permitted the spatial and temporal behavior of the events to be determined more precisely than was possible for most past studies. It was found that the most usual scenarios that were used to describe the type of dynamic injection event studied were not an adequate description. On the basis of these observations, an alternative scenario was developed in which these dynamic injections correspond to the passage across the spacecraft of a "precipitation-flow boundary." Although this type of structure has not been widely discussed in recent years, theoretical treatments of the formation of precipitation-flow boundaries can be found in the literature and earlier observations have been reported (see Moore et al. 1981 for references). The proposed structure is due to the precipitation of particles that are convecting in towards the earth under the influence of the magnetospheric electric field. It separates a region of hot quasi-maxwellian plasma far from the earth from a region of cooler plasma closer to the earth. At the time of substorms the boundary thins and moves radially inward past near-geosynchronous satellites at a speed of a few tens of m/sec in close association with an inward propagating magnetic disturbance. As the boundary recedes outward after the substorm it produces gradual decreases with higher energies decreasing first. Although our study showed that the usual models of substorm injections were invalid the validity of this new description of substorms can only be established by further research.

Electron Fluxes in the 10-80 keV Range

The importance of 10-80 keV electron flux levels to spacecraft charging has been established in empirical studies and is also reflected in the charging levels predicted in the NASCAP code. Intense 10 to 80 keV electron fluxes combined with an absence of low energy electrons are associated with major charging events both in sunlight and in eclipse. In order to define the

particle environment of 10-80 keV electrons an extensive survey of SCATHA data was carried out.

To describe the environment in a single and convenient format the near-geosynchronous region was divided into bins, each bin covering one hour in magnetic local time and one earth radius in equatorial distance. The frequency of occurrence of selected flux levels in each bin was determined. For each flux level and energy range, the "degree of hazard" for a bin was defined as the percentage of passes the satellite made through that bin that were accompanied by fluxes higher than the chosen level. The method of analysis and the resulting flux maps are described in more detail in Appendix II. At both energy levels the most hazardous time periods appear in the post midnight quadrant and into the early morning hours. The most hazardous region moves toward midnight for the higher flux levels. In addition, there is a clearly distinguishable 3 bin region between 0100 and 0400 MLT and between 6 and 7 Re in which high 10 to 80 keV electron fluxes are more than twice as common as in the surrounding region. Hence a satellite at geosynchronous orbit would have experienced significantly more frequent high flux levels than were experienced by SCATHA.

Worst Case Charging Environment

A survey of data from the first year of the P78-2 SCATHA satellite operations showed that the highest level spacecraft frame charging (φ_f) both in the sunlight (-340V) and in eclipse (>-8kV) occurred on 24 April 1979. Analysis of the data in Mullen et. al. (1981) (AFGL-TR-81-0231) showed that if the sunlight charging environment had been present during eclipse, the vehicle would have charged in excess of 15kV which is above any known charging level observed to data for the SCATHA satellite. Therefore, the environment at the peak of the sunlight charging at ~0650 UT 24 April 1979 was chosen for the "worst case" study. The environment at this time is characterized by an injection of high

energy (30-335 keV) electron fluxes whose combined current correlates with ϕ_f with a correlation coefficient of 0.95. The fluxes are highly anisotropic, maximizing perpendicular to the magnetic field. The low energy ions are near background. The measured electron distribution functions, when fit to double Maxwellians by a least squares technique, showed that the high and low temperatures remained nearly the same, while the density of the high energy component followed the charging levels. The injection occurred simultaneously with the rapid return of the magnetospheric magnetic field to a more dipole-like configuration.

STATUS OF NUMERICAL MODELING OF THE MAGNETOSPHERE

The purpose of the magnetospheric modelling effort is to develop a computer program to predict the particle and field environment of Air Force satellites. Beginning with the Rice University computer program developed by R. A. Wolf and M. Harel, we plan to extend the model to include more physical mechanisms and larger regions of the Earth's magnetotail. Tasks completed or in progress under this contract include the following:

(1). The Rice University magnetospheric simulation computer program has been run successfully on the VAX 11/780 at Boston College. Extensive tests done in close collaboration with the Rice group have shown that the program functions normally.

(2). We have developed an initial version of our own modificaion of the magnetospheric simulation program. The program solves the same equations as the Rice program and should give the same results. The approach is designed to eliminate difficulties associated with the Rice group's treatment of inner edges. One advantage of the present approach is that it can handle localized injection in a natural way.

(3). We have begun an effort to include parallel electric fields in the

9

model. The nature of the effort, which is in progress, is to establish a variational principle which simultaneously accounts for the particle distribution and profile of the potential along each magnetic field line, taking into account the thermal and drift motions of the particles.

SCATHA MISSION TIME GEOMAGNETIC CONDITONS AS A SAMPLE OF PAST AND FUTURE CONDITIONS

In order to apply our understanding of the relationship between spacecraft charging and particle and field environments to the problems of spacecraft design, it is necessary to be able to estimate the frequency with which particular hazardous environments can be expected to occur in the orbit of the vehicle. This problem is made tractable by the description of magnetospheric conditions in terms of typical conditions associated with different levels of geomagnetic activity and then by studying past geomagnetic activity with the aim of identifying trends and patterns that permit a reasonably accurate prediciton of activity levels that would be experienced by the satellite during its active lifetime. The complexity of this problem can be appreciated by considering the results of Feynman[1] (1979) who, in 1977 attempted to predict the annual average level of geomagnetic activity that would prevail in 1979 and 1980, the period of the SCATHA mission. Her predictions were made using all the then available knowledge of trends and periodicities in geomagnetic and solar data. She concluded that it was necessary to understand two types of cyclic variations in yearly average activity, a "long cycle" due to a variation with a period of about 90 years, and a solar cycle variation with a period of 11 years. The two variations are about equal in amplitude so neither can be neglected. Since little was known about the long cycle, Feynman had no alternative but to

---

[1]Feynman, J. The 21st solar cycle: aa index of geomagnetic, Solar Terrestrial Predictions Proceedings. Boulder, CO 1979.

base the prediciton on the assumption that the level of the long cycle variation would remain the same during the SCATHA period as it had been for the last 15 or 20 years.

The actual activity was barely within the range of the predicted levels during the first year of the SCATHA mission but was well below the range for the second year, suggesting that the long cycle variation was effecting the activity level in an important way. In the work carried out under this contract the problem of prediction was approached in two ways, one by comparing the positions of important magnetospheric boundaries to activity indices and the other by studying the past occurrence of activity.

Studies of the position of the high latitude trapping may also be possible from studies of low altitude DMSP data (Feynman and Hardy, in progress). We have tentatively identified the boundary between electron precipition characteristic of diffuse and of discrete aurora as the low altitude expression of the trapping boundary. Over two thousand boundaries in the Northern hemisphere were identified from the DMSP data and a statistical analysis of the relation of the boundary latitudes as a function of Kp was carried out. The time periods covered were 1900 to 2200 and 0400 and 0800 and correlation coefficients of about 0.4 to 0.8 were found.

The long term behavior of the plasma sheet position was studied by Feynman and Silverman, (1980) (appended paper 4) and Silverman and Feynman (1981) (AFGL-TR-81-0172) through studies of latitudes at which aurora were seen in Sweden and the United States during the period from 1721 to 1876. A more equatorward position of the observation of aurora indicates that the plasma sheet has moved inward. They found that during the period from 1868 to 1876. the number of aurora seen in Sweden was strictly proportional to Kp (a correlation coefficient of 0.97) but they warn that the relationship may change

11

from time to time. They also found that the data were most reasonably interpreted as indicating that a minimum of the long cycle (80-100 years) of geomagnetic activity occurred about 1811 and was characterized by a low level of activity occurring relatively far north. Comparison of Swedish and American sightings showed that throughout the 18th and 19th centuries aurora appeared in a characteristic band of latitudes for periods of perhaps 20 to 35 years and then, over a period of 2 or 3 years, moved to a new characteristic latitude. The causes of this behavior remain unknown but if it continues to occur during this century the average position of the plasma sheet within the magnetosphere would remain more or less constant for many years and then change relatively rapidly (in response to some change in the solar wind). This has not yet been observed to occur but systematic observation of plasma sheet positions have only a short history. Such a change would cause a relatively sudden and severe change in the average properties of the environment experienced by a geosynchronous satellite.

The problem of identifying patterns and trends in geomagnetic activity with the aim of advancing our predictive ability was studied in Feynman (1980a) (appended paper 5), and Feynman (1981) (appended paper 6). The question of how many indices are necessary to characterize the condition of the magnetosphere was approached by studying the behavior of the ring current index D_{st}, and the midlatitude three hour index am (or equivalently aa) over the last two solar cycles. Both am index an ap measure disturbance levels in a three hour interval. The D_{st} index is a measure of the magnetospheric particle population in the energy range of perhaps 10-100 keV. It was found (Feynman, 1980) that the annual averages of the midlatitude indices and the Dst appeared to be linearly related during solar cycle 19, but the annual average Dst remained remarkably constant in spite of a strong variation of the annual average

12

midlatitude indices during solar cycle 20. Further, the two types of indices were related to different functions of solar wind parameters, from which it can be concluded that the ring current is not directly produced by substorm injections. Apparently the increased ring current and substorm activity are two separate aspects of magnetospheric convection and ideally indices of both type are necessary to completely characterize the condition of the magnetosphere. These results were used in the selection of days made for the SCATHA Atlas in that care was taken to include data from periods with as wide a selection of both Dst and Kp conditions as possible.

In a second study of patterns, one hundred years of data on the yearly average aa index (aa is a less accurate version of am and is computed from two stations for early periods when am is not available) were studied (Feynman, 1981 appended paper 6) and remarkably systematic behavior was discovered. It has been known for at least 30 years that geomagnetic activity did not vary as sunspot number. During each 11 year sunspot cycle, in addition to the high activity associated with sunspot maximum, geomagnetic activity shows another peak about 3 years later. This second peak may be either stronger or weaker than the sunspot related peak. Further, whereas geomagnetic storms at sunspot maximum typically do not recur 27 days later, storms in the second peak are recurrent. It was found in Feynman (1981) that the yearly average aa index could be considered as the sum of two terms, one strickly proportional to the sunspot number and the other defined as the remainder. Dividing the time series of the annual average aa from 1870 to 1975 in this way it was found that the series decomposed into the sum to two equally strong periodic variaitons, each having the period of the sunspot cycle but differing in phase by almost but not quite 180°. The amplitudes of the two periodic variations are very closely related.

The amplitudes of both oscillations increase smoothly and steadily from

13

1900 to 1960, corresponding to the ascending branch of the Long Cycle of solar activity which has been established elsewhere as occurring in the solar wind with an average period since the Middle Ages of 87 years. The smooth and orderly evolution of the oscillation amplitudes was interrupted in 1960 when a pair of less intense oscillations occurred. This interruption of pattern suggests that we are now in the declining phase of the Long Cycle which is to be expected since the average cycle period is eighty-seven years and the last minimum was in the first decade of this century. Thus, all our space based studied have been made during a declining Long Cycle phase. We do not know if the solar wind is much the same or vastly different during the ascending phase. However, the small amount of data that we have since 1960 and from the last declining Long Cycle phase during the final quarter of the 19th century suggests that the value of the annual average aa index may be less well ordered during a declining phase than during an ascending phase. It may, therefore, be unusually difficult to predict geomagnetic behavior in the coming years, suggesting the wisdom of a conservative approach in the estimation of the expected frequency of hazardous space environments.

If a prediction of the annual average ap (or equivalently aa) index is made it is then required to evaluate what the prediction implies in terms of frequency of harzardous environments. In order to do this we studied the distribution of values of aa indices in years with a wide selection of annual average aa. (Feynman, in progress). Using the 730 half day aa indices for each year, we found that the distribution of values depended almost entirely on the value of the annual average, it did not depend on the phase of the 11 year sunspot cycle or on the phase of the Long Cycle. Further, the number of quiet half days (aa < 10 which corresponds to a 3 hour Kp > 4) is strongly related to the annual average aa. These results can be used to estimate the expected

14

number of disturbed and quiet days as a function of the expected annual average aa. For example, if the expected annual average aa is about 20 then approximately 30 to 40 disturbed half days and of the order of 200 to 250 quiet half days can be expected to occur. It is planned to include these results in the SCATHA Atlas.

OTHER TOPICS

Solar Flux Effects

In order to analyze the varying potentials during eclipse entry or exit, a detailed understanding of the variation of the solar-generated photoelectric flux is required. As materials can have radically different photo-emission properties as a function of wavelength, it is important that the amount of illumination as a function of wavelength be specified. A detailed model of photoemission was derived based on first principles (Forbes, and Garrett, 1980 AFGL-TR-80-0185, Garrett and Forbes, 1981 appended paper 7). The model allows a determination of the photoelectron flux as a function of wavelength which, when coupled with a model of atmospheric density, permits an estimation of the total photoelectron current as a function of satellite position in the earth's penumbra. The model of the variations in solar flux was developed in terms of wavelength, atmospheric attenuation and 11 year solar cycle.

As a test of the model it was successfully applied to the case of a tungsten surface on ATS 5, for which the photoemission properties were known. The model also fit observations of the photoelectron flux during eclipse passage at geosynchronous orbit and allowed estimates of the corresponding saturation current.

Ion Contaminant Clouds

The creation, ionization and subsequent transport of an artifically produced contaminant cloud in the immediate vicinity of a spacecraft at

geosynchronous orbit was examined by Garrett and Forbes (1979 AFGL-TR-80-0185). The results indicated that there was a small chance that X_e^+ emitted from SCATHA P78-2 would be detectable by GEOS II. An experiment of this type was carried out but it was unsuccessful. The analysis was also applied to roughly estimate the ionization cloud that could be expected from such projected systems as large space stations (air leakage) or a solar power satellite (argon thrusters). It was found that only for a truly large geosynchronous space habitat would the ion density exceed 1000 cm^{-3} over a significant volume.

Ion Trajectories

Particle trajectories in a model electric field were studied (Shima et al. 1981) (AFGL-TR-81-0167) in order to determine the feasibility of neutralizing the potential differences on a spacecraft. It has been proposed that the neutralization can be accomplished by emitting ions from the positively charged surface region of the spacecraft and by letting this current impact on the negatively charged surface region. In order to investigate the main features of the proposed scheme the geometry of the problem was approximated by two conducting infinite half planes. The trajectories of a positive ion emitted at some point on the positively charged infinite half plane with given initial velocity and given direction of emission where investigated.

<div align="center">PARTICLE BEAMS</div>

THE EVENTS OF MARCH 30, 1979

On March 30, 1979 The P78-2 electron gun, SC4-1, was operated for the first time to eject a beam of energetic electrons from the spacecraft. A wide dynamic range of electron currents and energies was available and was used to charge the spacecraft frame positive with respect to the ambient plasma. The use of the electron gun had many scientific and engineering results. Some of these results were unexpected and some not only unexpected but quite undesirable. In this

latter class are the failure of two instruments and the momentary interruption of the normal telemetry stream caused by the ejection of 6 mA of 3 keV electrons. The operation of the gun and its effects on the spacecraft on March 30 were studied by a team of experimenters (Cohen et al. 1981a) (AFGL-TR-81-0270).

The gun was operated before the satellite entered eclipse and during the time of eclipse. The ranges of ejected electron currents and energies were from 0.1 mA to 13 mA, and 0.3 keV to 3 keV. The spacecraft frame and dielectric surfaces on the spacecraft went positive with respect to points 50 meters from the satellite when the gun was opeated. Depending on ejected electron currents and energies, spacecraft frame-to-ambient-plasma potential differences between several volts and 3 kV were generated. Simultaneously, lower potential differences were created between the satellite and a point 3 meters from the satellite. Sample surface potentials were measured during gun operations. When the electron gun was turned off, the vehicle frame swung sharply negative.

Arcing was detected by pulse monitors in several electron beam modes of operation. The ejection of a beam of 6 mA of 3 keV electrons caused three distinct payload failures and created a transient problem in the telemetry system. An attempt was made to determine the exact time, nature, and cause of these failures; a specific effort was made to identify which components failed and why they failed. Analytical and modeling techniques were used to examine possible spacecraft and payload responses to the electron beam ejection which might have contributed to the arcing and payload failures. An analysis of circuitry has identified the components that were affected and has established the basis for determining the causes of the problems. Theoretical studies and measurements analysis have focused on two hypotheses: arcing along the boom to

17

the SC2 sphere, and impact of beam electrons on the SC2 sphere. These

investigations still left a great uncertainty as to the destructive mechanism.

During the March 30 electron beam operations, in sunlight and in eclipse,

the Rapid Scan Particle Detector, measuring electrons and ions in the energy

range ~0.05-10^3 keV, (both perpendicular and parallel to the spin axis of the

satellite), operated when the electron beam was operating. These data have been

studied by Gussenhoven et al. 1981b (AFGL-TR-81-02707, 1981). The shift in

the electron distribution function indicated that the satellite became

positively charged to a value much less than beam energy for 0.01 mA, and a

value approaching beam energy for 0.10 mA. Complex pitch angle modulations of

the spectra were separately decomposed for each beam operation. When electrons

were emitted perpendicular to the magnetic field with an energy of 3 keV and a

current of 0.10 mA they returned as a coherent beam only to the parallel

detector. Throughout the beam operations the pitch angle distributions showed

electrons with energy less than beam energy streaming along the field line.

Analytic expressions for the satellite electric field were constructed and

particle trajectories were determined for the observed initial conditions on the

electron beam.

DISCHARGING TECHNIQUES

Since spacecraft charging at geosynchronous altitude is caused by the

accumulation of negative charge due to high energy electrons, a method of

ejecting electrons should be used on satellites to discharge the spacecraft.

There are several different techniques of ejecting electrons from space vehicles,

with comparative advantages and disadvantages for each. The use of the

SC4 payloads on the P78-2 satellite presented the opportunity to compare three

techniques: the ejection of a beam of electrons from an electron gun; the

emission of electrons from a heated, baised filament; and the ejection of a

plasma containing energetic positive xenon ions and low energy electrons. Comparisons of these techniques were made during April, 1979 and are reported on by Cohen et al. (1981 AFGL-TR-81-0270). On April 22, 1979 when the P78-2 satellite ground-to-plasma potential difference reached several hundred volts, each of the three techniques was able to completely discharge the satellite. The comparative effectiveness of the techniques were clearly shown on this day. On April 24, 1979 the satellite charged to -8 kV upon entering eclipse. The electron gun, emitting 1 mA of electrons with 150 eV energy, reduced the difference in potential between satellite ground and the ambient plasma to -1 kV, but could not completely discharge the satellite. The plasma source completely discharged the satellite. It was concluded from these operations that a plasma source represents the best way of discharging spacecraft in geosynchronous orbit.

SPACECRAFT CHARGING ANALYSIS

NASCAP/AFGL

The NASCAP/AFGL code simulates the electrostatic charging of a three dimensional object at geosynchronous environments. The charge distribution on the spacecraft surfaces is calculated from the total current to the spacecraft taking into account proton and electron incidence, backscattering, and secondary emission (electrons only). The NASCAP/AFGL code has excellent graphics for object representations and external potential contour plotting.

A large number of runs of the NASCAP/AFGL code were made on the CDC-6600 computer at AFGL in order to update, verify and validate the code. These runs were documented and reported in the form of two AFGL technical memoranda, (Tautz et al. 1979, AFGL-TM-22, Tautz et al. 1980, AFGL-TM-39).

Every NASCAP/AFGL code run yields information about the spacecraft ground potential relative to plasma ground and about potentials of dielectric surfaces relative to spacecraft ground.

Careful modeling of the SCATHA spacecraft fed into the NASCAP/AFGL code and accurate automated modeling of the measured plasma environment, used as input to the code, resulted in spacecraft charging predictions which compare well to measured values of spacecraft ground potentials and to differential charging potentials which were measured by the SC-1 surface potential monitors. Details of the comparisons between theory and experiment can be found in Rubin et al. (1981) (AFGL-TR-81-0270) and in Saflekos et al. (1981b). Some of our principal results are stated below.

A quick approximation of the potential to which a material would charge in a geosynchronous plasma can be obtained using a subprogram of NASCAP/AFGL called MATCHG (Materials Charging).

The NASCAP/AFGL simulations for various days compare well to SCATHA data including conditions of sunlight, penumbra, eclipse and electron gun emissions.

Based on measured solar UV intensity profiles the NASCAP/AFGL predicts correct forms of sun-shade asymmetric surface potentials consistent with the SSPM (Spacecraft Surface Potential Monitor) measurements. Even transient potentials of deviation less than 30 seconds have been successfully simulated by the NASCAP/AFGL code.

In an active experiment simulation the NASCAP/AFGL code, with its single particle trajectory treatment of spacecraft potential affected by electron emissions, has predicted the spacecraft ground potential to within 200 volts.

An extensive study of spacecraft charging was undertaken using data from the SC-5 instrument on SCATHA and the NASCAP/AFGL code (Saflekos et al. 1981b). Investigated were the floating potential and the differential charging of the spacecraft as deduced from Liouville's theorem and computed by the NASCAP/AFGL code. The highest resolution data from the SCATHA SSPM experiemnt were compared to the SC-5 charged particle fluxes and to the NASCAP/AFGL computations. This study led to the following conclusions: a) Short-time charging events on the

spacecraft are associated with short-time increases of the intensity of 10 keV to 1 MeV electrons, b) Short-time changes of the spacecraft differential potential are associated with short-time changes of the spacecraft floating potential, c) Solar UV intensities in penumbra, as monitored by the solar panels total current, anticorrelate with the spacecraft floating potential, d) Based on the measured profiles of UV intensities, NASCAP predicts correct forms of sun-shade asymmetric surface potentials consistent with the SSPM measurements, e) Certain enhancements of the intensity of energetic ions ($E_i > 100$ keV) have been observed to diminish the absolute value of the spacecraft surface potential, f) Spacecraft discharging events in time shorter than 20 sec. have been observed without obvious changes in the spectrum of the energetic ($E > 10$ keV) plasma, g) Partial discharging of the spacecraft has occasionally been observed upon entry into a magnetically depleted region, h) Steady state potentials and transient potentials of duration less than 30 seconds have been successfully simulated by the NASCAP code.

HIGH LATITUDE AND PLASMA FIELDS

Studies were undertaken of the electric and magnetic fields at high latitudes. The studies were focused on the ionosphere-magnetosphere interaction. In addition, two studies of the lower latitude ionosphere were completed and are reported on in this section.

POLAR CAP

For the polar cap Smiddy et al. (1980 appended paper 8) presented relationships between convective electric fields, Birkeland currents and ionospheric conductivity at high latitudes. These phenomena were investigated using simultaneous measurements of S3-2 electric and magnetic fields and electron fluxes. Cases in which the polar cap was in sunlight and darkness were studied to assess the importance of ionospheric conductivity. It was found that when the ionospheric conductivity was high, as it normally is in the auroral

21

zones and the sunlit polar cap, Birkeland current sheets exist that deflect
the magnetic field approximately in the direction of the convection, typically
anti-sunward in the polar caps and sunward in the auroral zones. Under winter
conditions (a dark polar ionosphere), no large-scale anti-sunward deflection of
magnetic field lines is found in the polar cap. Magnetic field deflections in
the auroral zone are the result of the region 1/region 2 current systems. In
the cases studied, region 2 currents are not observed to extend significantly
poleward of the electric field reversal. This result was interpreted as
indicating the existance of strong conductivity gradients near the poleward
boundary of the auroral oval, even in sunlit conditions. Deflections of
magnetic field lines in the summer polar cap result from currents which serve to
link the high latitude generator to the polar ionospheric load. Two types of
linkage appeared in the data: (1) Region 1 currents are greater than region 2
with the excess region 1 current flowing across the polar cap from dawn to dusk.
(2) An extra set of field-aligned currents exists which is clearly detached
from those of region 2 and is entirely poleward of the convective electric field
reversal. It was found that the evidence for anti-sunward convection on closed
·ι· lines threading the boundary layer which had been reported by others
earlier, was inconclusive. With our more complete data set, there was some
evidence at ionospheric altitudes for a boundary layer, but in such cases there
was only a modest (few kV) potential drop across the layer and insignificant
Birkeland currents.

The electric and magnetic field characteristics of discrete arcs in the
polar cap were studied by Burke et al. (1982) (appended paper 9). Simultaneous
electric field, magnetic field and electron flux measurements from three dawn-
dusk passes of S3-2 were analyzed for signatures of sun-aligned arcs in the
polar cap. Two of the passes were over the summer and one over the winter polar
cap. In all three cases IMF had a strongly northward component. During the pass

over the winter polar cap the electric fields were highly irregular but tracked with nearly one to one correspondence to the transverse magnetic fluctuations. Upward Birkeland currents were embedded in regions of negative space charge. The carriers for the upward Birkeland currents were weakly field aligned fluxes of electrons with a temperature of a few hundred eV that had been accelerated through a potential drop of ~1 kV. The two summer polar cap passes differed from each other in their large scale electric field patterns. In one pass the electric field was irregular with the upward Birkeland currents in negative space charge regions. In the other summer hemisphere pass convection was sunward in the central polar cap. Small-scale Birkeland current systems, possibly signatures of arc-like structures were found in regions of both sunward and antisunward convection. In this pass variations in the electric and magnetic field did not always show the strong correlation found in the other two cases, due to the effects of electrojet activity near the flanks of the polar cap. The measurements were found to be consistent with a "static" model for the electrical coupling between the ionosphere and magnetosphere with the generator at the magnetopause.

AURORAL REGION

In the auroral zone studied, Saflekos et al. (1981a) (appended paper 10) presented the variability of field-aligned currents using dual spacecraft observations in the configuration of the mother-daughter experiment. From an analysis of four near-coincident passes of S3-2 and Triad satellites it was established for the first time that the field-aligned current sheets are a few degrees thick, extend to 1100 km in the east-west direction and cover an altitude range from 300 to 800 km. Furthermore, the field-aligned current sheets exhibit small motion in the north-south direction while preserving their latitudinal widths. The field-aligned current densities do not show pronounced gradients either with altitude or with longitude. The convective electric field

23

reversal is located at the poleward termination of regions 1 field-aligned current system or equatorward of this boundary, not deviating by more than one and a half degree from it. Simultaneous small scale magnetic and electric field variations superimposed on the region 1 disturbance and observed at widely separated local time may correspond to discrete auroral arcs on closed as well on an open magnetic field lines. To our knowledge, except for statistical studies, these are the first reported sets of measurements suitable for making the distinction between the spatial and the temporal nature of transverse magnetic field variations.

The paper by Shuman et al. (1981) (appended paper 11) discussed measurements by the S3-2 satellite of magnetic field, electric field, and auroral electron precipitation during a multiple polar magnetic substorm. The principal findings of this study are listed below:

(1) The observed direction of the electric field component indicated closure for the major field-aligned current pattern by Pedersen current flow in the ionosphere, consistent with a magnetospheric current source. (2) Values of the height-integrated Pedersen conductivity, calculated from the gradients of the electric and magnetic field components, were typically in the range of 10-30 Ω^{-1} in the current-carrying regions during active times. At such times, particle precipitation on the nightside became the major factor in controlling the magnitude of the ionospheric conductivity, outweighing the influence that sunlight has in quiet times. (3) In regions of increased fluxes of precipitating electrons in the nightside auroral oval, current densities calculated from electron fluxes in the energy range 0.08- to 17-keV accounted for up to 50% of the upward currents, increasing to better than 70% during the most intense substorms period. (4) In each of the three auroral oval crossings on the nightside, an intense upward current sheet was observed at the equatorward side of the westward electrojet, just poleward of the electric field

24

reversal associated with the Harang discontinuity. (5) During the most intense current period, the region of field-aligned currents was compressed down to L shell values 2.2 to 5.1 within the trapping region, indicating that the equatorial source of these currents was the inner magnetospheric plasma inside the outer Van Allen radiation zone rather than the distant plasma sheet or the boundary layer.

Burke et al. (1980a) (appended paper 12) presented detailed observation from a late evening sector pass of S3-2 over the northern auroral zone which were compared with nearly simultaneous DMSP imagery. High time resolution measurements were presented from electric field, magnetic field, energetic electron (80 eV < E < 17 keV), and thermal plasma detectors. The region of diffuse aurorae was characterized by nearly isotropic electron fluxes and slowly varying (< 20 m V/m) electric fields. The Birkeland currents in this region were predominantly into the ionosphere with embedded, narrow sheets of upward currents. Simultaneous magnetometer and satellite potential fluctuations show that the upward current sheets are real and that these upward currents are probably carried by precipitating, low-energy plasma sheet electrons. Poleward of the diffuse aurorae, the convective electric field varied rapidly in magnitude, anticorrelating with the intensity of precipitating electrons. An inverted-V structure was observed above a visible arc. An intense downward current sheet (> 10 μ A/m^2) was found near the equatorward edge of the arc. At this place the ionospheric thermal plasma was near marginal stability for the onset of 0^+ ion cyclotron turbulence. An electric field component parallel to B of ~ 10 mV/m was measured in this region of strong downward current. The plasma and electric field distributions in the vicinity of the arc suggest that the auroral electrojet was distributed over the region of diffuse aurora but was most intense near the equatorward boundary of the auroral arc.

25

In the subauroral latitudes an examination of regions of strong convection electric fields ($E > 50$ n V/m) equatorward of the auroral zone was made on the basis of data from the S3-2 satellite in 1976 (Rich et al. 1980 (appended paper 13)). Only seven examples were found, which indicated a low occurrence rate even after accounting for the gaps in data coverage. While this phenomenon did not correlate with the magnitude of Kp or AE, it was always substorm related. The electric field and magnetic field data indicated that the electric field is generated by plasma sheet ions being driven closer to the earth than plasma sheet electrons by magnetospheric convection in the evening sector. The existence of a net field-aligned current into the ionosphere through the region indicated the presence of latitudinal conductivity gradients. The depletions of ionospheric particles near regions of strong field-aligned currents (> 1 $\mu A/m^2$) into the ionosphere indicated that upward moving ionospheric electrons carry the current. The evacuation of the E region approximately 1 minute after the onset of the electric field as suggested elsewhere was not supported by the data, but it may occur on a time scale of ~ 30 min. If both the F region and E region are depleted in the strong convection regions, the result may be a naturally occurr- 'hole' in the ionosphere.

LOW LATITUDE IONOSPHERE

The interaction of the magnetosphere and ionosphere is discussed in several studies that utilized S3-2, as has already been noted. In addition, two studies concentrating on the ionosphere itself were carried out using Defense Meteorological Satellite Programs (DMSP) thermal ion density measurements. (Burke et al., 1979, Burke et al., 1980b) (appended papers 14 and 15). In one, the observations were used to study the longitudinal distribution of equatorial spread F occurrence in the topside ionosphere. The data were taken in the postsunrise local time sector during the September 1977 magnetic storm. In agreement with previous studies of the longitudinal variability of evening

26

sector spread F, a higher frequency of occurrence was found in the American than the Asian sector. The results were interpreted using a quasi-three-dimensional model of the collisional Rayleigh-Taylor instability. It was shown that for the same initial ionospheric conditions and the same initial depletion at the magnetic equator, large plasma bubbles are more apt to reach the topside at longitudes of the American sector than at longitudes of the Asian sector. In the other study (Burke et al., 1979) the plasma density measurements showed the existence of significant plasma depletions near the magnetic equator in the postsunrise hours at 840 km. The phenomenon was observed regularly during magnetically quiet times near the equinoxes. The magnitude of the depletion depended upon longitude and the time elapsed since sunrise in the lower F region. It was significantly less pronounced or absent near the solstices. During magnetically active periods the low-latitude topside ionosphere was modified due to vertical E x B plasma drifts in the predawn sector. The quiet time equinox observations were interpreted in terms of a diurnal flux tube filling model. It was suggested that the observed equatorial depletions result from a pair of plasma fronts that are moving upward from conjugate ionospheres and that are associated with the early stages of the postsunrise refilling process of the low latitude topside ionosphere.

27

PUBLICATIONS SUPPORTED IN PART BY USAF CONTRACT F19628-79-0031

1979

Burke, W. J., R. C. Sagalyn, R. G. Rastogi, M. Ahmed, D. E. Donatelli and
    R. J. L. Wildman, Post Sunrise Refilling of the Low Latitude Ionosphere, J.
    Geophys. Res. 84, 4201, 1979.

Feynman, J. and S. M. Silverman, Variations of the Solar Wind and Solar Cycle in
    the Last 300 Years, NASA Conf. Publ. 2098 Study of the Solar Cycle from
    Space, 265, 1979.

Hardy, D. A., M. S. Gussenhoven, A. Huber, The Precipitating Electron Detectors
    (SSJ/3) for the Block 5D/Flights 2-5 DMSP Satellites: Calibration and
    DataPresentation, AFGL TR-79-0210, 14 Sept. 1979. ADA083136

Sagalyn, R. C., R. O. Hutchinson, S. Gussenhoven, Editors, Proceedings of the
    Air Force Geophysical Laboratory Workshop on Geomagnetism, April 6-7, 1979,
    AFGL TR-79-0192, 20 August 1979. ADA082308

Tautz, M. F., K. H. Bhavanani, N. A. Saflekos, R. E. McInerney, A. G. Rubin,
    SSPM Experiment Simulation Study for the April 24, 1979 Charging Event,
    AFGL Technical Memorandum 23, 1979.

1980

Burke, W. J., D. A. Hardy, F. J. Rich, M. C. Kelley, M. Smiddy, B. Shuman,
    R. C. Sagalyn, R. P. Vancour, R. J. L. Wildman and S. T. Lai,
    Electrodynamic Structure of the Late Evening Sector of the Auroral Zone, J.
    Geophys. Res. 85, 1335, 1980b.

Burke, W. J., D. E., Donatelli and R. C. Sagalyn, The Longitudinal Distribution
    of Equatorial Spread F Bubbles in the Topside Ionosphere, J. Geophys. Res.
    85, 1335, 1980b.

Feynman, J., and S. M. Silverman, Auroral Changes Druing the 18th and 19th
    Centuries and Their Implications for the Solar Wind and the Long-Term
    Variation of Sunspot Activity, J. Geophys. Res., 85, 2991, 1980.

Feynman, J., Implications of Solar Cycles 19 and 20 Geomagnetic Activity for
    Magnetospheric Processes, Geophys. Res., Ltrs; 7, 971, 1980.

Forbes, J. M., and H. B. Carrett, Atmospheric Effects on the Time-Varying
    Photo-Electron Flux from Satellite Surfaces, AFGL TR-80-0185, ERP 706,
    1980. ADA092446

Garrett, H. B. and J. M. Forbes, The Evolution of Ion Contaminant Clouds at
    Geosynchronous Orbit, AFGL TR-80-0033, 1980. ADA080783

Gussenhoven, M. S., D. A. Hardy, W. J. Burke, Comment on "Diurnal Variation of
    the Auroral Oval Size" by C. I. Meng, J. Geophys. Res., 85, 2373-2374, 1980.

Gussenhoven, M. S., Comparison of SC-2, Sc-5, and SC-9, informal report, 1980.

1980

Rich, F. J., W. J. Burke, M. C. Kelley and M. Smiddy, Observations of Field
Aligned Currents in Association with Strong Convective Electric Fields at
Sub-auroral Latitudes, J. Geophys. Res., 85, 2335, 1980.

Saflekos, N. A. and T. A., Potemra, The Orientation of Birkeland Current Sheets
in the Dayside Polar Regions and its Relationship to the IMF J. Geophys.
Res., 85, 1987, 1980.

Smiddy, M., W. J., Burke, M. C. Kelley, N. A., Saflekos, M. S. Gussenhoven, D. A.
Hardy and F. J. Rich, Effects of High Latitude Conductivity on Observed
Convection Electric Fields and Birkeland Currents, J. Geophys Res., 85,
6811, 1980.

Tautz, M. F., N. A. Saflekos, A. G. Rubin, SSPM Experiment Simulations for 1979
Day 87 and Day 114 Charging Events, AFGL Technical Memorandum #39, 1980.

1981

Carini, P., G. J. Kalman and Y. Shimia, Particle Trajectories in a Model Electric
Field, II, AFGL-TR-82-0149, 1982. ADA116950

Cohen, H. A., R. C. Adamo, T. Aggson, A. L. Chesley, D. R. Croley, S. A. Damron,
D. E. Delorey, J. F. Fennell, M. S. Gussenhoven, F. A. Hanser, D. A. Hardy,
W. B. Huber, I Katz, H. C. Koons, S. T. Lai, P. F. Mizera, E. G. Mullen, J.
E. Nanevicz, R. C. Olsen, A. G. Rubin, G. W. Schnuelle, N. A. Saflekos, M.
F. Tauz, and E. C. Whipple, P78-2 Satellite and Payload Reaponses to
Electron Beam Operations on March 30, 1979, Spacecraft Charging Technology,
1980, p 509, AFGL TR-81-0270, 1981. ADA114426

Cohen, H. A., A. L. Chesley, T. Aggson and M. S. Gussenhoven, A Comparison of
Three Techniques of Discharging Satellites, Spacecraft Charging Technology,
1980, p 888, AFGL TR-81-0270, 1980. ADA114426

Feynman, J., N. A. Saflekos, H. B. Garrett, D. A. Hardy and E. G. Mullen,
Disappearance of Particles of Energies >50 keV as seen by P78-2 (SCATHA) at
Near Geosynchronous Orbit, Spacecraft Charging Technology Conference, 1980,
p 755, AFGL TR-81-0270, 1981. ADA114426

Garrett, H. B. and J. M. Forbes, A Model of Soalr Flux Attenuation During Eclipse
Passage and its Effects on Photoelectron Emission from Satellite Surfaces,
To be published, Planet & Space Sci., 1981.

Gussenhoven, M. S., D. A. Hardy, W. J. Burke, DMSP/F2 Electron Observations of
Equatorward Auroral Boudaries and their Relationship to Magnetospheric
Electric Fields, J. Geophys. Res., 86, 768, 1981(a).

Gussenhoven, M. S., H. A. Cohen, D. A. Hardy, W. J. Burke and A. Chesley,
Analysis of Ambient and Beam Particle Characteristics During the Ejection of
an Electron Beam from a Satellite in Near-Geosynchronous Orbit on March 30,
1979, Spacecraft Charging Technology, 1980, p 642, AFGL-TR-81-0270, 1981.

Gustafsson, G., T. A. Potemra, S. Favin and N. A. Saflekos, Distant Magnetic
Field Effects Associated with Birkeland Currents (Made Possible by the
Evaluation of Triad's Attitude Oscillations), Submitted to JGR.

1981

Hanser, F. A., B. Sellers, D. A. Hardy, H. A. Cohen, J. Feynman and M. S. Gussenhoven, Operation of the SC-5 Rapid Scan Particle Spectrometer on the SCATHA Satellite, Sapcecraft Charging Technology, 1980, p. 386, AFGL-TR-81-0270, 1981. ADA114426

Moore, T. E., R. L. Arnoldy, J. Feynman, and D. A. Hardy, Propagating Substorm Injection Fronts, J. Geophys. Res., 86, 6713, 1981.

Mullen, E. G., M. S. Gussenhoven, H. B. Garrett, A. "Worst Case" Spacecraft Charging Environment as Observed by SCATHA on 24 April, 1979. AFGL-TR-81-0231,1981. ADA 108680

Rubin, A. G., H. A. Cohen, D. A. Hardy, M. F. Tautz and N. A. Saflekos, Computer Simulation of Spacecraft Charging on SCATHA, Spacecraft Charging Technology Conference, 1980, p. 632, AFGL-TR-81-0270, 1981. ADA114426

Saflekos, N. A., B. M. Shuman, T. A. Potemra, and M. Smiddy, Dual Satellite Observations of Geomagnetic Disturbances in Auroral Regions, Submitted to J. Geophys. Res., 1981(a).

Saflekos, N. A., M. F. Tautz, A. G. Rubin, D. A. Hardy, P. M. Mizera and J. Feynman, Three Dimensional Analysis of Charging Events on Days 87, and 114, 1979 from SCATHA, Spacecraft Charging Technology Conference, 1980, p. 608, Sapcecraft Charging Technology, 1980, AFGL-TR-81-0270, 1981(b).ADA114426

Shima, Y., G. J. Kalman, and P. Carini, Particle Trajectories in a Model Electric Field I. AFGL-TR-81-0167, 1981. ADA104507

Shuman, B. M., R. R. Vancour, M. Smiddy, N. A. Saflekos and F. J. Rich, Field-Aligned Current, Convective Electric Field and Auroral Particle Measurements During a Major Magnetic Storm. J. Geophys. Res. 86, 5561, 1981.

Silverman, S. M. and J. Feynman, The Changing Aurora of the Past Three Centuries, AFGL-TR-81-0172, 1981. ADA100982

1982

Burke, W. J., M. S. Gussenhoven, M. C. Kelley, D. A. Hardy, F. J. Rich, Electric, and Magnetic Field Characteristics of Discrete Arcs in the Polar Cap, J. Geophys. Res., 87, 2431, 1982

Feynman, J. Geomagnetic and Solar Wind Cycles, 1900-1975, 87, 6153, J. Geophys. Res., 1982.

Appendix I

Operation and Data Processing of the SC-5 Rapid Scan Particle Spectrometer

Considerable effort was expended in studying the data collected by the Air Force Geophysics Laboratories Rapid Scan Particle Spectrometer, SC-5, on the SCATHA, P78-2 satellite. This data formed the basis of many of the investigations undertaken in the fulfillment of this contract. Before this data could be used for these studies extensive investigations had to be carried out to understand completely the operation, strengths and limitations of the instrument as it actually operated in space. Some of the results of these investigations have been included in formal reports (Hanser et al., 1981), other results have been presented somewhat less formally (Gussenhoven, 1980) (appended paper 16) or simply taken account of the way the data was processed and used (Feynman, Gussenhoven, Saflekos and Spjeldvik).

The SC-5 instrument has two identical sets of particle detectors viewing parallel and perpendicular to the satellite spin axis. A complete spectral measurement is made every second, so 58 complete spectra are measured every satellite rotations (58 seconds). In order to handle this enormous amount of information various methods of data presentation were devised that condensed the information while maintaining the essential characteristics. Of course, the characteristics that are considered essential will vary according to the use to which the data is put. One convenient presentation used in several of the studies performed under this contract involved one minute averages of the ocunt rate collected by the detector parallel to the satellite spin axis (nominally perpendicular to the earth's field). Using this data format almost a complete set of data for the first year of operation of SC-5 was made available for study under this contract. Unfortunately, the full year's data was not completed for our use until the last four months of the contract period. However, data for special events and a more limited set of survey data was available and used earlier.

31

The quality of the data received from SC-5 was excellent. Each of the two particle detector sets consist of two electron/ion electrostatic analyzers (ESA's), a low energy set (0.05 to 1.7 keV) and a high energy set (1.7 to 60 keV) and, in addition, a pair of solid state detector spectrometers (30-1X10^3 keV electron and 1X10^3 to 8X10^3 keV protons). ESA's normally degrade with the total number of counts made during their lifetimes. This effect was controlled by several methods; shutting off the detectors when they would view the sun prevented the accumulation of high count rates due to solar ultraviolet rays; operating ESA's every other day permitted partial recovery; and inflight calibration allowed corrections for degradation to be made. The alternate-day ESA operations, while resulting in a much less complete data set in the ESA energy range than in the solid state range, allowed reliable ESA operation for in excess of one year.

Comparisons of SC-5 with SC-2-3 and SC-9 were made by Gussenhoven (1980) of SC-5 and SC-9 by Saflekos, (1981b) and between SC-5 and SC 2-6 by Feynman and Spjeldvik. In evaluating the differences found with SC 2-3 and SC-9 is should be remembered that SC-5 was the most extensively cailbrated instrument. The SC 2-6 and SC-5 agreed remarkably well for the ions in the SC-5 solid state energy range. At lower energies (20-80 keV) the causes of the differences between the observations from the two instruments is not entirely understood.

Appendix II

Electron Fluxes in the 10-80 keV Range

A complete survey was made of flux levels for 365 days of SC-5 electron data in the 10-80 keV range. The region of space swept out by the SCATHA P78-2 orbit was divided into bins, each bin covering one hour in magnetic local time and one Re in equatorial distance. The frequency of occurrence of fluxes exceeding a selected flux levels in each of two energy bands was determined. For each flux

level and energy range, the 'degree of hazard' for a bin was defined as the percentage of passes the satellite made through that bin that were accompanied by fluxes higher than the chosen level. The data used was from the AFGL Rapid Scan Particle Detector, SC-5, and more particularly from the electrostatic analyzer mounted parallel to the spin axis. The two energy steps studied were the 9 to 35 keV range and the 27-80 keV range. One minute averages of the electron count rates were scanned for the entire first year of data. For each of the three flux levels selected in each channel the periods (in magnetic local time, MLT) during which the flux exceeded the chosen levels were identified from the graphical printouts of the data. Because the SC-5 electrostatic analysers were not always turned on it was necessary to scan all of the data to see how many data collecting passes were made in each bin, regardless of flux level, during the year. The results are shown in Figure 1. The number of samples in each bin varies from a high of 128 data collecting passes in the MLT 03-04, Re 5.0-6.0 bin to a low of 37 in the MLT 11-12, Re 6.0-7.0 bin. The percentages of passes during which the flux exceeded the assigned values are shown in Figure 2 through Figure 7.

For the lowest flux level in both energy bands the region near dusk had the smallest incidence of intense fluxes. For the lowest flux level of the 23 keV channel the hours betwee about 0200 MLT and 1000 MLT had the highest incidence of intense flux. About 90% of the passes between 6 and 9 Re exceeded the selected flux level. The incidence of flux exceeding that level was generally lower between 5 and 6 Re then at greater distances and fell off towards midnight where eclipse charging occurs. The high incidence of enhanced flux observed in the 11 to 12 MLT and 6 to 7 Re bin may be a statistical fluctuation since only 37 passes were made through that bin. Note also that although in the region of 0600 hours the incidence was low for R = 5 to 6 Re relative to larger radii; it was relatively high at 5 to 6 Re in the region around 1800 hours.

The 23 keV channel flux-level in Fig. 3 shows a somewhat different pattern of high flux level incidence at this level the maximum incidence is about 50% which again appear in the region of 0600 MLT. However, the distribution in distance has changed markedly with 5-6 Re being considerably more hazardous then 7-8 Re. The most hazardous time period for 7-8 Re has shifted in the direction of midnight and is now centered at 0200 MLT. At the highest flux level for 10-35 keV electrons Figure 4 shows that 0600 is no longer the most hazardous region. Instead, the most hazardous region has shifted to be centered on 0300 and the degree of hazard is above 10% in the region from about 2200 to 0700 UT, with the precise boundaries depending somewhat on region. There is a well marked region of maximum hazard (which is not > 25%) between 6 and 7 Re centered at 0230 MLT. Hence a satellite in geosynchronous orbit would be expected to have experienced more frequent high level electron fluxes in sunlight during SCATHA's first year than did a satellite in SCATHA's orbit. The variation with radius at this level was less marked in the midnight sector so that eclipse charging would not be affected by a change in radial distance.

At the flux levels chosen, the pattern of hazard in the 27-80 keV energy range is somewhat different from the pattern in the 10-35 keV range. The most hazardous region in the 6 to 7 and 7-8 Re distance range is centered at about 0400 MLT, with the 5 to 6 Re hazard region shifted towards noon. Also, in the predawn sector, the hazard at 5-6 Re is definitely lower than that at the larger distances. This dependance on distance does not appear in the morning sector. In Fig. 6 the most hazardous region is centered on 0230, as it was for the 10-35 keV electrons shown in Fig. 4. In fact these two hazard patterns are very much the same, with the maximum hazard at about 30% between 6 and 7 Re for both energy ranges and less frequent at larger and smaller distances.

The results for the very highest flux level in the 27-80 keV range are shown in the last graph. In this figure the number represent the actual number of

34

passes rather than percentages. These data are from 4 different days, two of which were highly disturbed geomagnetically with Kp's of 7- and 8- and the other two were more moderate with Kp of 4 and 4-.

It is planned to include these results in the SCATHA Atlas.

DMSP/F2 Electron Observations of Equatorward Auroral Boundaries and Their Relationship to Magnetospheric Electric Fields

M. S. GUSSENHOVEN

Physics Department, Boston College, Chestnut Hill, Massachusetts 02167

D. A. HARDY

Air Force Geophysics Laboratory, Hanscom Air Force Base, Massachusetts 07131

W. J. BURKE

Physics Department, Boston College, Chestnut Hill, Massachusetts 02167

Energetic electron measurements from a particle detector on the DMSP/F2 satellite have been used to determine the corrected geomagnetic latitude Λ_{CGM} of the equatorward boundary of the auroral oval. The satellite was launched into a nearly sun-synchronous, polar orbit centered on the 0700-1900 MLT meridian. Because of the wobble of the dipole and a very slow precessional motion of the orbit more than 6000 boundary crossings could be studied in the 1600-2300 and 0400-1000 MLT sectors. The detectors, which have large geometric factors, look radially away from the earth and detect precipitating electrons with energies between 50 eV and 20 keV. In the evening sector the equatorward boundaries are precisely determined from the rise in the total electron flux. The morningside boundary cannot always be clearly delineated. Data were divided into 1-hour magnetic local time bins with ~400 samples per bin. In each of the MLT bins, Λ_{CGM} was found to be linearly correlated to the AP index. Regression values of Λ_{CGM} were projected to the magnetic equatorial plane by using the Mead-Fairfield magnetic field model. The projected boundaries are not in good agreement with the injection boundaries of Mauk and McIlwain (1974). They are best fit to boundaries derived by using Volland-Stern type electric fields with the axis of symmetry rotated into the evening sector for $AP < 2$ and into the afternoon sector for $KP > 2$.

INTRODUCTION

The dynamics and sources of auroral electrons have long been of concern within the geophysical community. Whether 'inverted V' [*Frank and Ackerson*, 1971] electrons come directly from the magnetosheath [*Frank*, 1971], the magnetospheric boundary layer [*Winningham et al.*, 1975], the neutral sheet [*Speiser*, 1967], or some other location in the magnetosphere remains a controversial topic. It appears to be widely accepted, however, that diffuse auroral electrons come from the central plasma sheet [*Lui et al.*, 1977]. Thus it is expected that the equatorward boundary of the auroral oval reflects the dynamics of the position of the inner boundary of the plasma sheet, R_{b}. In a general sense this appears to be true in that the equatorward boundary of the oval moves equatorward and R_{b} moves earthward as the level of magnetic activity increases [*Vasyliunas*, 1968].

Studies of the position of the equatorward boundary of the auroral oval have been conducted by using imagery from the Isis 2 [*Lui et al.*, 1975] and DMSP [*Sheehan and Carovillano*, 1978] satellites. In both instances the boundary was observed to move equatorward with increasing magnetic activity. A more comprehensive study by *Kamide and Winningham* [1977] used data from the soft particle spectrometers on Isis 1 and 2 to identify the position of the boundary and to show that it shifts by ±4° with interplanetary magnetic field (IMF) $B_z =$ ±5 nT. The statistical sample was large enough to show that for the same value of B further equatorward shifts occur (1) if a substorm is in progress, (2) during the summer, and (3) with increasing magnetic local time. A comparison of the low-latitude boundary of the oval projected into the magnetic

equatorial plane with the shape of calculated zero-energy Alfvén layers [*Kivelson*, 1976; *Southwood and Kaye*, 1979] met with mixed success. For the remainder of this paper we refer to the work of *Sheehan and Carovillano* [1978] and *Kamide and Winningham* [1977] as S-C and K-W, respectively.

The purposes of this report are (1) to present comprehensive measurements of the corrected magnetic latitude of the equatorward boundary of the auroral oval, Λ_{CGM}, and (2) to compare these results to model predictions of R_{b}, the inner boundary of the plasma sheet. The measurements were made with an electron spectrometer on board the Defense Meteorological Satellite Program (DMSP) satellite F2. In the following section we describe the instruments, the criteria for identifying Λ_{CGM}, and the methods used for binning data. It is shown that negative linear relationships exist between Λ_{CGM} and KP in both the evening and the morning sector. The discussion section is divided into three parts. (1) A comparison with ionospheric measurements of S-C and K-W is made. The comparison shows a high level of agreement between the three data sets. (2) The DMSP boundaries are projected via the Mead-Fairfield magnetic field model to the magnetic equator and compared with the injection boundaries of *Mauk and McIlwain* [1974]. We find the agreement to be poor. (3) The boundaries are then compared with the semiempirical model of magnetospheric electric fields of *Volland* [1973] and *Stern* [1975]. The best fits to DMSP observations are found by using shaping factors between 2 and 3 and with the axis of symmetry rotated away from the dawn-dusk meridian.

INSTRUMENTATION AND DATA SELECTION

DMSP/F2 is a three-axis stabilized satellite in a nearly sun-synchronous, circular orbit at an altitude of 840 km. The or-

36
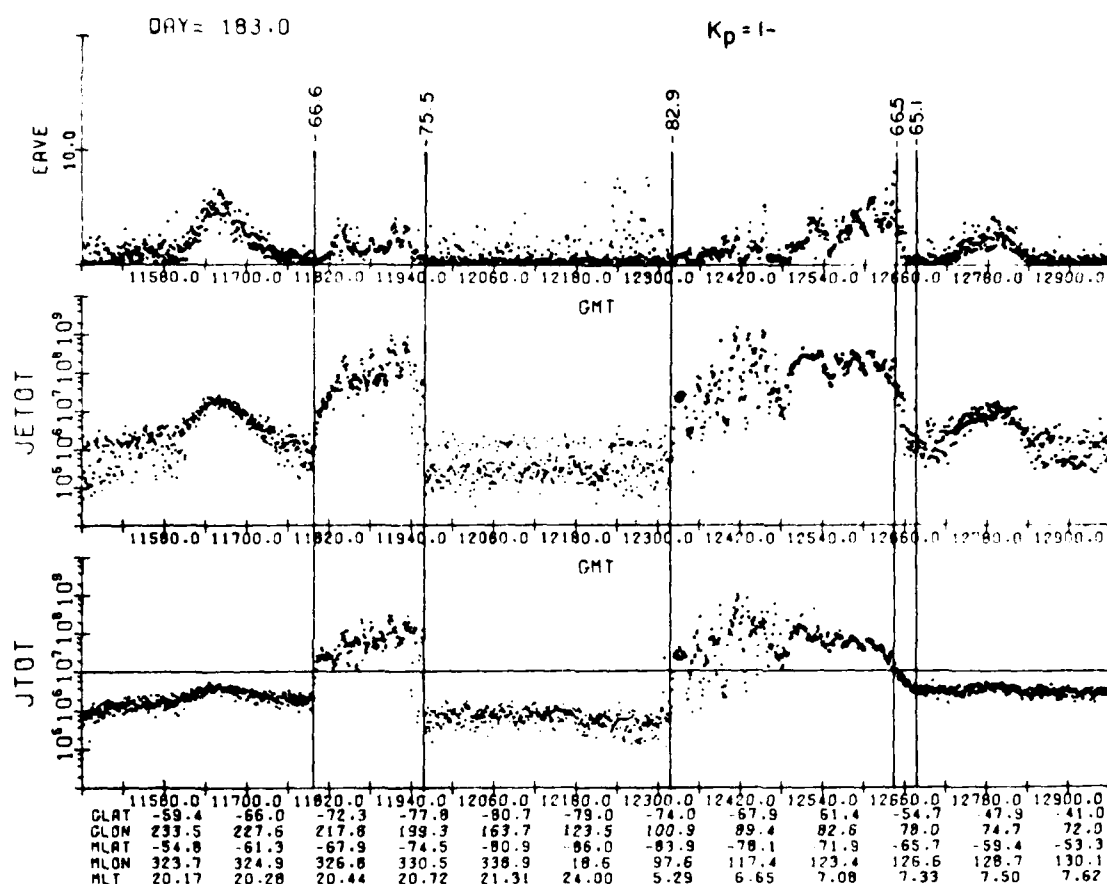
Fig. 1. Integral flux in (cm² sr s)⁻¹ (bottom panel), energy flux in keV (cm² sr s)⁻¹ (middle panel), and average energy in keV (top panel) of precipitating electrons measured by the DMSP/F2 satellite passing over the south pole on July 2, 1978. These values are plotted as functions of universal time (in seconds), geographic latitude and longitude of the subsatellite position, corrected geomagnetic latitude and longitude of the satellite position projected along a Jensen-Cain magnetic field to 100 km, and magnetic local time. The vertical lines indicate equatorward and poleward boundaries of precipitating auroral electrons.

bital period is 101 min; the nominal inclination is 98.75°. At launch the orbit was centered near the 0700-1900 meridian, but it is subject to a very slow precession toward later local times. Owing to the offset between the earth spin axis and the magnetic axis, the orbit is subject to significant diurnal and seasonal variations in the magnetic local time–magnetic latitude frame of reference. Thus Λ_{CGM} is sampled in a wider range of MLT than might be assumed from the restricted geographic local time locations of the orbit. It should also be noted that DMSP is an operational Air Force satellite. Except during periods of downlink transmissions, data are almost always being recorded.

The particle detector on DMSP/F2 consists of two curved plate electrostatic analyzers that measure the fluxes of electrons in 16 energy channels between 50 eV and 20 keV once per second. The apertures of the analyzers always face local vertical such that at auroral and polar cap latitudes they detect precipitating rather than backscattered and/or trapped electrons. One analyzer covers the energy range from 50 eV to 1 keV with a geometric factor of 4×10^{-4} cm² sr and a $\Delta E/E$ of 10%. The other analyzer covers the energy range from 1 to 20 keV with a geometric factor of 10^{-3} cm² sr and a $\Delta E/E$ of

12%. The large geometric factors insure that the flux level for the electrons in the diffuse aurora is well above the detector's sensitivity. A detailed description of the detector is given by *Hardy et al.* [1979].

An example of DMSP/F2 electron data, taken from a south polar pass on July 2, 1978, is given in Figure 1. Data are plotted as J_{tot}, the directional integral flux (cm² sr s)⁻¹ in the bottom panel; J_{Etot}, the directional energy flux (keV/cm² sr s) in the middle panel; and E_{ave}, the average energy in keV in the top panel. The scale for E_{ave} is linear. These quantities are plotted as functions of universal time in seconds of the day, the geographic latitude and longitude of the subsatellite position, the corrected geomagnetic latitude and longitude of the satellite projected to an altitude of 100 km, and the magnetic local time. Values of the equatorial boundaries Λ_{CGM} of the auroral oval are assigned to the corrected geomagnetic latitudes >45° at which J_{tot} rises noticeably above background. This is essentially the same method as that used by K-W. In the example given in Figure 1, Λ_{CGM} is at −66.6° on the eveningside (~2000 MLT) and at −65.1° on the morningside (~0700 MLT).

Several characteristics of the electron precipitation that per-

tain to the choice of auroral boundaries are illustrated in Figure 1. First, we have found that the condition $J_{tot} > 10^7$ (cm^2 sr s)$^{-1}$, indicated in the figure by the horizontal line, provides a generally useful criterion for selecting both the poleward and the equatorward boundaries of the oval. The poleward boundaries selected in the case given in Figure 1 are marked for purposes of illustration. They and their attendant selection problems will not be discussed here. Second, the evening equatorward boundary is sharper than its morningside counterpart. On the morningside, J_{tot} rose from background to 10^7 (cm^2 sr s)$^{-1}$ over 1.4° latitude, whereas the eveningside rise was nearly instantaneous. Generally, flux gradients are found near both equatorward boundaries. The gradient never extends more than a few degrees of latitude in the evening sector but can cover as much as 10° on the morningside, where it is always perceptibly present. Third, equatorward of the evening

Fig. 3 Same as Figure 2, but for a pass over the morningside auroral zone boundary

and morning values of Λ_{COM} there are slight rises in J_{tot} with relatively large values of J_{hot} and E_{ave}. These increases are due to radiation belt particles that penetrate the detector casing and directly stimulate the channeltrons; they must be differentiated from the auroral electrons when determining boundaries. Because of the geometrical configurations of the two detectors, radiation belt contamination is largely limited to the energy channels of the 1- to 20-keV detector.

The boundary of the oval, Λ_{COM}, cannot always be determined unambiguously. On both the morningside and the eveningside of the oval the onset of electron precipitation can be obscured in various ways. In the evening the principal problem is contamination of the low-energy channels of the detector by photoelectrons. As an example, in Figure 2 we have plotted the count rates in representative channels of the detector as a function of increasing geographic latitude. Arrows show where there is a significant increase in counts due to the

Fig. 2 Counts in selected channels of the SSJ/3 detector plotted as a function of increasing geographic latitude for a pass over the eveningside auroral zone boundary.

Fig. 4. Precipitating electron data for a south pole pass on February 28, 1978. The format is the same as that in Figure 1.

onset of precipitating auroral electrons. The increase in counts is observed first in the lowest-energy channel and then, progressively, in higher-energy channels. In the 50-eV channel, significant counts are observed equatorward of the arrow. These counts arise from photoelectrons from the conjugate ionosphere. The effect of photoelectrons can be observed at energies as high as several hundred electron volts. Since the photoelectrons are observed in the same channels as the onset of precipitation, the ambiguity in the boundary is introduced by having to separate the two effects. Also shown in Figure 2 are increased counts in the 5.5-keV channel equatorward of auroral electron precipitation. This is an example of radiation belt contamination. As is discussed above, the effect is seen only in the channels of the high-energy detector. In the evening sector, auroral precipitation is first detected in the lowest-energy channels. At times when the radiation belt and the auroral oval overlap, the combination of high-energy channel contamination and increased low-energy count rates produces an increase in J_{tot} and a decrease in E_{ave}. Thus the auroral boundary determination is unaffected.

Uncertainties in identifying the position of the boundary in the morning sector are more severe. There are three sources of uncertainty: (1) overlap between regions of energetic electron precipitation and radiation belt contamination of corresponding energy channels, (2) a much more gradual latitudinal onset of precipitation than is found in the evening, and (3) the existence of energetic plasma close to but detached from the boundary. In Figure 3 we have plotted the counts for the morning auroral zone as in Figure 2. The figure shows that for

this case the onset of electron precipitation in the morning appears first in the high-energy channels and then progressively in lower-energy channels. For this case the region in which penetrating particles are producing counts is equatorward of the onset of auroral precipitation. In active periods the two regions can overlap. Since the count levels are comparable, for the cases of overlap it is difficult to separate the two effects, and our ability to determine the boundary is affected.

The second effect causing ambiguity in identifying the morningside boundary is illustrated in Figure 4, which shows a complete south polar pass from February 28, 1978. On the morningside a gradient in J_{tot} continues into the region of radiation belt contamination. J_{tot} and E_{ave} fall sharply at $-64.7°$ CGM, but J_{tot} remained too high to be explained as contamination until $-58.5°$. At $-58.5°$, E_{ave} rose with significant scatter indicating the presence of dominant radiation belt contamination and obscuring the possible presence of keV electron precipitation. In cases such as this the boundary was chosen to be at the lowest magnetic latitude at which precipitating electrons could be identified; in this case, $\Lambda_{CGM} = -58.5°$.

The third effect which can be found in both morning and evening regions is shown in Figure 5. This example shows a north pole pass on January 21, 1978, during a time of magnetospheric quiet. On the eveningside there are small regions of energetic electrons near to but detached from the more poleward precipitation region. These can occur during active times as well and are ignored in selecting the boundaries.

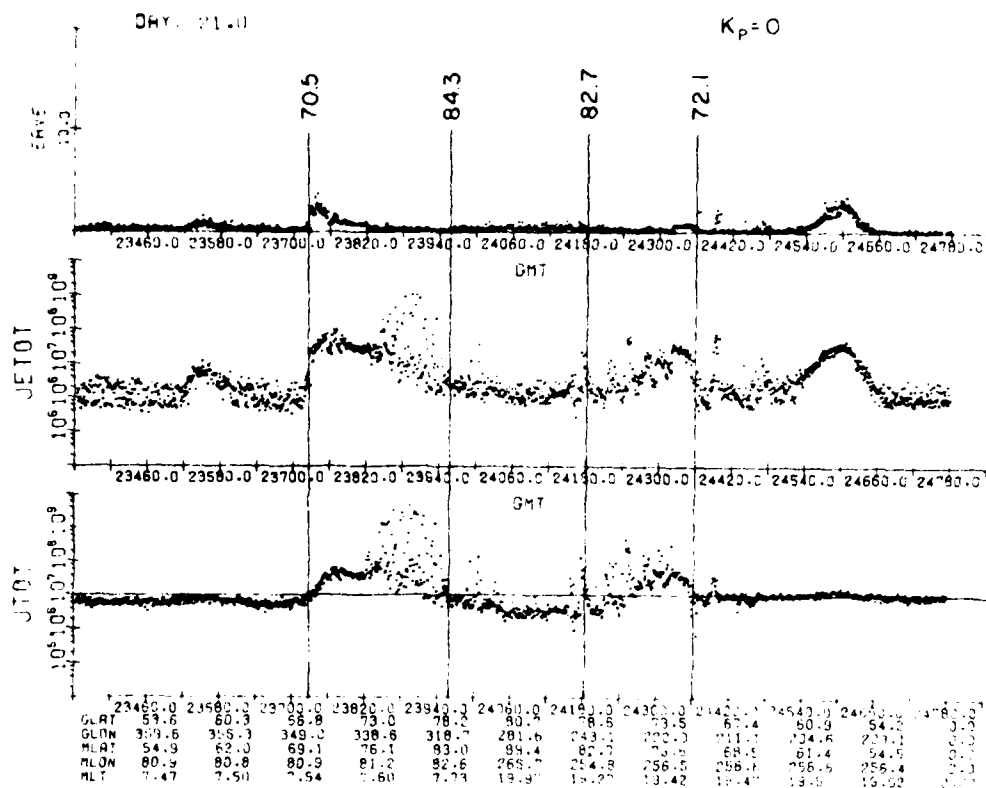The above effects produced greater than 1° of uncertainty

39

Fig 5. Precipitating electron data for a north pole pass on January 21, 1978. The format is the same as that in Figure 1

in the equatorial boundary only for a small percentage of the total cases. On the eveningside, approximately 90% of the boundaries were determined with no ambiguity. On the morningside the figure was approximately 70%.

More than 6000 auroral oval boundary crossings were determined by using data from September 1977 to December 1978. Over two thirds of the crossings occurred during north pole fall and winter months. It was necessary to use spring and summer data to obtain a good statistical sample for high KP values. The measurements are binned into 1-hour units of MLT and to all steps in KP (0, 0+, 1−, ···). Cases were selected to insure that 20–25 samples were included in each KP ≤ 6 element. In some MLT sectors a statistically significant number of samples were available for KP > 6 elements. Owing to the orbital characteristics of DMSP/F2, these criteria were largely met in the 1700–2300 and 0400–1000 MLT sectors of the northern hemisphere and the 1700–2100 and 0400–0800 sectors of the southern hemisphere. The major exceptions were the 1800–1900 MLT sector of the northern hemisphere, in which only 103 samples were found, and the 1500–1600 MLT sector in the southern hemisphere, having 107 samples. The small sample size resulted from the fact that the DMSP/F2 orbit drifted slowly out of (and into) these regions over the time interval used.

OBSERVATIONS

Examples from the evening (1900–2000) and morning (0700–0800) MLT sectors in which coverage is available from both the northern hemisphere (top traces) and the southern hemisphere (bottom traces) are given in Figures 6 and 7. The average value and the standard deviation of the boundaries within each KP bin are shown. Solid lines represent linear regressions performed with all the points in the MLT sector versus KP (not with the mean values). The equation for the line is given in the upper right-hand corner of each plot. The correlation coefficient (cc) is also given.

From an examination of data contained in these figures several points can be made. (1) KP orders the equatorward auroral boundaries linearly throughout the entire range. The mean values lie on or very near the line. The fit is exceptional for the evening values, and while there is more variation in the morning, no trend other than linear is apparent. The correlation coefficients across the whole KP range are very high: ≤−0.81 for the four cases shown. (2) Standard deviations about mean values tend to increase with increasing KP. Also standard deviations in the morning sector are greater than those found in the evening sector. This reflects our general observation that auroral electron precipitation patterns are far more variable in the morning than in the evening sector. (3) In MLT regions of overlap, Λ_{eCM} has lower values in the southern hemisphere. The difference is greater in the morning for low KP values. The slopes in the straight-line fit have larger negative values in the north pole, and the difference between the boundaries approaches zero for large KP. The difference may be due to north-south asymmetries in mirror points of plasma sheet electrons. It may also reflect a summer-winter asymmetry due to the tilt of the dipole noted by K-W. Recall
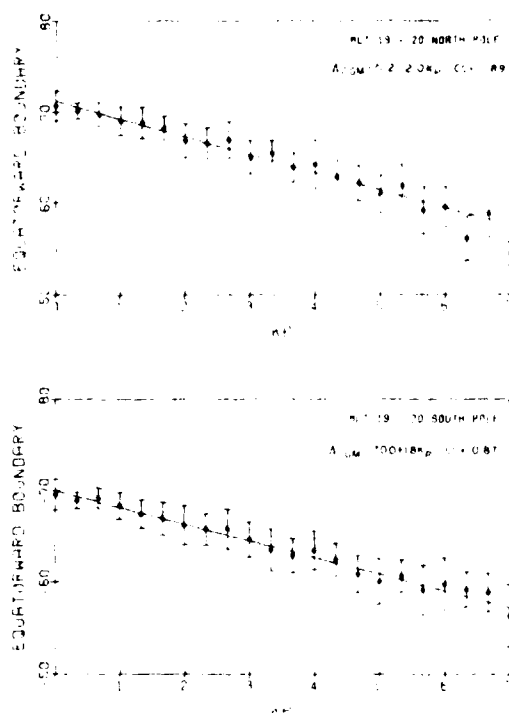
Fig. 6. Mean values and standard deviations of equatorward boundaries in each KP line plotted as a function of KP for the north and south poles in the 1900–2000 MLT sector. The solid line results from a linear regression performed with individual boundary determinations. Linear regression results are summarized for given KP ranges.

that most of the data points used in the present study were acquired within 3 months of the December 1977 solstice.

The entire data set is summarized for the morning and evening sectors in Tables 1 and 2, respectively. Here we have listed values of Λ_0 and α calculated from the regression formula $\Lambda_{CGM} = \pm(\Lambda_0 + \alpha KP)$, where the plus (minus) sign refers to the north (south) pole. Also listed are the number of cases N and the correlation coefficient cc. Even including the MLT sectors for which the statistical sample was small the correlation coefficients lie in the range $-0.58 \geq cc \geq -0.90$. For the full samples, correlation coefficients were less than -0.7 in the morning and less than -0.8 in the evening. This suggests that KP is better than IMF B_z for organizing Λ_{CGM}. Correlation coefficients reported by K-W were in the $-0.4 \geq cc \geq -0.7$ range. Evening sector values of Λ_{CGM} for a given value of KP decreased with increasing MLT. According to K-W this decrease continues into the postmidnight sector. In the dawn sector, Λ_0 increases with increasing MLT. However, at $KP = 6$, dawn and postdawn sector values of Λ_{CGM} approach a constant value of ~57°. Values of α fall in the restricted range -1.6 ± 0.4 in the evening sector and -1.75 ± 0.4 in the morning sector. The largest negative values of α were at 0700–0800 MLT and 1800–1900 MLT, indicating that the greatest variability in the boundaries occurs near dawn and dusk.

DISCUSSION

Comparison With Measured Ionospheric Boundaries

Direct quantitative comparisons of results presented in the previous section with the work of S-C and K-W are not pos-

sible for many reasons. Correlated quantities were not the same and were sampled largely in different MLT sectors. S-C used optical rather than particle signatures to identify the corrected magnetic latitude of the equatorward boundary as a function of KP. K-W studied the invariant latitude of the boundary as a function of IMF B_z. Although B_z influences geomagnetic activity, its relationship with KP is not a simple one. However, some semiqualitative comparisons of the various results can be made if we assume that times when $B_z = +(-)5$ correspond to periods of low (high) geomagnetic activity. With these simplifying assumptions we have plotted in Figure 8 'values' of Λ_{CGM} observed by the various DMSP and Isis satellites for periods of magnetic quiet and disturbance. The encircled dots and the crosses refer to DMSP/F2 northern and southern hemisphere observations, respectively. The high- (low-) latitude points were calculated for cases of $KP = 0$ (5) using the regression coefficients of Tables 1 and 2. The triangles refer to boundary values calculated using regression coefficients given in Table 1 of K-W with $B_z = \pm 5 \gamma$. The squares refer to measurements at MLT = 0100, 2000, and 2200 for $KP = 0$ and 5 as taken from Figures 2 and 8 of S-C.

The auroral boundary derived from the three data sets for periods of magnetic quiet shows a remarkable consistency. In MLT sectors of common measurements the quiet time results are within 1° of each other. The boundary appears to be continuous across the entire nightside. The one anomalous point in the 0300–0400 MLT sector was based on a data set of eight points and is virtually without statistical significance. It is interesting to note that Meng et al. [1977] have shown that the poleward boundary of the quiet auroral oval can be represented by an offset circle. During magnetically quiet times the oval tends to be of narrow latitudinal width. Perhaps not sur-
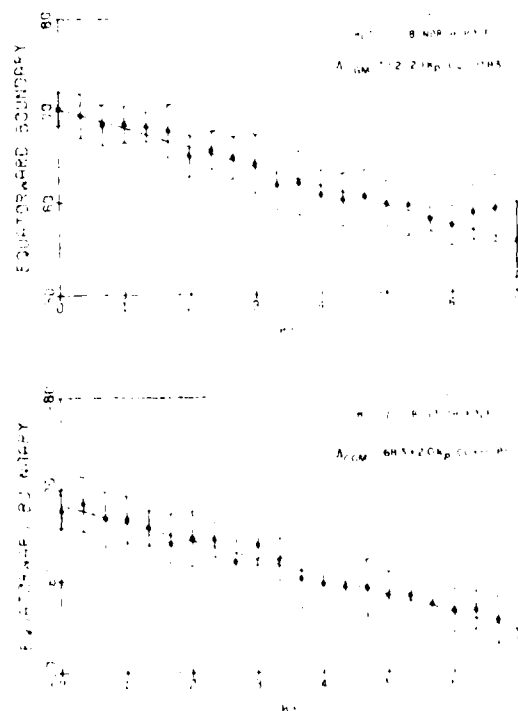

Fig. 7. Same as Figure 6, but for the 0700–0800 MLT sector.

TABLE 1. Summary of the Results of Performing a Linear Regression Analysis on the Auroral Equatorward Boundaries and KP for a Given Magnetic Local Time (MLT) in the Morning Sector

MLT	North				South			
	Λ_0	a	N	cc	Λ_0	a	N	cc
0400–0500	67.4	−1.35	171	−0.58				
0500–0600	67.8	−1.87	365	−0.75				
0600–0700	68.5	−1.96	403	−0.82	67.4	−1.67	376	−0.74
0700–0800	70.2	−2.15	367	−0.83	68.3	−1.97	411	−0.81
0800–0900					68.7	−1.88	302	−0.72
0900–1000					69.1	−1.64	217	−0.67

The linear relationship may be written $\Lambda_{\text{GM}} = \Lambda_0 + aKP$, where Λ_0 is the intercept and a the slope. N is the number of boundaries used, and cc the correlation coefficient. Values are given for both the northern and the southern hemisphere.

prisingly, Λ_t can also be well fit to an offset circle. (The symbol Λ_t is used in comparing DMSP with equatorward boundaries of S-C and K-W, rather than the symbol Λ_{GM}, which is reserved for DMSP/F2 data alone.) In Figure 8 the quiet time boundary is fit to a circle of radius 21° that is centered at 88.0° and 02.7 MLT (dashed line). DMSP/F2 values fall within the circle at 1800–2000 MLT and 0600–0800 MLT, deviations which will later be shown to have significance.

At times of high geomagnetic activity, agreement between the data sets is not as good. The boundary for $KP = 5$ derived from DMSP/F2 measurements is smooth in the evening and morning sectors. The high-activity boundaries from S-C and K-W are mutually consistent but are displaced poleward of F2 results by 2° in the premidnight region. No comparison is possible for the postmidnight region. Variation from S-C data can be accounted for as a difference between optical and particle boundaries. On the other hand, in their analysis, K-W noted that for the same value of B_z the value of Λ_t could be shifted equatorward by several degrees if a substorm was in progress. During times of $KP = 5$ it is expected that substorms would almost always be in progress. Examining the distribution of points in Figure 8 of K-W, we see that in the 2000–2100 MLT sector for $B_z = -5$ nT, Λ_t was observed at 61° and 59°, where the regression value is 63°. In general, most of K-W's data points taken during times when substorms were in progress lie well below the regression line. Evidently, the value of Λ_t reflects the dynamic state of the magnetosphere, which depends on physical parameters other than just the hourly average of B_z.

Comparison With Magnetospheric Boundaries

The notion of an injection boundary was first proposed by Mauk and McIlwain [1974] to systematize magnetic local

times ϕ at which the ATS 5 satellite at 6.7 R_e encountered sharp increases in low-energy (keV) plasma fluxes as a function of KP. A least squares regression analysis gave the relationship

$$\phi(L = 6.7) = 25.5 - 1.5KP \qquad KP \leq 5+ \qquad (1)$$

To extend these points and to give a generalized plasma boundary, Mauk and McIlwain used *Carpenter and Park's* [1973] relationship between the position of the plasmapause at $\phi = 0600$ (L_p) and KP; $L_p = 5.7 - 0.47KP$. The Carpenter and Park relationship was derived by using the highest values of KP in the previous 24 hours rather than its current value. Mauk and McIlwain assumed that the shape of the boundary was of the form

$$L(\phi, KP) = SL_p/(\phi + C) \qquad (2)$$

By forcing the boundary to pass through $L = 6.7$ at local times specified in (1) it can be shown that the constants S and C have values of 21.4 and −7.3, respectively.

The term injection boundary is not without ambiguity [*Kivelson et al.*, 1979]. It may either signify a dynamic plasma boundary which is suddenly pushed earthward to the position of the satellite or refer to a quasi-static boundary that is crossed by the satellite. In the dynamic case the electron flux shows little or no energy-time dispersion. In the quasi-static case, electrons are first detected at low energies and then at higher energies as the satellite penetrates further into the boundary. *Kivelson et al.* [1979] have suggested that this energy-time dispersion is characteristic of the satellite's crossing the Alfvén boundaries of electrons with higher and higher energies. As is discussed below, Alfvén boundaries mark boundaries between open and closed magnetospheric trajectories for particles of given charge and magnetic moment. The

TABLE 2. Summary of the Results of Performing a Linear Regression Analysis on the Auroral Equatorward Boundaries and KP for a Given Magnetic Local Time (MLT) in the Evening Sector

MLT	North				South			
	Λ_0	a	N	cc	Λ_0	a	N	cc
1600–1700					71.3	−1.19	107	−0.65
1700–1800					70.7	−1.20	256	−0.69
1800–1900	71.6	−2.00	103	−0.90	70.6	−1.60	327	−0.80
1900–2000	71.2	−1.96	426	−0.89	70.0	−1.82	447	−0.87
2000–2100	69.4	−1.85	452	−0.82	69.5	−1.89	345	−0.84
2100–2200	68.7	−1.66	556	−0.63				
2200–2300	68.3	−1.79	184	−0.63				

The linear relationship may be written $\Lambda_{\text{GM}} = \Lambda_0 + aKP$, where Λ_0 is the intercept and a the slope. N is the number of boundaries used, and cc the correlation coefficient. Values are given for both the northern and the southern hemisphere.

SHEEHAN CAROVILLANO K_p 0.5
▲ KAMIDE-WINNINGHAM $B_z = \pm 5\,Y$
● NORTH POLE ⎫
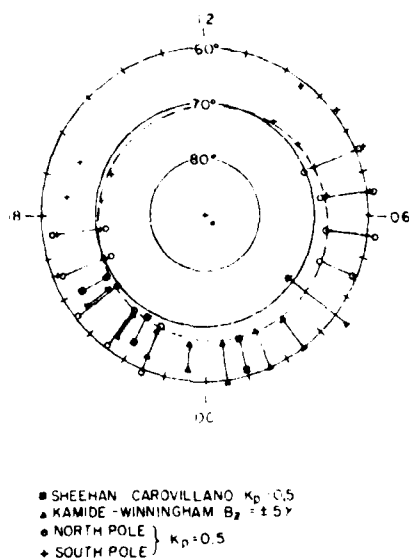✦ SOUTH POLE ⎭ $K_p \geq 0.5$

Fig. 8. Equatorward boundary of the auroral oval as a function of MLT for high and low levels of magnetic activity. Data marked by the encircled dots, crosses, triangles, and squares come from the north and south hemisphere measurements of DMSP/F2 ($KP = 0, 5$), measurements of Isis ($B_z = \pm 5\,\gamma$), and DMSP optical imagery ($KP = 0, 5$), respectively. The quiet time oval has been fit to an offset circle (dashed line).

zero-energy Alfvén layer is thus the boundary between open and closed equipotential surfaces in the magnetosphere. For the remainder of this paper we treat quasi-static injection boundaries and Alfvén layers as equivalent concepts.

The energy-latitude dispersion shown in Figure 2 to be characteristic of the equatorward edge of auroral precipitation in the evening sector is precisely what would be expected from mapping a quasi-static injection boundary into the ionosphere and gives credence to our association of the DMSP/F2 boundaries with the inner edge of the established plasma
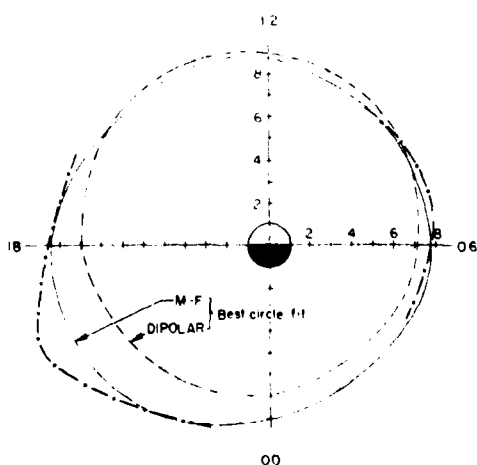
Fig. 9. Projections of the circular fit of $KP = 0$ boundaries to the ecliptic plane using a dipolar projection (dashed line), and the Mead-Fairfield (M-F) magnetic field model (solid line). The dashed-dotted curve is the projection by means of a Mead-Fairfield magnetic field model of a smooth fit to the individual boundary values for $KP = 0$
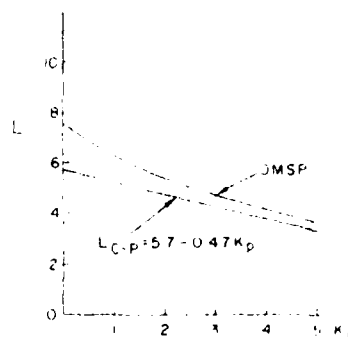
Fig. 10. Comparison of the Carpenter-Park values of the plasmapause at dawn to the inner edge of the plasma sheet at dawn as determined by the DMSP/F2 boundaries.

sheet. A quasi-static injection boundary R_i can be determined from Λ_{COM} by mapping these latitudes into the equatorial plane, where comparison can then be made to the Mauk-McIlwain injection boundary.

Before making this comparison several points should be kept in mind. First, the mapping is extremely sensitive to magnetic field models, and small variations in Λ_{COM} appear as large variations in L shell. Figure 9 illustrates both of these points. Here we have mapped the best circle fit to the quiet auroral oval shown in Figure 8 onto the equatorial plane using a dipolar projection (dashed line) and a projection using the Mead-Fairfield magnetic field model for $KP < 2$ (solid line) [see Fairfield and Mead, 1975]. The difference between the two can be as large as 2 R_i in the evening sector. Also shown in Figure 9 is the best smooth fit to the data points, Λ_{COM}, mapped by using the Mead-Fairfield magnetic field (dashed-dotted line). The north and south pole values are averaged for overlapping MLT sectors. The small deviation of Λ_{COM} from the circular fit in the 1800-2000 MLT sector, which was pointed out previously, results in a significant boundary change in the equatorial plane.

Because the representation of the Mauk-McIlwain boundary given in (2) is valid only at local times prior to 0200, comparisons with DMSP/F2 boundaries are limited to the evening sector. We can, however, directly compare the DMSP/F2 boundary with Carpenter and Park's [1973] plasmapause measurements at dawn. Figure 10 shows this comparison. The DMSP values are calculated from averages of Λ_{COM} in the 0500-0600 and 0600-0700 MLT sectors. The inner edge of the plasma sheet as determined by DMSP/F2 auroral boundaries lies beyond the plasmapause, asymptotically approaching a constant separation of ~0.3 R_i for large KP. This separation is within that of the standard deviation in Λ_{COM}. The deviation from linearity for small KP cannot be accounted for in this way and indicates that the assumption $L \propto L_i$ in (2) for a given local time is a poor one for low KP.

Figure 11 compares the Mauk-McIlwain injection boundaries (dashed lines) for $KP = 0, 2$, and 5 to the inner edge of the plasma sheet as determined from Λ_{COM} values for the same KP levels (solid lines). For $KP = 2$ and 5 the Mauk-McIlwain injection boundaries lie within the plasma sheet. This is consistent with photometric auroral observations at the foot of the ATS 5 field line by Eather et al. [1976]. They found that substorm-related injections occurred within the existing plasma sheet in the premidnight sector. These injections were furthest from R_i at dusk and approached R_i near midnight.

Mauk-McIlwain statistics include all injection boundaries encountered, a mix of dynamic and quasi-static boundaries. The boundary that results, R_{M-M}, should then lie within the plasma sheet, or at $R_{M-M} > R_P$. This is the relationship that the Mauk-McIlwain boundary has to the DMSP/F2-determined boundary for $KP = 2.5$, with $R_{M-M} \rightarrow R_P$ near midnight.

For $KP = 0$ the two boundaries differ greatly, particularly in the evening sector. The local time at which ATS 5 statistically crosses the quiet time injection boundary is 0130, which point compares very favorably with the inner edge of the plasma sheet as measured by DMSP/F2. Using higher values for the inner edge of the plasma sheet at dawn than those given by Carpenter and Park will expand the Mauk-McIlwain boundary, but the essentially different shape of the DMSP/F2 boundary indicates that for low KP values the Mauk-McIlwain boundary is valid over a very restricted local time range. This is not surprising, since geosynchronous orbits rarely enter the plasma sheet during very quiet times and when they do, it is postmidnight, far from the dusk boundary in question.

A Quasi-Empirical Representation of the Observed Boundaries

Charged particles in the magnetosphere are subject to gradient curvature and to $E \times B$ drifts. The gradient curvature drift depends on the charge and energy of the particle, while the electric field drift does not. The electric field is a superposition of the general dawn to dusk convective field, the corotation field, and fields due to charge separations within the system. The latter type of field is primarily due to shielding charges near the plasmapause [Jaggi and Wolf, 1973] and to polarization charges at conductivity gradients near the terminator in the ionosphere [Wolf, 1970]. The shape and position of magnetospheric boundaries for low-energy plasma sheet electrons under the assumption of a uniform cross-tail electric field has been discussed by Kivelson [1976]. The electrons drift earthward from the tail along equipotential surfaces and then eventually exit the magnetosphere across the dayside magnetopause. The zero-energy Alfvén boundary delineates regions of allowed and forbidden access. Its characteristic teardrop shape is that of the last closed equipotential. On the basis of electric field measurements at ionospheric altitudes [Heppner,
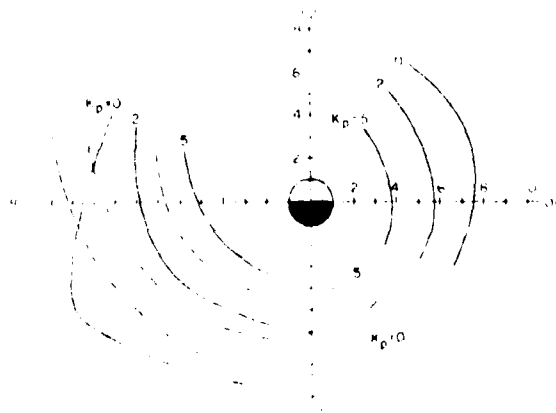

Fig. 11 Comparison of the inner edge of the plasma sheet as determined by the DMSP/F2 boundaries to the Mauk-McIlwain injection boundaries for various KP

1972], Volland [1973] and Stern [1975] suggested that the convective field is not uniformly dawn to dusk. Ejiri et al. [1978] derived an analytic expression for the zero-energy Alfvén boundary under nonuniform electric field situations that uses a shaping factor γ. Recently, Kaye and Kivelson [1981] suggested that the value of γ reflects the degree to which space charges shield the convective electric field from the inner magnetosphere. The case $\gamma = 1$ corresponds to situations of uniform dawn to dusk fields in which there is no shielding. The major effect of the near-terminator conductivity gradient is to rotate the dusk bulge of the Alfvén boundary into the evening sector [Wolf, 1970].

In the equatorial plane of the magnetosphere the potential from which the total electric field is derived is assumed to be of the form

$$\Phi(R, \phi) = -(\Omega B_0 R_e^3/R) + AR^2 \sin(\phi - \phi_0) \quad (3)$$

where Ω is the angular spin velocity of the earth, B_0 is the magnetic field strength at the magnetic equator on the earth's surface, R is the distance from the center of the earth, and ϕ is the local time measured counterclockwise from midnight. The phase angle ϕ_0 represents the rotation of the axis of symmetry away from the dawn-dusk meridian. The boundary between open and closed equipotentials is calculated by assuming that at a distance R_S and a local time $\phi - \phi_0 = 3\pi/2$ the convection and corotational electric fields cancel each other. The condition that $\partial\Phi/\partial R = 0$ at this point allows a determination of the constant $A = \Omega B_0 R_e^3/\gamma R_S^{\gamma+1}$. Following Ejiri et al. [1978], it is easily shown that the equation for the boundary is

$$(R_P/R_S)^{\gamma+1} \sin(\phi - \phi_0) + (\gamma + 1)(R_P/R_S) - \gamma = 0 \quad (4)$$

Southwood and Kaye [1979] have shown that an excellent approximation to the solution of (4) is

$$R_P \approx R_S[1 + (2^{1-2s}/\gamma)]^{-1} \quad (5)$$

where

$$s = \left|\cos\frac{90 - (\phi - \phi_0)}{2}\right|$$

For $\gamma = 1$ the solution is exact. The boundary has a teardrop shape, becoming less eccentric for higher values of γ.

From the shape of the boundary illustrated in Figure 9 it is obvious that the axis of symmetry for the equatorial projection of the DMSP/F2-measured boundary is not the dawn-dusk meridian, that is, $\phi_0 \neq 0$. The degree of rotation from the dawn-dusk meridian, as well as the shapes of the boundary in the $0 \leq KP \leq 5$ range, is given in Figure 12. For $KP = 0$ and 1 the rotation is counterclockwise by 23° and 8°, respectively. For $KP = 2, 3$, and 5 the axis of symmetry is rotated clockwise (into the afternoon local time sector) by approximately 30°, 45°, and 45°, respectively. The exact degree of clockwise rotation cannot be determined at this time because of the absence of DMSP/F2 data in the afternoon and postmidnight sectors. The rotation of the boundary's axis of symmetry into the evening sector at times of low KP is due to ionospheric charge pileup near the day-night terminator [Wolf, 1970]. Increasing particle precipitation at times of high KP weakens the ionospheric conductivity gradient near the terminator. It is thus expected that for higher KP the axis would rotate back toward the dawn-dusk meridian. Calculations by Nopper and Carovillano [1979] show that the rotation of the axis of symmetry into the afternoon sector may be due to the requirements of iono-
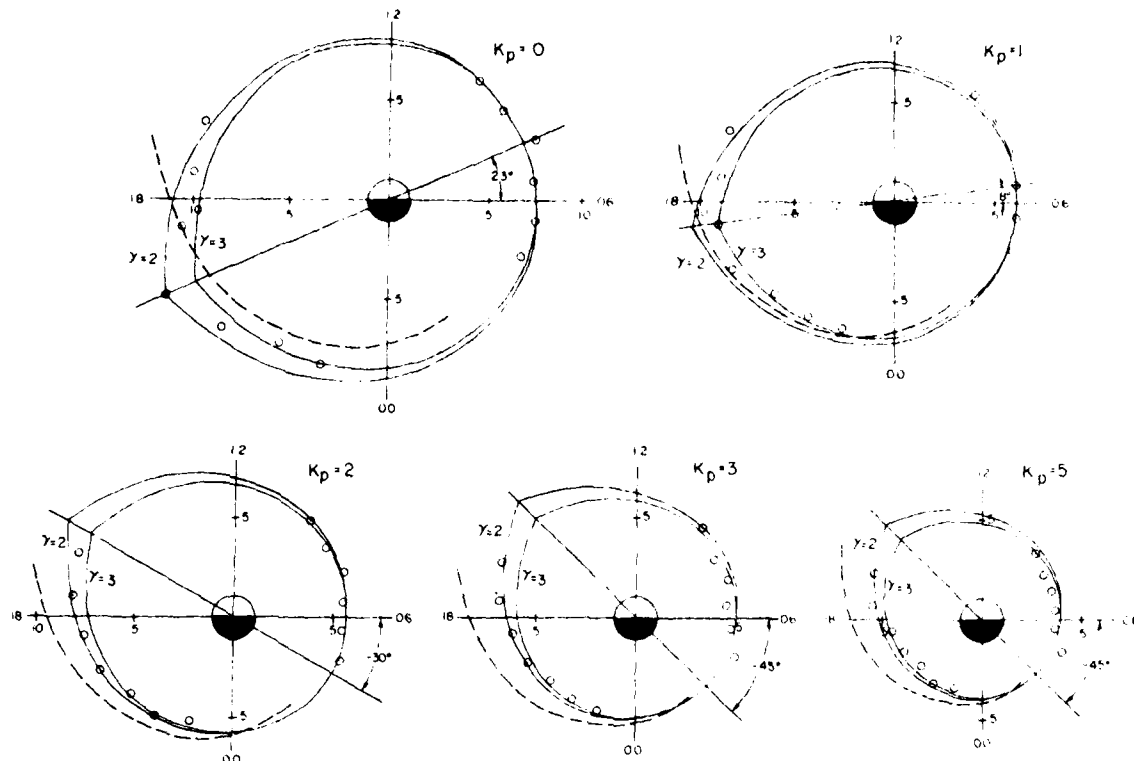
Fig. 12. Volland-Stern injection boundaries for $\gamma = 2$ and $\gamma = 3$, rotated to fit the inner edge of the plasma sheet as determined by the DMSP/F2 auroral boundaries, for various KP. The Mauk-McIlwain injection boundary is also shown (dashed line).

spheric current conservations, as the ratio of region 2 to region 1 Birkeland currents [*Iijima and Potemra*, 1976] increases during time of high KP.

Figure 12 also shows results of fitting the zero-energy Alfvén boundary for $\gamma = 2$ and 3 by using empirical values of ϕ_0. The method used for deriving the boundary values is as follows. (1) Data points marked by an encircled dot are obtained for a given KP by using regression coefficients from Tables 1 and 2. Where north and south data sets overlap in local time, average boundary values are used. The Mead-Fairfield model is then used to map points into the equatorial plane. (2) Because the boundary represented by (4) gives a shape but not a distance for a given value of γ, the data points closest to the boundary minimum (i.e., opposite the duskside stagnation point) are used to 'anchor' the boundary. This procedure is justified because the radial distance of the boundary varies slowly in the morning local time sector and the boundary shape is nearly the same for all values of γ. Boundaries derived for the $\gamma = 1$ case are not shown in Figure 12 because their stagnation points lie well outside the $\gamma = 2$ values. Dashed lines representing the Mauk-McIlwain boundaries are provided for reference. The data points in Figure 12 lie close to the $\gamma = 2$ and $\gamma = 3$ curves with a tendency toward slightly lower values of γ for higher values of KP. Values of γ between 2 and 3 are in agreement with a variety of equatorial observations reported by *Ejiri et al.* [1978], *Southwood and Kaye* [1979], and *Hughes et al.* [1979]. *Kaye and Kivelson* [1981] use *Heppner's* [1972] electric field data to show a radical dependence on the convection electric field which, when ordered by

KP, can be modeled by a γ that decreases with magnetic activity. Further verification of the KP dependence of γ awaits DMSP data acquisition in the afternoon sector.

Data presented in Figure 12 can also be used to provide an empirical expression for the electrostatic potential. Equation (3) can be written

$$\Phi(L, \phi) = \Omega B_0 R_i^2 \left[\frac{L^\gamma}{\gamma L_s^{\gamma+1}} \sin(\phi - \phi_0) - \frac{1}{L} \right] \qquad (6)$$

where $L = R/R_E$ and $L_s = R_s/R_E$. It is useful to define a parameter $\xi = 1/\gamma L_s^{\gamma+1}$. Using stagnation distances derived from Figure 12 as a function of KP, a linear relationship

$$\xi = (1.6 + 2.4\ KP) \cdot 10^{-4} \qquad cc = 0.97 \qquad (7)$$

was found for the case $\gamma = 2$. In the case $\gamma = 3$ the quadratic relationship

$$\xi = (4.2 + 2.3\ KP)^2 \cdot 10^{-6} \qquad cc = 0.99 \qquad (8)$$

was found. Thus for the case $\gamma = 2$ the total potential is

$$\Phi(L, \phi) = \Omega B_0 R_i^2 [(1.6 + 2.4\ KP)$$
$$10^{-4} L^2 \sin(\phi - \phi_0) - (1/L)] \qquad (9)$$

It should be recalled that ϕ_0 is a function of KP that is not describable in a simple analytic form.

SUMMARY

By associating the equatorward boundaries of auroral electron precipitation as measured by the DMSP/F2 satellite with

45

the inner edge of the plasma sheet in a very large statistical sample we find the following results

1. KP orders the data well, particularly in the evening sector. In a given MLT sector the latitude of the equatorward edge of the precipitation decreases linearly with KP, indicating that the inner edge of the plasma sheet moves earthward.

2. The inner edge of the plasma sheet is earthward of the Mauk-McIlwain injection boundary for $KP \geq 2$.

3. The inner edge of the plasma sheet is not symmetrical about the dawn-dusk axis but is symmetrical about an axis whose angle to the dawn-dusk axis depends on KP, reaching a constant value at $KP = 3$. That is, the cross-tail electric field is not always dawn to dusk but has an antisunward component for low KP and a sunward component for $KP \geq 2$.

4. The inner edge of the plasma sheet can be modeled as the zero-energy Alfvén layer in a magnetosphere whose large-scale electric field is obtained from a Volland-Stern potential with $\gamma \geq 2$. For $\gamma = 2$ the KP dependence of the potential is found to be

$$\Phi = \Omega B_0 R_s^2[(1.6 + 2.4\ KP) \cdot 10^{-4}L^2 \sin(\phi - \phi_0) - (1/L)]$$

Here ϕ is dependent on KP as well but is not easily described analytically.

REFERENCES

Carpenter, D. L., and C. G. Park, On what ionospheric workers should know about the plasmapause-plasmasphere, *Rev. Geophys. Space Phys., 11,* 133, 1973.

Father, R. H., S. B. Mende, and R. J. R. Judge, Plasma injection at synchronous orbit and spatial and temporal auroral morphology, *J. Geophys. Res., 81,* 2805, 1976.

Ejiri, M., R. A. Hoffman, and P. H. Smith, The convection electric field model for the magnetosphere based on Explorer 45 observations, *J. Geophys. Res., 83,* 4811, 1978.

Fairfield, D. H., and G. D. Mead, Magnetospheric mapping with a quantitative geomagnetic field model, *J. Geophys. Res., 80,* 535, 1975.

Frank, L. A., Comments on a proposed magnetospheric model, *J. Geophys. Res., 76,* 2512, 1971.

Frank, L. A., and K. L. Ackerson, Observations of charged particle precipitation in the auroral zone, *J. Geophys. Res., 76,* 3612, 1971.

Hardy, D. A., M. S. Gussenhoven, and A. Huber, The precipitation electron detectors (SSJ/3) for the block 5D/flights 2-5 DMSP satellites. Calibration and data presentation, *Rep. AFGL-TR-79-0210,* Air Force Geophys. Lab., Hanscom Air Force Base, Mass., 1979.

Heppner, J. P., Electric field variations during substorms, *Planet Space Sci., 20,* 1475, 1972.

Hughes, W. J., R. L. McPherron, J. N. Barfield, and B. H. Mauk, A compressional Pc4 pulsation observed by three satellites in geostationary orbit near local midnight, *Planet Space Sci., 27,* 821, 1979.

Iijima, T., and T. A. Potemra, The amplitude distribution of field-aligned currents at northern high latitudes observed by Triad, *J. Geophys. Res., 81,* 2165, 1976.

Jaggi, R. K., and R. A. Wolf, Self-consistent calculation of the motion of a sheet of ions in the magnetosphere, *J. Geophys. Res., 78,* 2852, 1973.

Kamide, Y., and J. D. Winningham, A statistical study of the 'instantaneous' nightside auroral oval: The equatorial boundary of electron precipitation as observed by the Isis 1 and 2 satellites, *J. Geophys. Res., 82,* 5573, 1977.

Kaye, S. M., and M. G. Kivelson, The influence of geomagnetic activity on the radial variation of the magnetospheric electric field between $L = 4$ and 10, *J. Geophys. Res., 86,* in press, 1981.

Kivelson, M. G., Magnetospheric electric fields and their variations with geomagnetic activity, *Rev. Geophys. Space Phys., 14,* 189, 1976.

Kivelson, M. G., S. M. Kaye, and D. J. Southwood, The physics of plasma injection events, in *Dynamics of the Magnetosphere,* edited by S.-I. Akasofu, pp. 385-394, D. Reidel, Hingham, Mass., 1979.

Lui, A. T. Y., C. D. Anger, and S.-I. Akasofu, The equatorward boundary of the diffuse aurora and auroral substorms as seen by the Isis 2 auroral scanning photometer, *J. Geophys. Res., 80,* 3603, 1975.

Lui, A. T. Y., D. Venkatesan, C. D. Anger, S.-I. Akasofu, W. J. Heikkila, J. D. Winningham, and J. R. Burrows, Simultaneous observations of particle precipitations and auroral emissions by the Isis 2 satellite in the 19-24 MLT sector, *J. Geophys. Res., 82,* 2210, 1977.

Mauk, B. H., and C. E. McIlwain, Correlation of Kp with the substorm-injected plasma boundary, *J. Geophys. Res., 79,* 3193, 1974.

Meng, C.-I., R. H. Holzworth, and S.-I. Akasofu, Auroral circle delineating the poleward boundary of the quiet auroral oval, *J. Geophys. Res., 82,* 164, 1977.

Nopper, R. W., and R. L. Carovillano, On the orientation of the polar cap electric field, *J. Geophys. Res., 84,* 6489, 1979.

Sheehan, R. E., and R. L. Carovillano, Characteristics of the equatorward auroral boundary near midnight determined from DMSP images, *J. Geophys. Res., 83,* 4749, 1978.

Southwood, D. J., and S. M. Kaye, Drift boundary approximations in simple magnetospheric convection models, *J. Geophys. Res., 84,* 5773, 1979.

Speiser, T. W., Particle trajectories in model current sheets, 2, Application to auroras using a geomagnetic tail model, *J. Geophys. Res., 72,* 3919, 1967.

Stern, D. P., The motion of a proton in the equatorial magnetosphere, *J. Geophys. Res., 80,* 595, 1975.

Vasyliunas, V. M., A survey of low-energy electrons in the evening sector of the magnetosphere with Ogo 1 and Ogo 3, *J. Geophys. Res., 73,* 2839, 1968.

Volland, H., A semiempirical model of large-scale magnetospheric electric fields, *J. Geophys. Res., 78,* 171, 1973.

Winningham, J. D., F. Yasuhara, S.-I. Akasofu, and W. J. Heikkila, The latitudinal morphology of 10-eV to 10-keV electron fluxes during magnetically quiet and disturbed times in the 2100-0300 MLT sector, *J. Geophys. Res., 80,* 3148, 1975.

Wolf, R. A., Effects of ionospheric conductivity on convective flow of plasma in the magnetosphere, *J. Geophys. Res., 75,* 4677, 1970.

Comment on 'Diurnal Variation of the Auroral Oval Size' by C.-I. Meng

M. S. GUSSENHOVEN

Physics Department, Boston College. Chestnut Hill. Massachusetts 02167

D. A. HARDY

Space Physics Division, Air Force Geophysics Laboratory, Bedford, Massachusetts 01731

W. J. BURKE

Physics Department, Boston College, Chestnut Hill, Massachusetts 02167

The position of the equatorward boundary (Λ_E) of the quiet time auroral oval has been studied by *Meng* [1979] using measurements from an electron spectrometer on board the DMSP (Defense Meteorological Satellite Program) satellite F_2. A diurnal variation of ~4° was found in the corrected geomagnetic latitudes (CGL) at which the satellite encountered this boundary. The variation was attributed to a physically unexplained 30% increase in the size of the polar cap as the north magnetic pole rotated from local midnight to local noon. Here we suggest that most of the observed variations in auroral boundaries simply reflect diurnal shifts in the satellite's trajectory in the magnetic local time-magnetic latitude (MLT-CGL) frame of reference.

The DMSP satellite is in a nearly sun-synchronous circular orbit, with an inclination of 98.8°, centered on the 0700-1900 local time meridian. Owing to the offset between the earth's spin axis and the axis of the magnetic dipole the orbit has significant diurnal variations in magnetic frames of reference. This is illustrated in Figures 1 and 2, where we have plotted the northern and southern high-latitude portions of the satellite's MLT-CGL trajectories for January 21, 1978 (the quietest day in Meng's study). These trajectories are representative of those followed by DMSP during the 1977-1978 winter months. At the beginning of the UT day the north polar orbit is roughly dawn to dusk crossing the noon-midnight meridian at 83° CGL in the night hemisphere. The most poleward excursions of the orbit occur between 0700 and 0800 UT; the most equatorward nighttime excursions are found near 1700 UT. The orbits in the southern hemisphere have the same type of motion in the opposite direction. They move from the region of the magnetic pole toward the cusp (or noon sector), often falling outside the oval entirely, and then return poleward. Since the oval lies at higher latitudes in the noon sector than in the midnight sector, there are fewer possible boundary determinations to be made in the south pole data. On the whole, the data after 1200 UT on a given day is unusable for this purpose, and this is reflected in the boundary data presented by Meng.

Figure 3 illustrates how diurnal variations of the DMSP orbit give rise to systematic variations in the CGL of the equatorward auroral boundary. Here we have plotted the northern hemisphere values of Λ_E detected on January 21, 1978. *Meng et al.* [1977] have shown that the poleward boundaries of the oval (Λ_P) during quiet times, as marked by discrete auroral arcs, are well represented by offset circles. During the period

of *Meng's* [1979] study, emissions from the oval were below the detectability levels of the DMSP optical scanner. We have assumed that during this period the oval is latitudinally narrow and that the positions of Λ_E can also be represented by offset circles. The circle in Figure 3 was chosen to fit the morning and evening values of Λ_E for the first DMSP pass of the UT day. It has a radius of 18° and is centered at 86° CGL and 0100 MLT. The circle best fitting the entire data set, in the least squares sense, has a radius of 18.5° and is centered at 86° CGL and 0115 MLT. The corresponding southern hemisphere circle is of 19° radius, centered at −87° CGL and 0120 MLT. These values are consistent with quiet time averages reported by *Meng et al.* [1977]. As is seen in Figure 3, the evening oval boundary is very stable, lying along the chosen circle. The morning oval boundary is close to the plotted circle but shows much greater variability. This is consistent with results from a large set of DMSP measurements reported by *Gussenhoven et al.* [1979], who show that (1) the morning equatorward boundary is much more variable than the evening boundary for a given magnetic activity and (2) for extended periods of quiet magnetic activity the oval does not become entirely stable but can fluctuate greatly in its poleward boundaries and to a lesser extent in its equatorward boundaries.

Predicted UT modulations of Λ_E found by combining offset circles and DMSP orbital variations for the northern and
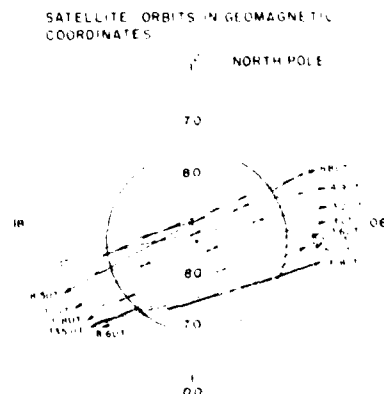

Fig. 1. The orbital paths of the DMSP-F_2 satellite over the north pole for January 21, 1978. The orbits are plotted in corrected geomagnetic latitudes and magnetic local time. The approximate universal time for each polar crossing is given. The quiet oval is represented by an offset circle.

2373

47

SATELLITE ORBITS IN GEOMAGNETIC
COORDINATES
SOUTH POLE
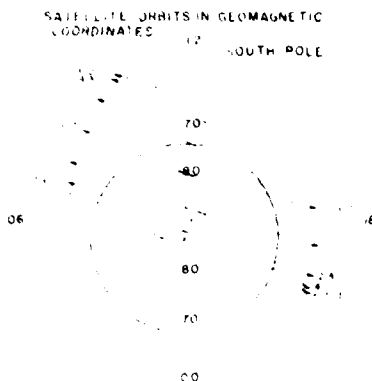
Fig. 2 Same as Figure 1, but for south pole crossings
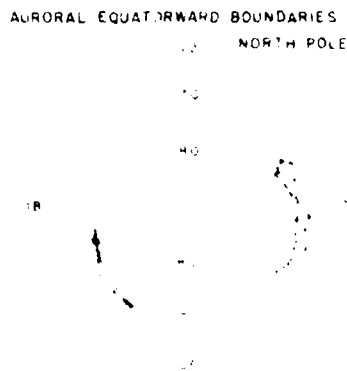
AURORAL EQUATORWARD BOUNDARIES
NORTH POLE

Fig. 3 The boundaries for the northern auroral zone as determined by Meng, plotted in corrected geomagnetic latitude and magnetic local time for January 21, 1976, along with the offset circle used to predict the diurnal variation. The small plus marks the geomagnetic pole, the large plus the center for the offset circle
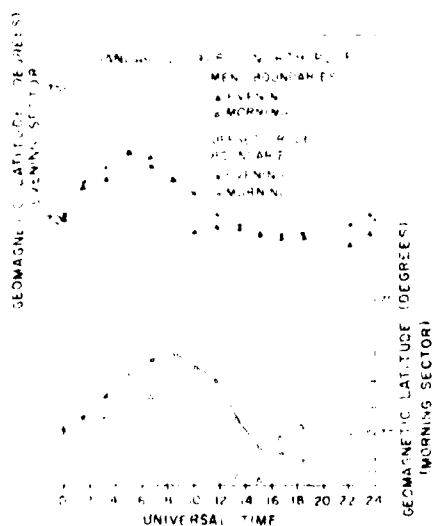

Fig. 4 The solid lines show the expected diurnal variation in the equatorward boundary of the auroral zone in the northern hemisphere for both morning and evening sectors when the variation in the orbit has been taken into account and when the oval has been represented by an offset circle. The evening boundaries are shown in the upper panel (for latitude marks on the left), and the morning boundaries in the lower panel (for latitude marks on the right). The boundaries as determined by Meng are plotted as solid (evening side) and open (morning side) triangles
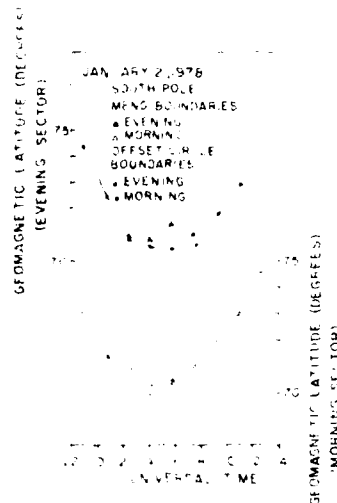
Fig. 5 Same as for Figure 3, but for the south pole

southern hemispheres are given in Figures 4 and 5, respectively. The upper (lower) traces represent the afternoon-evening (morning) equatorial boundaries. Observed values of Λ_i, as determined by Meng, are plotted as triangles. Both the afternoon and morning southern hemisphere as well as the evening, northern hemisphere observations are in remarkable agreement with their predicted estimates. The morning, northern hemisphere measurements show less agreement. The overall differences would be less had we used the least squares circle as our predictor. It should also be noted that morning and evening values tracked each other better on the other days presented by Meng than they did in the first half of January 21. Thus on the other days the predicted and observed values of Λ_i would be in better agreement than in the case presented here.

We therefore conclude that a very large portion if not all of the diurnal auroral boundary variation reported by Meng can be explained by variations in the satellite orbit across an oval represented by an offset circle. We suggest that in order to determine the universal time variation, either a correction for the effect of orbit change in local time could be made or a much greater restriction in magnetic local time could be imposed.

REFERENCES

Gussenhoven, M. S., D. A. Hardy, and W. J. Burke, DMSP electron observations of equatorward auroral electron boundaries and their relationship with magnetospheric electric fields, Eos Trans. AGU (abstract), 60, 916, 1979.
Meng, C.-I., Diurnal variation of the auroral oval size, J. Geophys. Res., 84, 5319-5324, 1979.
Meng, C.-I., R. H. Holzworth, and S.-I. Akasofu, Auroral circle delineating the poleward boundary of the quiet auroral belt, J. Geophys. Res., 82, 164-172, 1977.

48

Propagating Substorm Injection Fronts

T. E. MOORE AND R. L. ARNOLDY

Space Science Center, University of New Hampshire, Durham, New Hampshire 03824

J. FEYNMAN

Department of Physics, Boston College, Chestnut Hill, Massachusetts 02167

D. A. HARDY

Air Force Geophysics Laboratory, Bedford, Massachusetts 01731

The geosynchronous ATS 6 environmental measurements experiment was operated during 15 evening passes when the SCATHA spacecraft was within 1-2 R_L and both spacecraft were very near the geomagnetic equator. Numerous, well-defined substorm injections were recorded at both spacecraft with varying local time and radial separations. Accurate delay timing was possible since these events exhibit abrupt and essentially dispersionless (to within 10 s) plasma flux changes which replace cool preexisting plasma with hot quasi-Maxwellian distributions. The hot plasma propagates earthward in close association with an equally abrupt magnetic field increase at velocities in the range of 10-100 km/s. On this basis we identify the agent of injection as the induced electric field of the earthward propagating compression wave observed by Russell and McPherron (1973), and we refer to the propagating particle structure as the injection front. These dramatic synchronous orbit electron injection signatures are produced mainly by a boundary motion rather than by local acceleration of plasma. However, we find some evidence that the plasma sheet electrons are weakly 'heated' by the passage of each compression wave, the energy appearing mainly in the high-energy tail of the distribution. The spectral change we observe argues convincingly that the boundary in question is a precipitation-flow boundary layer (Kennel, 1969) and that the near-earth plasma sheet is significantly degraded in average energy by the addition of ionospheric plasma, especially secondary electrons emitted by the ionosphere due to precipitating energetic electrons. The presence of significant $\partial B/\partial t$ requires that a change of mapping occur between the equatorial plane and the ionosphere, the sense being such as to map the inward moving injection front to a relatively fixed latitude in the ionosphere. Such an earthward plasma injection would not therefore require equatorward auroral motion.

INTRODUCTION

The term 'injection' has been defined [*Kivelson et al.*, 1980] as an 'increase in the particle flux in a detector of finite energy bandwidth.' The process by which energetic plasma is 'injected' into the auroral magnetosphere is of fundamental importance to the dynamics and energetics of magnetospheric substorms and storms. Changes in particle flux observed by spacecraft [*DeForest and McIlwain*, 1971; *Smith and Hoffman*, 1974; *Ejiri*, 1978] have shown that injection processes occur impulsively in the evening to midnight local time sector and result in drifting clouds of hot plasma electrons and ions.

Two rather distinct schools of thought appear to exist concerning injection processes. The first postulates a time-varying, spatially localized acceleration or heating process with subsequent flow in a quasi-static convection pattern. The term 'injection boundary' has been used for the surface in whose vicinity the acceleration takes place [*McIlwain*, 1974]. The second postulates a time-varying convection pattern which deflects earthward a flowing plasma of quasi-static properties. 'Quasi-static' here means static over the injection time scale. Though idealized, both models have found success in describing injection observations. In fact, for certain types of events, it has been found that some aspects of the signature at geostationary orbit can be reproduced equally well by an injection boundary model, or a model with varying convection electric field, or a hybrid model with spatially limited time-varying electric and magnetic fields [*Kivelson et al.*, 1980, and refer-

ences therein]. This situation illustrates the nonuniqueness of conclusions drawn from a single-satellite data set and the need for multiple-satellite observations to constrain the modeling process. This paper is an attempt to learn from the comparison of plasma data sets from ATS 6 and SCATHA relating to several substorm events.

An example of the success of the first point of view appears in the paper by *Barfield et al.* [1977], in which an impulsive injection of plasma is observed at ATS 5 and then 11 min later at Explorer 45, 1.2 R_I earthward and at approximately the same local time. Assuming that an energetic plasma was created and released beyond a sharp, azimuthally extended boundary outside synchronous orbit, the authors were able to build a fairly consistent picture of the subsequent flow of the plasma past the two spacecraft. They found that large-scale electric fields inferred from the location of apparent convection boundaries, the travel time between the satellites, and the value of μ for which $J_{ATS}(\mu) = J_{EXP}(\mu)$ were all fairly consistent. However, the fact that the fluxes matched only at one μ implies that the source region was not azimuthally uniform as assumed. Moreover, some of the detailed observations suggest that the large-scale convection electric field was decreasing or that the magnetic geometry was changing during the period after the event (drift echoes were observed).

The second point of view has developed partly in response to these difficulties and partly in recognition of the importance and tractability of time-varying convection calculations. It has been used to interpret specific observations by *Kaye and Kivelson* [1979] and *Hultqvist et al.* [1981]. In this process, an

6713

49

enhancement of the convection electric field deflects the sun-
ward flow of the plasma sheet to lower equatorial altitudes
where it becomes observable at synchronous orbit and inter-
acts with the atmosphere and plasmasphere. Trapping of the
deflected flow onto closed convection orbits to form a stable
ring current occurs when the enhanced convection subsides.
However, as pointed out by *Kivelson et al.* [1980], such a
model is only adequate for a limited class of events, termed
'electric substorms' by J. R. Winckler. In particular, this ap-
proach has found success in describing events with large posi-
tive energy dispersion ($dt/dW > 0$) and little, if any, magnetic
perturbation at the satellite. Note that this model does not in
voke time-varying heating or acceleration of plasma, but
rather assumes a steady source, the plasma sheet. Evidently,
these electric field changes are not inductive in nature.

'Dynamic' injections of plasma are characterized by a mag-
netometer signature that represents a single point observation
of an inward propagating, compressional wave front. *Russell
and McPherron* [1973] have reported clear observations of this
phenomenon from ATS 1 and OGO 5. They clocked the front
at approximately 140 km/s, i.e., 94 s between 9 and 6.6 R_E,
and were thus able to estimate the induced electric field asso-
ciated with the wave as a few millivolts per meter. Such an in-
duced field is of great significance for plasma transport.

The aim of the present study is to extend the work of *Bar-
field et al.* [1977] by examining plasma data of a similar nature
from the ATS 6 and SCATHA spacecraft during active peri-
ods when the vehicles are near local time conjunction. In the
following section we display representative data from a rather
extensive data set, including many evening passes when the
two satellites were near local time conjunction but separated
by 1-2 R_E in radius or azimuth. Both vehicles are generally
within a few degrees of the geomagnetic equator at these
times. In subsequent sections, the data are analyzed in terms of
energy spectral comparisons, relative timing of plasma
changes seen at the two locations, and energy dispersion ob-
served in the increases at each point individually. A discussion
of the results obtained and conclusions regarding the nature
of this type of injection process form the final two sections.

OBSERVATIONS

Instrumentation

The University of New Hampshire (UNH) ATS 6 plasma
instrument consists of four double cylindrical electrostatic an-
alyzers, each measuring electrons and ions over the approxi-
mate energy range 50 eV to 20 keV in eight steps with a geo-
metric factor of ~10^{-3} cm^2 sr and an energy band pass $\Delta E/E$
~ 0.10. The analyzers employ blackened, serrated, 90° sector
plates and postacceleration of both electrons and ions onto
channel multipliers. Energy spectra were recorded every 8 s in
two directions while eight readouts per second at a fixed en-
ergy were recorded for the other two directions.

The Air Force Geophysics Laboratory (AFGL) rapid scan
particle detector consists of a set of electrostatic analyzers for
energies up to 60 keV and solid-state detectors for the range
up to 1 MeV for electrons and several MeV for protons. The
electrostatic analyzers differed from the UNH detectors
mainly in that they had a very wide energy band pass $\Delta E/E$ ~
1, resulting in contiguous energy channels. This has the effect
of smearing energy dispersive flux changes, so that the magni-
tude of dispersion measured by this instrument is an upper
limit. The data reported here are from detectors viewing along
the spacecraft spin axis, nominally at ~90° pitch angle.

The ATS 6 magnetometer data reported here are from a pe-
riod after the failure of N-S channel. Based on the marked
similarity of the two operating channels to those recorded on
the GOES 3 satellite 20 min east of ATS 6, we will at times
take the GOES 3 field to be representative of the ATS 6 field.
Magnetic data from SCATHA are available only after day 52
of 1979 (February 21).

General Description of Events

Figure 1 shows energy-time spectrograms of ATS 6 plasma
data for days 42, 43, and 50 of 1979, the periods which have
been chosen as representative of substorm activity for this
study. The general nature of the data set is familiar from data
of a similar nature published by the University of California,
San Diego (UCSD), Group and co-workers. We wish to focus
mainly upon the relatively abrupt and dispersionless increase
seen in the dusk to midnight sector in association with mag-
netic activity at the ground and the spacecraft (see Figure 2).
Examples of this type of event occurred at ATS 6 at 0930 and
0945 on day 42, at 0458, 0740, and 1040 on day 43; and at
0730 on day 50. The relative locations of ATS 6 and
SCATHA at these times are shown in Figure 1 as MLT versus
R. Also shown are the locations of the satellites at times of in-
creases in low-energy electrons and ions corresponding to en-
try into the 'old' or preexisting plasma sheet. In general, this
occurs at quite different times at the two satellites. The *Mauk
and McIlwain* [1974] substorm-injected plasma boundary for
the appropriate Kp on day 42 is also shown.

In Figures 3-6 we display ATS and SCATHA data for se-
lected energy channels in line plot form on an expanded time
scale showing 12 hours per frame. The data points represent
24-s and 1-min averages for ATS and SCATHA, respectively.
A striking degree of correspondence may be seen between im-
pulsive events in the two data sets. As noted above, dusk sec-
tor low-energy changes occur at quite different times.

We wish to firmly establish the association between the
types of events selected for study and substorms. Figure 2 re-
veals significant associated negative bays in the horizontal
magnetic field component at International Magnetospheric
Study (IMS) magnetometers, a well-known substorm signa-
ture. In defining the term 'substorm,' *Rostoker et al.* [1980]
have stated that substorm onset can be identified by the first
appearance of significant Pi 2 activity at the ground. As part
of this study, we have examined data from the AFGL magne-
tometer chain of five stations across the northern United
States. Clear Pi 2 was found in association with most of the
events we will discuss and was associated with all of the events
which appeared as abrupt spectral changes. The earliest time
of Pi 2 onset is to be regarded as the latest possible time of
substorm onset. In each case, this time coincided very nearly
(±1 min) with the appearance of the injection at ATS 6, while
appearance of the injection was, in general, significantly de-
layed at SCATHA. An example is shown in Figure 2.

It should be noted that the type of event on which we are
focusing is a very commonplace occurrence and is not patho-
logical or unusual in any way, representing rather a 'typical'
evening substorm signature at the equatorial plane on auroral
field lines. As may be seen in Figure 2, these events are ac-
companied by clear magnetometer perturbations which mark
them as dynamic events involving induced fields. In particu-
lar, the magnitude of B increases by a factor of 2-3, and there
is generally a slight rotation to a more dipolar orientation with
each injection event, as observed from locations near the geo-
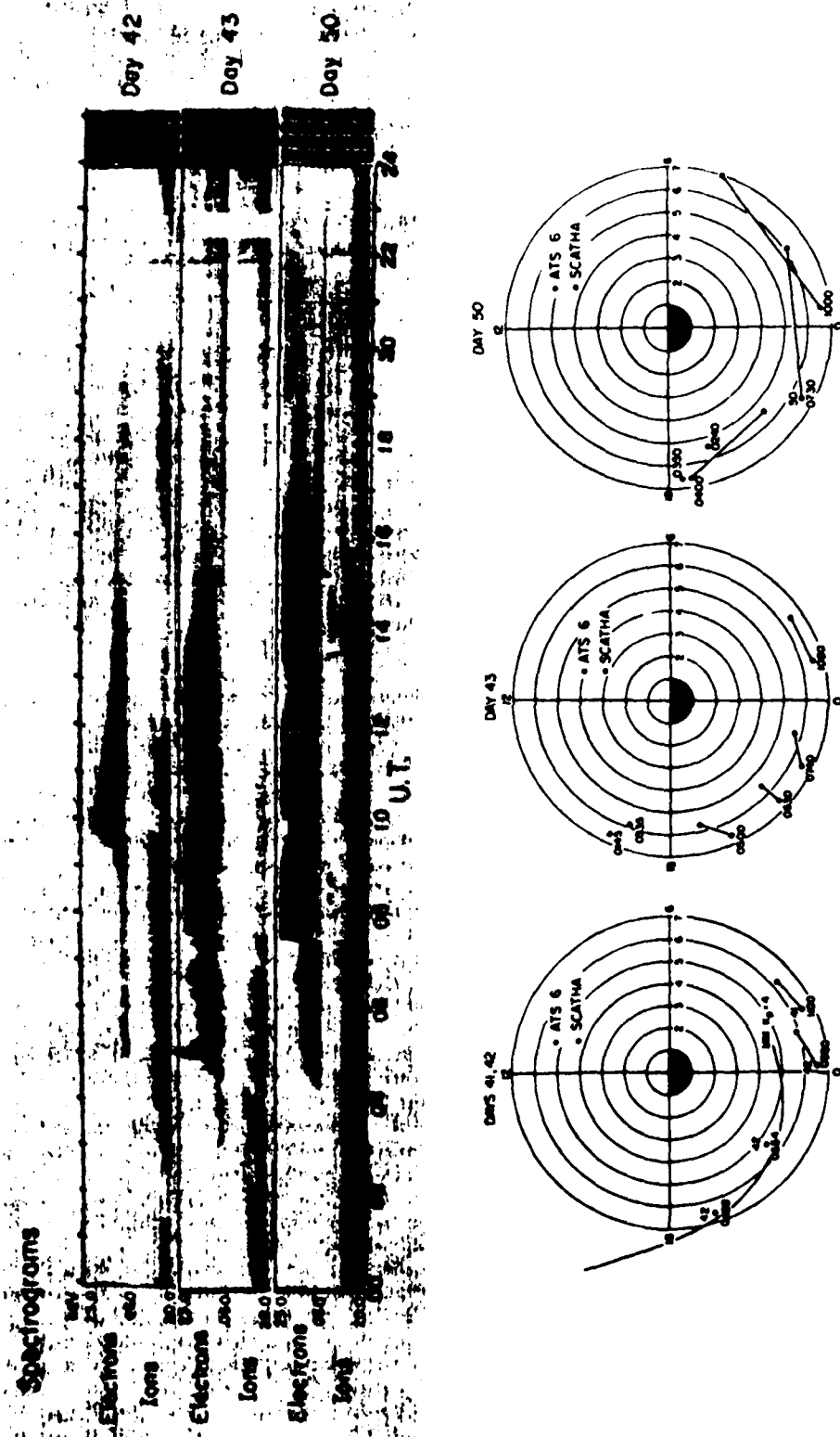magnetic equator.

Fig. 1 Hot plasma and orbit summary: (Top) Energy-time spectrograms for 3 days of this study. Ion energy increases downward. (Bottom) Orbit plots showing the MLT-R coordinates of ATS 6 and SCATHA for selected plasma events.

Day 42, 1979

The isolated injection event seen on day 42 (see Figure 3) essentially at midnight local time, together with the duskside plasma signature prior to the event, displays most of the characteristics we have observed in the ATS/SCATHA data set.

As the satellites passed dusk local time, ATS 6 recorded large enhancements of 70- and 470-eV electrons, with the 70-eV increases leading by ~20 min. Increases at comparable

DAY 43, 1979

AFGL Magnetometer Network

energies were recorded some 3 hours later at SCATHA, suggesting that a spatial boundary connecting these two points persisted throughout the intervening period.

At 0930, ATS recorded the hot plasma injection consisting in the line plot format of increases at higher energies, simultaneous decreases at the lowest energies, and little change at intermediate energies. A similar signature is also seen by SCATHA, but with a ~10-min time delay.

This event exhibits another characteristic feature of injection events, namely, the substantial increases at a few keV energy prior to the simultaneous high- and low-energy changes which we have somewhat arbitrarily defined as the injection signature. This 'precursor' is observed at both spacecraft, but with much less time delay. Moreover, considerable dispersive structure appears in the SCATHA precursor which is not nearly as evident at ATS 6.

A second injection event of a similar nature but without precursor is seen ~15 min after the first, again with an appreciable delay between appearance at the two spacecraft. This multiple-event phenomenon is not uncommon. Following the double injection, fluxes at all energies decayed back toward preevent levels. We shall return in the discussion section to some of the details, such as the precursor increase at ~5 keV and the lack of dispersion between high- and low-energy channels during the abrupt changes. Figure 7 gives a spectral time series view of the ATS 6 fluxes during this period. It may be noted that the electron fluxes tend to Maxwellian as a result of the injections.

Day 43, 1979

This is a considerably more active period exhibiting numerous injection events resembling that of day 42. The first feature to note (see Figure 4) is the very early, low-energy increase at ATS which actually occurred prior to dusk local time. Increases at ~100 eV were seen by SCATHA at ~0335. A comparison with day 42 suggests that the satellites are encountering a low-energy boundary about 2-3 R_E earthward of that seen at dusk, early in day 42.

The first substorm injection occurred at 0458 at ATS and ~5 min later at SCATHA. The similarity to the day 42 injection signature is striking, despite the fact that it occurred some 4.5 hours earlier in local time. The spectral change in this event is also shown in Figure 7. After a period of decay back toward flux levels present prior to the event, fluxes at both spacecraft entered a period of fluctuations without a clear injection signature until 0740. One might identify injections at 0530 and 0550, but they are not seen clearly at SCATHA and do not extend to the higher energies. Note that the fluctuations at ATS are very narrow in energy bandwidth, so similar fluctuations would have much smaller amplitude when viewed with the wide-band SCATHA instrument. The electron drop and recovery at ATS at 0630 was accompanied by large increases in energetic ions at SCATHA, as will be discussed below.

Another clear injection occurred at 0740 nearly simultaneously at both satellites. Increases at SCATHA extended to the few hundred keV channel. Though ATS 6 low energies again decayed upward to preevent levels, the energetic fluxes remained approximately constant for a few hours before another event at 1020. Figure 8 shows the 0740 event at higher time resolution and reveals a delay of ~1.0 min.

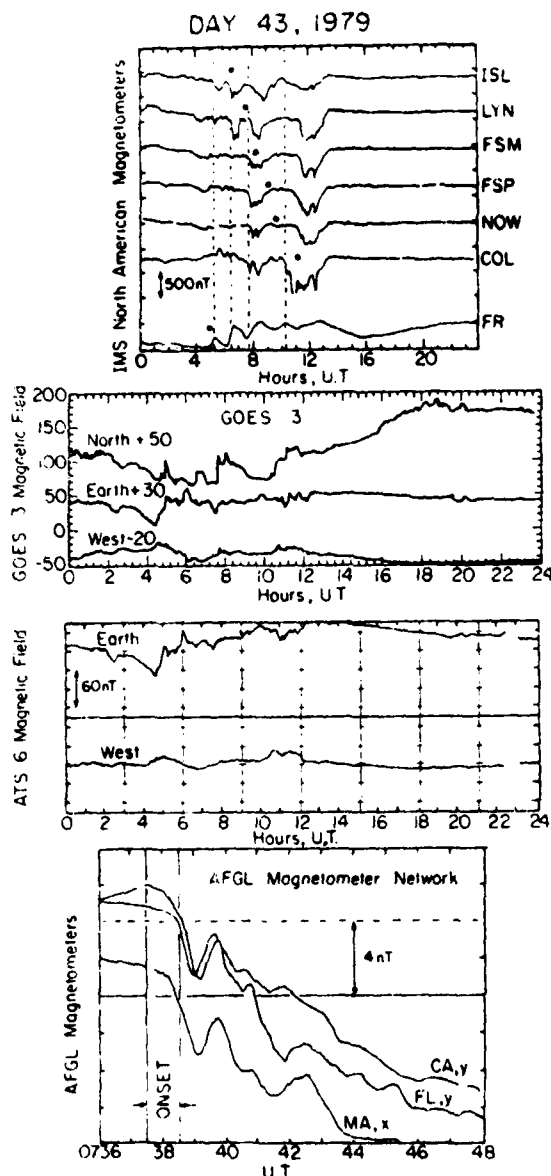The event at 1020 differs considerably in appearance from the earlier events, though it probably represents the post
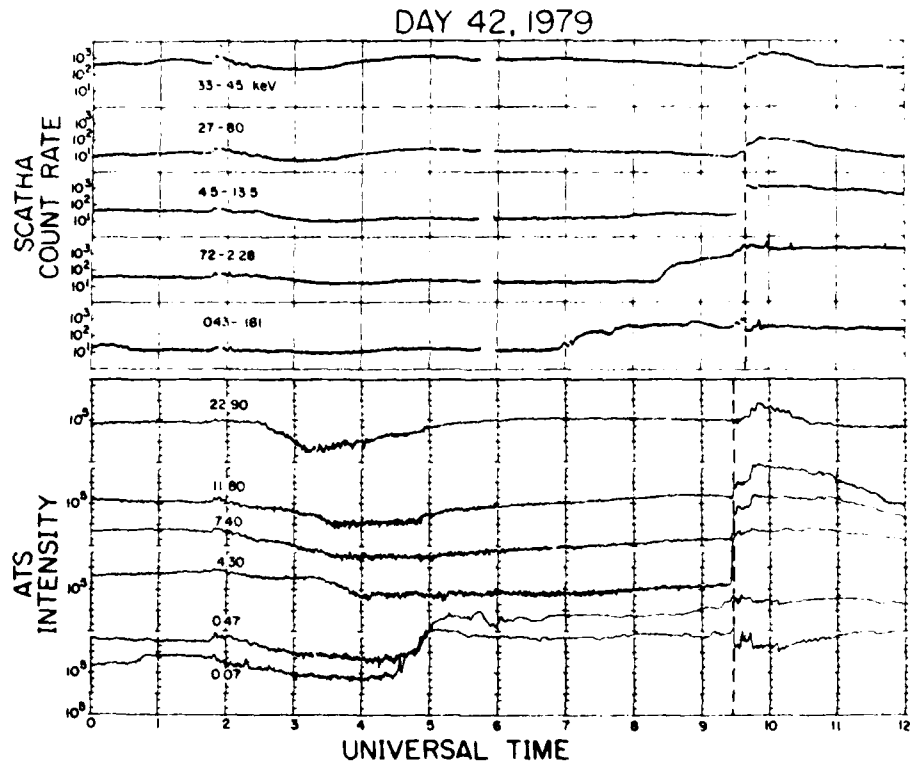
DAY 42, 1979

Fig. 3. ATS 6 and SCATHA electron data at selected energies and ~90° pitch angle for day 42 (February 11, 1979).

DAY 43, 1979
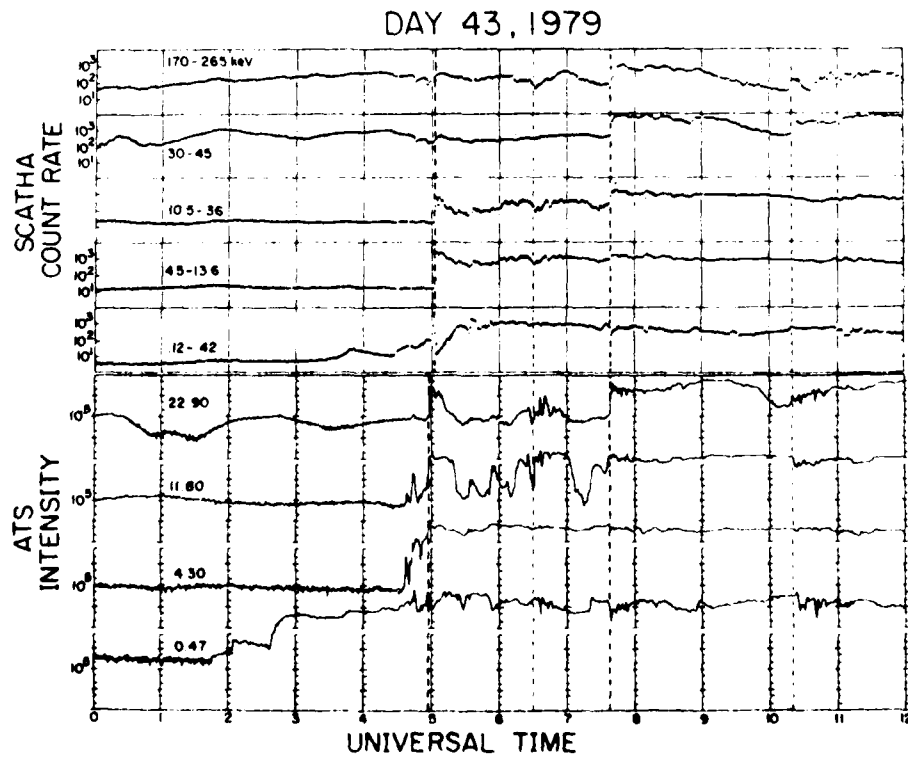

Fig. 4. Same as Figure 3, but for day 43 (February 12, 1979).

DAY 43, 1979
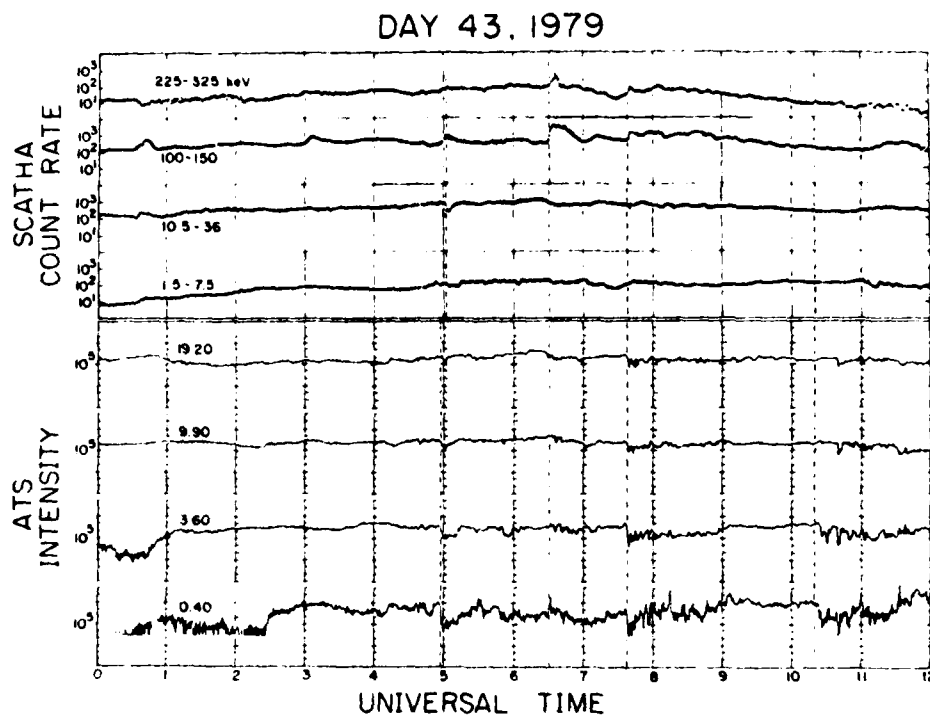

Fig 5. ATS 6 and SCATHA ion data at selected energies and ~90° pitch angle for day 43 (February 12, 1979).

midnight signature of the same injection process. The spacecraft are no longer separated in radial distance, but SCATHA is ~1.5 hours later in local time. Very energetic electrons appear approximately simultaneously at the two locations con-

sistent with rapid gradient/curvature drift, while lower-energy electrons are delayed at SCATHA, exhibiting negative dispersion characteristic of drifting plasma clouds [*Arnoldy and Chan.* 1969; *DeForest and McIlwain.* 1971].

DAY 50, 1979
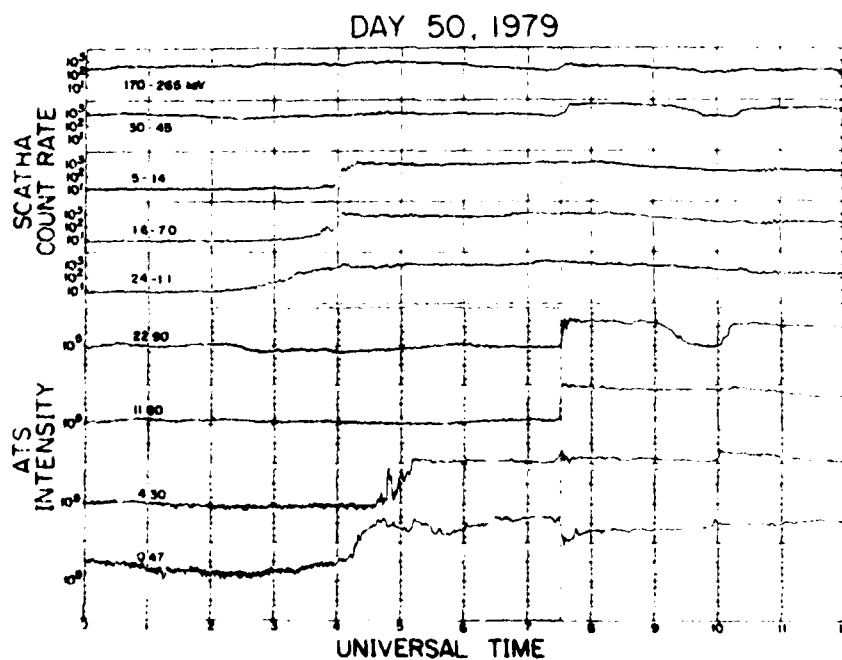
Fig. 6. Same as Figure 3, but for day 50 (February 19, 1979).

Figure 5 shows the ion signature of these multiple substorms. For each event, ion increases are seen only at energies above some variable level ~15-25 keV. This means that ion increases are often out of the 20-keV range of the ATS instrument. At lower energies, decreases are seen with the largest drops at the lowest energy. The ion behavior is thus much like the electron behavior except that (1) amplitudes are generally smaller and (2) the energy of little change is somewhat higher, perhaps an order of magnitude. Note the large energetic ion increases at SCATHA at ~0630, which had no electron counterpart. This event may represent a substorm injection which originated abnormally far to the east at or beyond midnight. The main features of interest for the other events are the lack of ion energy dispersion and the simultaneity with the electron events.

Day 50, 1979

The comparison of plasma behavior on day 50 (Figure 6) is dominated by the increasing local time separation of the spacecraft, with SCATHA leading by 3-5 hours. SCATHA is able to encounter low-energy electron increases well before ATS, despite its lesser radial distance from earth. At ~0400, SCATHA observed a weak injection event not observed at ATS 6 3 hours to the west. Then at 0740, ATS recorded a 'typical' injection which was seen by SCATHA 4 hours to the east only as dispersed drifting energetic electrons. Finally, an event at ~1020 was seen as a drifting cloud by both vehicles. The large azimuthal separation of the vehicles does not lend itself to the study of 'injections,' as defined above, but does show that individual injections have an azimuthal extent of a few hours local time and are commonly observed in the dawn to midnight sector.

Selected Events at High Time Resolution

In order to give a more detailed two-point view of the impulsive injection events, we present data on an expanded time scale for selected events in Figures 7 and 8. Each event is depicted in plasma data from ATS 6 and SCATHA together with magnetic data from ATS 6 and GOES 3 nearby. Time resolution in these plots is approximately 10 s.

Figure 8 shows the clear association of the local magnetic field increase and the arrival at ATS 6 of the abrupt and (to within 10 s) dispersionless spectral change (Figure 7). It also demonstrates the considerable variability we observe in the delay time between arrival at ATS 6 and SCATHA approximately 1 R_E closer to earth, ranging from 10 min at ~0930 on day 42 to 1 min at ~0740 on day 43. Also evident are the marked increases at a few keV prior to the abrupt spectral change. These precursor increases show little, if any, delay between the two spacecraft for the first of these events and a delay comparable to that of the spectral change for the second and third events. The precursor increase for the first event shows considerable energy dispersion at SCATHA. Though such precursor increases are commonplace, it would appear that there is more than one type of responsible physical process.

ANALYSIS

In this section we examine in more detail the temporal and spectral relationships of the plasma data sets and compare these details with expectations based on theories of time-dependent acceleration or convection.

As pointed out above, injection events replace plasma ini-

tially present with hot Maxwellian electrons. In Figure 9 we display preinjection and postinjection spectrums at ATS 6 and SCATHA for the day 43, 0500 UT injection. The phase space density versus energy plot illustrates the Maxwellian nature of the injected plasma, which is essentially identical at the two spacecraft despite their radial separation of ~1R_E. Adiabatic heating in a steady dipolar magnetic field would have raised the temperature at SCATHA by ~50%, yet the increase observed is at most 15%. It seems that the plasma travels inward over both vehicles from a region fairly homogenous in azimuth, since drift of the more energetic electrons does not appear to alter the spectrum.

The lack of adiabatic heating between the spacecraft must be related to the temporal changes occurring in the magnetic configuration during injection events. As mentioned above, it is common knowledge that the nightside magnetic field increases in magnitude and becomes closer to dipolar as part of

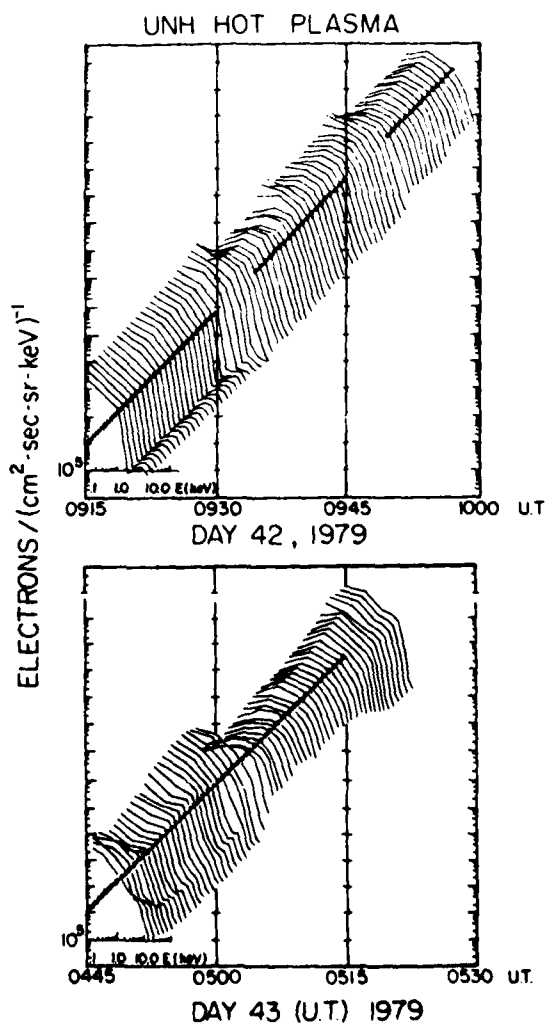

UNH HOT PLASMA

DAY 42, 1979

DAY 43 (U.T.) 1979

Fig. 7. Detailed energy distribution time series for injection events at (a) 0930 UT, day 42 and (b) 0458 UT day 43. Each curve represents intensity (cm² s sr keV)⁻¹ versus energy on logarithmic axes with the origin (60 eV, 10⁶/cm²s sr keV, marked by +) aligned with the time of the data and displaced upward to separate the curves.
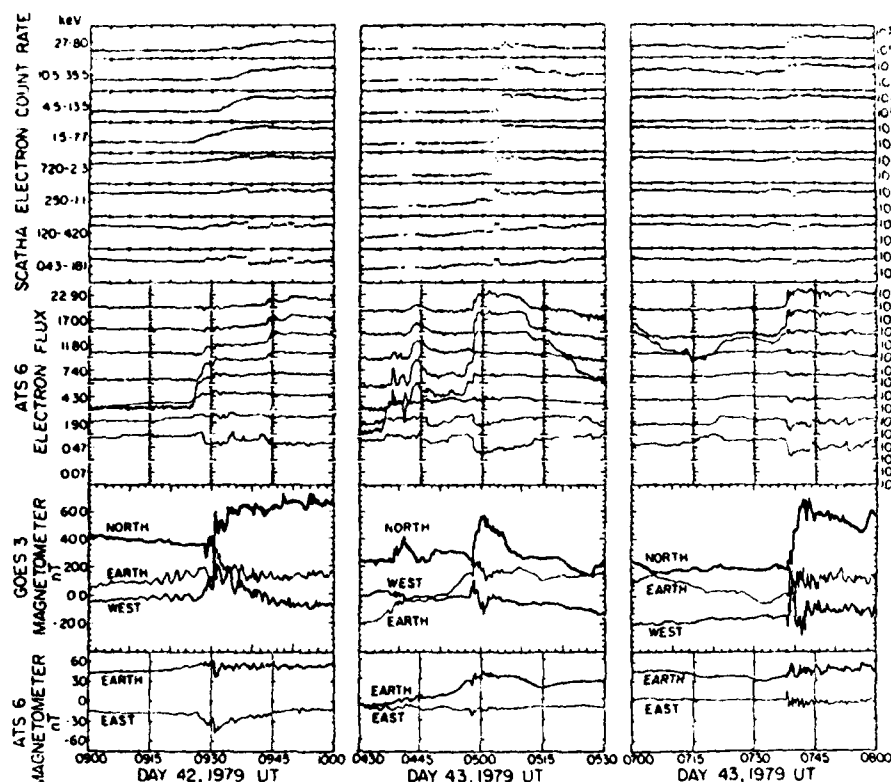
Fig. 8. Detailed line plots of ATS 6 and SCATHA electron plasma and GOES 3 magnetic field for three substorm injection events. Time resolution is 10 s. Radial spacecraft separation is ~1 R_E. See Figure 1 for orbit relationships.

the substorm. This corresponds to a reduction of the cross-tail current in the near-earth plasma sheet. *Russell and McPherron* [1973] showed clear evidence that the magnetic reconfiguration is accomplished by an inward propagating compressional wave. This compressional wave may be thought of as a thin dawn-dusk current sheet with stronger magnetic field behind, propagating inward through the inner plasma sheet and representing the collapse of field lines formerly inflated by a quasi-stationary dawndusk current. The magnetic field strength behind the wave front may not increase strongly with inward propagation. Hence particles traveling behind the front may not experience much adiabatic heating. We will comment further on this subject in later sections where we will argue that plasma tends to be swept along with these fronts and will use the term 'injection front' for the propagating particle structure.

An important aspect of the data set presented here lies in the timing and energy dispersion of the events as seen at the two spacecraft. The delay between injections is a measure of the electric field which moves the plasma inward. Together with the timing, the energy dispersion observed at each spacecraft contains information about the spatial dimensions of structures moving past the spacecraft. Our observations show that injection appears abruptly at ATS 6 and subsequently at SCATHA with a delay of 1-10 min when the satellites are near the same local time. A comparison of ATS 6 and GOES 3 magnetic signatures (Figure 8) suggests that the compression wave front arrives at points separated in azimuth with a delay

which is small compared with the delay between radially separated points. An earlier study of ATS 5 and ATS 6 data [*McIlwain*, 1975] when those two satellites were separated in local time, but at the same radius, showed that injected plasma appears simultaneously over some azimuthal range in the evening sector. We conclude that the injected plasma has a nearly radial velocity of 0.1-1.0 R_E/min ~10-100 km/s near synchronous orbit, corresponding to a convection electric field of ~1-10 mV/m or 7-70 kV/R_E. This corresponds to a cross-tail potential of a few hundred kilovolts to a few megavolts if this field is taken as representative of a large-scale potential field. These values are in excess of that of *Barfield et al.* [1977] by a factor of 1-10, though considering the scatter of delay values we have found, the numbers are essentially in agreement.

We may get an estimate of the preexisting convection field from the observed location of the low-energy plasma boundary. The boundary approximations published by *Southwood and Kaye* [1979] are particularly handy for this purpose. In general, for an electric potential described by

$$V = CL^2 \sin \phi - 91/L$$

(κ the shielding parameter, is taken equal to 2) the electric field parameter C required to place the energy W electron boundary at radius L and azimuth ϕ is

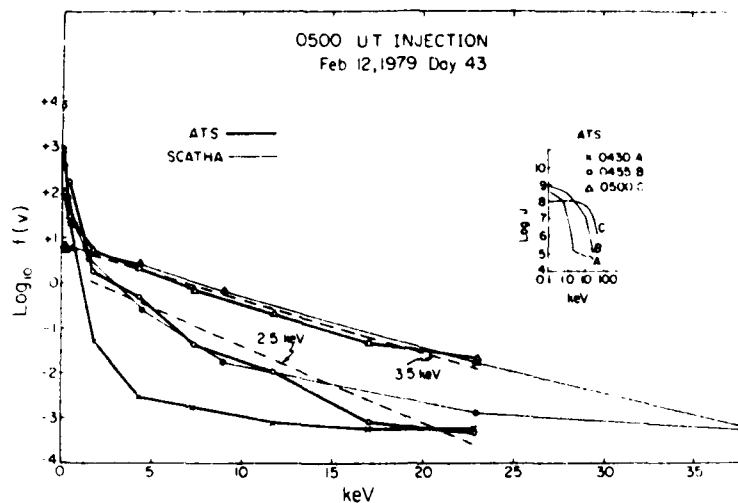$$C = \frac{\alpha(\phi)W}{L} + \frac{\beta(\phi)}{L^2}$$

Fig. 9. Comparison of energy distribution at ATS 6 and SCATHA for 0458 UT, day 43 injection, plotted as phase space density versus energy to illustrate the Maxwellian character of the postinjection plasma.

where α and β are tabulated by those authors. Evaluating, we find dawn/dusk electric fields near synchronous orbit for observed boundary locations of 0.77 kV/R_E for day 42 and 1.4 kV/R_E for day 43. These values are more than an order of magnitude below those inferred from the delay times, suggesting that indeed the substorm injection was accomplished by a large increase in the electric field. The $\kappa = 1$ case (no shielding) results in field estimates approximately twice as large as those above but still small compared with the delay time inferred values. See below for an additional discussion of the choice of κ.

Next we consider energy dispersion. The events we have selected have very small dispersion by choice, though this is typical for well-defined substorms and in a sense defines the synchronous orbit substorm signature. It may be seen in Figure 8 that the decreases at lowest energy and the increases at highest ATS 6 energy are simultaneous to within ≤ 10 s. Dispersion in the SCATHA data is comparable for this type of event but larger in others. If we define a thickness d as $v\Delta t$, where v is front velocity and Δt is the dispersion time from zero energy to some energy E_{max}, we may make a first-order estimate of the injection front energy dispersion thickness as ≤ 0.1 R_E when $E_{max} \sim 23$ keV, corresponding to the upper limit of ATS 6 observations. One may also define a thickness in terms of the rise time of the leading edge of particle changes. This rise time is somewhat longer than the dispersion time differences. Hence, by this criterion, the fronts are somewhat thicker, up to nearly 1 R_E depending on how one defines the rise time. Since this front passes both satellites without a decrease at ATS 6, we are seeing a sharp boundary between the inner plasma sheet and a relatively uniform hot plasma region, the radial depth of which is at least 1 R_E beyond the boundary.

Referring to the first model of injection described in the introduction, we find that the impulsive acceleration region, if one exists, must create hot plasma behind a thin, azimuthally extended boundary. Such a plasma region would be expected to move nearly radially inward past ATS 6 and SCATHA in the evening sector under the combined influence of convection and corotation electric fields, provided the convection

field was sufficiently strong. Ejiri et al. [1980] have performed calculations of the orbits of electrons and ions initially exhibiting such a sharp inner edge under the action of a strong Volland-Stern ($\kappa = 2$) electric field. Though many of the features of their results are in general agreement with our electron observations (lack of dispersion or weak positive dispersion, dt/dW, in the evening sector; increasing negative dispersion east of midnight), there is one aspect of our data on successive events in the same evening which appears inconsistent with their model. Inspection of Figure 4 shows a striking tendency for the flux at some energies to vary between two states, high corresponding to postinjection and low corresponding to the period between injections, for example, the 11.8-keV electrons at ATS 6. If the flux remains high after one injection, e.g., 4.3-keV electrons, it is not further increased by later injections. This behavior seems to argue strongly for boundary motion rather than impulsive acceleration. Moreover, the assumption of sudden particle acceleration beyond an arbitrary boundary is somewhat ad hoc, as Ejiri et al. [1980] point out. They propose that such a sharp inner edge could be set up by a steady convective flow with a weak electric field prior to the substorm injection, appealing to the time-dependent convection calculation of Kaye and Kivelson [1979] and to the well-known presence of the plasma sheet. However, Kaye and Kivelson [1979] apparently dispute this, pointing out that the inner edge of the plasma sheet formed by steady convection should be quite dispersed and that consequently, injections produced by an abrupt increase of the large-scale convection field should produce electron increases showing considerable positive dispersion in the evening sector.

Our line of reasoning has brought us to the second model of injection, described in the introduction, involving motion of a boundary between hot and cool plasma. It has been proposed that this boundary is the boundary between open and closed large-scale convection orbits. If this is so, the energy dispersion of observed plasma increases is equivalent to the radial dispersion of the convection boundaries with energy, as the structure convects under an increased electric field. We have seen that typical substorm increases exhibit very small

dispersion even considering the speed with which they move past synchronous orbit. This dispersion corresponds to a radial thickness (0-20 keV) of $\leq 0.1 R_E$, which may be compared with convection boundary spacings by use of the *Southwood and Kaye* [1979] approximations. For initial parameters we take the electric field estimates from above and calculate energy W as a function of L at 2100 MLT, displaying the result in Figure 10. It can be seen that the Volland-Stern field predictions for the convection structure thickness over the 0-to 20-keV energy range are of the order of a few earth radii, much larger than those inferred from the present observations. Moreover, there is another problem in that our field estimates assume the low-energy boundaries to extend well inside $L = 6$, but injection changes are observed at the lowest observed energies If we instead estimate the field to be that value which places the zero-energy boundary just outside synchronous orbit, an even larger radial dispersion results (see third curve, Figure 10).

One way to steepen the dispersion of the convection boundaries is to increase the shielding parameter κ. However, very large values would be required to achieve a 0- to 20-keV thickness of a fraction of an earth radius. Moreover, based on the discussion of *Southwood* [1977] and *Kaye and Kivelson* [1981], one does not expect extreme shielding prior to a substorm outside synchronous orbit, but rather at the inner edge of the ring current. If we adopt a postinjection electric field value estimated from the injection front transit time, 14 kV/R_E, we do find that the 20-keV thickness is reduced to less than 1 R_t (see Figure 10). However, the point made by *Kaye and Kivelson* [1979] is that the spatial boundary dispersion should reflect the preinjection conditions, not the post-injection field. If such a large field were present initially, the inner edge of the plasma sheet would be at unreasonably low L.

We conclude, as did *Kivelson et al.* [1980], that the simple time-dependent convection boundary picture does not describe typical dynamic injections. However, a boundary motion is indeed involved in the injection process. This boundary is too thin and is in the wrong place to be understood as a convection-drift structure. The net effect is to produce a signature much like that in the calculations of *Ejiri et al.* [1980], who assumed an arbitrary sharp boundary to exist, initially at $L = 10$. In the next section we discuss a qualitative model of

this boundary in an attempt to remove this ad hoc assumption.

We have noted above that a clear magnetic perturbation accompanies each injection front. This perturbation is dominated by an increase of the northward or H component so that it can be understood as a propagating current sheet oriented in the east to west direction with a magnitude sufficient to abruptly reverse the normal radial gradient of $|B|$. Insisting that $\nabla \times E = 0$ in the wave frame and then transforming back to the upstream plasma frame (nearly the same as the satellite frame), one finds that the magnetic field compression ratio (2 3) determines the relative speeds of the plasma and the wave ahead of it:

$$v_{wave}/v_{plasma} = (1 - B_{up}/B_{down})^{-1} = 1.4 - 2.0$$

Evidently, the compression wave should be regarded as moving somewhat faster than the plasma injection front observed by us. In the corotating frame of the satellites, we can estimate

$$\nabla \times E \cong \Delta E/d \cong \Delta B/\Delta t$$

with $\Delta B \cong 30$ nT, $d/\Delta t \sim v_{wave} \sim 15$-150 km/s, and

$$\Delta E \cong 0.5-5. \text{ mV/m or } 3-30 \text{ kV}/R_E$$

Comparing with initial state convection fields estimated at ~ 0.1 mV/m or 0.6 kV/R_E, we see that such a disturbance is indeed consistent with an enhancement of plasma convection in crossing the front.

Note that during a mildly active period like day 43, 1979, with several substorm injections occurring in a single evening sector pass, we observe that fluxes in a given energy channel appear to have two stable levels, each substorm producing a fast transition and then a more gradual return to the 'quiet level.' This argues strongly for a large, fairly uniform body of hot plasma behind the injection front, continuous with the body of the plasma sheet, rather than simply a thin shell-like source of hot plasma at the front. However, the day 43 data suggest that each successive injection may raise the temperature of this hot plasma or raise a nonthermal energetic tail in it. This indicates that while the boundary motion may dominate the sudden plasma changes observed, local acceleration may play a role as well. Since the compression front propagation time is much smaller than convection flow time scales, several fronts can propagate through essentially the same plasma sheet material, with cumulative effects on it.

Fig 10 Electron convection boundary spacing for a Volland-Stern (shielding exponent of 2) electric field [*Southwood and Kaye.* 1979]. Each curve gives the location of the convection boundary as a function of energy for a different zero-energy position (electric field strength).

DISCUSSION

Our data indicate that the collapse, motion, and expansion of a persistent boundary layer near synchronous orbit are of great importance to the dynamics of substorms. In what follows we offer a qualitative description of the physics of this boundary layer and its motions. This description is based on the work of several other authors but leads to a somewhat modified view of substorm plasma injection.

Theoretical motivation for another convection-related boundary layer outside of the usual boundaries (between orbits with different topologies) may be found in the work of *Kennel* [1969] and *Southwood and Wolf* [1978]. The boundary is referred to by these authors as a 'precipitation-flow boundary' and is produced when convection time scales are comparable to particle lifetimes against precipitation loss. Some level of pitch angle diffusion is clearly required for this to take place, and it can be argued that the strong diffusion limit is t'
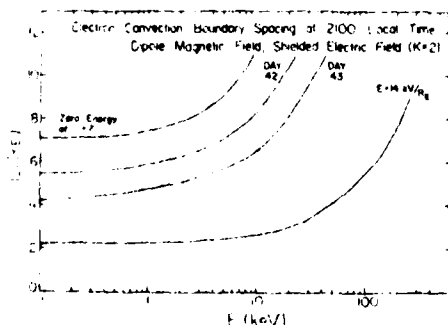
lustrative if not always accurate. Under such conditions, particles are lost to the ionosphere fast enough so that they cannot penetrate beyond a boundary across the convection flow, regardless of drift orbit geometry. The quiet precipitation-flow boundary should exhibit some energy dispersion, since energetic particles have shorter lifetimes ($t \sim E^{-h}$) and will be depleted further upstream. This phenomenon is clearly exhibited in the Rice University modeling efforts [Harel et al., 1981, and references therein].

Energetic electrons lost into the ionosphere tend to produce copious numbers of lower-energy secondary and backscattered primary electrons moving back upward along field lines [Banks et al., 1974; Evans, 1974; Stamnes, 1980; Pulliam et al., 1981]. Moreover, Evans and Moore [1979] have shown evidence that conditions of diffuse aurora with small field-aligned potential drops produce significant contamination of the hot equatorially trapped plasma by these ionospheric electrons. Lundin [1977] and Evans [1981] have performed calculations in which a flux tube initially filled with hot Maxwellian electrons is allowed to degrade in time by interaction with the ionosphere. Lundin's Figure 2.2 and Evans' Figure 2 are reproduced here as Figure 11. It shows that energetic electrons are eroded away, reducing the temperature of the Maxwellian and as low-energy electrons traveling up along field lines are diffused in pitch angle onto trapped orbits, adding to the low energy flux, which tends to have a power law form. We note that time derivatives on a fixed flux tube correspond to spatial derivatives in a steady convective flow. This figure therefore shows the evolution of the electron distribution along the convective flow path through the precipitation-flow boundary layer. Rather than a simple loss of energetic electrons, one expects a transition from hot quasi-Maxwellian to power law with low average energy. The assumption of a Maxwellian source plasma is justified in view of our observations of the post-injection electrons. Moreover, during quiet times, the Maxwellian nature of the plasma sheet is well documented [e.g., Hones et al., 1971].

We note further that the spectral change depicted in Figure 11 is exactly the reverse of the transition which occurs during substorm injections. On this basis we propose that the outer boundary seen as an advancing and retreating injection front is the precipitation-flow boundary between fresh hot plasma sheet electrons and inner plasma sheet electrons contaminated with ionospheric electrons by interaction along field lines. Scale lengths for the boundary thickness may be estimated from inferred flow speeds and from the fact that calculations yield scale times of the order of 500 quarter bounce periods of an electron of characteristic energy for the Maxwellian. For fields corresponding to active but presubstorm conditions (~ 0.7-1.4 kV/$R_E \rightarrow 1$-2 km/s flow velocity) and scale times of the order of 1 hour for 2 keV-electrons, the precipitation-flow boundary layer will be of the order of 1 R_E thick for strong pitch angle diffusion and thicker still if diffusion is not strong. The location of the boundary will be determined by the condition that the flow time scale be of the order of the minimum particle lifetime. Thus strong flows will move the boundary inward.

We will now argue that a compression wave, propagating inward through the above quiet situation and having an associated flow enhancement of an order of magnitude, will steepen preexisting plasma gradients and displace them further inward from their initial locations. Again, in the frame of the wave front, plasma approaches rapidly from upstream and then moves away more slowly downstream. Gradients in the upstream material are steepened by passage through the front. In the frame of the upstream plasma, gradients are compressed and subsequently moved inward at a large fraction of the wave speeds, given above, as the wave passes. This is schematically illustrated in Figure 12. The inclusion of atmospheric interactions at the feet of the field lines using a transport equation approach [Stamnes, 1980] should lead to a more quantitative description of the interaction of the wave with the inner plasma sheet and conjugate ionosphere.

As pointed out by Kennel [1969], ions have much longer minimum lifetimes due to their long bounce periods (for given energy). If ion scattering is not much more effective than electron scattering, this implies that ion depletions due to precipitation have considerably longer scale length along convection paths. Hence, ion depletion in a given path length should be considerably smaller than electron depletion at comparable
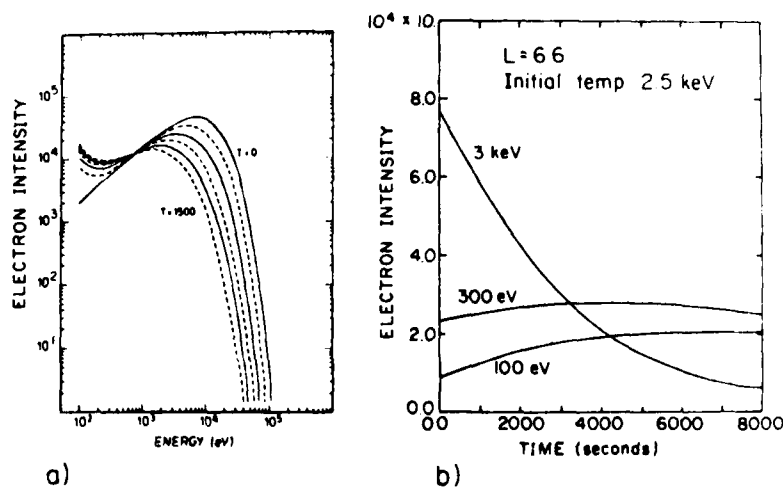

Fig. 11. Calculated degradation of initial Maxwellian by contact with the atmosphere under strong pitch angle diffusion: (a) Lundin [1977], and (b) Evans [1981].

energies. This is in accord with the relatively small amplitude ion responses in our data.

Finally, we would like to comment on the nature of the observed compressive wave associated with substorms. They have many of the characteristics of shock waves. Evidence supporting such an identification is as follows:

1. The magnetic field magnitude increases by a factor of 2 3, and the measured plasma pressure increases as well in crossing through the front.

2. Fluctuations in the magnetic field appear suddenly as the wave front is crossed, indicating some source of disorder.

3. Assuming a wave front roughly normal to the radial direction, the magnetic field change is mainly a change of magnitude of the tangential component.

4. The estimated front thickness (≤ 0.1 R_E) corresponds to a few hot ion gyroradii and is hence quite thin with respect to ion orbits.

It is interesting to consider how such a wave might be launched. *Arnoldy and Moore* [1980] have shown that very similar injection signatures are produced by SI and SC pulses (rapidly increasing *Dst*) driven by abrupt changes in the solar wind, which in turn produce rapid compressions of the whole magnetosphere. However, such a driving mechanism is not present for the typical substorm event, suggesting an internal effect. It may be that the tail-supporting dawn-dusk current is unstable to the separation and earthward propagation of thin current sheets from its innermost regions.

In the above discussion it has been implicitly assumed that the propagating magnetic field increase is in fact compressional in nature, i.e., that plasma flows through the wave front and is compressed as a result. There is a very serious problem with this assumption in that the observed propagation speed is quite low compared with Alfvén speeds expected near synchronous orbit (15-150 km/s versus 1000 km/s). Conservation laws show that shocklike disturbances must propagate perpendicular to the magnetic field faster than the upstream magnetosonic speed, which in turn is higher than the Alfvén speed.

In the absence of direct plasma bulk flow or electric field measurements to settle the issue, one must consider the possibility that the magnetic field increase is actually a tangential discontinuity, having no motion relative to the plasma and moving at an enhanced (by a factor of ~10) convective flow speed. However, there is an equally serious difficulty here, since the conservation laws require pressure balance across such convecting discontinuities. Although all particles have

not been directly measured, there is every indication that these substorm injections produce a net increase in both plasma pressure and magnetic field energy density. The most significant particle category not measured by the UNH instrument, the ions of energy greater than 20 keV, are known from other studies to be additional contributors to this pressure increase. Such evidence tends to preclude the possibility that the magnetic field increase is simply a convecting discontinuity.

The resolution of this problem may lie in the actual value of the upstream Alfvén speed. Conditions prior to injection include a depressed magnetic field and enhanced numbers of low-energy electrons and ions. Moreover, the low-energy ions may often have a significant component of heavy ions such as O^+ from the ionosphere. These factors all work to reduce the local Alfvén speed in the preinjection plasma. With a typical field depression to 30 nT and an O^+ contribution to number density of 10%, the Alfvén speed is reduced to observed injection front speeds (~100 km/s) for a density of ~5 cm^{-3}. Such values of these parameters are not unreasonable and have the merit of reconciling the wave front observations with the conservation laws.

If the observed compression wave is a magnetosonic shock, it is an extremely interesting astrophysical phenomenon. Propagating as it does through a $\beta \sim 1$ collisionless plasma, it may be capable of accelerating some plasma particles to very high energies in a manner analogous to shock acceleration of cosmic rays [*Fisk*, 1971].

Relationship to Low-Altitude Observations

As a check on the interpretation we have proposed, we now compare our observations with the low-altitude phenomenology of substorms and general auroral precipitation. Such comparisons depend upon some assumptions about, or model of, the mapping between the auroral oval and the equatorial plane. While it is conceptually simpler to think in terms of a time-steady mapping, we feel that it is essential to admit that changes in magnetic geometry are of fundamental importance during substorms.

A long-standing mystery of substorm dynamics is the paradox presented by the prevalent poleward expansion of various low-altitude auroral substorm features despite the equally prevalent thinking that hot plasma must be transported radially inward from the tail, i.e., equatorward when mapped through a fixed magnetic geometry to low altitude. It is well known that the optical aurora expands poleward at substorm times [*Akasofu et al.*, 1974; *Eather et al.*, 1976]. and this is also seen in electron precipitation [*Winningham et al.* 1975] and in the auroral electrojet signature [*Rostoker et al.* 1975]. The inward flow model of injection has been invoked by many investigators to explain substorm plasma increases, and we have joined *Barfield et al.* [1977] in providing confirmed, unambiguous two-point observations of an inward propagating injection front with each substorm viewed in the evening sector.

We feel that this paradox can be partially resolved by following for change in magnetic field topology as an integral part of substorms. The concept of frozen-in, moving magnetic field lines would lead to a serious source of confusion. *Vasyliunas* [1972] has discussed several equally valid but non-unique ways of heuristically ascribing motion to magnetic field lines. We adopt his first case, in which field line motion is taken to be just enough to account for temporal changes of field geometry. That is "field line motion" is identical to in
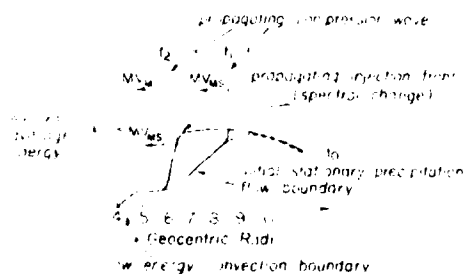

Fig. 12. Schematic one-dimensional illustration of the interaction between an earthward propagating compression wave and preexisting quasi-static plasma boundaries near synchronous orbit. This figure is not based on a calculation. The wave front is shown at two times: first outside then inside synchronous orbit.

motion of zero-energy particles due to induced electric fields only. This is in some sense the minimum field line motion, and the field lines are taken to be essentially attached to fixed points on the earth, since fractional temporal changes are minimal there. In this view, the magnetic perturbation which passes the satellites near the injection front represents a rapid inward motion of field lines which were formerly stretched out in the tail.

Note that a frame traveling inward with the injected plasma therefore maps to a fixed latitude location at the ionosphere, thus explaining why inward motion of plasma does not produce equatorward motion of precipitation at the conjugate ionosphere during the transient period of the substorm. The satellite frame of reference, meanwhile, is mapping to more poleward locations at the ionosphere, toward the polar cap boundary. The observation of a poleward expanding auroral region at low altitude during substorms may not require tailward motion of a plasma source; one at fixed radius or moving slowly earthward would suffice. However, the present observations originate within the inner part of the plasma sheet and do not permit inferences concerning the poleward boundary of the auroral zone or the outer boundary of the plasma sheet.

CONCLUSIONS

We believe these two-satellite observations lead to a somewhat clarified view of substorm plasma injection, in which boundary motion plays a major role. We have focused upon a specific type of injection event which we have found to be ubiquitous in our observations. This type of event is characterized by very abrupt dispersionless changes in electron intensities and a coincident magnetic perturbation consisting generally of an increase in the field magnitude combined with a small rotation toward more dipolar orientation (at locations near the geomagnetic equator). Comparing plasma observations at two points separated in radial distance from earth, we have found the following:

1. Low-energy plasma increases usually observed in the dusk sector prior to substorm activity confirm the presence of a quasi-static boundary having a shape like that of the *Mauk and McIlwain* [1974] substorm-injected plasma boundary. Injection events, as described above, generally occur well after this boundary is encountered but can at times occur nearly simultaneously with the boundary encounter, or perhaps with little evidence of the low-energy plasma boundary. We attribute these low-energy increases to spacecraft penetration of quasi-static low-energy convection boundaries [*Kivelson et al.*, 1980] separating closed orbits from those traceable to the deep plasma sheet. Sometimes, for example, the day 42, 0930 event, dispersive electron increases at a few keV energy are observed prior to the abrupt dispersionless injections. We attribute such increases to substorm-associated inward motion of the low-energy convection boundaries.

2. Injection events are observed at the two satellites with little dispersion and a well-defined time delay corresponding to radial propagation at a speed of 10–100 km/s, in general agreement with data reported by *Barfield et al.* [1977]. Decreases are not observed at the outer satellite until well after the 'injection front' has reached the inner satellite, indicating that the front represents a moving boundary between two different plasmas, the region of hot plasma behind the front being at least 1 R_e deep. Using energy dispersion measured at

each satellite and the time delay between satellites, a first-order estimate of the front thickness gives ≤0.1 R_e.

Spectral study of the plasma changes show that both ions and electrons experience increases above some energy E_c and decreases below E_c, where E_c is somewhat larger for ions than for electrons, at times reaching the upper limit of UNH ATS 6 plasma observations, ~20 keV. Moreover, the spectrum of hot injected plasma is often nearly Maxwellian, especially for the electrons, and suffers little energization of compression in propagating from 6.6 to 5.6 R_e.

3. Commonly observed magnetometer signatures for these injection events indicate that a current sheet oriented generally east to west propagates near the injection front and has an associated $\partial B/\partial t$ and therefore $\nabla \times E$. The induced electric field of such a current sheet represents an enhancement of the inward convection and may be thought of as a motion of field lines in the sense of a change of mapping between the equatorial plane and the ionosphere.

We have compared these observational facts with theoretical models of injection and arrived at the following interpretation:

In active, but preinjection conditions, the inner part of the plasma sheet has two important features: (1) the low-energy convection boundary (convection boundary for near-zero energy particles, determined by the magnitude of the large-scale convection electric field) and (2) the precipitation-flow boundary layer between hot plasma sheet and atmospherically contaminated inner plasma sheet (see Figure 12).

In general, boundary 2 is not a sharp boundary, having a highly variable structure determined by convection and particle lifetimes. It may be thought of as the transition region in which hot plasma sheet (approximately Maxwellian) and atmospheric backscatter and secondary electrons (power law $\sim E^{-1}$ or E^{-2}) comingle in varying proportions, hot electrons generally decreasing inward and eastward until, near boundary 1 above, little hot plasma is found.

One orbit through the evening and morning sectors in the absence of substorm activity therefore consists of an encounter with boundary 1 and then a grazing encounter with boundary 2 in which the amount of hot plasma seen depends on the large-scale convection field and on whether any small disturbances of it occur.

One or more dispersionless injections may occur during such a pass through the evening, usually after the low-energy boundary has been crossed. Thus the *Mauk and McIlwain* [1974] 'substorm-injected plasma boundary' is not the site of dynamic injections but does mark the approximate inner limit of substorm activity. Each substorm consists of the following effects on the quiet situation described above:

Due to an unspecified process or instability, a partial tail collapse is initiated well outside synchronous orbit. The collapse propagates earthward in the form of a compression pulse. After the pulse passes a given location, B is larger and, at off-equator locations, more northward than it was prior to pulse passage. The $\nabla \times E$ associated with the pulse is consistent with a rapid intrusion of hot plasma from outside, overtaking preexisting plasma at the propagating wave front and collapsing the boundary layer 2 to a thin structure, producing dramatic injection signatures without any requirement for dramatic energization.

The role of local acceleration in such a phenomenon is not entirely clear. However, there is some indication that the hot plasma sheet is further 'heated' by each successive substorm

during an active period, suggesting that an appreciable fraction of the energy carried from the tail by the compression wave is dissipated in the equatorial plasma during passage of the wave front, while the rest is dissipated in the ionosphere or in accelerating ionospheric particles into the magnetosphere. Any 'heating' which occurs appears to affect chiefly the high-energy tail of the approximately Maxwellian plasma, which is often observed to have a power law rather than exponential form.

Most of the scenario proposed here is based on already well-established ideas. The major new ingredient is the earthward propagating compression wave, though even this was, in fact, observed over a decade ago. However, this study suggests that understanding the launch, propagation, and dissipation of this wave should be a major goal of magnetospheric theory.

REFERENCES

Akasofu. S-I., S DeForest, and C. Mcllwain, Auroral displays near the 'foot' of the field line of the ATS-5 satellite, *Planet. Space Sci.*, 22, 25 1974

Arnoldy. R L., and K W. Chan, Particle substorms observed at the geostationary orbit, *J. Geophys. Res.*, 74, 5019, 1969.

Arnoldy, R L., and T E. Moore, Plasma injection events at synchronous orbit related to positive Dst (abstract), *Eos Trans. AGU*, 61, 1084 1980.

Banks, P. M., C. R Chappell, and A. F. Nagy, A new model for the interaction of auroral electrons with the atmosphere: Spectral degradation, backscatter, optical emission. and ionization, *J Geophys. Res.*, 79, 1459, 1974

Barfield, J. N., S. F. DeForest, and D. J. Williams, Simultaneous observations of substorm electrons: Explorer 45 and ATS 5, *J. Geophys Res.*, 82, 531, 1977

DeForest, S. E., and C. E. Mcllwain, Plasma clouds in the magnetosphere, *J. Geophys. Res.*, 76, 3587, 1971.

Eather, R. H., S. B. Mende, and R. J. R. Judge, Plasma injection at synchronous orbit and spatial and temporal auroral morphology, *J. Geophys Res.*, 81, 2805, 1976

Ejiri, M., Trajectory traces of charged particles in the magnetosphere, *J Geophys. Res.*, 83, 4798, 1978

Ejiri, M., R. A. Hofhnan, and P. H. Smith, Energetic particle penetration into the inner magnetosphere. *J. Geophys. Res.*, 85, 653, 1980.

Evans. D. S., Precipitating electron fluxes formed by a magnetic field aligned potential difference, *J. Geophys. Res.*, 79, 2853, 1974.

Evans, D. S., The time evolution of a trapped electron population undergoing strong pitch angle diffusion, submitted to *J. Geophys. Res.*, 1981

Evans, D. S., and T. E. Moore, Precipitating electrons associated with the diffuse aurora: Evidence for electrons of atmospheric origin in the plasma sheet, *J Geophys Res.*, 84, 6451, 1979.

Fisk, L. A., Increases in the low-energy cosmic ray intensity at the front of propagating interplanetary shock waves, *J. Geophys. Res.*, 76, 1662, 1971.

Harel, M., R. A Wolf, P. H. Reiff, and R. W. Spiro, Quantitative simulation of a magnetospheric substorm, 1, Model logic and overview. *J. Geophys. Res.*, 86, 2217, 1981.

Hones, E. W., J. R. Asbridge, S. J. Bame, and S. Singer, Energy spectra and angular distributions of particles in the plasma sheet and their comparison with rocket measurements over the auroral zone. *J. Geophys. Res.*, 76, 63, 1971

Hultqvist, B., B. Aparicio, H. Borg, R. Arnoldy, and T. E. Moore, Decrease of keV electron and ion fluxes during the early phase of magnetospheric disturbances, *Planet. Space Sci.*, 28, 107, 1981.

Kaye, S. M., and M. G. Kivelson, Time dependent convection electric fields and plasma injection. *J. Geophys. Res.*, 84, 4183, 1979

Kaye, S. M., and M. G. Kivelson, The influence of geomagnetic activity on the radial variation of the magnetospheric electric field between L = 4 and 10, *J. Geophys. Res.*, 86, 863, 1981.

Kennel, C. F., Consequences of a magnetospheric plasma, *Rev Geophys Space Phys.*, 7, 379, 1969.

Kivelson, M. G., S. M. Kaye, and D. J. Southwood, The physics of plasma injection events, in *Dynamics of the Magnetosphere*, edited by S.-I. Akasofu, p. 385, D. Reidel, Hingham, Mass., 1980.

Lundin, R., Investigations of auroral electron precipitation by means of sounding rockets, thesis, *Rep. 77:1*, Kiruna Geophys. Inst., Kiruna, Sweden, 1977.

Mauk, B H., and C E. Mcllwain, Correlation of Kp with the substorm injected plasma boundary, *J. Geophys Res.*, 79, 3193, 1974.

Mcllwain, C. E., Substorm injection boundaries, in *Magnetospheric Physics*, edited by B. M. McCormac, p 143, D. Reidel, Hingham, Mass., 1974

Mcllwain, C. E., Auroral electron beams near the magnetic equator, in *Physics of the Hot Plasma in the Magnetosphere*, edited by B Hultqvist and L. Stenflo, p. 91, Plenum, New York, 1975.

Pulliam. D. M., H. R. Anderson, K. Stamnes, and M. H. Rees, Auroral electron acceleration and atmospheric interactions, *J. Geophys. Res.*, 86, 2397, 1981.

Rostoker, G., J. L. Kisabeth, R. D. Sharp, and E. G. Shelley, The expansive phase of magnetospheric substorms, 2, The response at synchronous altitude of particles of different energy ranges, *J. Geophys. Res.*, 80, 3557, 1975.

Rostoker, G., S.-I. Akasofu, J. Foster, R. A. Greenwald, Y. Kamide, K. Kawasaki, A. T. Y. Lui, R. L. McPherron, and C. T. Russell, Magnetospheric substorms—definitions and signatures, *J Geophys. Res.*, 85, 1663, 1980.

Russell, C. T., and R. L. McPherron, The magnetotail and substorms, *Space Sci Rev.*, 15, 205, 1973.

Smith, P. H., and R. A. Hoffman, Direct observations in the dusk hours of the characteristics of the storm time ring current particles during the beginning of magnetic storms, *J. Geophys. Res.*, 79, 966, 1974.

Southwood, D. J., The role of hot plasma in magnetospheric convection, *J. Geophys. Res.*, 82, 5512, 1977.

Southwood, D. J., and S. M. Kaye, Drift boundary approximations in simple magnetospheric convection models, *J. Geophys. Res.*, 84, 5773, 1979.

Southwood, D. J., and R. A. Wolf, An assessment of the role of precipitation in magnetospheric convection, *J Geophys. Res.*, 83, 5227, 1978.

Stamnes, K., Analytic approach to auroral electron transport and energy degradation, *Planet. Space Sci.*, 28, 427, 1980.

Vasyliunas, V. M., Nonuniqueness of magnetic field line motion, *J Geophys. Res.*, 77, 6271, 1972.

Winningham, J. D., F. Yasuhara, S.-I. Akasofu, and W. J. Heikkila, The latitudinal morphology of 10-eV to 10-keV electron fluxes during magnetically quiet and disturbed times in the 2100–0300 MLT sector, *J Geophys. Res.*, 80, 3148, 1975.

Auroral Changes During the Eighteenth and Nineteenth Centuries and Their Implications for the Solar Wind and the Long-Term Variation of Sunspot Activity

J. Feynman

Department of Physics, Boston College, Chestnut Hill, Massachusetts 02167

S. M. Silverman

Air Force Geophysics Laboratory, Hanscom Air Force Base, Massachusetts 01731

Both auroral and geomagnetic activity provide information from which the behavior of the magnetosphere and the solar wind can be inferred. Swedish auroral sightings during the eighteenth and nineteenth centuries show a remarkable pattern of changes in the latitudes at which the auroras were observed. Auroral reports from New England confirm that these variations were hemisphere-wide. The pattern of changes took place over an 106-year period and is easily distinguished from the much smaller changes that are related to single sunspot number cycles. We infer that the pattern reflects corresponding changes in the solar wind and the resultant magnetospheric configuration and that these changes were much greater than those observed since in situ measurements began. Our results show that a minimum solar wind occurred at the beginning of the nineteenth century. It has been argued elsewhere that minimum solar winds also occurred around the beginnings of the eighteenth and twentieth centuries. Since all these periods are also the reported minimums of the '80- to 100'-year variation in sunspot activity, we conclude that both the changes in the solar wind and in the strength of the cycle in sunspot number reflect underlying fundamental long-term changes in the sun itself.

1. Introduction

Because the solar wind drives both geomagnetic activity and aurora, the past history of the wind can be inferred from records of these phenomena. Other recent work has dealt with the periods of the Maunder minimum in the last half of the seventeenth century, and with the twentieth century [*Suess*, 1979; *Feynman and Crooker*, 1978]. Here we study the period from the last part of the eighteenth century until about 1870 using auroral data, and seek for evidence of changes in the solar wind on time scales long compared to a single solar cycle.

In the remainder of this introduction we review the work that has already been done on inferences concerning seventeenth and twentieth century solar wind. In section 2 of the paper we discuss eighteenth and nineteenth century auroras and also include a short review of the current state of knowledge concerning the relationship of auroral sightings to interplanetary and solar parameters. Section 3 describes the changes in the positions of the auroras that have been observed during the current epoch so that they can be compared to changes in earlier epochs. The final section presents our conclusions.

Auroral and ^{14}C data from the Maunder minimum period have been considered by *Suess* [1979], who concluded that the solar wind speed and/or the interplanetary field intensity were low and not variable. The history of the solar wind from 1868 to 1967 has been studied through the use of *Mayaud*'s [1973] index, which increased markedly between 1900 and 1960 [*Russell*, 1975; *Svalgaard*, 1977]. The aa index has been related to the solar wind velocity and southward component of the interplanetary magnetic field for the last solar cycle [*Crooker et al.*, 1977]. When this relationship was extrapolated to the extreme magnetic calm of 1901 [*Feynman and Crooker*, 1978], it yielded the result that the solar wind at that time

could not have simultaneously fitted into the range of velocities and southward fields that exist today. Either the yearly average velocity was less than 200 km/s, or the average southward field was a factor of 3 lower, or both quantities changed; that is, the solar wind has changed markedly during this century.

These indications of significant changes in the behavior of the solar wind underscore the importance of and the need for additional studies to clarify the nature of this behavior over long periods of time.

2. Eighteenth and Nineteenth Century Auroras

The sunspot cycle from 1610 to 1975 is shown in Figure 1, taken from *Eddy et al.* [1976] The accuracy of the data is discussed at length by *Eddy* [1976]. He rates the annual data post 1848, which was collected from a network of stations, as 'reliable,' and that from 1818 to 1847 as 'good.' The annual numbers from 1749 to 1847 are considered less reliable the earlier the year. Eddy restudied the values from the seventeenth and early eighteenth centuries, and although the yearly numbers are not accurate, the general trend is well established. The Maunder minimum appears in the top panel of Figure 1. The second panel shows three weak cycles between 1798 and 1833, and the third panel shows a series of weak cycles centered on about 1900. These three periods of reduced activity around 1710, 1810, and 1900 led to the hypothesis that there was an '80- to 100'-year cycle in sunspot activity, sometimes called the 'Gleissberg cycle,' though the term 'Gleissberg variation' may be more appropriate in view of the rediscovery of the Maunder minimum. It has been suggested [*Feynman and Crooker*, 1978] that the gradual increase in geomagnetic activity at solar cycle minimums from 1901 to 1954 indicates that the solar wind exhibited a change with the Gleissberg cycle. If this is the case, then the wind should also show some pattern

63   2991

ANNUAL MEAN SUNSPOT NUMBERS FROM 1610 TO THE PRESENT

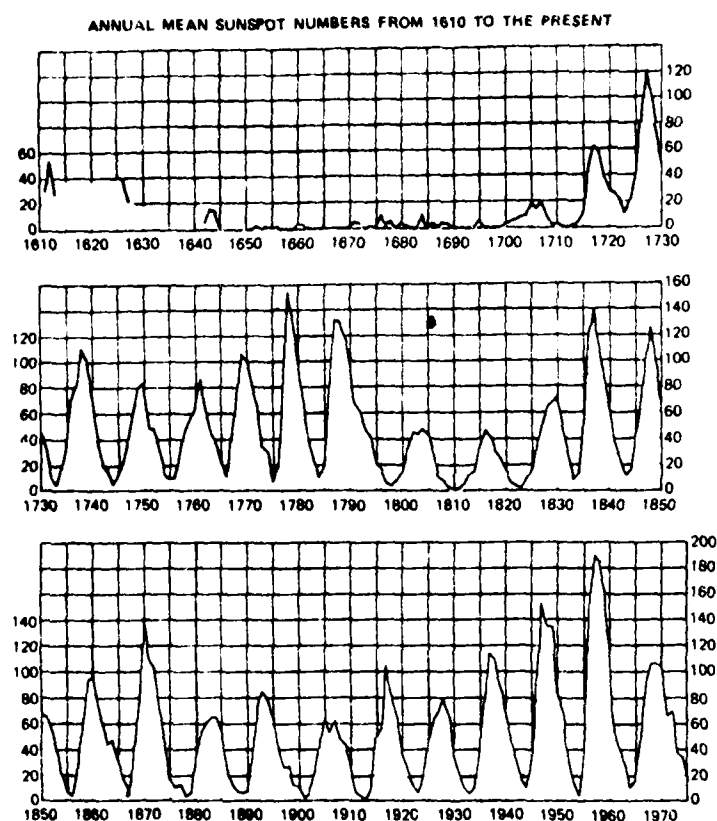Fig 1   The sunspot cycle 1610–1975, from *Eddy et al.* [1976].

of change centered on early 1800's. Auroral data can be used to examine this question.

Figure 2 shows the yearly auroral frequency data from Sweden for the years 1721–1876. The data were collected by *Rubenson* [1879, 1882], the Director of the Central Meteorological Institute of Sweden, from publications, newspapers, journals, and manuscript sources. Since the series was very carefully collected by a single knowledgeable person and refers to a geographically restricted area, it forms as nearly consistent a set of data as can be available from this period. The auroral frequency in Figure 2 is defined as the number of nights per year on which auroras were seen. If more than one observer reported the same auroral display, it was nevertheless counted as a single aurora. The year is counted from July of one year to June of the next. Since there is little darkness in Sweden during the summer months, there are very few auroras reported for May, June, and July.

We note the paucity of auroras during the period from 1809 to 1815. In the entire period of 156 years of data, only 14 years had fewer than 10 auroras, but of these, 6 occurred in this period, an indication that the solar wind was in some sense 'weak' around 1810, as it had been at the end of the 1600's and would be again in 1900. The functional relationship between the parameters of the solar wind and the magnetic activity and auroras which are driven by the wind is not accurately known at this time. As is noted below, however, we can at least qualitatively use the terms weak and strong as de-

scriptors of the relative magnitude of this functional relationship.

Geomagnetic activity and auroral sightings are closely correlated. Figure 3 shows the comparison between the auroral frequency in Sweden and the *aa* index for the years 1868–1876, for which the Rubenson catalog and Mayaud tabulation overlap. The *aa* yearly average has been calculated for the July to June year of the auroral data. The correlation coefficient is 0.97, indicating a remarkably good fit. Studies of auroral observations at specific sites indicate that extrapolation of the curve to other time periods is hazardous because of the changes in auroral distribution discussed below. However, even though the relationship between geomagnetic activity and auroral sightings may change, we may still expect the number of auroral sightings, like geomagnetic activity, to depend on some function of the solar wind velocity, southward field component, and perhaps other parameters in a secondary way. An unusually low number of auroral sightings is then almost certain to reflect low values of some of all of these solar wind parameters.

In order to examine the period around the beginning of the nineteenth century more closely the geographic distribution of Swedish auroras is shown in Figure 4. Rubenson has divided Sweden into four geographic latitude regions: from 55°N to 58°30'N, from 58°30'N to 61°30'N, from 61° 30'N to 65°N and from 65°N to 70°N. He reports on the number of auroras seen in each region so that in contrast to the count shown in
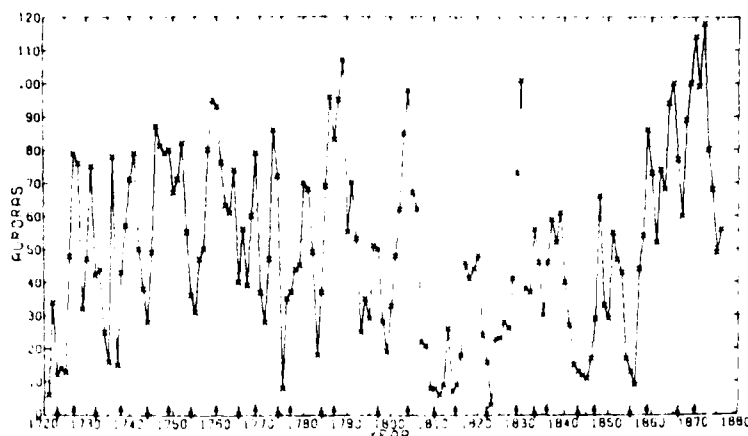
Fig. 2. The annual number of auroras seen in Sweden 1720-1876; data from *Rubenson* [1879, 1882].

Figure 2, if an aurora is seen over a wide enough distribution of latitudes, it will be reported once for each district in which it is seen. Figure 4 shows a comparison of the number of auroras reported for the two most northerly districts taken together to the number reported for the two most southerly districts taken together. We have plotted the ratio of the difference between the number of nothern and southern auroras to the sum. Thus +1 indicates that auroras occurred only in the north, and −1 indicates that they occurred only in the south.

The figure shows a remarkable pattern of auroral occurrence. From 1807 to 1822, except for 2 years, the auroras were seen predominately in the north. The second of the three weak solar cycles of the Gleissberg 1800 minimum spanned the period from 1810 to 1822, but the cycle began with a broad minimum in 1807. Hence this period of predominately northern auroras spanned the second weak solar cycle. This period of extreme northerly auroras is consistent with the notion of a weak solar wind resulting in relatively weak auroras occurring in a contracted oval. It is interesting to note that the ^{14}C count was anomalously high during the early decades of the 1800's [*Damon et al.*, 1978], which also is consistent with a weak solar wind.

There are two periods before 1807 and after 1822 when auroral frequency was somewhat more equally distributed between the north and the south in that auroras were seen about 1 to 3 times more frequently in the north. The first of these periods started in 1793 or 1794. This is 2 or 3 years before the 1797 minimum, and the sunspot number at that time was about the same as it was for the maxima of the first two weak cycles. The second period went from 1823 to 1837. This is from a solar minimum to a year after the large maximum of 1836. Thus there does not seem to be a close relationship between the maximums or minimums of sunspot cycles and the onset, ending, or changes within the period of northerly auroras from 1793 to 1837.

During the 23 years before 1793 and the 20 years after 1837, Figure 4 shows that almost all the aurora that were seen appeared only in the south of Sweden. At that time the frequency of aurora in all of Sweden was within the normal range (see Figure 2). The first period of southern auroras ended a year after the 1796 maximum of the sunspot cycle, and the second southern auroral period began a year after the

1856 minimum. From 1858 to the end of the series, auroras occurred about equally in the north and south.

From 1771 to 1876 we have then a period of 106 years, or about 9½ solar cycles, during which the Swedish auroras underwent a well defined systematic change in the pattern of occurrence, first appearing only in the south, moving north, then appearing only in the south again, and finally moving to mid-Sweden.

It had originally been our intention to also use the entire auroral catalog of *Tromholt* [1902] of Norwegian auroras as a comparison data set. A careful examination of this data, however, revealed several problems. Almost all of Norway is geomagnetically 'north,' according to the division of Rubenson's Swedish data. Also, from 1787 to 1816, the ratio of the number of auroras seen in Norway to the number seen in Sweden is typically below 0.2, suggesting some difficulty in the Norwegian data during that period. The small Norwegian numbers also lead to poor statistics. From 1826 to the end of the series the ratio of reported auroras in Norway to Sweden typically ranged from 1 to 3. Cutting the Norwegian data into northern and southern regions at a line which is geomagnetically 2°
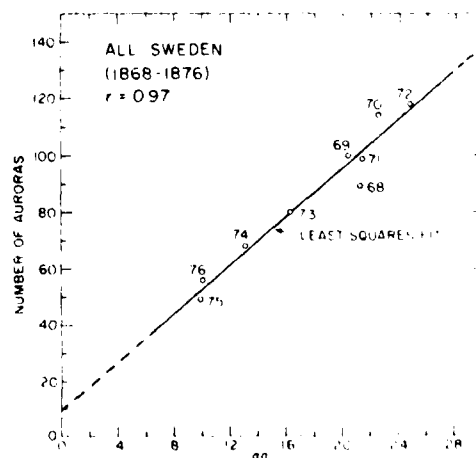

Fig. 3. The number of auroras observed in Sweden versus the *aa* indices of geomagnetic activity for the period during which data were available for both time series.
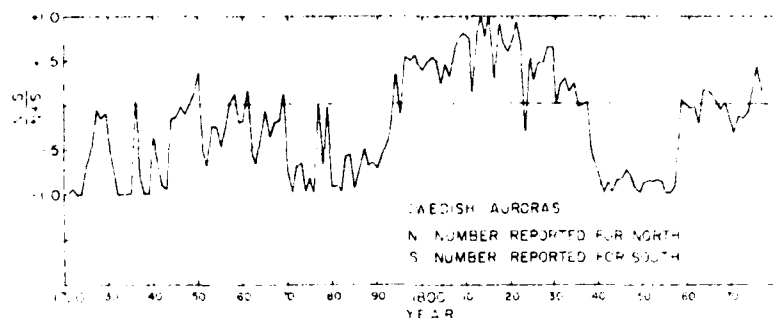
65

Fig. 4. A comparison of the number of auroras listed by Rubenson for the two northernmost Swedish districts to the number listed for the two southernmost districts. Note the well-marked pattern between 1770 and 1876.

north of Rubenson's cut, we find that from 1826 to 1839 the auroral ratio $(N - S)/(N + S)$ was >0 for 10 of the 14 years, from 1840 through 1858 it was ≤ 0.05 for 14 of 18 years, and after 1858 to the end of the series in 1876 there were only 2 years when the ratio was not >0. Thus where the Norwegian data are sufficiently ample, they tend to confirm the results obtained from the Swedish data.

A change in the pattern of observed occurrence of auroras can be due to several factors, including a change in the number of character of observers, a change in the earth's dipole field, or a change in the solar wind driving the auroras. From the Swedish data in Figure 4 it appears very unlikely that the observed change of pattern can be due to either a change in observers or in the earth's dipole field. Sweden, during the period covered, was a highly developed and major continental power, and there are no historical events which lend themselves to a change of observational patterns of the required scope. A change in the earth's dipole field of the character required can be ruled out. Barraclough [1974] had calculated the latitudes and longitudes of the northern geomagnetic pole of the centered dipole field as 79.9° and 307.2°, respectively, in 1750, 78.7° and 296.0° in 1850, and 78.8° and 294.8° in 1890. The effect of this motion on a point in Sweden which is at about 60°N geographic is to move it from about 60°N geomagnetic in 1750 to about 61°N geomagnetic in 1850. This 1° or 2° shift is insufficient to cause large effects in the auroral occurrence patterns. Furthermore, the dipole motion was not

cyclic as would be required to produce the observed change in occurrence pattern; the dipole drifted in the same direction throughout the period.

The nonlocal nature of the change in auroral occurrence frequency is confirmed by comparing the Swedish data with data from New England, collected by Loomis [1866], who was one of the pioneers of American auroral research in the nineteenth century. His data were culled from published sources such as journal articles and observatory reports. Figure 5 shows the number of auroras reported per year in Boston and New Haven. We note that from about 1792 to about 1836 almost no auroras were seen, but that before and after those times auroral sightings were very frequent. When the data from Sweden and Boston-New Haven are superposed, as in Figure 6, the agreement is remarkable. When auroras were seen predominately in southern Sweden, they were also seen in New England, which is at a more southerly geomagnetic latitude. When they were seen more frequently in northern Sweden, they were rarely observed in New England. Since the change in auroral pattern took place simultaneously at two such widely separated locations, the cause must be in the driver of the aurora, the solar wind. It should be noted that the changes to and from southern auroras were remarkably sudden, and that therefore the changes that took place in the wind must also have occurred suddenly. We also note that any sunspot cycle changes (Figure 4) are small in comparison with the major changes in auroral frequency pattern that we discussed.
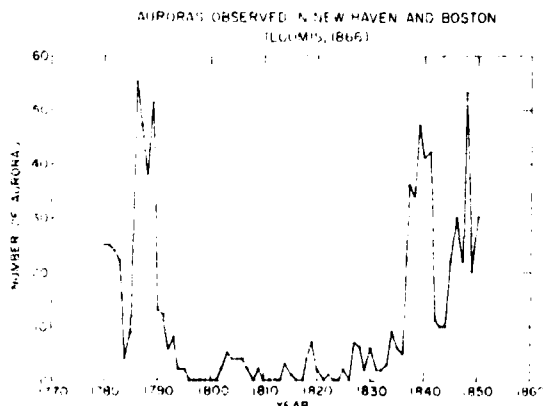
At our present stage of knowledge it is not possible to identify unequivocally the solar wind parameters that must have changed to affect either the annual frequency or latitudinal distribution of auroral observations. The problem can be approached either through direct studies of auroras or of the closely related geomagnetic activity. It was early suggested that geomagnetic activity should be related to some function of the solar wind velocity v and the southward component of the interplanetary field B, [Rostoker and Fälthammer, 1967]. Numerous studies have found that high values of indices of geomagnetic activity are associated with southward B, [cf Hirshberg and Colburn, 1969; Arnoldy, 1971; Tsurutani and Meng, 1972] and that large southward B, occurs in flare-produced disturbances [cf. Hirshberg and Colburn, 1969] and at the leading edges of fast solar wind streams [Hirshberg and Colburn, 1973] which in turn are usually associated with coronol holes [Neupert and Pizzo, 1974]. However, a recent study [Burlaga and King, 1979] found that about 20% of interplanetary magnetic field enhancements were not

Fig. 5. Auroral observations in the Boston-New Haven area from 1780 to 1850; data from Loomis [1886].
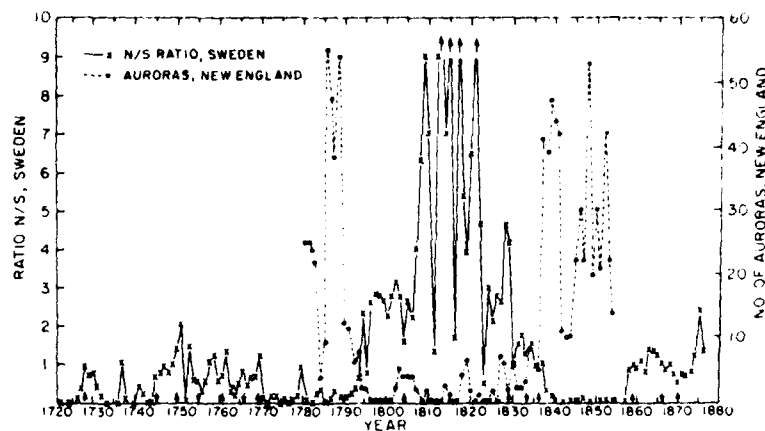
66

Fig. 6. A superposition of Figure 5 and the ratio of northern to southern auroras in Sweden showing that the auroras disappeared from the Boston-New Haven area at the same time as they become more common in the north of Sweden. Later they reappeared in Boston-New Haven and were not seen in the north of Sweden.

related to either flares or streams. Other studies of the correlations of geomagnetic indices and interplanetary parameters show high correlations with functions of B_z and v as expected, but they also show that other interplanetary parameters such as the magnitude of the interplanetary field or the density may also be involved in a secondary role [Garrett et al., 1974; Maezawa, 1978]. In any case, however, the matter of identifying the solar wind parameter that causes geomagnetic changes is not as simple as it might first appear, since it has been found that B_z is the most important parameter for processes taking place on the time scale of hours [Foster et al., 1971], whereas v is the most important parameter for changes on the time scale of the solar cycle [Crooker et al., 1977]. It would certainly be premature to speculate if the 80- to 100-year variation is expressed in changes of B_z or v or some unknown combination of both.

The studies of the relation of auroras directly to solar wind parameters have yielded less information. The first difficulty is that most modern studies use DMSP (Defense Meteorological Satellite Program) satellite imagery or particle precipitation to determine the boundary of the auroral oval as defined by the diffuse auroras. The eighteenth and nineteenth century auroral sightings are of discrete auroras, of course. Although the discrete auroras are imbedded in the auroral oval, a knowledge of the oval's response to solar wind gives at best only approximate information on the discrete auroras. A second difficulty is that although it may be expected that the auroras respond to the same solar wind parameters as geomagnetic activity, the studies of oval boundaries to date use only B_z. As southward B_z increases, the oval boundary move equatorward [Kamide and Winningham, 1977; Pike and Dandekar, 1979], and the probability of substorms also increases [Kamide et al., 1977]. Sheeley [1978] showed that for the 1973-1974 Skylab period, which was dominated by the recurrent geomagnetic storms typical of the descending portion of the sunspot cycle, the equatorward oval boundary was related to the southward B_z and hence to solar flares and coronal holes. It therefore appears that although we know that auroral sightings will be dependent on solar wind B_z and we expect them to depend on some function of v and B_z, neither the work on the auroral oval nor the work on geomagnetics allows us to speculate on

whether the change in the solar wind was primarily expressed in B_z or in v or in both during Gleisberg variations.

3. AURORAL DISTRIBUTIONS IN THE CURRENT EPOCH

It is interesting to compare the data in Figure 2 with studies of changes in the distribution of auroras that occurred between the minimum and maximum of a recent solar cycle.

An estimate of the ratio of northern to southern auroras for that cycle can be obtained from the work of Sandford [1968], who studied the latitudes of the auroras in the southern hemisphere during the 1958-1959 IGY and the 1963 IQSY. Using the geomagnetic latitudes corresponding to the Swedish data, we find that discrete auroras appeared equatorward of 60° on about 40% of the nights in the IGY 1958-1959. In the band between 60° and 70°, auroras were visible on 60% of the nights. Therefore if all auroras that occurred were observed, the ratio comparable to that of Figure 4 would be 0.2. For the IQSY, in 1963, discrete auroras occurred equatorward of 60° on 20% of the nights and between 60° and 70° on 80% of the nights, giving a ratio of 0.6. Thus though the ratio was higher for the IQSY than for the IGY, the change was not nearly as dramatic as that between, say, 1810 and 1850. Unfortunately, there are no solar wind data for the IGY, so that the changes in auroral occurrence frequency reported by Sandford can not be directly related to solar wind changes.

Two effects of changes in the solar wind that could cause a change in auroral occurrence frequency at a particular latitude are changes in the number of geomagnetically disturbed days per year and changes in the position of auroras for the same level of geomagnetic activity. Both types of changes occurred between the IGY and IQSY.

Feldstein and Starkov [1968] show the location of the northern hemisphere auroral oval edges as a function of magnetic activity as measured by the Q index for the IGY when the average aa index was 29 and for the IQSY when the average aa was 21. During both periods the width of the oval increases with increasing geomagnetic activity. The equatorward boundary expanded southward in both periods, whereas the poleward boundary moved northward with Q except for Q's of 1 or 2 during the IGY. The excursion of the southward boundary was about 6° during the IQSY and 10° during the

IGY. The southward excursion was more marked than the northward excursion during the IGY. Feldstein and Starkov state that the center line of the oval moved northward 1.5° between the IGY and the IQSY.

Sandford [1968] has also reported on changes in the latitude of southern hemisphere auroral occurrences as a function of geomagnetic activity. He studies discrete auroras occurring at midnight as a function of the local K index and, in agreement with Feldstein and Starkov, found marked differences between the 2 years. Sandford found, for example, that at $K = 0$ the most common latitude of auroras was 75° in 1958–1959 and 70° in 1963. In fact, no auroras were seen at 75° for $K = 0$ in 1963. For higher K the distributions were much wider, and auroras were seen at much more equatorward positions in 1958–1959 than in 1963. For $K = 4$, auroras occurred at 60° for 50% of the IGY nights and 25% of the IQSY nights. Sandford also found a tendency for the position of most frequent occurrence to move equatorward with increasing K during the IGY but not during the IQSY.

The studies of Feldstein and Starkov and of Sandford shows that the position and dynamics of the auroral oval can change noticeably in a period as short as 4 years, at least during the current epoch. The changes that took place during the eighteenth and nineteenth centuries were, of course, much more extreme.

4. CONCLUSIONS

1. The latitude at which auroras occurred underwent a clearly patterned change during the 106-year interval from 1771 to 1876. These changes were considerably greater than those reported between the IGY and the IQSY. We conclude therefore that the variation of the configuration of the magnetosphere during the eighteenth and nineteenth centuries was much greater than has been observed since space observation began.

2. The change in auroral occurrence pattern was due to the solar wind. The wind was strong in some sense in 1771–1793, became weaker with a minimum in 1809–1815, and returned to a strong state in 1837–1858.

3. The changes in the strength of the solar wind can be remarkably rapid. This is implied by the enormous changes of auroral appearance pattern which occurred over a period of 2 to 3 years several times during the 106-year interval. The times of these changes (circa 1793, 1839, and 1858) have no apparent relationship to phases of the sunspot number cycle.

4. Because the solar wind exhibited minima in 1901, in 1809–1815, and during the Maunder minimum, it appears likely that the wind varies with the Gleissberg variation. This observation leads to the conclusion that the strength of the sunspot cycle and the solar wind are both related to some underlying 80- to 100-year variability of the sun. This must be taken into account in models of the solar cycle in that models must now explain simultaneously not only the 22-year cycle in sunspot number but the equally fundamental 80- to 100-year Gleissberg variation in the strength of the solar wind.

The long-term underlying solar variability has caused significant changes in the earth's environment on time scales of from 2 to 100 years in the recent past, and we can expect that it will continue to do so in coming years.

REFERENCES

Arnoldy, R. L., A signature for substorms in the interplanetary medium, J. Geophys. Res., 76, 5189, 1971.

Barraclough, D. R., Spherical harmonic analysis of the geomagnetic field for eight epochs between 1600 and 1910. Geophys. J. Roy. As. tron. Soc., 36, 497, 1974.

Burlaga, L. F., and J. H. King, Intense interplanetary magnetic fields observed by geocentric spacecraft during 1963–1975. J. Geophys. Res., 84, 6633, 1979.

Crooker, N. U., J. Feynman, and J. Gosling, On the high correlation between long-term averages of solar wind speed and geomagnetic activity, J. Geophys. Res., 82, 1933, 1977.

Damon, P. E., J. C. Lerman, and A. Long, Temporal fluctuations of ^{14}C: Causal factors and implications, Annu. Rev. Earth Planet. Sci., 6, 457, 1978.

Eddy, J. A., The Maunder minimum, Science, 192, 1189, 1976.

Eddy, J. A., P. A. Gilman, and D. E. Trotter, Solar rotation during the Maunder minimum, Solar Phys., 46, 3, 1976.

Feldstein, Y. I., and G. V. Starkov, Auroral oval in the IGY and IQSY period and a ring current in the magnetosphere, Planet Space Sci., 16, 129, 1968.

Feynman, J., and N. U. Crooker, The solar wind at the turn of the century, Nature, 275, 626, 1978.

Foster, J. C., D. H. Fairfield, K. W. Ogilvie, and T. J. Rosenberg, Relationship of interplanetary parameters and occurrence of magnetospheric substorms, J. Geophys. Res., 76, 6971, 1971.

Garrett, A. B., A. J. Dessler, and T. W. Hill, Influence of solar wind variability on geomagnetic activity, J. Geophys Res., 79, 4603, 1974.

Hirshberg, J., and D. S. Colburn, Interplanetary field and geomagnetic variations, a unified view, Planet. Space Sci., 17, 1183, 1969.

Hirshberg, J., and D. S. Colburn, Geomagnetic activity at sector boundaries, J. Geophys Res., 78, 3952, 1973.

Kamide, Y., and J. D. Winningham, A statistical study of the 'instantaneous' nightside auroral oval: The equatorward boundary of electron precipitation as observed by the Isis 1 and 2 satellites, J. Geophys Res., 82, 5573, 1977.

Kamide, Y., P. D. Perrault, S. I. Akasofu, and J. D. Winningham, Dependence of substorm occurrence probability on the interplanetary magnetic field and on the size of the auroral oval, J. Geophys. Res., 82, 5521, 1977.

Loomis, E., The aurora boreales or polar light; its phenomena and laws, Annu. Rep. Smithson. Inst., 13, 1866.

Maezawa, K. Dependence of Geomagnetic activity on solar wind parameters: A statistical approach, Solar Terr. Environ. Res. Jap., 2, 103, 1978.

Mayaud, P. N., A hundred year series of geomagnetic data, 1868–1967, Bull. 33, Int. Ass. Geomagn. Aeron., Zurich, 1973.

Neupert, M., and V. Pizzo, Solar coronal holes as sources of recurrent geomagnetic disturbances, J. Geophys. Res., 79, 3701, 1974.

Pike, C. P., and B. S. Dandekar, Evening sector auroral oval dynamics from DMSP photographs, J. Geophys. Res., 84, 3389, 1979.

Rostoker, G., and C. G. Fälthammar, Relationship between changes in the interplanetary magnetic field and variations in the magnetic field at the earth's surface, J. Geophys. Res., 72, 5853, 1967.

Rubenson, R., Catalogue des aurores boréales observées en Suède, Kgl. Sv. Vetenskapsakad. Handl., 15(5), 1879.

Rubenson, R., Catalogue des aurores boréales observées en Suède, Kgl. Sv. Vetenskapsakad. Handl., 18(1), 1882.

Russell, C. T., On the possibility of deducing interplanetary and solar parameters from geomagnetic records, Solar Phys., 42, 259, 1975.

Sandford, B. P., Variations of auroral emissions with time, magnetic activity and the solar cycle, J. Atmos. Terr. Phys., 30, 1921, 1968.

Sheeley, N. R., Jr., The equatorward extent of auroral activity during 1973-1974, *Solar Phys.*, *58*, 405, 1978.

Suess, S. T., The solar wind during the Maunder minimum, *Planet. Space Sci.*, *27*, 1001, 1979.

Svalgaard, L., Geomagnetic activity: Dependence on solar wind parameters, in *Coronal Holes and High Speed Wind Streams*, edited by Jack B. Zirker, Colorado Associated University Press, Boulder, 1977.

Tromholt, S., *Catalog der in Norwegen bis Juni 1878 beobachteten Nordlichter*, edited by J. Fr. Schroeter, Jacob Dybwad, Kristiania, Norway, 1902.

Tsurutani, B. T., and C. I. Meng, Interplanetary magnetic field variations and substorm activity, *J. Geophys. Res.*, *77*, 2964, 1972.

IMPLICATIONS OF SOLAR CYCLES 19 AND 20

GEOMAGNETIC ACTIVITY FOR MAGNETOSPHERIC PROCESSES

Joan Feynman

Department of Physics, Boston College, Chestnut Hill, Massachusetts 02167

Abstract. The solar cycle variations of geo-magnetic indices are compared for the last two solar cycles. It is found that the midlatitude aa index and the ring current index, D_{st}, exhibit a markedly different relationship to one another in the two cycles.

During solar cycle 20 the yearly averaged aa has been shown to be linearly related to either the yearly averaged $|B_z|v^2$ or v^2, where B_z is the north-south component of the interplanetary field and v is the solar wind velocity. However, the yearly averaged D_{st} is well represented by a linear function of $B_z v$ and not by a function v^2. A combination of regression formulas for D_{st} and aa allows estimates to be made of the annual average v and B_z from 1957 until 1965, when in situ measurements of the solar wind became available. Most interesting, however, is the point that the dependence of aa and D_{st} on different functions of solar wind parameters implies that the ring current is not directly produced by substorm injections. This result is in agreement with models of magnetospheric processes in which the increased ring current and substorm activity are two separate aspects of increased magneto-spheric convection.

Solar Cycle Variation of Geomagnetic Activity

The solar wind has been studied in situ for more than a solar cycle and a question now arises as to the extent to which observations made during the most recent cycle can be generalized to other solar cycles. A convenient method of approaching this problem is through the study of geomagnetic indices and their relation to solar wind parameters. To search for differences that may exist among solar cycles, the ring current index, D_{st}, has been compared to the aa index which characterizes the range of midlatitude geomagnetic variations. The aa index is very closely related to the more familiar A_p index as discussed in Allen and Feynman (1980). For both data sets, yearly averages are used to eliminate effects of the annual and semiannual components of the variations. The annual averaged D_{st}, $<D_{st}>$, for the 19 years from 1957 through 1975 are shown as solid lines in figure 1. The D_{st} has not been determined for earlier periods. The annual averaged aa shown as dashed lines has been used because it is available from 1868 until the present and its use will facilitate extension of this study to earlier time periods. Of course, it is closely related to A_p (see Allen and Feynman, 1980, for further discussion of geomagnetic indices). Note that in solar cycle 19 the major peak occurs in both $<aa>$ and $<D_{st}>$ three years after the 1957 sunspot maximum and a small secondary flattening

occurs about 1963, when extensive space data was first collected for several months (Neuge-bauer and Snyder, 1966). In contrast, only a flattening occurs near maximum in 1968, and there is a small peak in $<D_{st}>$ in 1972 and a large peak in $<aa>$ in 1974. The cycle 20 $<aa>$ peak has been discussed by Gosling et al. (1977) and was due to long lived fast solar wind streams.

The relative behavior of the two indices is also very different during solar cycles 19 and 20. The $<D_{st}>$ and the $<aa>$ appear to have been linearly related from 1957 through 1968, i.e. from cycle 19 sunspot maximum to cycle 20 sun-spot maximum. However, there is no apparent relation between $<D_{st}>$ and $<aa>$ from 1969 to 1975. For example, a comparison of the data for the years 1960 and 1974 presents a striking difference. Although $<aa>$ was the same for both years $<D_{st}>$ was almost -30 nT in 1960 and -12 nT in 1974. It is thus clear that $<D_{st}>$ and $<aa>$ are not simply functionally related.

Relationship to Solar Wind Parameters

The ring current index and mid-latitude indices can be compared to solar wind parameters. Crooker et al. (1977) found that the A_p index and $<v^2>$ were linearly correlated with a co-efficient of 0.9, and that there was no statis-tically significant change in the correlation coefficient when $<|B_z|>\times<v^2>$ was used as the independent variable in place of $<v^2>$. The same is of course true of the relation between $<aa>$ and $<v^2>$ and $<|B_z|>$. Approximating $<v^2>$ by $<v>^2$ for the years 1965 to 1974 the relationships are

$$<aa> = 12.4 \times 10^{-5} <v>^2 - 2.2 \qquad (1)$$

or

$$<aa> = 5.5 \times 10^{-5} <|B_z|>\times<v>^2 - 2.4 \qquad (2)$$

where the correlation coefficient is 0.9 in both cases and $<v>$ is in km/sec and $<|B_z|>$ in nT.

The correlation coefficient of $<D_{st}>$ with $<v>^2$ is less than 0.2, indicating no particular relationship. With $<v>$ the correlation coeffi-cient is less than 0.4. However, Burton et al. (1975) have shown that the hourly D_{st} is related to vB_s where B_s is the southward interplanetary field component. The yearly averages of D_{st} and vB_s are compared in figure 2 where recalling that $<|B_s|> = <|B_N|> = <|B_z|>$, $<vB_s>$ has been approxi-mated by $<v><|B_z|>$. The values of $<v>$ and $<|B_z|>$ are taken from Crooker et al. (1977). The corre-spondence between the quantities is very satis-factory except perhaps for 1972. The linear regression is given by

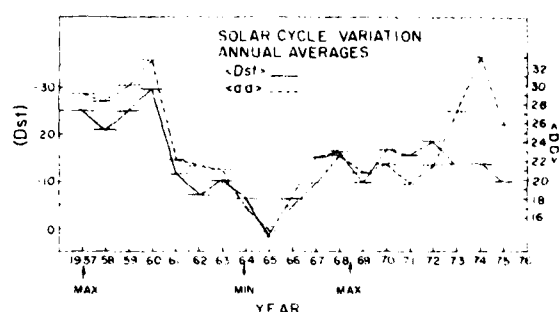$$<D_{st}> = 0.45 <|B_z|><v> - 29.9 \qquad (3)$$

Fig. 1. The annual mean ring current index D_{st} and midlatitude disturbance index aa for nineteen years. The maxima of cycle 19 and 20 are indicated by arrows as is the minimum which marks the end of cycle 19.

with a correlation coefficient of 0.8. The deviation of 1972 from the pattern in figure 2 may be due to the effects of the great solar flares at the beginning of August. The actual velocity of the solar wind was not measured near earth and hence is not included in the yearly average, but from other measurements it can be inferred that during this period it was sometimes greater than 1,000 km/sec (Ricket, 1975, Davis and Feynman, 1977). Spjeldvik and Fritz (1980) report that a very large increase of MeV helium ions was seen in the magnetosphere at L values as low as 2 after the August 1972 storms, but not after three other major storms in 1972. Although no measurements are reported for the KeV energy range which makes up most of the ring current, it appears likely that the composition was altered in August of 1972, in such a way as to increase the decay time of the D_{st} leading to the unusual relationship between the interplanetary parameters and D_{st}. Flares of the intensity of August 1972 are very unusual since the August flares produced the most intense solar proton event yet observed (Reid et al., 1976).

Implications for Solar Cycle 19

The observed values of <aa> and $<D_{st}>$ can be used to calculate an approximate <v> and $<B_z>$ for all the years since 1957. For the ten years of good solar wind data coverage from 1965 to 1974,
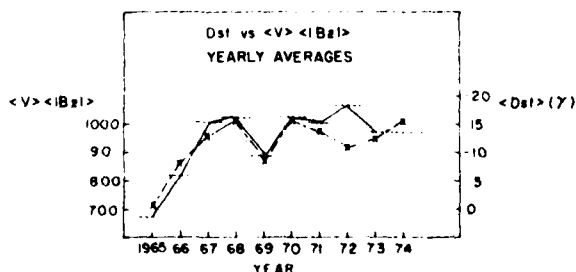

Fig. 2. The measured annual mean D_{st} shown as dashed lines is compared to solar wind velocity and mean southward field. Except for 1972, which is discussed in the text, the correspondence is very good.

the accuracy of the procedure is expected to be good since the correlation coefficients were high. The mean errors in <v> calculated from expressions 1 and 2 and using the measured value of $<|B_z|>$ are 3.5% and 5% respectively. Since this difference is not statistically significant, an expression of form 1 will be used since that choice will permit <v> to be calculated without performing algebra on the regression lines, which is a questionable procedure. The regression line with <v> as the dependent variable is given by

$$<v> \times 10^{-6} = .067 \cdot aa + 0.478 \qquad (4)$$

The resulting values of <v> are shown in figure 3. For the period from 1965 to 1974 the mean error in <v> is 2.7%. This can be compared to the mean difference between <v> determined by Diodato et al. (1974) and by the Los Alamos Scientific Laboratory instrument as given by Bridge (1976). For the seven years when both data sets are available the mean difference is 2.8%. Thus, the errors in the estimates from 1965 to 1974 are no larger than the uncertainty of the data. It should also be recalled that interplanetary data coverage was never complete during these years (Hundhausen, 1979).

The values of the velocity determined from (4) for 1957 to 1964 are quite reasonable. The solar wind annual average velocity was near 500 km/sec from 1957 through 1960 and then fell to about 440 km/sec for three years and finally to 400 km/sec at solar wind minimum. The estimated value in 1964 agrees well with the observed values in 1965 and 1966.

The $<|B_z|>$ can now be estimated from the regression between $<|B_z|><v>$ and D_{st}, which is written as

$$<|B_z|><v> = -13.9 \cdot D_{st} + 768 \qquad (5)$$

Since <v> is determined from (4) and the correlation coefficient for (5) is 0.8, this procedure is not expected to be as accurate as the procedure for <v>. The results are shown in the lower panel of figure 3. The years 1965 to 1974
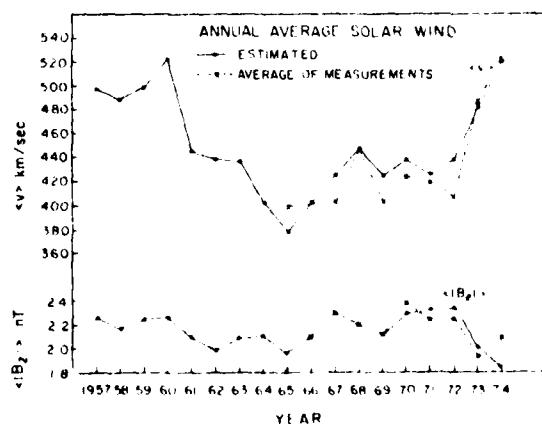

Fig. 3. The annual average solar wind velocity and southward field estimated from the linear regression formulas are compared with the available measured values.

show an average error of 3.4% using <v> from (4) rather than the measured v. Again, the estimated values of $\cdot|B_z|>$ in solar cycle 19 appear very reasonable.

Discussion and Conclusions

The difference of the relative behavior of D_{st} and aa can be readily explained by noting that the two magnetic indices respond to different functions of the solar wind parameters. Use of the regression formulas to find <v> and $<|B_z|>$ for the 19th solar cycle yield very reasonable values for both parameters so that the difference in the relative behavior of D_{st} and aa in the two solar cycles can be explained by differences in the solar wind.

The method used in this study to estimate past <v> and $<|B_z|>$ from <aa> and $<D_{st}>$ can be extended to earlier periods through the determination of the D_{st} for those periods. The period about 1900 will be particularly interesting since the solar wind could not have displayed <v> and $<|B_z|>$ simultaneously in the range they have had since 1957 (Feynman and Crooker, 1978).

The physical meaning of <aa> is not immediately obvious. However, the midlatitude indices were designed to be a measure of the range of activity having a characteristic time of less than three hours. Thus, aa is expected to be closely related to substorm activity. This expectation is confirmed by noting that the ratio $\frac{<aa>}{<AE>}$ is almost constant for the years when both are available, 1965 to 1974, ranging only from 0.10 to 0.12. Since <AE> is a measure of substorm activity (Rostoker, 1972) even though AE may fail to detect substorms accurately under some extreme circumstances, it follows that <aa> is also a measure of the annual mean substorm activity.

It can be concluded then that substorms and the ring current, although closely related, respond to different parameters in the solar wind. These results do not agree with the concept that the ring current is fed directly by substorm injections. Rather they strongly support the concept that the ring current and injections are separate aspects of increased particle convection (Siscoe, 1979, Lyons and Williams, 1980).

References

Allen, J. H. and J. Feynman, Review of selected geomagnetic activity indices, Solar Terrestrial Predictions Proceedings, Vol. II, (ed. R. F. Donnelly) U.S. Department of Commerce, 1980.

Bridge, Herbert S., Solar cycle manifestations in the interplanetary medium, Physics of Solar Planetary Environments, Proceedings of the Int. Symposium on Solar-Terrestrial Physics, Boulder, CO, (ed. D. J. Williams) published by Am. Geophys. Union, 1976.

Burton, R. K., R. L. McPherron and C. T. Russell, An empirical relationship between interplanetary conditions and D_{st}, J. Geophys. Res., 80, 4204 (1975).

Crooker, N. U., J. Feynman and J. T. Gosling, On the high correlation between long-term averages of solar wind speed and geomagnetic activity, J. Geophys. Res., 82, 1933 (1977).

Davis, W. D. and Joan Feynman, Type II emission mechanism, J. Geophys. Res., 82, 4699 (1977).

Diodato, L., G. Moreno, C. Signormi, and K. W. Ogilvie, Long-term variations of the solar wind parameters, J. Geophys. Res., 79, 5095 (1974).

Feynman, J. and N. U. Crooker, The solar wind at the turn of the century, Nature, 275, 626 (1978).

Gosling, J. T., J. R. Asbridge, S.J. Bame, An unusual aspect of solar wind speed variations during solar cycle 20, J. Geophys. Res., 82, 3311 (1977).

Hundhausen, A. J., Solar activity and solar wind, Rev. of Geophys. and Space Phys., 17, 2034, 1979.

Lyons, L. R. and D. J. Williams, A source for the geomagnetic storm main phase ring current, J. Geophys. Res., 85, 523 (1980).

Neugebauer, M. and W. Snyder, Mariner 2 observations of the solar wind, J. Geophys. Res., 21, 4469 (1966).

Reid, G. C., I.S.A. Isaksen, T. E. Holzer, and P. J. Crutzen, Influence of ancient solar-proton events on the evolution of life, Nature, 259, 177 (1976).

Rickett, B. J., Disturbances in the solar wind from IPS measurements in August 1972, Solar Phys., 43, 237 (1975).

Rostoker, G., Polar magnetic substorms, Rev. of Geophys. and Space Phys., 10, 157 (1972).

Siscoe, G. L., A quasi-self-consistent axially symmetric model for the growth of a ring current through earthward motion from a pre-storm configuration, Planet. Space Sci., 27, 285, (1979).

Spjeldvik, W. N. and T. A. Fritz, Observations of energetic helium ions in the earth's radiation belts during a sequence of geomagnetic storms, to be published, J. Geophys. Res., 1980.

GEOMAGNETIC AND SOLAR WIND CYCLES, 1900-1975

Joan Feynman

Department of Physics, Boston College

Chestnut Hill, Massachusetts, 02167

Abstract. Recent research has established the reality of the 80 to 100-year cycle (long cycle) in solar-terrestrial phenomena that for many years has been suspected to occur. This paper investigates some of the systematic changes that took place during the most recent long cycle. The variations of one hundred years of data on the aa index of geomagnetic activity are reinvestigated. Since the solar wind drives geomagnetic activity the results of the study are interpreted in terms of the solar wind. It is shown that the 11-year solar cycle as expressed by the number of sunspots (the sunspot cycle) is very different from the 11-year solar cycle as expressed by the solar wind and geomagnetics (the solar wind cycle). With an objective technique, using only sunspot numbers and not involving any judgement as to the transient or recurrent nature of any geomagnetic activity, the solar wind cycle is decomposed into the sun of two equally strong periodic variations, each having the period of the sunspot cycle, but differing in phase. One term in the decomposition, the R component, is chosen to have the phase and relative amplitude of the sunspot cycle. The other term in the decomposition, the I component, is found to be almost, but not quite, 180° out of the phase with R and to have very closely related amplitudes. The source of the R component is shown to be sporadic or short-lived solar events and that of the I component is shown to be long lived solar features such as coronal holes. The amplitudes are interpreted as being due to solar wind parameters, probably $1B_Z1V^2$. The solar wind observed at earth oscillates rhythmically between the two sources. The amplitude of both the oscillations increased smoothly and steadily from 1900 to 1960, corresponding to the ascending branch of the long cycle of solar activity which has been established elsewhere as occuring in the solar wind with an average period since the Middle Ages of 87 years. From these results it is concluded that there is a very strong relationship between coronal conditions at the sites of origin of long lived streams of solar wind and the corresponding sites of sporadic and/or short lived events 5 or 6 years later. Moreover, there is a remarkable and orderly evolution of these conditions over at least 60 years. The interruption of the smooth evolution in 1960 suggests we are now in the declining phase of the long cycle, which is to be expected since the average cycle period is 87 years and the last minimum was in the first decade of this century.

Introduction

Since the solar wind produces geomagnetic variations and auroras, a great deal of information about past behavior of the wind and the sun itself can be derived from studies of geomagnetics and of the behavior of auroras. The results of earlier studies have demonstrated remarkable regularities that form the background for this study. Here these studies are continued with emphasis on the systematic changes that have occured in solar terrestrial phenomena during the last century.

The variation of the solar output during the eleven year solar cycle has many manifestations, including for example, sunspot number, development of polar coronal holes, major solar flares and the solar wind. Hirshberg [1973] pointed out that distinctions should be made between the solar cycle variations will have the same period but may have different phases, relative amplitudes and/or shapes of variation. It has become common practice to use the variations of the sunspot number as the standard for the solar cycle and to compare the changes in all other relevant quantities to the sunspots, but this approach is sometimes not based on physical relationships. Even the shape of the corona observed from 1839 to 1945 did not have the same phase as the sunspots [Hirshberg, 1973]. The 'minimum' ('maximum') eclipse form occurred about 1 1/2 years before sunspot minimum (maximum). Hirshberg introduced the notion of a 'solar wind cycle' that is, the 11-year solar cycle as expressed in the variations of the solar wind, which need not have the same phase or shape as the sunspot cycle.

Since we have now observed the solar wind for more than 11-years, changes due to the solar cycle should have been observed. Such changes have indeed taken place in the interplanetary field magnitude [King, 1979, 1981], in $1B_Z1$, the absolute value of the field component perpendicular to the ecliptic plane [Siscoe et al., 1978] and in the helium abundance of the wind [Neugebauer, 1981]. In addition, stable high-speed streams developed during the period of the cycle corresponding to a decreasing number of sunspots [Gosling et al., 1977]. These streams produced the recurrent geomagnetic storms [Neupert and Pizzo, 1974] that are so typical of that phase of the sunspot cycle [Newton, 1948]. Not surprisingly the variations in solar wind parameters are not necessarily in phase with the solar cycle as expressed by the numbers of sunspots. For example, the helium abundance may lag the sunspot number by a year or so [Neugebauer, 1981]. The solar cycle variation of the interplanetary field intensity, showed a broad plateau between the well marked minima in about 1965 and 1976 [King, 1979]. The value of
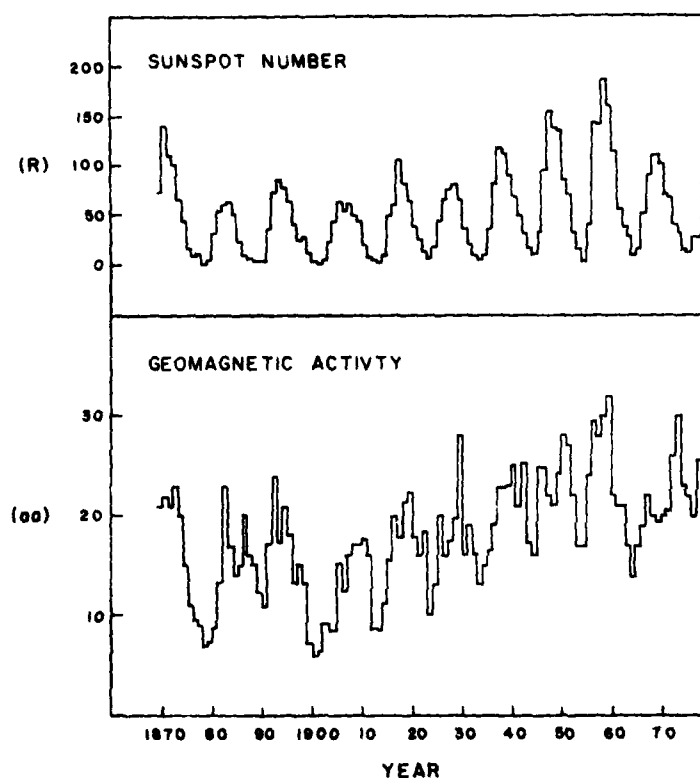
Fig. 1. The annual number, R and the annual average aa index, (aa), from 1868 to 1975. (aa) is measured in units of nanoteslas.

the annual average of hourly values of B_z tracked the sunspot number fairly well [Siscoe et al., 1978]. The yearly averaged solar wind velocity had a well marked maximum during the period of declining sunspot number and returned to smaller values in about 1977, a year after minimum sunspot number.

In addition to an 11-year cycle, for over a hundred years it has been suspected that there is a longer cycle in the frequency and/or intensity of aurora. This variation is interpreted by modern workers as a solar wind change. Early workers suggested periods ranging from 50 to 100 years [Hansteen, 1981; Olmstead, 1856; Fritz, 1881]. Siscoe [1980] has recently reviewed both the history of early recognition of the long cycle and the evidence for it in the auroral record for Europe and the record for the Orient since the Middle Ages. He concludes that the auroral record from 1090 to 1700 shows a variation of the occurrence frequency with a mean period of 87 years. Gleissberg [1965] has reported a period of approximately 80 years in auroral frequency for 16 centuries and Link [1962] discussed the same period variation in auroral intensity since A. D. 600. Recent minima of this long cycle occurred about 1700, 1810 and 1901. Evidence for the 1700 minimum comes from the work of Eddy [1976] and Link [1964] who show there was a decline in the number of auroral observations per decade during the latter half of the 1600s, ending in a strong upsurge of reports

in the early decades of the 1600's. The minimum circa 1800 was noted widely by observers at the time and is discussed by Fritz [1881]. Feynman and Silverman [1980] studied the positions at which aurora were observed in Sweden between 1771 and 1858 and concluded that the solar wind in 1809-1815 was in some sense weak with a minimum at the time. This conclusion is consistent with the observation of anomalously high levels of C^{14} during the early decades of the 1800's [Damon et al., 1978]. Concerning the 1900 minimum, Russell [1975] noted that there was a general rise in the sunspot cycle averaged value of the aa index of geomagnetic activity between 1900 and 1960. Feynman and Crooker [1978] pointed out that there was a steep rise in the level of geomagnetic activity at sunspot minimum between 1900 and 1960 such that the annual average value of the aa index, (aa), at the 1905 maximum, when the sunspot number was 63, was 2 nT less than the (aa) at the 1954 minimum when the sunspot number was 4. They suggested this rise was a manifestation of the long cycle since this trend toward increasing (aa) at each minimum was in sharp contrast to the behavior of the sunspot number. For sunspots, although the maximum of each succeeding cycle was stronger than the preceding one, the sunspot number returned to near zero at each minimum. Feynman and Silverman [1980], noted that the long cycle as seen in the gradual change in the strength of successive sunspot cycles and the long cycle as expressed by

74

**R SUNSPOT NUMBER VS
aa GEOMAGNETIC ACTIVITY
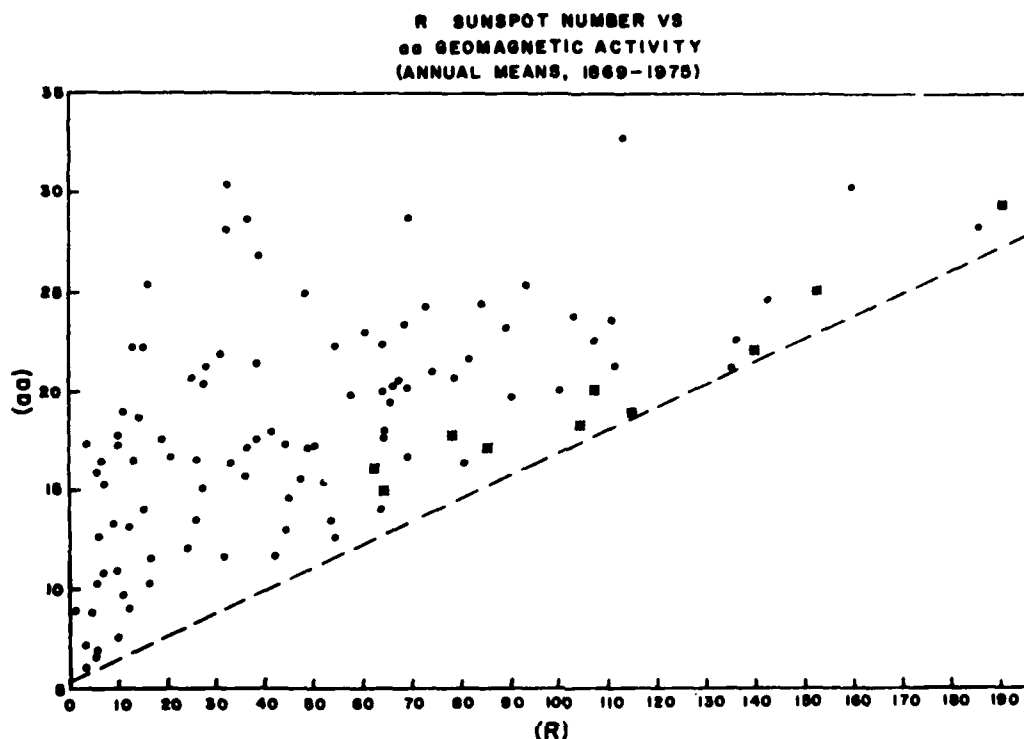(ANNUAL MEANS, 1869-1975)**

Fig. 2. The relation between sunspot numbers and (aa). Stars indicate sunspot
number maximum years. No points lie below the dashed line.

the change of the solar wind implied from auroral
positions and geomagnetics were separate aspects
of the solar activity cycle. The presence of one
did not imply the presence of the other. They
invoked the simultaneous changes in these two
quantities as another indication that the long
cycle was a real effect and not merely apparent
due to a statistically random change in the
number of sunspots at maximum.

Earlier studies of the 11-year cyclic
variations of geomagnetic activity have also been
fruitful. It has been well known for many years
that the actiivity in a given cycle has a maximum
of sudden commencement storms near sunspot
maximum and a second maximum of recurrent storms
a few years later [Newton, 1948]. Ohl [1971]
compared the annual average Kp with the annual
average sunspot number and discussed the distinct
second maxima that were apparent during the
decline of the sunspot number during some 11-year
cycles. These second maxima were due to
recurrent storms. He showed that the level of
this activity was a good predictor of the sunspot
number maximum in the next cycle but was not as
closely related to the preceeding sunspot number
maximum. He concluded that the true beginning of
the solar activity cycle occurred several years
before sunspot minimum and that the sources of
the recurrent storms developed before the
sunspots of a given cycle.

In this paper, studies of both the long cycle
variations and the 11-year cycle variations are
carried forward by an analysis of the 100 years
of aa data prepared by Mayaud. The interpreta-

tion of aa as a reflection of solar wind
parameters is based on many studies of the
relationship of this type of index to the solar
wind [c.f. Hirshberg and Colburn, 1969; Garrett
et al., 1974; Svalgaard, 1977; Feynman and
Crooker, 1978]. In the first section of this
paper the relationship of (aa) to the yearly
average sunspot number (R) is examined and
decomposed into two terms. The second section
discusses the relationship of these terms to each
other and to their solar sources. The results
are discussed and summarized in the third and
fourth sections, respectively.

The Sunspot Number and the Decomposition of
Geomagnetic Variations

The study of past geomagnetics and solar wind
has been aided immeasurably by the work of Mayaud
[1973], who painstakingly studied 100 years of
data at two antipodal stations (Melbourne and
Greenwich) and derived a commensurate set of half
day values for a three hour range index, aa, for
the entire period. The yearly averages of aa and
the sunspot number R are shown in Figure 1
adapted from from Mayaud [1975]. The broad (aa)
maximum in each sunspot cycle is evident, as is
the remarkable rise in (aa) at successive sunspot
minima from 1900 1960. The (aa) does not track
the sunspot number. Indeed, comparing the (aa)
with (R) suggests that almost any yearly (aa)
would be compatible with a given yearly sunspot
number. However, this is not the case, as is
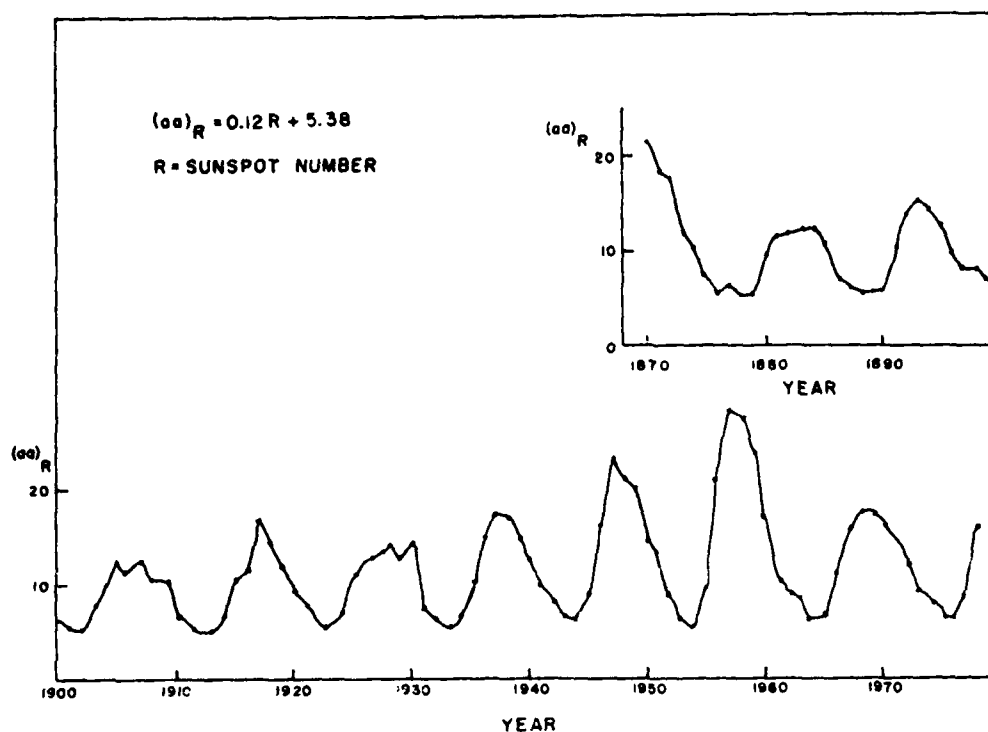shown in Figure 2 where (aa) has been plotted as

Fig. 3. The R component of activity $(aa)_R$. This component is strictly proportional to sunspot number.

a function of (R) for the years from 1869 to 1975 (see also Simon, 1979). The data points all lie above a minimum value, given by the dashed line, although they appear to be more or less randomly scattered in the region above the line and below an (aa) of 33 nT. The ten sunspot maximum years are shown as stars in the figure. Each of the (aa) for the sunspot maximum years lies less than 5 nT from the dashed line. That is, the geomagnetic activity during sunspot maximum years was near the lowest levels observed or that sunspot number.

In order to analyse this data further it is useful to examine the amount by which each year's (aa) exceeded the minimum value appropriate for that year's sunspot number. To do this, an $(aa)_R$ value corresponding to the minimum line is subtracted from each (aa). The equation of the minimum line is given by

$$(aa)_R = 0.12R + 5.38$$

The remainder is designated $(aa)_I$ so that (aa) in any year is given by $(aa)_R$ plus $(aa)_I$. Since $(aa)_R$ is strictly proportional to the sunspot number it will show the same periodicity and phase and an equivalent cycle magnitude, as shown in Figure 3. The remainder, $(aa)_I$ shown in Figure 4, also has a very strong periodicity. The arrows in the figure indicate sunspot maxima and sunspot minima. A minimum in the remainder $(aa)_I$ occurs close to the time of sunspot maximum for each of the sunspot maxima in the 20th century. This is particularly well marked for the four sunspot maxima since 1932, when the

$(aa)_I$ minimum tends to occur year or so after sunspot maximum. Conversely, during the 20th century, the largest values of $(aa)_I$ tend to occur shortly before sunspot minimum. The $(aa)_I$'s are less well organized during the 19th century. The periodicity of $(aa)_I$ was not imposed on it by data handling. This can be seen by considering what other forms the remainders could have taken. For example, if (aa) were approximately proportional to the sunspot number, the remainder would have been random. Hence the periodicity of $(aa)_I$ represents an attribute of the way in which the driver of geomagnetic activity, the solar wind, changes during a solar cycle. The amplitude of the oscillations increase from 1900 to 1957. Since the minimum of the long cycle occurred circa 1900, this growth in amplitude may well be the solar wind expression of the ascending part of the long cycle variation.

The phase of the $(aa)_I$ variation apparent in the last five cycles shown in Figure 4 suggests an interesting relationship to the phase of the sunspot cycle. To examine this further the $(aa)_R$ and $(aa)_I$ time series were smoothed to suppress the high frequencies. The numerical filter used had weights of 1, 2, 1 and was applied to each point in the time series. The two resultant time series for the period from 1900 to 1974 are compared in Figure 5, where straight lines have been drawn between the data points to guide the eye. In the upper panel the left-hand scale and solid line refer to $(aa)_R$ and the right-hand line scale refers to $(aa)_I$. The only difference between the two scales is the placing of the zero
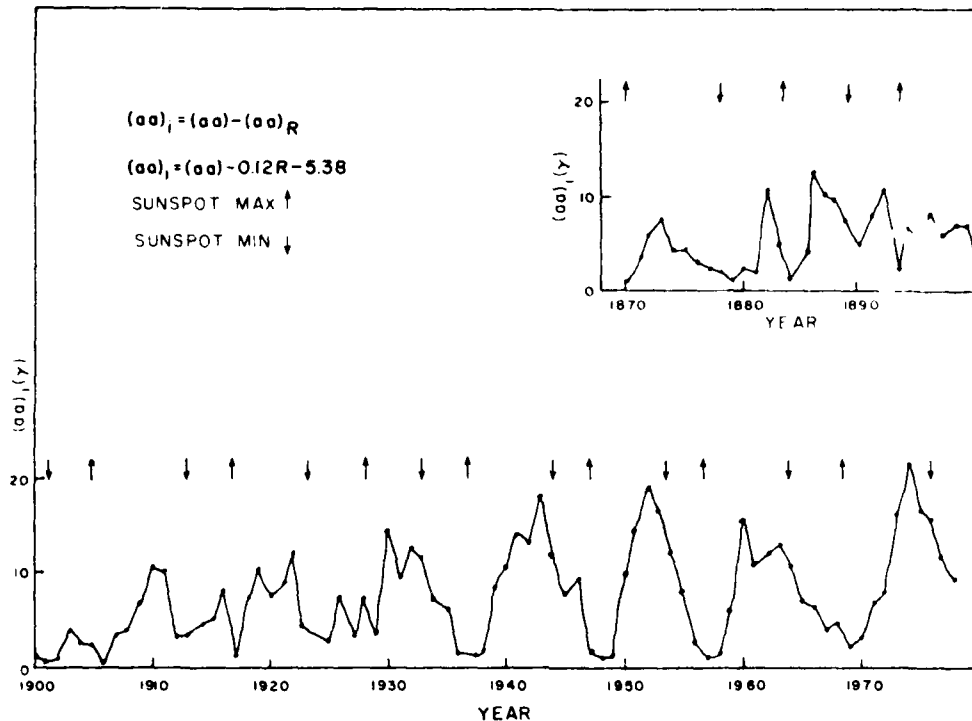
$$(aa)_i = (aa) - (aa)_R$$

$$(aa)_i = (aa) - 0.12R - 5.38$$

SUNSPOT MAX ↑

SUNSPOT MIN ↓

Fig. 4. The I component of activity $(aa)_I$. This component is defined so that (aa) is given by the sum of the R and I components. Note the periodicity of the I component.

value, which was adjusted so that zero on the right-hand scale corresponds to f've on the left-hand scale. This choice of scale offset gives a very good match for the minimum values of the two time series. A different choice of the additive constant in the definition of $(aa)_R$ would lead to a different offset between the scales to accomplish equivalent matching. The value of 5.38 was chosen in expression (1) because it is the intercept of the minimal line in Figure 2 with the (aa) axis. It has no physical meaning as far as the amplitudes of the variation of $(aa)_R$ and $(aa)_I$ are concerned. Note that an outstanding characteristic of the data data from 1900 to 1960 is that the amplitudes of the variations of the two components are approximately equal and increase systematically.

The data for the pre-1900 era are not shown in Figure 5 because they do not appear to be as well ordered. This can be expected from Figure 4. It is not clear if this lack of order occurs because the early geomagnetic data were not accurate or because that period was actually not well ordered. The lack of order may be a characteristic of the declining part of the 19th century long cycle.

Relationship of terms to Solar Sources and to each other

The outstanding characteristic of Figure 5 is the oscillatory nature of the two curves. The solar cycle variation of geomagnetics, and hence the solar wind, appears to have been decomposed

into two similar periodic components. Before discussing phase and amplitude relationships further it is convenient to investigate the physical meaning of the two components. The $(aa)_R$ time series will be called the R component and the $(aa)_I$ the I component.

The R component was defined solely in terms of the sunspot number, and so the correlation coefficient with the sunspot number is 1. It will, therefore, have the same correlation to any other time series as does the sunspot number. In particular, Mayaud [1973] has generated a list of sudden commencements for the same period as that for which he generated aa, and he has found a correlation of 0.85 between sunspot number and the number of sudden commencements. It follows that $(aa)_R$ has a correlation of 0.85 with sudden commencements, which are usually caused by shocks in the solar wind [Burlaga and Ogilvie, 1969]. Shocks in turn are often caused by solar flares. Geomagnetic storms occurring at the time of sunspot maximum show little or no tendency to recur during the next solar rotation [Newton, 1948; Sargent, 1979]. It appears then that the R component is associated with solar events that are short lived compared to a solar rotation. Although Hedeman and Dodson-Prince [1981] have shown that flares with large 'flare indices' are usually followed by geomagnetic disturbances, it should not be assumed that the solar events causing the R component are flares alone. Joselyn and McIntosh [1981] discuss the prediction of geomagnetic activity from solar observations and conclude that the sudden
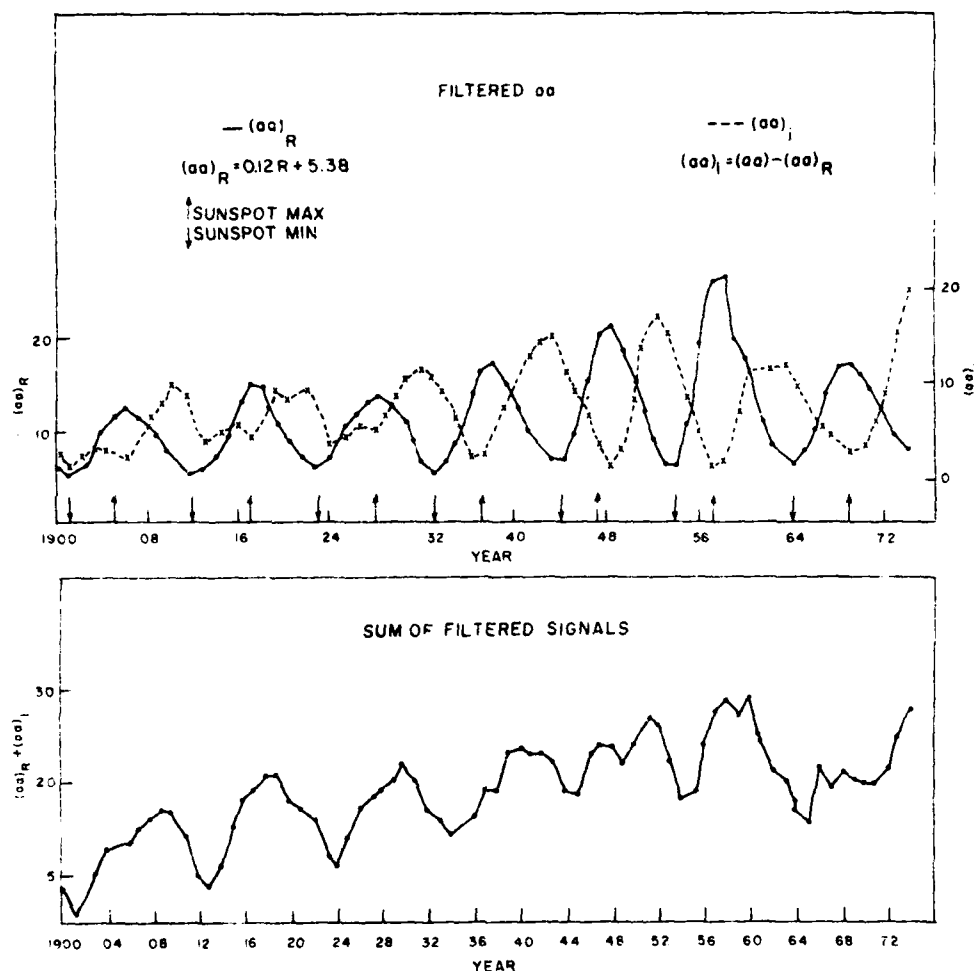
Fig. 5. The upper panel shows a comparison of the smoothed R and I components. The oscillations of the two components have closely related amplitudes and are almost, but not quite, 180° out of phase. The lower panel shows the sum of the smoothed R and I components.

disappearances of filaments known as 'disparition brusque' are often indicative of impending magnetic storms. Filament disappearances in turn have often been observed in connection with coronal transients [Munro et al., 1979]. R events may also be caused by temporary coronal holes. Sheeley and Harvey [1981] reported that during the 1979-1980 sunspot maximum holes lived only a few months. Such holes may produce nonrecurrent activity. Considering all the possible causes of interplanetary shocks at 1 AU and of nonrecurrent disturbances, the R component represents the geomagnetic effect of short lived events that can be observed to occur on the sun.

The physical meaning of the I component is implicit in the data shown in Figure 6, where the 'recurrence index' is compared with the proportion of (aa) that is represented by $(aa)_I$. The recurrence index is defined by Sargent [1979], who calculated the correlation of each 27 day time series of aa with the next 27 day series. Each day in turn was used as the center

day of the first of the two 27 day intervals. The correlation coefficients were then multiplied by 100, and the resultant number was called the recurrence index. Here the annual average recurrence index is shown. This is compared with the annual average of the ratio of the unfiltered $(aa)_I$ to (aa), that is, the annual fraction of geomagnetic activity caused by the I component. The correspondence between the two quantities is very good. Although the two quantities shown in Figure 6 are calcualted from the same time series, the processes involved in the two calculations are so different that there is no a priori reason why these two resulting functions should have any relation to one another. One process involves only correlations, the other involves only subtracting numbers from one another and dividing one number by another. The relationship apparent in Figure 6, then, must be a physical one, and the I component is due to solar wind from structures on the sun long lived compared to a solar rotation. The identification
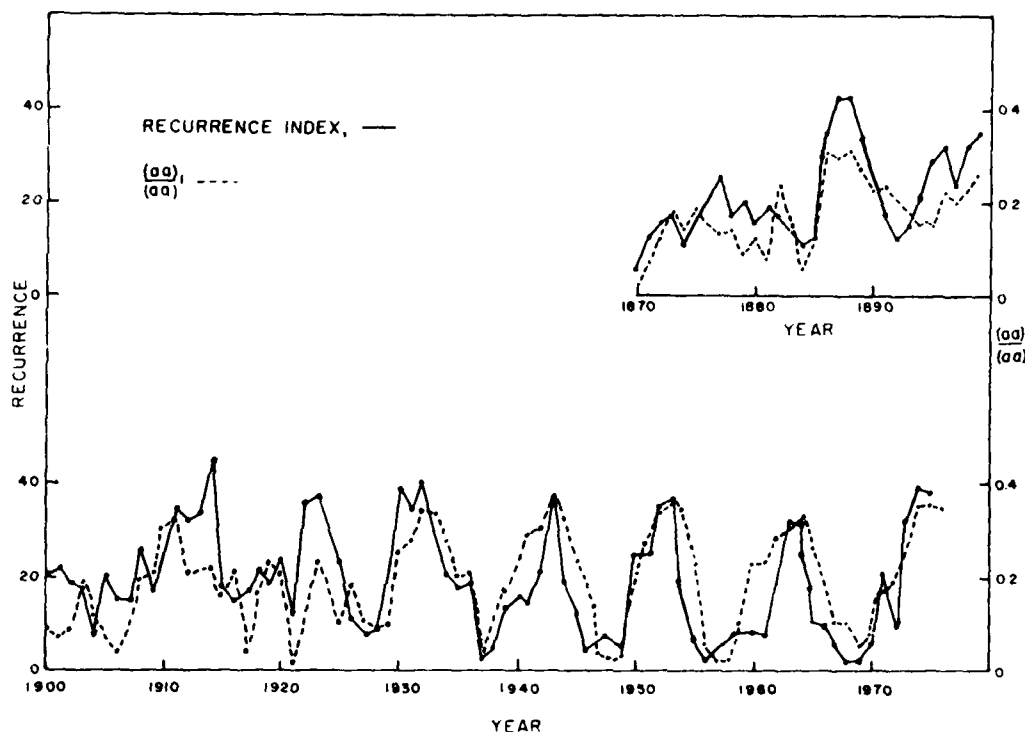
Fig. 6. A comparison between the behavior of the I component and the recurrence index.

of polar coronal holes as the source of the solar wind streams responsible for the 1973 peak in the recurrence index [Neupert and Pizzo, 1974] leads to the suggestion that the I component is do to long lived holes. This suggestion is strengthened by the Hundausen et al. [1981] study of the evolution of the coronal density structures in which they find the polar coronal holes were decreasing in size during 1965-1967 when $(aa)_I/(aa)$ was decreasing. The polar holes were absent in 1969-1970 when $(aa)_I/(aa)$ was at minimum, and polar holes were prominent features from 1971 to 1978 and the $(aa)_I/(aa)$ increased rapidly from 1971 until its maximum in 1974, which was sustained until the end of the data set in 1976.

Returning to Figure 5 the decomposition of (aa) into the R and I components corresponds to the decomposition of the solar wind cycle into a component composed of short lived events and a component composed of slowly varying events. The figure represents these two components since the time of the #UU minimum of the long cycle, i.e., during an ascending part of the long cycle and perhaps through the maximum and variation and partway into the descending phase. Note that during the period from 1900 to 1960 the amplitude of the variations of both the R and I components increase smoothly and together. This is in agreement with the observation [Ohl, 1971; Sargent, 1978] that the level of the next sunspot maximum (proportional to $(aa)_R$) can be predicted from the average level of geomagnetic activity measured by (aa) a few years before the preceding

minimum and corrected according to the number of sunspots at sunspot minimum. The function used in the prediction of the maximum sunspot number depends on $(aa)_I + (aa)_R$ just before minimum, corrected by a number proportional to $(aa)_R$ at sunspot minimum. The generally rising amplitude of the I component oscillations are responsible for the trend of (aa) at sunspot minimum evident in Figure 1 and discussed by Feynman and Crooker [1978].

The smooth rise in the amplitude of the oscillations is interrupted in 1961 by the appearance of an I oscillation that is very much decreased in amplitude. This is followed by an R oscillation of the same small amplitude. Because 1960 is 60 years after the minimum of the long cycle, this probably represents the onset of the declining phase. If so, all our in situ data on the solar wind is from the declining long cycle phase. Although the equality of magnitude of the I and R cycle pair beginning in 1960 suggests that the 11 year solar cycle consists of an I oscillation always followed by an R oscillation of nearly the same amplitude even during the descending phase of the long cycle, such a speculation would be premature since it is based on one example. Furthermore, the data from 1870 to 1900, taken during the last descending phase of the long cycle, appears to be relatively unordered.

The phase relation between the I and R components also is quite regular. The I component peaks within a year of half way between two successive R maxima. Although the phase of

the R component is impressed on it by the definition of $(aa)_R$ as proportional to the sunspot numbers, because this decomposition led to such an orderly result, the phase cannot be very far wrong. For example, decomposition according to the variation of the number of filament disappearances or the number of major flares might give a somewhat different phase to the R component and would be based on a more physical decomposition, since sunspots are certainly not the actual sources of the solar wind. In any case, this analysis leads to a picture in which the ascending part of the long cycle was characterized by well ordered out of phase oscillations between solar wind from long lived and short lived sources.

Discussion

It has been shown that the geomagnetic variations during the ascending part of the long cycle can be decomposed into two periodic variations nearly, but not quite, 180° out of phase with one another. The amplitude of these two oscillations increased smoothly and together for over 60 years, and then, in about 1960, the oscillations amplitudes suddenly decreased together. The physical interpretation of the amplitude of the R and I components in terms of solar wind parameters is open to several alternatives as discussed below. However, there are attributes of the interpretation that are independent of any details. For example, the outstanding characteristic of the decomposed variations is that the shapes and amplitudes of the R and I variations are very strongly related to one another, in spite of the fact that the solar sources of the solar wind causing them are supposedly so different. This leads to two interesting conclusions. First, since the sources are distributed over all solar latitudes, the solar wind sampled at the earths' orbit, near the sun's equatorial plane, represents a characteristic of the sun as a whole rather than a strictly local effect. Second, since the magnetosphere acts as a solar wind detector, the data imply that although the two types of sources have such different geometries and/or time histories, the parameters of the solar wind due to short lived events during a particular R cycle are very strongly related to wind parameters from long lived equatorward extensions of polar coronal holes during the preceding I cycle. However, these wind parameters change from one 11-year solar cycle to the next and, for 3/4 of a century, do so in a very orderly fashion. The fact that the amplitudes of the R and I oscillations are so strongly related requires that the values of the responsible parameters in the solar wind cannot be due to strictly local phenomena but must reflect sun-wide properties. For example, if the responsible parameter is the solar wind velocity, which is not unlikely, we must conclude that the velocity produced in the stable coronal holes at the maximum of a particular I cycle is closely related to the velocity produced by short lived events in the subsequent R cycle. This results in a curious problem. If it is assumed, as it often is, that the geomagnetic activity at maximum sunspot number is produced by sporadic events such as

flares or coronal transients, then the wind velocity produced by such events must be closely related to that produced by the earlier long lived coronal holes. However, the physical process involved in these sporadic events is supposed to depend on geometry, or more probably, wave fluxes. It seems highly unlikely that two such different processes could produce such closely related solar wind parameters. One possible explanation would be that solar wind at sunspot number maximum came from short lived holes. If solar wind from flares and/or transients were rare enough, then the yearly averages of v and B_z would not be seriously affected by wind from these sources. To evaluate this possibility, note that the number of sudden commencements for a year and R equal to 100 to 150 is about 50 [Mayaud, 1973]. If each of the SC's were to represent a sporadic event and each sporadic event dominated solar terrestrial phenomena during a two day storm, then the sources of the wind would be sporadic for about 100 days, which appears to be often enough to cause the high annual averages of aa. However, if the number of the SC's and/or the duration of the subsequent storm are significantly over-estimated, wind from short lived coronal holes might predominate. In that case, the theoretical problem of explaining the velocity of the wind would be very much simplified.

The correct interpretation of the amplitude of the R and I components in terms of specific values of solar wind parameters cannot be definitely decided upon at our present state of knowledge. Theories of geomagnetic variations are still incomplete and empirical. Studies of the relationship between solar wind parameters and geomagnetic variations result in different fuctional relationships, depending on the type of geomagnetic activity, the quantity used to measure it, and the time scale involved [Hirshberg and Colburn, 1969; Feynman, 1980; Svalgaard, 1977; Garrett et al., 1974; Perreault and Akasofu, 1978; Maezawa, 1978; Holzer and Slavin, 1981]. The studies that are most directly applicable here are those of Crooker et al. [1979] and Feynman [1980], who looked at the relationships for annual averages of ap and aa and found a correlation coefficient of 0.8 between (ap) or (aa) and $(v)^2$ or (v^2), where v is the solar wind velocity. Crooker et al. [1979] also used the term (Bz) (v^2) where (Bz) is the annual average of the magnitude of the interplanetary magnetic field perpendicular to the ecliptic and should be equal to the annual average southward component. Including (Bz) did not change the correlation with (ap) for available data but produced a function that was valid on all time scales. Extrapolation of that relation, or the equivalent expression using (aa), (Feynman, 1980), to the earlier times dealt with here would result in the conclusion the (Bz) (v^2) or more properly (Bz v^2) at R and I maximum changed in an orderly fashion from 1900 to 1960, during the ascending phase of the long cycle of the sun. There is no information that permits a choice to be made as to whether it is more likely that the change was in the velocity of the wind or in the magnetic field because there is no reason to suppose that the changes occurring during a single 11-year solar cycle are in the

same parameters that gradually changed over 60 years of the long cycle.

Summary and Conclusions

Using a criterion not based on judgement as to the type of geomagnetic activity involved, but on the sunspot number alone, the time series of annual average aa, (aa), has been decomposed into two periodic functions R and I, which are nearly, but not quite, 180° out of phase and have amplitudes that are very closely related to one another. The R and I components were interpreted in terms of the solar wind and it was found that the R component had a correlation coefficient of 0.85 with the number of sudden commencements per year and was due to sporadic or short lived solar wind sources such as solar flares, disappearing filaments and/or short lived coronal holes. The I component was compared to annual average recurrence indices and shown to be due to long lived solar wind sources such as polar coronal holes.

From 1900 to 1975 the sources of the solar wind oscillated rhythmically and regularly between sporadic or short lived sources and long lived source regions. The alternating nature of the source regions is so well ordered that it appears to be a fundamental part of the 11-years solar cycle in this century. The amplitude of the oscillations increased smoothly from a low during the first cycle of this century to a high at the 1957 R cycle. The amplitude tripled in that time. This gradual build up is interpreted as the increasing phase of the solar long cycle which has been shown to have an average period of about 87 years, [Siscoe, 1980] and was last at minimum in 1901. The orderly rise in the oscillation amplitude ended abruptly in 1960, just before extensive solar wind observations began. This sudden change may well indicate that we entered the declining phase of the long cycle. The small amount of data that we have since 1960 and from the last declining long cycle phase during the last part of the 19th century suggests that the solar wind cycle is less well ordered during declining periods than during the ascending period. It may therefore be unusually difficult to predict solar wind and geomagnetic behavior in coming years. Since (aa) is related to (Bz V^2) in the solar wind, the orderly relationships between the I and R components indicate that a given pair of I and R oscillations represent solar wind with closely related values for Bz and v^2, although the sources of the wind have commonly been thought to be very different. This presents the problem of why the long lived and sporadic and/or short lived sources produce solar wind with such similar properties. Possible sporadic sources include solar flares, and coronal transients causing disappearing filaments and short lived sources might be special coronal holes. The evolution of the amplitudes of I and R during the first 60 years of this century indicates a gradual evolution in the properties of the sun as a whole at those depths which are responsible for the production of the solar wind.

References

Burlaga, L. F., and K. W. Ogilvie, The causes of sudden commencements and sudden impulses, J. Geophys. Res., 74, 2815, 1969.

Crooker, N. U., J. Feynman, and J. Gosling, On the high correlation between long-term averages of solar wind speed and geomagnetic activity, J. Geophys. Res., 82, 1933, 1977.

Damon, R. R., J. C. Lerman, and A. V. Long, Temporal fluctuations of ^{14}C: Casual factors and implications, Ann. Rev. Earth Planet. Sci., 6, 457, 1978.

Eddy, J. A., The Maunder minimum, Science, 192, 1189, 1976.

Feynman, J., Implications of solar cycle 19 and 20 geomagnetic activity for magnetospheric processes, Geophys. Res. Lett., 7, 971, 1980.

Feynman, J., and N. U. Crooker, The solar wind at the turn of the century, Nature, 275, 626, 1978.

Feynman, J., and S. M. Silverman, Auroral changes during the 18th and 19th centuries and their implications for the solar wind and long term variation of sunspot activity, J. Geophys. Res., 85, 2991, 1980.

Fritz, H., Das Polarlicht, F. Brockhaus, Leipzig, 1881.

Garrett, A. B., A. J. Dessler, and T. W. Hill, Influence of solar wind variability on geo-magnetic activity, J. Geophys. Res., 79, 4603, 1974.

Gleissberg, The eighty-year solar cycle in auroral frequency numbers, J. Br. Astron. Assoc., 75 227, 1965.

Gosling, J. T., J. R. Asbridge, and S. J. Bame, An unusual aspect of solar wind speed variations during solar cycle 20, J. Geophys. Res., 82, 3311, 1977.

Hansteen, C., II Beobachtungen uber das nordlicht vom Januar 1830, Poggendorffe's Annalen XXII, 536, 1831.

Hedeman, E. R., and H. Dodson-Prince, Study of geomagnetic storms, solar flares, Rep. AFGL-TR-81-0024, Air Force Geophys. Lab., Bedford, Mass., 1981.

Hirshberg, J., The solar wind cycle, the sunspot cycle and the corona, Astrophys. Space Sci., 20, 473, 1973.

Hirshberg, J., and D. S. Colburn, Interplanetary field and geomagnetic variations, a unified view Planet, Space Sci., 17, 1183, 1969.

Holzer, R. E., and J. A. Slavin, The effect of solar wind structure on magnetospheric energy supply during solar cycle 20, J. Geophys. Res., 86, 675, 1981.

Hundhausen, A. S., R. T. Hansen, S. F. Hansen, Coronal evolution during the sunspot cycle: Coronal holes observed with Mauna Loa K-coronameter, J. Geophys. Res., 86, 2079, 1981.

Joselyn, J. A., and P. S. McIntosh, Disappearing

solar filaments: A useful predictor of geomagnetic activity, J. Geophys. Res., 86, 4555, 1981.

King, J. H., Solar cycle variations in the IMF intensity, J. Geophys. Res., 84, 5938, 1979.

King, J. H., On the enhancement of the IMF magnitude during 1978-1979, J. Geophys. Res., 86, 4828, 1981.

Link, F., Observations et catalogue des auroras boreales apparues en occident de 626 a 1600, Geofys. Sb., X, 297-387, 1962.

Link, F., Observations et catalogue des aurores boreales apparues en occident de 1601 a 1700, Geophys. Sb. XII, 501-547, 1964.

Maezawa, D., Dependence of geomagnetic activity on solar wind parameters: A statistical approach, Solar Terr. Environ. Res. Jpn. 2, 103, 1978.

Mayaud, P. N., A hundred year series of geomagnetic data 1886-1967, Indices aa, Storm sudden commencements, Bull. 33, Int Assoc. of Geomagn. and Aeron., 1973.

Mayaud, P. N., Analysis of storm sudden commencements for the years 1868-1967, J. Geophys. Res., 80, 111, 1975.

Munro, R. H., J. T. Gosling, E. Hildner, R. M. MacQueen, A. I. Poland, C. L. Ross, The association of coronal mass ejection transients with other forms of solar activity, Solar Phys., 61, 201, 1979.

Neugebauer, M. M., Observations of solar wind helium, Fundam. Cosmic Phys., 7, 131, 1981.

Neupert, W. M., and V. Pizzo, Solar coronal holes as sources of recurrent geomagnetic disturbances, J. Geophys. Res., 79, 3701, 1974.

Newton, H. W., Sudden commencements in the Greenwich magnetic records (1879-1944) and related sunspot data, Monthly Not. R. Astron. Soc. 5, 159-185, 1948.

Ohl, A. I., Physics of the 11-year variation of

magnetic disturbances, Geomagn., Aeronomy., 11, 549, 1971.

Olmstead, D., On the recent secular period of the aurora borealis, Smithson. Contrib. Knowl., 8, 1, 1856.

Perreault, P., and S. -I. Akasofu, A study of geomagnetic storms, Geophys. J. R. Astron. Soc., 54, 547, 1978.

Russell, C. T., On the possibility of deducing interplanetary and solar parameters from geomagnetic records, Solar Phys., 42, 259, 1975.

Sargent, H. H., A prediction for the next sunspot cycle, Paper presented at 28th IEEE Vehicular Technology Society, Denver, Colo., 1978.

Sargent, H. H., A 27-day geomagnetic recurrence index, 1868-1978, in Solar-Terr. Phys. and Meteor. Working Document III, World Data Center A, Boulder Colo., 1979.

Sheeley, N. R., Jr., and J. W. Harvey, Coronal holes, solar wind streams, and geomagnetic disturbances during 1977 and 1978, Solar Phys., 70, 237-247, 1981.

Simon, P. A., Polar coronal holes and solar cycles, Solar Phy., 63, 399, 1979.

Siscoe, G. L., Evidence in the auroral record for secular solar variability, Rev. Geophys. Space Phys., 18, 647, 1980.

Siscoe, G. L., N. U. Crooker, and L. Christopher, A solar cycle variation of the interplanetary magnetic field, Solar Phys., 18, 647, 1980.

Svalgaard, L., Geomagnetic activity: Dependence on solar wind parameters, in Coronal Holes and High Speed Wind Streams, edited by Jack B. Zirker, Colorado Associated University Press, Boulder, 1977.

A MODEL OF SOLAR FLUX ATTENUATION
DURING ECLIPSE PASSAGE AND ITS EFFECTS
ON PHOTOELECTRON EMISSION FROM SATELLITE SURFACES

H. B. GARRETT*

Jet Propulsion Laboratory (MC 144–218), California Institute of Technology, 4800 Oak Grove Drive,
Pasadena, CA 91109, U.S.A.

and

J. M. FORBES

Space Data Analysis Laboratory, Boston College, Chesnut Hill, MA 02167, U.S.A.

Abstract—The basic theory of solar flux attenuation by the Earth's atmosphere is reviewed and a model of the time-varying flux observed by a satellite during eclipse passage developed. The general model is applied to the specific problem of variations in photoelectron flux during penumbral passage and the effects of wavelength, solar activity, and atmospheric constituents on photoelectron emission investigated. Predictions of the photoelectron current expected from tungsten and aluminum surfaces are then successfully compared with actual observations from the ATS-5 and Injun 5 satellites confirming the validity of the model.

1. INTRODUCTION

Variations in solar flux and in photoelectron current from surfaces in space during penumbral passage are important issues in a number of space physics problems. They are of particular concern in the computation of satellite potential (Whipple, 1965; DeForest, 1972; Grard, 1973) as the potential between a satellite and the ambient plasma may rise as high as −20 kV in seconds during passage through the Earth's penumbra. Such potential variations and the associated photoelectron currents have been modeled in detail for penumbral passage by Garrett and DeForest (1979). In that paper, however, a wavelength-independent, empirical model of the attenuation of the solar flux was assumed. The intent of this paper is to develop a general model of the variations in solar flux observed by a body passing through the Earth's penumbra as a function of wavelength, atmospheric attenuation, and solar cycle (scattering and diffraction are ignored). This general model will then be tested by utilizing its predictions in the study of the specific problem of variations in photoelectron flux during penumbral passage.

In the first section of the paper the basic theory of solar attenuation and photoelectron flux de-

* Previous address: Space Physics Division, Air Force Geophysics Laboratory, Hanscom AFB, Bedford MA 01731, U.S.A.

veloped in Garrett (1978a) and Garrett and DeForest (1979) is reviewed. The model is modified to include the effects of variations with wavelength and then used to estimate the photoelectron current to be expected from two common satellite materials—aluminum and tungsten. The effects of wavelength response, atmospheric constituents, and solar cycle variations on the photoelectron yield from these materials are investigated. The paper concludes with a comparison between the predicted penumbral variations and actual measurements from the Injun 5 and ATS-5 satellites.

2. EQUATIONS AND GEOMETRICAL CONSIDERATIONS

The geometric relationships involved in determining the attenuation of solar flux reaching a satellite due to atmospheric absorption and partial obscuration of the solar disk by the Earth during eclipse passage have been derived by Garrett (1978a) and Garrett and DeForest (1979). The geometry of an eclipse as seen by a satellite is illustrated in Fig. 1. The problem of calculating the solar attenuation for this geometry is greatly simplified if the concept of X_m, the minimum ray path altitude, is introduced. As shown in Fig. 2, X_m is defined as the minimum distance from the Earth that a ray of light passes in going from the center of the Sun to the satellite. The problem of calculating the percentage of the solar disk that is obscured
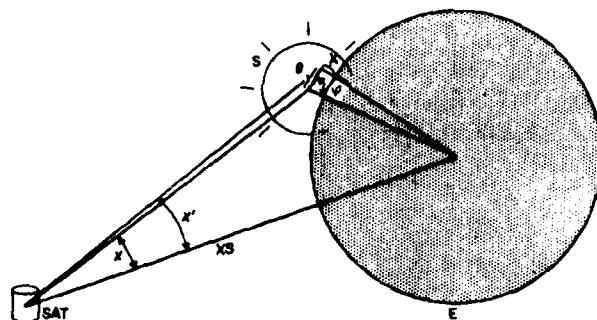
FIG. 1. GEOMETRIC REPRESENTATION OF THE OBSCURATIONS OF THE SOLAR DISK UPON ECLIPSE ENTRY.
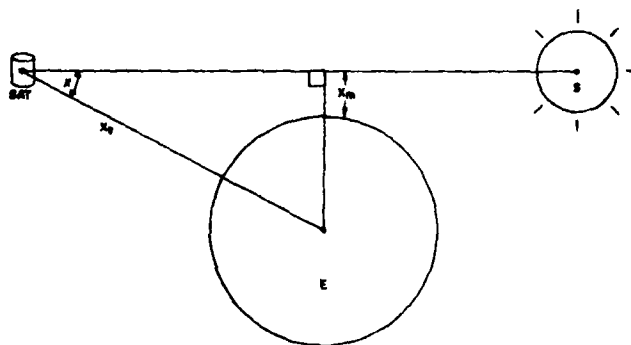The variables are defined in the text.

FIG. 2. ILLUSTRATION OF THE MEANING OF χ, THE ANGLE BETWEEN THE SUN (S) AND THE EARTH'S (E)
CENTER, X_s, THE DISTANCE FROM THE SATELLITE (SAT) TO THE CENTER OF THE EARTH, AND X_m, THE
MINIMUM RAY PATH ALTITUDE.

reduces to finding the atmospheric attenuation as a function of X_m rather than of the time or position in orbit which vary greatly for a given satellite. All observations will therefore be presented in terms of X_m.

Referring to Figs. 1 and 2 and modifying Garrett's (1978a) equations to include the dependence on wavelength, the total photoelectron flux at the satellite is given by*

$$J_\tau(X_m) = \int_0^{\alpha_\odot} d\theta \int_0^{2\pi} d\phi \int_{\lambda_1}^{\lambda_2} [F(\lambda, X(\theta, \phi))$$

$$p(\lambda) \sin \theta \cos \theta] d\lambda \quad (1)$$

---

* Note equation (1) includes a cos θ term for the angle of incidence of the sunlight originally neglected by Garrett (1978a) and Garrett and DeForest (1979).

where

$X = (XS \sin \chi') - R_e$ = minimum altitude above the Earth's surface of ray to arbitrary point on Sun (see Fig. 1);

XS = distance from satellite to center of Earth;

R_e = radius of Earth;

$\chi' = \cos^{-1} (\cos \theta \cos \chi + \sin \theta \sin \chi \cos \phi)$;

χ = angular separation between the center of the Sun and the Earth;

F = solar flux as a function of λ and X (photons per unit area per unit time per unit wavelength per steradian);

p = photoemission yield of metal surface (electrons/photon);

λ = wavelength;

θ, ϕ = see Fig. 1;

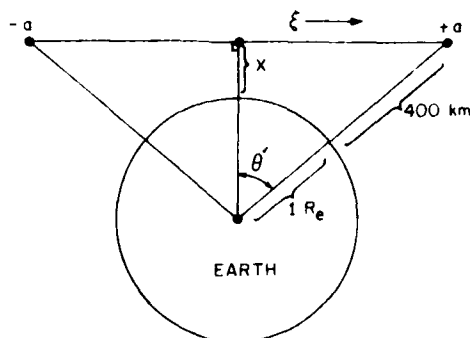$\alpha_\odot$ = angular radius of Sun.

FIG. 3. GEOMETRY FOR CALCULATION OF COLUMN DEN-
SITIES OF ABSORBING SPECIES

The attenuated solar flux F at wavelength λ and an altitude X is obtained by multiplying the unattenuated flux by the transmission coefficient $T(\lambda, X)$

$$F(\lambda, X) = F_\infty(\lambda) T(\lambda, X) \qquad (2)$$

where

$$T = \exp\left[-\sum_j \sigma_j(\lambda) N_j(X)\right];$$

$$N_j = \int_{-a}^{+a} n_j(\xi)\, d\xi;$$

n_j = number density of jth species;

σ_j = absorption cross-section of jth species at wavelength λ (H_2O, O, O_2, O_3, NO, and N_2 were considered);

ξ = ray path through atmosphere for a ray passing from the sun to the satellite at minimum altitude X (see Fig. 3). Therefore, $\xi = (R_e + Z)$ sin θ' and it is assumed that zero absorption occurs for $Z > 400$ km.

The unattenuated photoelectron flux (in electrons $cm^{-2} s^{-1}$ or $nA\ cm^{-2}$) is given by

$$J_T(\infty) = \pi \sin^2 \alpha_\odot \int_0^\infty F_\infty(\lambda) p(\lambda)\, d\lambda. \qquad (3)$$

A useful quantity for comparison purposes is

$$P(X_m) = \frac{J_T(X_m)}{J_T(\infty)}. \qquad (4)$$

3. MODEL ASSUMPTIONS

Four models are necessary for the computation of the photoelectron fluxes during penumbral pas-

sage. The first model is for the unattenuated solar flux. The second and third, for the atmospheric consituents and the corresponding cross-sections, account for atmospheric effects. The fourth, for the photoelectron emission as a function of wavelength, takes into account material properties. Each of these models is briefly described in the following.

The solar flux as a function of wavelength is plotted in Fig. 4. The flux is not constant but varies in time due to a number of factors, one of which is the solar cycle variability. Following Richmond (1972), the solar cycle variability of the fluxes is parameterized in terms of the 10.7 cm radio flux:

$$F_n = F_n^0 (F_{10.7}'/F_{10.7,n}^0)^{P_n} \qquad (5)$$

where

$F_{10.7}' = F_{10.7} - 0.0573(F_{10.7} - 143)$
$\qquad\qquad - 0.001273(F_{10.7} - 143)^2$;

F_n = flux for the nth band or line at $F_{10.7}$

F_n^0 = flux at reference solar activity level $F_{10.7,n}^0$;

P_n = a power derived from experimental data;

$F_{10.7}$ = 10.7 cm flux for desired conditions.

The atmospheric model is derived from several sources. The number densities of O, O_2, O_3, and N_2 below 100 km are from Strobel (1976). The values have been modified slightly within the 85–100 km height range to merge smoothly with the U.S. Standard Atmosphere (1976) above 100 km. The NO profile assumed is an average one based on data in Swider (1972). Absorption by N_2 and NO have little effect on the computation of satellite photoelectron fluxes but have been included for possible use in other environmental problems such as photoionization, atmospheric heating, or absorption by rocket effluents.

The O, O_2, O_3, and N_2 cross-sections adopted in this study have been obtained from compilations of various experimental data representative of average solar conditions. The absorption cross-sections for 2–1027 Å are from Richmond (1972), 1027–1260 Å from Keneshea and Huffman (1972), and 1260–7500 Å from Strobel (1976). For solar radiation absorption by the O_2 Schumann–Runge bands (1750–2050 Å), the parameterization used by Strobel (1976) for the cross-sections in each band i were adopted:

$$\sigma_{O_2} = \gamma_i + \delta_i N_{O_2}^{1/2} \qquad (6)$$

where γ_i, δ_i = constants for band i from Strobel (1976); NO cross-sections are from Banks and Kockarts (1973).
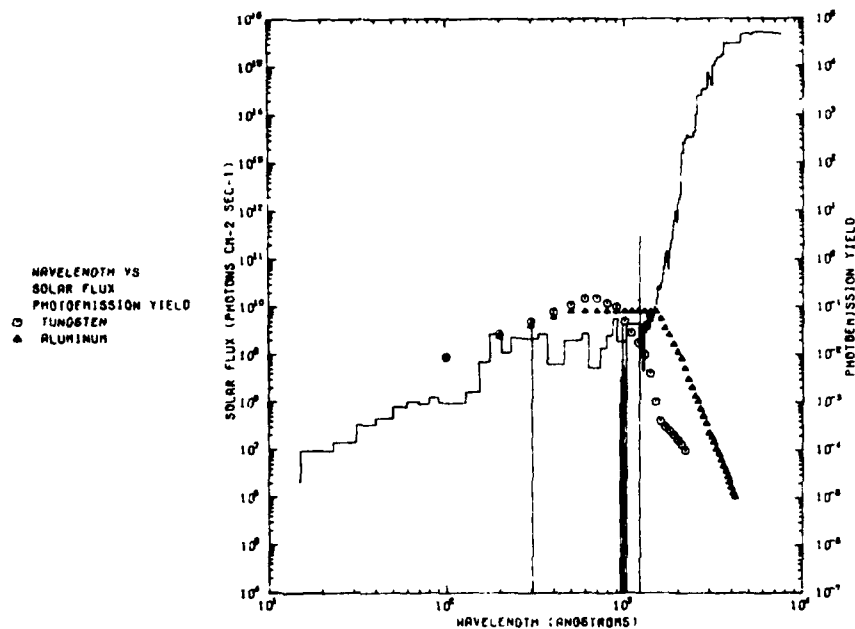
FIG. 4. SOLAR FLUXES CORRESPONDING TO $F_{10.7} = 150$, AND PHOTOEMISSION YIELDS OF ALUMINUM AND TUNGSTEN, AS FUNCTIONS OF WAVELENGTH.

Two materials, aluminum and dirty tungsten, were chosen as test cases. Their photoemission yields with wavelength (Whipple, 1965) are plotted in Fig. 4. The long wavelength cut-off for dirty tungsten is dependent on the state of the metal surface. According to Whipple (1965) this cut-off varies between 1900 Å and 2700 Å. As will be discussed, a value of 2300 Å was found empirically to give a "best fit" to the data.

4. RESULTS

Insight into the process of photoemission from a satellite surface is obtained by examing results from the present model as functions of surface material, wavelength, and atmospheric absorbing species. In Fig. 5 the percentage of unattenuated photoelectron flux, given by:

$$P(\lambda) = \frac{\int_{\lambda_1}^{\lambda} F_\infty(\lambda) p(\lambda) \, d\lambda}{\int_{\lambda_1}^{\infty} F_\infty(\lambda) p(\lambda) \, d\lambda} \tag{7}$$

is plotted as a function of wavelength for tungsten and aluminum assuming $F_{10.7} = 150$. Fifty per cent of the unattenuated photoelectron current is due to wavelengths less than 2000 Å for tungsten and 3000 Å for aluminum. Ninety per cent can be attributed to wavelengths less than 2300 Å and
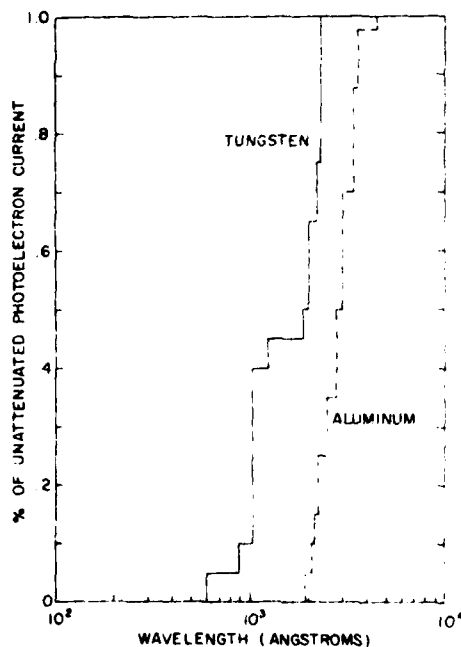

FIG. 5. PER CENT OF PHOTOELECTRON CURRENT FOR TUNGSTEN AND ALUMINUM, ASSUMING ABSORPTION BY O, O_2, O_3, AND N_2, AND AN $F_{10.7}$ VALUE OF 150.
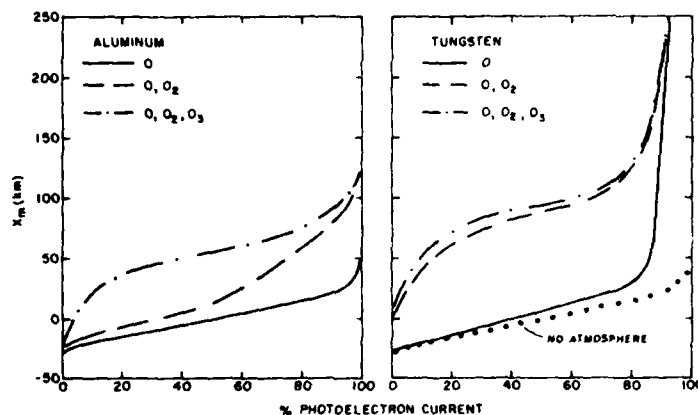
FIG. 6. PER CENT OF PHOTOELECTRON CURRENT VS X_m FOR ALUMINUM AND TUNGSTEN FOR DIFFERENT
COMBINATIONS OF ABSORBING SPECIES AND AN $F_{10.7}$ VALUE OF 150.

3600 Å, respectively. The saturation photoelectron currents corresponding to aluminum and tungsten ($\lambda_c = 2100$ Å) are 293 nA cm^{-2} and 1.67 nA cm^{-2} at solar minimum ($F_{10.7} = 50$), and 305 nA cm^{-2} and 2.28 nA cm^{-2} at solar maximum ($F_{10.7} = 250$). Thus photoemission from tungsten, due to its greater dependence on shorter wavelengths, is more variable than aluminum with solar activity (since most atmospheric absorption occurs below 150 km, solar cycle variations in composition have been neglected).

The differences in wavelength dependence of photoemission for the different materials suggest differences exist with regards to the relative importance of absorbing species. For example, O, O_2, and O_3 are strong absorbers in the e.u.v., u.v., and visible, respectively. Further, from the height dependences of these constituents, it would be expected that e.u.v., u.v., and visible radiations are absorbed at progressively lower heights in the atmosphere. This effect is illustrated in Fig. 6 (the satellite was at an altitude of ~2500 km) where it is demonstrated that O_3 absorption in the near-visible can be neglected for tungsten photoemission and that O absorption in the e.u.v. can be neglected for both tungsten and aluminum photoemission. Note also that the 50% and 90% levels of the saturation current are attained above 55 km and 85 km for aluminum, but are above 95 km and 225 km for tungsten.

S. COMPARISONS WITH EXPERIMENTAL DATA

Two different sources of experimental data were compared with the theoretical predictions of the

model. As both data sources were described in Garrett and DeForest (1979), only a short description will be given here. The first source is the Air Force Geophysics Laboratory spherical electrostatic analyser on the Injun 5 satellite. When the spherical tungsten collector of the ion detector was exposed to sunlight, the photoelectron flux was found to dominate the ambient ion flux. This allowed a direct determination of the percentage change in photoelectron current as the satellite passed into the Earth's shadow. The second source was the plasma and potential measurements from the University of California at San Diego (UCSD) electrostatic analysers on the ATS-5 satellite. As these measurements are much more involved than the Injun 5 measurements, they will be discussed below. Here it is important to note that the Injun 5 measurements allowed estimates of the photoelectron current from a known surface at an altitude of ~2500 km above the Earth's surface. The ATS-5 measurements allowed an estimate of the satellite potential (and hence photoelectron current) as a function of ambient conditions at geosynchronous orbit. The attenuation profiles are substantially different at these altitudes allowing a cross-check on the accuracy of the model.

In Fig. 7 the percentage of photoelectron current measured by the Injun 5 tungsten detector is compared with the model predictions for 5 cases: no atmosphere, aluminum as the surface material, and tungsten as the surface material with λ_c equal to 1900 Å, 2300 Å, and 2700 Å. Good agreement is attained for $\lambda_c = 2300$ Å and $F_{10.7} = 150$. The sensitivity of satellite photoemission yield to material properties in this height regime is evident in Fig. 7.
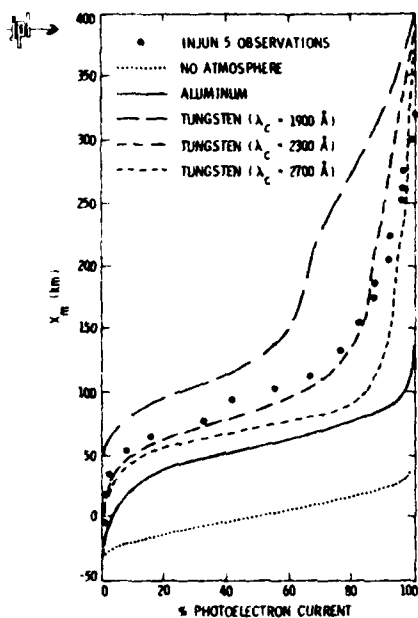
FIG. 7. THEORETICAL CALCULATIONS OF % OF PHOTO-
ELECTRON CURRENT VS X_m FOR MODELS ASSUMING TUNG-
STEN, ALUMINUM, AND "NO ATMOSPHERE" AND AN $F_{10.7}$
VALUE OF 150 COMPARED TO INJUN 5 OBSERVATIONS.

As outlined in DeForest (1972) and Garrett and
DeForest (1979), the ATS-5 UCSD plasma data
yield information on the ambient electron and ion
environments between 50 eV and 50 keV and on
the satellite potential. This latter information can
be used to estimate the photoelectron flux escaping
from the satellite (note: as a portion of the photo-
electron flux could be trapped in the sheath, this
flux estimate is actually a lower bound on the flux
leaving the surface). Briefly, a spacecraft charging
model (DeForest, 1972; Garrett, 1978b) is used to
estimate, from the ambient plasma measurements
and the satellite potential, the currents flowing to
the satellite. At equilibrium these currents must
balance to zero. The residual current necessary to
give a net current of 0 after accounting for all
ambient and ambient-induced fluxes is assumed to
be the escaping photoelectron current.

In Fig. 8 estimates of the residual (or photoelec-
tron) current density necessary to balance the am-
bient currents for 21 ATS-5 eclipse passages are
plotted as functions of X_m. These current densities
have been computed assuming a ratio of satellite
area to solar flux cross-section of 4.4 for ATS-5
(this ratio can vary between 4.4 and 7). As the
composite photoelectron emission characteristics of
the ATS-5 materials are not known, the saturation
current cannot be calculated exactly. The nor-
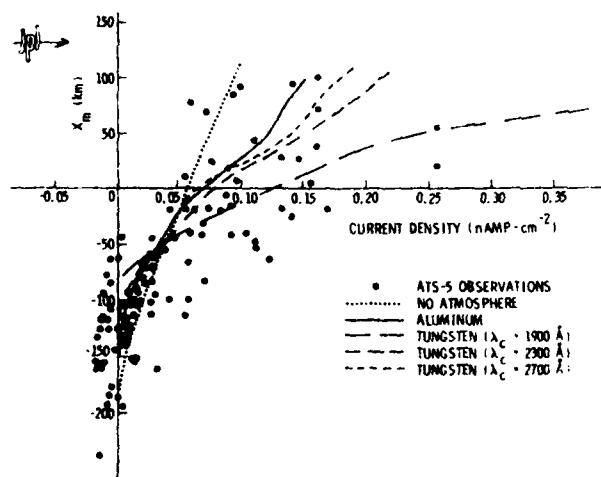malized profiles can, however, be used to estimate

FIG. 8. THEORETICAL CALCULATIONS OF PHOTOELECTRON CURRENT DENSITY VS X_m FOR MODELS ASSUM-
ING TUNGSTEN, ALUMINUM, AND "NO ATMOSPHERE" AND AN $F_{10.7}$ VALUE OF 150 COMPARED TO ESTIMATES
OF THE RESIDUAL CURRENT DENSITIES OBSERVED BY THE GEOSYNCHRONOUS ATS-5 SATELLITE DURING
PENUMBRAL PASSAGE

the shape of the attenuation profile and to approximate the range for the actual saturation current density corresponding to Fig. 8.

The geosynchronous attenuation profiles ($F_{10.7} = 150$) for the five cases of no atmosphere, tungsten ($\lambda = 1900$ Å, 2300 Å, and 2700 Å), and aluminum were normalized to yield a current density of 0.035 nA cm^{-2} at $X_m = -50$ km. These are plotted in Fig. 8 and, as shown, bracket the observations. The saturation currents corresponding to the normalized profiles are 1.4 nA cm^{-2} (tungsten, $\lambda_c = 1900$ Å), 0.43 nA cm^{-2} ($\lambda_c = 2300$ Å), 0.318 nA cm^{-2} ($\lambda_c = 2700$ Å), 0.233 nA cm^{-2} (aluminum), and 0.11 nA cm^{-2} (no atmosphere). For comparison, Grard (1973) has computed the saturation current density for a number of other satellite materials and found values between 0.4 nA cm^{-2} (graphite) and 4.2 nA cm^{-2} (aluminum oxide). Based on these values, the tungsten profiles, particularly for a λ_c between 1900 Å and 2300 Å, are more representative of the composite ATS-5 satellite photoelectron emission than the aluminum or no atmosphere profiles which predict values of the saturation current which are too low. This confirms the earlier result of Garrett and DeForest (1979) which found that the Injun 5 (tungsten) profile adequately fit the residual ATS-5 currents and gave a saturation current of 0.55 nA cm^{-2}. From our previous statements, this result implies that composite satellite surfaces are more sensitive to variations in the u.v. range and O_2 absorption.

6. CONCLUSION

The purpose of this paper has been to develop a general model of the variations in solar flux observed by a body passing through the Earth's penumbra. Such a model has been developed in terms of wavelength, atmospheric attenuation, and solar cycle. When applied to a specific material sample for which the photoemission properties were known (a tungsten surface on Injun 5), the model accurately fit the observations. The model similarly fit observations of the photoelectron flux during eclipse passage at geosynchronous orbit and allowed estimates of the corresponding saturation current. For the tungsten model, these agreed with typical satellite material saturation currents computed by Grard (1973).

To conclude, the model developed here allows a self-consistent computation of the photoelectron flux variations during penumbral passage provided the materials are known. The model is, however, sufficiently general that it can be adapted to a number of problems requiring information on atmospheric attenuation. Of particular interest are environmental problems such as photoionization, atmospheric heating, and absorption by rocket effluents. Finally, as the model has been independently calibrated with the Injun 5 and ATS-5 data, it provides useful confirmation of the models of solar attenuation and absorption employed in the study.

REFERENCES

Banks, P. M. and Kockarts, G. (1973). *Aeronomy*, Part A. Academic Press, New York.

DeForest, S. E. (1972). Spacecraft charging at synchronous orbit. *J. geophys. Res.* **77**, 651.

Garrett, H. B. (1978a). Effects of a time-varying photoelectron flux on spacecraft potential. AFGL-TR-78-0119.

Garrett, H. B. (1978b). Spacecraft potential calculations—a model. AFGL-TR-78-0116.

Garrett, H. B. and DeForest, S. E. (1979). Time-varying photoelectron flux effects on spacecraft potential at geosynchronous orbit. *J. geophys. Res.* **84**, 2083.

Grard, R. J. L. (1973). Properties of the satellite photoelectron sheath derived from photoemission laboratory measurements. *J. geophys. Res.* **78**, 2885.

Keneshea, T. J. and Huffman, R. E. (1972). Solar photoionization rate constants and ultraviolet intensities. AFCRL-72-0667.

Richmond, A. D. (1972). Numerical model of the equatorial electrojet. AFCRL-72-0668.

Strobel, D. F. (1976). Parameterization of the atmospheric heating rate from 15 to 120 km due to O_2 and O_3 absorption of solar radiation. NRL Memorandum Report 3398.

Swider, W. (1972). E-region model parameters. *J. atmos. terr. Phys.* **34**, 1615.

Whipple, E. C. (1965). The equilibrium potential of a body in the upper atmosphere. NASA X-615-65-296.

Effects of High-Latitude Conductivity on Observed Convection Electric Fields and Birkeland Currents

M. SMIDDY,[1] W. J. BURKE,[1,2] M. C. KELLEY,[3] N. A. SAFLEKOS[2]
M. S. GUSSENHOVEN,[2] D. A. HARDY,[1] AND F. J. RICH[4]

Relationships between convective electric fields, Birkeland currents, and ionospheric conductivity at high latitudes are investigated by using simultaneous measurements of electric and magnetic fields and electron fluxes from the S3-2 satellite. Cases in which the polar cap is in sunlight and darkness are studied to assess the importance of ionospheric conductivity. We find that when the ionospheric conductivity is high, as it normally is in the auroral zones and the sunlit polar cap, Birkeland current sheets exist that deflect the magnetic field approximately in the direction of the convection, typically antisunward in the polar caps and sunward in the auroral zones. Under winter conditions (a dark polar ionosphere), no large-scale antisunward deflection of magnetic field lines is found in the polar cap. Magnetic field deflections in the auroral zone are the result of the region 1/region 2 current systems discussed by Iijima and Potemra (1976). In the cases studied, region 1 currents are not observed to extend significantly poleward of the electric field reversal. We interpret this result as indicating the existence of strong conductivity gradients near the poleward boundary of the auroral oval, even in sunlight conditions. Deflections of magnetic field lines in the summer polar cap, first reported by McDiarmid et al. (1978), result from currents which serve to link the high-latitude generator to the polar ionospheric load. Two types of linkage appear in the data. (1) Region 1 currents are greater than region 2 currents, with the excess region 1 current flowing across the polar cap from dawn to dusk. (2) An extra set of field-aligned currents exist which are clearly detached from those of region 1 and are entirely poleward of the convective electric field reversal. We find that the evidence for antisunward convection on closed field lines threading the boundary layer, cited by McDiarmid et al. (1978), is inconclusive. With our more complete data set there is some evidence at ionospheric altitudes for a boundary layer, but in such cases there is only a modest (a few kilovolts) potential drop across the layer and there are insignificant Birkeland currents.

INTRODUCTION

The relationships between the high-latitude ionospheric boundaries of particle precipitation, field-aligned currents, and convective electric fields and their magnetospheric or extramagnetospheric source regions have been studied extensively over the last decade. Opinions in this regard are evolving and are not without disagreement in ways which directly reflect the growing detection capabilities of observers. At local times away from the dayside cusp, Frank and Ackerson [1971] identified two distinct types of precipitation: (1) highly structured inverted V events which frequently are associated with discrete auroral arcs and (2) relatively uniform precipitation which is associated with diffuse aurorae. It is generally accepted that the latter kind of precipitation originates in the central plasma sheet [Lui et al., 1977]. Because inverted V structures are frequently found poleward of the 45-keV trapping boundary, Frank [1971] speculated that inverted V electrons were directly accelerated along open field lines from the magnetosheath. However, a subsequent detailed analysis of the pitch angle distribution of these electrons showed that inverted V structures in the auroral oval occur on closed magnetic field lines [Venkatarangan et al., 1975].

In the auroral zone both large- and small-scale field-aligned current systems have been observed. Small-scale systems are

often associated with discrete auroral arcs [Anderson and Vondrak, 1975] and are characterized by quasi-equal, parallel sheets of current into and out of the ionosphere with latitudinal thicknesses of several tens of kilometers. Large-scale systems, which extend for several degrees of magnetic latitude, have been described by Iijima and Potemra [1976] in terms of 'region 1' and 'region 2' systems. Regions 1 and 2 are located in the poleward and equatorward portions of the field-aligned systems, respectively. In the evening and afternoon magnetic local time sectors, current flows into the ionosphere in region 2 and out in region 1. The currents flow in the opposite sense in the postmidnight and morning local time sectors. Simultaneous measurements from the Triad satellite and all-sky cameras indicate that in the evening sector, discrete arcs are embedded in region 1 and diffuse aurorae span region 2 [Armstrong et al., 1975; Kamide and Akasofu, 1976].

Near the dawn-dusk meridian the high-latitude electric fields E are configured to drive sunward convection in the auroral zone. In the polar cap, electric fields usually have a dawn to dusk orientation. Whether the resulting antisunward convection has a maximum near the dawn or dusk flank of the polar cap depends on the sign of the interplanetary magnetic field (IMF) component B [Heppner, 1972]. Gurnett and Frank [1973] have found that in the afternoon and evening sector, inverted V's occur close to the electric field reversal. They suggested that since the electric field reversal marks the boundary between sunward and antisunward convecting plasma at low altitudes, it also marks the boundary between open and closed magnetic field lines. Recently, Crooker [1979], expanding on an idea of Eastman et al. [1976], postulated the existence of a latitudinally narrow region of closed, antisunward convecting field lines that maps into the magnetospheric boundary layer, which has a thickness of ≤ 1 R_r. Crooker's work implies that

[1] Air Force Geophysics Laboratory, Hanscom Air Force Base, Massachusetts 01731.

[2] Physics Department, Boston College, Chestnut Hill, Massachusetts 02167.

[3] Cornell University, Ithaca, New York 14853.
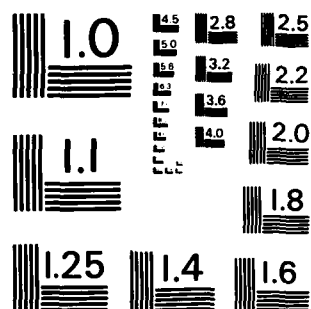
[4] Regis College, Weston, Massachusetts 02193.

6811

MICROCOPY RESOLUTION TEST CHART
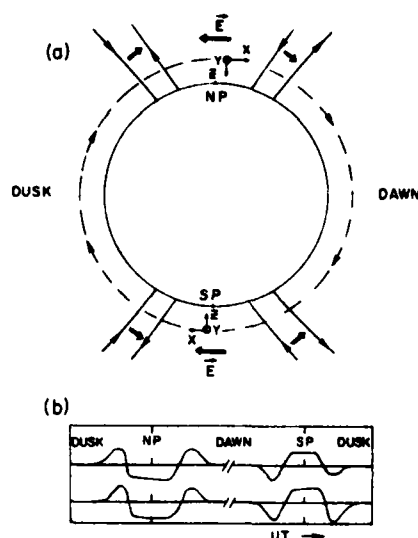
NATIONAL BUREAU OF STANDARDS–1963–A

Fig. 1. (a) Schematic representation of high-latitude electric fields in the ionosphere. The satellite-centered coordinate system is illustrated in the north and south polar regions. (b) Sketch of E_x and ΔB_y measurements for constant ionospheric conductivity.

the two working definitions of the polar cap, that is, the region bounded by the last closed field line and the region bounded by the line of electric field reversal, are not the same. In this paper we use the term 'polar cap' to mean the region poleward of the electric field reversal, leaving the question of open and closed magnetic field lines temporarily aside.

In order to sort out the interrelationships between flow patterns, particle fluxes, and field-aligned currents, simultaneous measurements of all three are necessary. To date, only a few examples of simultaneous satellite measurements of electric fields and Birkeland current systems have appeared in the literature [*Mozer et al.*, 1979; *Burke et al.*, 1980a; *Bythrow et al.*, 1980]. *McDiarmid et al.* [1978] have tried to circumvent this lack of data by using simultaneous measurements of only two quantities: the vector magnetic fields and fluxes of energetic electrons from Isis 2. Their procedure relies in part on establishing a magnetic field baseline for their sensor at low latitudes. East-west magnetic field components depart from the baseline in region 2 then return toward it in region 1. They found that often the deflection in region 1 overshoots the baseline and produces transpolar traces similar to electric field patterns seen by *Heppner* [1972]. The results were interpreted in terms of sunward and antisunward tilts of the magnetic field lines from the unperturbed positions. By invoking the concept of line tying, *McDiarmid et al.* [1978] argue that the tilting gives the direction of the electric field convection. On this basis they maintain that the point in region 1 where the magnetic field perturbation crosses the baseline marks the electric field reversal. Pitch angle distributions of electrons were then used to indicate whether field lines are open or closed. Inverted V structures found in region 1 poleward of the baseline crossing were interpreted as mapping into the magnetospheric boundary layer.

The purpose of this paper is to present measurements pertaining to the relationship between electric fields, field-aligned currents, and electron fluxes near ionospheric boundaries and to evaluate the hypothesis of *McDiarmid et al.* [1978]. Measurements were taken by an electric field dipole probe, a tri-

axial flux-gate magnetometer, and an electron spectrometer on the polar-orbiting satellite S3-2. Satellite orbital parameters, the scientific package, and the methods of data reduction are discussed in detail by *Burke et al.* [1980a]. Briefly, the satellite is spinning in a cartwheel mode with a nominal period of 20 s. The measurements were taken during the fall months of 1976 when the S3-2 orbit was near the dawn-dusk meridian. The electric field detector is a spinning dipole with a tip to tip length of 29.72 m. Data are presented as 5-s-averaged values of the meridional component of E. Magnetic field measurements were taken and are presented at a rate of 32 samples per second with a 1-bit resolution of 5 nT. Data are presented as the difference between the measured and the international geomagnetic reference field (IGRF) 1975 models of the spin axis component of B. Fluxes of electrons were measured in 32 energy channels between 80 eV and 17 keV with a full spectrum compiled every second.

In the following section we review briefly the assumptions and pertinent equations of the infinite current sheet model. Qualitative features expected in E and B measurements with different ionospheric conductivity distributions are described. Observations from four dawn-dusk polar passes of S3-2 are presented. Results are compared with those of *McDiarmid et al.* [1978] in the final section. We show that under summerlike ionospheric conditions, high-latitude electric and magnetic patterns have many similar features. This is not true in the winter polar cap. We present evidence from the electron spectrometer of having detected the eveningside, ionospheric projection of the magnetospheric boundary layer. The potential drop across this latitudinally narrow region is only a few kilovolts, and there are no significant Birkeland currents in the region.

THE INFINITE CURRENT SHEET APPROXIMATION

Before examining data from several S3-2 high-latitude passes we first consider some qualitative features expected in dawn-dusk measurements of E and B if the infinite current sheet approximation is valid. In the steady state the governing equations are the equations of current continuity

$$\nabla \cdot \mathbf{J} = 0 \qquad (1)$$

Maxwell's equation

$$\nabla \times \mathbf{B} = \mu_0 \mathbf{J} \qquad (2)$$

and Ohm's Law

$$\mathbf{J} = \sigma \cdot \mathbf{E} \qquad (3)$$

where $\mathbf{J}$, μ_0, and σ are the current density, the permittivity of free space, and the conductivity tensor, respectively.

We adopt a system of coordinates with its origin at the satellite center of mass (Figure 1a). X is positive along the satellite velocity, Z is positive in the downward direction, and Y completes the right-hand system. For dawn-dusk passes, Y is positive in the antisunward direction. In the infinite current sheet approximation it is assumed that no quantity has a Y dependence and that field-aligned currents close via ionospheric Pedersen currents. For dawn-dusk passes of S3-2, far from the dayside cusp and the Harang discontinuity the largest components of E are along our x axis, and the largest magnetic field deflections along the y axis.

Equations (1) and (3) can be combined to give

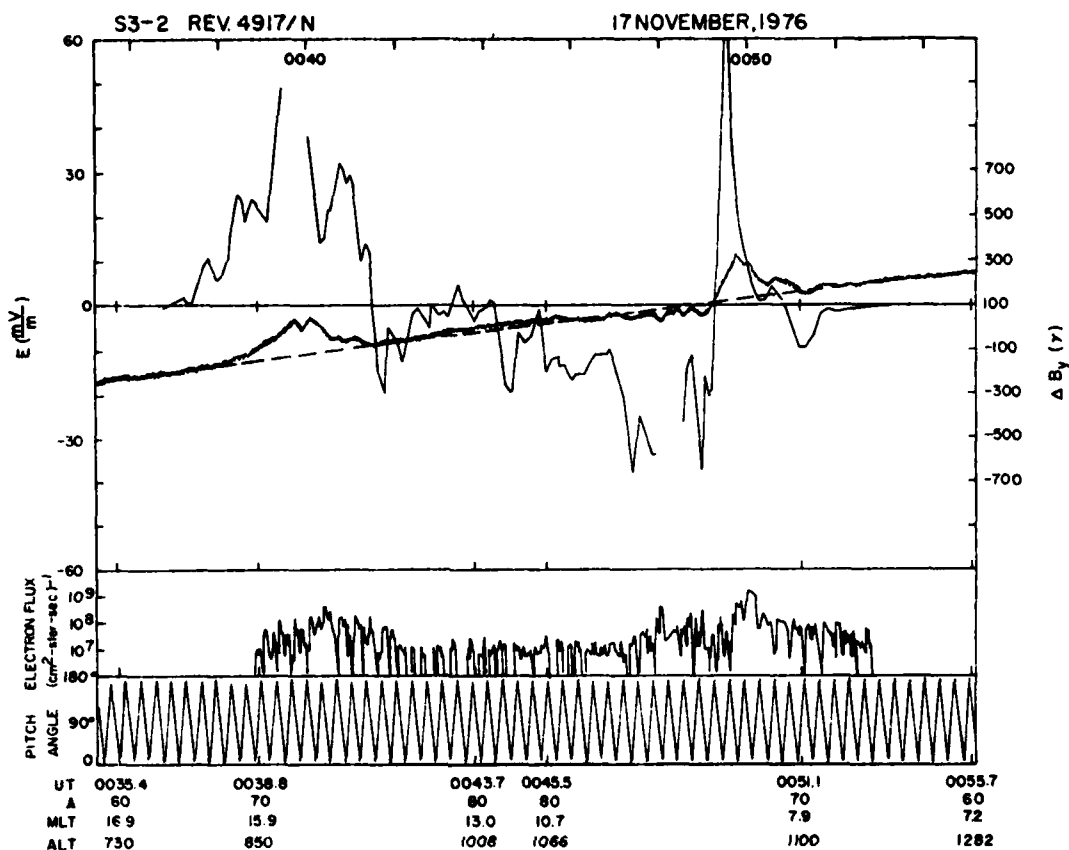$$\partial_z j_{\parallel} = -\partial_x(\sigma_p E_x) \qquad (4)$$

Fig. 2. S3-2 observations from north polar pass of orbit 4917 on November 17, 1976. The top panel gives the component of the electric field along the satellite trajectory and the cross-trajectory magnetic field component (heavy curve). The dashed line is a best guess unperturbed value for ΔB_Y determined from its low- and mid-latitude values. The directional flux of electrons with energies between 80 eV and 17 keV are given in the middle panel, and their pitch angles in the bottom panel. The data which are evenly spaced in UT are also presented as functions of invariant latitude, magnetic local time, and altitude. Tick marks along the top line are separated in UT by 2 min.

Integrating (4) from the satellite ($z = 0$) to the bottom of the ionosphere gives

$$j_{\parallel}(z) = \partial_x(\Sigma_P E_x) \tag{5}$$

where Σ_P is the height-integrated Pedersen conductivity. In our coordinate system, (2) can be written

$$\partial_x \Delta B_y = \mu_0 j_{\parallel}$$

or

$$\partial_x(\Delta B_y - \mu_0 \Sigma_P E_x) = 0 \tag{6}$$

In regions of constant ionospheric conductivity there should be a one-for-one correspondence between ΔB_y and E_x. Using the commonly employed units for ΔB_y (nanoteslas), E (millivolts per meter), and Σ_P (mhos), (6) becomes

$$\Delta B_y - 1.256 \Sigma_P E_x = \text{const} \tag{7}$$

We use the symbol ΔB_y to indicate that data are presented as the difference between measured values of the Y component of B and the corresponding curl-free IGRF model values.

Qualitative features of the E_x and ΔB_y measurements may be anticipated by considering the relationship between ΔB_y, Σ_P, and E_x in (7). Assume that the electric field is primarily

generated externally by a viscous interaction and/or by field line merging mechanisms. For simplicity, assume that the electric field is of constant magnitude and directed from dawn to dusk across the polar caps [Heppner, 1972, type A] and in the auroral ovals is directed from dusk to dawn with bell-shaped magnitude distributions. A schematic of a complete dawn-dusk orbit of S3-2 E_x measurements is given in Figure 1b. If it is assumed that the ionospheric conductivity has a uniform, nonzero value, then ΔB_y would have exactly the same shape as E_x (bottom trace of Figure 1b). This is the solution assumed by McDiarmid et al. [1978]. In this case, region 1 currents would indeed extend poleward of the E_x reversals. Region 1 currents are considered to extend over the entire region of continuous positive (negative) slope in ΔB_y on the poleward edge of the auroral zone in the dawn (dusk) sector.

Ionospheric conductivities are a complex superposition of contributions from ionization produced by solar illumination, charged particle precipitation, and plasma transport [Knudsen et al., 1977]. This implies that the relationship between E_x and ΔB_y will vary with season and the level of magnetic activity. Under summerlike conditions (i.e., illumination of the polar cap ionosphere below 200-km altitude) the polar ionosphere can easily support dawn to dusk Pedersen currents, but the winter ionosphere cannot. An equivalent expression would be
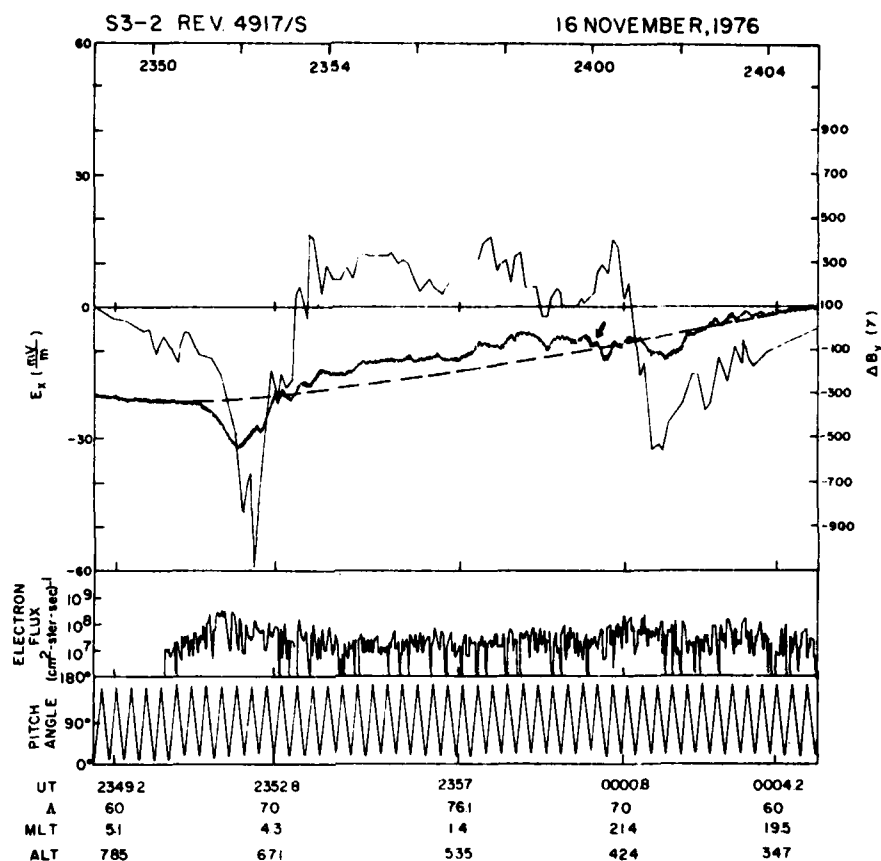
Fig. 3. S3-2 observations from the south polar pass of orbit 4917 on November 16, 1976, just prior to the data set of Figure 2. The data presentation format is the same as in Figure 2.

that convection in the polar cap demands less current under winter (darkened) than under summer (sunlit) conditions. Inverted V structures frequently have sharp boundaries, thus leading to severe latitudinal conductivity gradients even under summerlike conditions. Since inverted V structures are close to the electric field reversal, it is expected that the relationship between E_x and ΔB_y is much more complex than the simple relationship suggested in Figure 1b.

DATA PRESENTATION

In this section, measurements from four polar passes of S3-2 are presented. Data were chosen to be representative of winter (dark) and summer (sunlit) ionospheric conditions during which IMF $B_z \leqslant 0$. Under these IMF conditions, normal region 1/region 2 Birkeland currents are observed, and polar cap electric field patterns are similar to those reported by *Heppner* [1972]. During periods of a strongly northward IMF, much more complex structures are observed and are discussed elsewhere [*Burke et al.*, 1979; 1980b].

The data in Figures 2–5 are presented in a common format. In the top panel, E_x (light curve) and ΔB_y are plotted as functions of UT (equally spaced), invariant latitude Λ, magnetic local time, and altitude. Gaps separated by 512 s in the E_x data are from times when the electric field instrument was in a calibration sequence. Nearly horizontal dashed lines give baselines representing our 'best guess' as to what ΔB_y would

be in the absence of Birkeland currents. It is based on systematic variations in ΔB_y found at low to middle latitudes where no Birkeland currents are expected. From (6) it is seen that it is the slopes of ΔB_y and E_x that have physical significance. It is also recognized that our baseline method contains a certain level of subjectivity. However, because of the intriguing results derived by McDiarmid and co-workers using the tilting of field lines concept, which necessarily involves baselines, the baseline method is also used here for the sake of direct comparisons. The integral, directional flux of electrons with energies between 80 eV and 17 keV is given in the middle panel. Electron pitch angles are given in the bottom panel.

The data presented in Figure 2 come from a winter north polar pass early on November 17, 1976. The hourly averaged values of the solar magnetospheric Y and Z components of the IMF for 0000–0100 UT were 2.8 and 0.4 nT, respectively. The IMF had a southward component during the previous 2 hours. Ground magnetometers near local midnight indicate that the pass occurred during the growth phase of a weak (200 nT) substorm.

The evening sector electric field rose above zero at 0037 UT ($\Lambda = 65.1°$). Approximately 1 min later, ΔB_y and the electron flux rose above background levels. The region 2 current system extended to 0040 UT ($\Lambda = 73.4°$), the aproximate maximum in E_x, which is obscured by a calibration sequence. At 0041.4 UT ($\Lambda = 76.5°$) the direction of E_x reversed, indicating
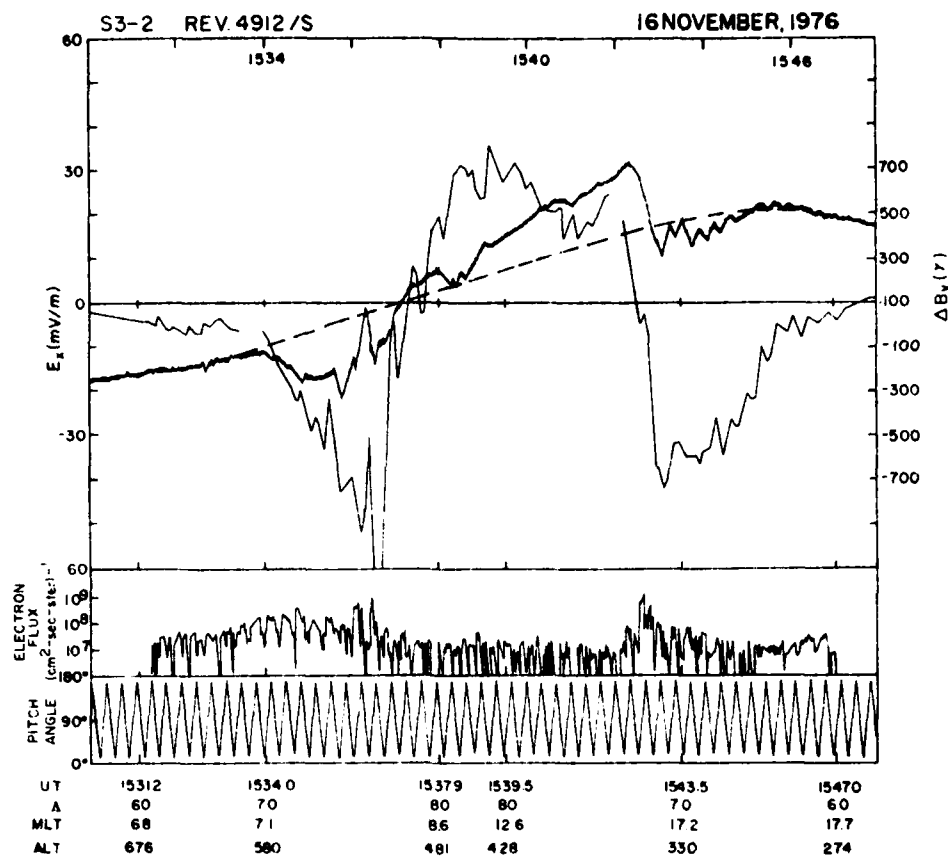
93

Fig. 4 S3-2 observations from another south polar pass on November 16, 1976. The data presentation format is the same as in Figure 2.

that the satellite had passed into either the ionospheric projection of the boundary layer or the region of open magnetic field lines. Simultaneously with the reversal in E_x, ΔB_y returned to its baseline value, and the electron flux softened. Between $\Lambda = 76.5°$ and $77.7°$ a modest flux of electrons with peak energies of ~200 eV and a trapped pitch angle distribution was detected. Equatorward of the reversal in E_x, electron fluxes were generally more intense, had peak energies of ≈1 keV, and were either field aligned or isotropic over the downcoming hemisphere. The potential drop across the latitudinally narrow flux of soft, trapped electrons poleward of the E_x reversal was ~2.5 kV. The total cross-polar cap potential drop was 42 kV. No discernable Birkeland currents can be seen in this region.

Particle fluxes and electric fields were weak and irregular in the central polar cap and then increased in intensity near the dawn flank of the polar cap. The latter observation is consistent with the IMF B_y effect reported by Heppner [1972]. Within the polar cap, ΔB_y remained close to its 'baseline' value until 0047.5 UT ($\Lambda = 77.6°$, MLT = 09.3). Between this time and the morningside reversal in E_x, ΔB_y departed from and returned to its baseline value several times. In each instance, electron count rates increased, suggesting that the ΔB_y fluctuations were due to currents associated with discrete arcs in the polar cap [Saflekos et al., 1978]. Nearly simultaneous imagery from a Defense Meteorological Satellite Program satellite indicates the presence of a series of sun-aligned arcs near the dawn flank of the polar cap. Because of the presence of at least some sort of discrete phenomena and the spin of the particle detector it is not possible to determine whether there is also a soft, trapped electron population just poleward of the morningside E_x reversal. We do note that the morningside region 1 field-aligned current appears to begin 10 s (0.5°) prior to the electric field reversal. In the morning auroral oval, E_x, ΔB_y, and the particle flux behave in an expected fashion, all three quantities falling to background values at $\Lambda = 68°$. Based on a survey of 10 passes over the winter polar cap the example given in Figure 2 is quite typical of winter situations.

The second example (Figure 3) comes from the southern hemisphere prior to the previously studied case. Despite IMF Y and Z components of 2.0 and −2.1 nT between 2300 and 2400 UT, ground-measured magnetic conditions at this time were quiet. The overall electric field pattern is closest to Heppner's type A. The region 1/region 2 auroral zone patterns of ΔB_y are again clear. Across the polar cap there is a systematic deflection of ΔB_y, with a signature which is reasonably similar to that of the electric field. The tilt of the field lines in the auroral zones is toward the sun and in the polar cap away from the sun. Note that in the vicinity of the electric field reversals on both the dawnside and the duskside, ΔB_y returned to and hovered near the baseline value for more than 1° invariant latitude. Two additional field-aligned current sheets are re-
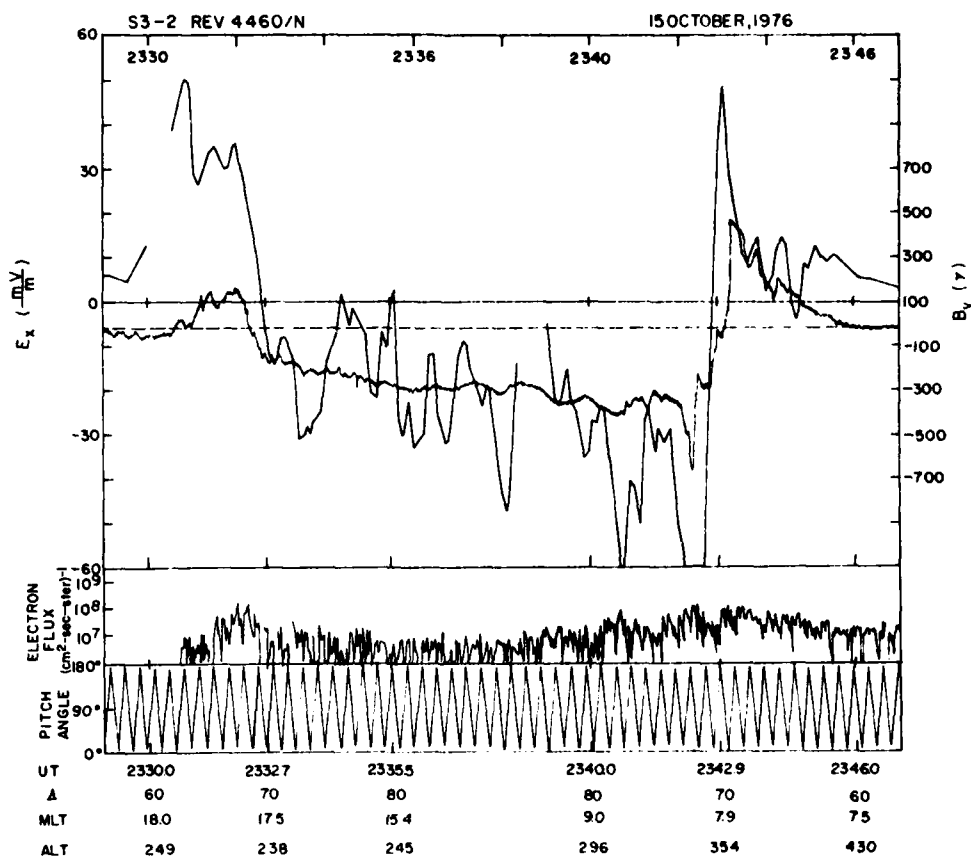
94

Fig. 5.   S3-2 observations from a north polar pass on October 15, 1976. The data presentation format is the same as in Figure 2.

quired to produce the positive deflection in ΔB_y found in the polar cap. The extra current sheet near the dawn flank is directed into the ionosphere, and the one at dusk away from the ionosphere. That is, they have the same sense as the respective region 1 systems in the auroral oval. The data published by *McDiarmid et al.* [1978] were from the summer hemisphere and thus correspond closely to those presented in Figure 3. Their conjecture that the electric field reversal corresponds to a point where the magnetic field deflection crosses the baseline fits the dawn data fairly well. The region of 'extra' current out of the ionosphere on the duskside of the polar cap (marked by an arrow in Figure 3), however, was encountered between 2359.9 and 0000.4 UT, a full half minute before the electric field reversal. In this region, ΔB_y was decreasing, while E_x was increasing. In the infinite current sheet approximation (equation (6)) this can only occur if Σ_p is sharply decreasing.

A second example from the southern hemisphere under summer conditions is given in Figure 4. The hourly averaged values of the B_y and B_z components of the IMF (1500–1600 UT) were 1.3 and -1.2 nT, respectively, and a moderate substorm ($\Delta H \simeq 200$ nT) was in progress. On both the dawnside and the duskside of the auroral oval the region 1/region 2 current systems show the irregularities which are nearly in phase with structures in E_x. In the polar cap both ΔB_y and E_x are structurally similar to Heppner's type A pattern. The ΔB_y trace shown in Figure 4 differs from that in Figure 3 in that

the extra currents are largely confined to the region equatorward of the E_x reversal.

Attention is directed to the particle fluxes observed near the duskside electric field reversal. Here sharp flux increases are observed in two steps. Prior to 1542.2 UT, fluxes had polar rain values of 5×10^6 $(cm^2 \ s \ sr)^{-1}$. Between 1542.2 and 1542.5 UT, the time of the electric field reversal, the flux had local maxima of 8 and 5×10^7 $(cm^2 \ s \ sr)^{-1}$ at pitch angles of 90° with a strong minimum at 180° (downcoming). This narrow region of trapped electrons is similar to that found in the north polar pass given in Figure 2. A weak extension of region 1 field-aligned currents is found in this narrow strip. Owing to the calibration sequence, it is not possible to calculate the potential drop across the layer. Equatorward of the E_x reversal the electron flux rose abruptly to a maximum of 10^9 $(cm^2 \ s \ sr)^{-1}$ at 1542.6 UT ($\Lambda = 73.1°$). An examination of individual spectra (not shown) indicates that this particle event had the structure of an inverted V. Although the inverted V structure is poleward of the place where ΔB_y crosses its baseline value, it is clearly equatorward of the electric field reversal.

Our final example (Figure 5) is a north polar pass that came at the end of the disturbed day ($\Sigma K_p = 34$), October 15, 1976. Although IMF data are not available for this day, ground magnetograms near local midnight showed that the pass occurred late in the expansion phase of a 600-nT substorm. In the polar cap, summerlike conditions prevailed. Along the

95

high-latitude trajectory of the satellite the ionosphere at altitudes of >100 km was in sunlight.

The electric field pattern in the polar cap is somewhat irregular but with the strongest convection along the dawn flank. The ΔB_y traces show well-defined region 1/region 2 structures in the dawnside and duskside of the auroral oval. In the polar cap, ΔB_y increased in magnitude from dusk to dawn, but with few of the large variations found in E_x. On both the duskside and the dawnside, ΔB_y crossed the baseline value well equatorward of the reversal in E_x. At the eveningside electric field reversal the electron flux decreases in intensity and in energy content. Just poleward of the reversal there is a 1.2°-wide region of soft (100 eV) electrons with a trapped pitch angle distribution. The potential drop across this region is 400 V out of a total cross-polar cap drop of 78 kV. The region 1 current system extends 0.5° (out of 1.2°) into this region. Poleward of this region, electron fluxes are erratic, often falling below the detection capacity of the instrument. On the dawnside of the polar cap the electron fluxes started to increase at ~2339 UT, reaching a maximum value of 10^8 (cm^2 s sr)$^{-1}$ at 2342.3 UT (Λ = 72.8°). This was coincident with a decrease in E_x to -79 mV/m and a 350-nT excursion in ΔB_y. It appears that the structure encountered by S3-2 at 2342.3 UT was a short-lived local current system possibly associated with a discrete polar cap arc rather than an extension of the region 1 current system into the polar cap. This interpretation is based on measurements from the magnetometer on S3-3, which passed over the same place 30 min after S3-2 (C. A. Cattell, private communication, 1979). The same large-scale current observed by S3-2 in the auroral oval was detected by S3-3. No large depression in ΔB was observed by S3-3 poleward of the electric field reversal. A change of 350 nT in ΔB, over ~1° is easily resolved by the S3-3 magnetometer. The poleward boundary of the region 1 current and the E_x reversal were detected simultaneously at 2342.8 UT.

DISCUSSION AND CONCLUSIONS

The electric field, magnetic field, and electron flux observations may be summarized as follows:

1. Under winter polar cap conditions the region 1/region 2 current systems are confined to the auroral oval. This implies that there are significant conductivity gradients at the poleward boundary of the oval. The fact that ΔB_y remains at or near its unperturbed value across the polar cap despite significant dawn to dusk electric fields implies that in the winter, polar cap conductivity is too low to support significant transpolar Pedersen currents.

2. Under summerlike polar cap conditions the region 1 currents exceed those of region 2. In these cases the polar cap conductivity is sufficient to support significant transpolar Pedersen currents. The region 1 currents are confined to latitudes equatorward of the E_x reversal. This indicates that there are strong Σ_p gradients at the poleward boundary of the auroral oval even under sunlit conditions. In one case (Figure 3) an extra set of currents is found significantly poleward of the electric field reversal.

3. In three out of the four cases presented here a latitudinally narrow region of soft, trapped electrons occurs just poleward of the electric field reversal on the duskside. Perhaps because of the presence of discrete structures, no similar region is found on the dawn flank of the polar cap.

These observations both support and limit conclusions arrived at by McDiarmid et al. [1978]. Data from the summer

hemisphere support their contention that sunward and antisunward tilts of magnetic field lines can and often do correspond to sunward and antisunward convection. However, owing to the importance of particle flux induced gradients in the conductivity, detailed conclusions about the direction of E_x cannot be drawn from ΔB_y signatures.

One of the most interesting conclusions arrived at by McDiarmid et al. [1978] concerned the origin of inverted V structures in the boundary layer. They presented a case in which an inverted V structure was found poleward of the position where ΔB_y crossed its baseline value, that is, in a region of closed magnetic field lines tilting in the antisunward direction. In Figure 4 we also presented an example of an inverted V structure found on field lines tilting in the antisunward direction. However, the electric field experiment clearly shows that the convective flow remains sunward.

This does not imply that boundary layer signatures do not exist at ionospheric altitudes. Although they are not definitive in this regard, we have presented three cases (Figures 2, 4, and 5) of significant fluxes of soft electrons with trapped pitch angle distributions. These extended ~1° poleward of the electric field reversal on the duskside and could be electrons of magnetosheath origin that entered the antisunward convecting boundary layer. The peak energies and pitch angle distributions are similar to those of low-latitude boundary layer electrons reported by Eastman and Hones [1979]. Clearly, much more work must be done to identify and assess the role of the boundary layer's ionospheric projection. We note that in the cases of possible boundary layer signatures, no significant field-aligned currents were found and the potential drop across the layers was quite small (<3 kV).

REFERENCES

Anderson, H. R., and R. R. Vondrak, Observations of Birkeland currents at auroral latitudes, Rev. Geophys. Space Phys., 13, 243, 1975.

Armstrong, J. C., S.-I. Akasofu, and G. Rostoker, A comparison of satellite observations of Birkeland currents with ground observations of visible aurora and ionospheric currents, J. Geophys. Res., 80, 575, 1975.

Burke, W. J., M. C. Kelley, R. C. Sagalyn, M. Smiddy, and S. T. Lai, Polar cap electric field structures with a northward interplanetary magnetic field, Geophys. Res. Lett., 6, 21, 1979.

Burke, W. J., D. A. Hardy, F. J. Rich, M. C. Kelley, M. Smiddy, B. Shuman, R. C. Sagalyn, R. P. Vancour, P. J. L. Widman, and S. T. Lai, Electrodynamic structure of the late evening sector of the auroral zone, J. Geophys. Res., 85, 1179, 1980a.

Burke, W. J., M. S. Gussenhoven, F. J. Rich, D. A. Hardy, M. Smiddy, and M. C. Kelley, Electrodynamic structures in the polar cap during a period of geomagnetic quieting, paper presented at Chapman Conference on High Latitude Electric Fields, AGU, Yosemite, Calif., Jan. 30 to Feb. 2, 1980b.

Bythrow, P. F., R. A. Heelis, W. B Hanson, and R. A. Power, Simultaneous observations of field-aligned currents and plasma drift velocities by Atmospheric Explorer C, J. Geophys. Res., 85, 151, 1980.

Crooker, N U., Antiparallel merging, the half-wave rectifier response of the magnetosphere, and convection, paper presented at Chapman Conference on Magnetospheric Boundary Layers, AGU, Alpbach, Austria, June 11-15, 1979.

Eastman, T. E., and E. W. Hones, Jr., Characteristics of the magnetospheric boundary layer and magnetopause layer as observed by Imp 6, J. Geophys. Res., 84, 2019, 1979.

Eastman, T. E., E. W. Hones, Jr., S. J. Bame, and J. R. Asbridge, The magnetospheric boundary layer: Site of plasma, momentum and

energy transfer from the magnetosheath into the magnetosphere, *Geophys. Res. Lett.*, *3*, 6856, 1976.

Frank, L. A., Comments on a proposed magnetospheric model, *J. Geophys. Res.*, *76*, 2512, 1971.

Frank, L. A., and K. L. Ackerson, Observations of charged particle precipitation into the auroral zone, *J. Geophys. Res.*, *76*, 3612, 1971.

Gurnett, D. A., and L. A. Frank, Observed relationship between electric fields and auroral particle precipitation, *J. Geophys. Res.*, *78*, 145, 1973.

Heppner, J. P., Polar cap electric field distributions related to their interplanetary field direction, *J. Geophys. Res.*, *77*, 4877, 1972.

Iijima, T., and T. A. Potemra, The amplitude distribution of field-aligned currents at northern high latitudes observed by Triad, *J. Geophys. Res.*, *81*, 2165, 1976.

Kamide, Y., and S.-I. Akasofu, The location of the field-aligned currents with respect to discrete auroral arcs, *J. Geophys. Res.*, *81*, 3999, 1976.

Knudsen, W. C., P. M. Banks, J. D. Winningham, and D. M. Klumpar, Numerical model of the convecting F_2 ionosphere at high latitudes, *J. Geophys. Res.*, *82*, 4784, 1977.

Lui, A. T. Y., D. Venkatesan, C. D. Anger, S.-I. Akasofu, W. J. Heik-
kila, J. D. Winningham, and J. R. Burrows, Simultaneous observations of particle precipitations and auroral emissions by the Isis 2 satellite in the 19–24 MLT sector, *J. Geophys. Res.*, *82*, 2210, 1977.

McDiarmid, I. B., J. R. Burrows, and M. D. Wilson, Comparison of magnetic field perturbations at high latitudes with charged particle and IMF measurements, *J. Geophys. Res.*, *83*, 681, 1978.

Mozer, F. S., C. A. Cattell, M. Temerin, R. B. Torbert, S. Von Glinski, M. Woldorff, and J. Wygant, The dc and ac electric field, plasma density, plasma temperature, and field-aligned current experiments on the S3-3 satellite, *J. Geophys. Res.*, *84*, 5875, 1979.

Saflekos, N. A., T. A. Potemra, and T. Iijima, Small-scale transverse magnetic disturbances in the polar regions observed by Triad, *J. Geophys. Res.*, *83*, 1493, 1978.

Venkatarangan, P., J. R. Burrows, and I. B. McDiarmid, On the angular distribution of electrons in 'inverted V' substructures, *J. Geophys. Res.*, *80*, 66, 1975.

Electric and Magnetic Field Characteristics
of Discrete Arcs in the Polar Cap

W. J. BURKE,[1] M. S. GUSSENHOVEN,[2] M. C. KELLEY,[3] D. A. HARDY,[1] AND F. J. RICH[1]

Simultaneous electric field, magnetic field, and electron flux measurements from three dawn-dusk passes of S3-2 were analyzed for signatures of sun-aligned arcs in the polar cap. Two of the passes were over the summer and one over the winter polar cap. In all three cases the IMF had a strong northward component During the pass over the winter polar cap the electric fields were highly irregular but tracked with nearly one-to-one correspondence to the transverse magnetic fluctuations. Upward Birkeland currents were embedded in regions of negative space charge. The carriers for the upward Birkeland currents were weakly field aligned fluxes of electrons with a temperature of a few hundred eV that had been accelerated through a potential drop of ~1 kV. The two summer polar cap passes differed from each other in their large-scale electric field patterns. In one pass the electric field was irregular with the upward Birkeland currents in negative space charge regions. In the other summer hemisphere pass, convection was sunward in the central polar cap. Small-scale Birkeland current systems, possibly signatures of arclike structures, were found in regions of both sunward and antisunward convection. In this pass, variations in the electric and magnetic field did not always show the strong correlations found in the other two cases, due to the effects of electrojet activity near the flanks of the polar cap. The measurements are found to be consistent with a 'static' model for the electrical coupling between the ionoshere and magnetosphere with the generator at the magnetopause.

INTRODUCTION

Information concerning the visual characteristics of polar cap arcs comes from ground-based [*Lassen and Danielsen,* 1978] aircraft [*Eather and Akasofu,* 1969] and satellite-borne [*Berkey et al.,* 1976, *Ismail et al.,* 1977; *Meng and Akasofu,* 1976; *Gussenhoven,* this issue] spectroscopic instrumentation. This information is supplemented by direct measurements of electrons bombarding the polar cap [*Hoffman and Evans,* 1968; *Winningham and Heikkila,* 1974; *Burch et al.,* 1979] occasionally accompanied by simultaneous measurements of visual emmisions [*Whalen et al.,* 1971; *Ismail et al.,* 1977; *Hardy et al.,* this issue]. From these observations it can be said that polar cap arcs tend to be sun aligned, appear most frequently during periods of magnetic quieting when the IMF has a northward component, and are twice as often found on the morning side as on the evening side of the polar cap [*Ismail et al.,* 1977; *Gussenhoven,* this issue]. Visible arcs in the polar cap are caused by precipitating electrons with average energies ≤2 keV [*Eather and Akasofu,* 1969]. *Weber and Buchau* [1981] have identified a class of subvisual arcs at F region altitudes which result from the structured precipitation of electrons with average energies of a few hundred eV. Direct [*Hoffman and Evans,* 1968] and indirect [*Eather and Akasofu,* 1969] evidence suggests that the primary electrons responsible for polar cap arcs are field aligned owing to field-aligned accelerations. However, electron fluxes over polar cap arcs that are nearly isotropic over the downcoming hemisphere have also been reported [*Burch,* 1968; *Whalen et al.,* 1971].

The development of physical models of polar cap arcs requires knowledge of the small-scale electric fields. Birkeland currents, and the precipitating particles in the polar cap. Transverse magnetic irregularities observed by Triad have been interpreted as signatures of Birkeland currents coupling polar cap arcs with magnetospheric or extramagnetospheric source regions [*Saflekos et al.,* 1978]. *Burch et al.* [1979] have reported simultaneous measurements of accelerated elecrons and shears in the ionospheric plasma drift velocity. Electric fields associated with these velocity shears were found to point toward the cores of the acceleration regions. Simultaneous measurements of small-scale electric fields and Birkeland currents associated with polar cap arcs have not been available to date. It is the purpose of this paper to present a set of electric field, magnetic field, and electron flux measurements taken by means of instrumentation on the U.S. Air Force satellite S3-2 over the polar caps during perids when the IMF had a northward component following a period of moderate magnetospheric activity. In the absence of simultaneous optical measurements, this assures us of maximum likelihood that the phenomena observed give the signatures of discrete polar cap arcs.

Burke et al. [1979] have previously reported on S3-2 large-scale electric field measurements taken at high latitudes during periods of northward IMF. The electric field component approximately in the dawn-dusk direction was studied during orbits which passed to invariant latitudes (Λ) greater than 80°. With IMF $B_z > 0.7$ nT, electric fields in the polar cap were always highly regular in the winter polar cap and occasionally irregular in the summer (sunlit) cap. More frequently under summer conditions, regions of antisunward convection (dawn to dusk E fields) were found near the flanks of the polar cap and regions of sunward convection (dusk to dawn E fields) in the auroral zones and in the central polar cap. The latter result is consistent with polar cap convection patterns deduced by *Maezawa* [1976] from ground magnetograms. Following Maezawa, *Burke et al.* [1979] interpreted the observations as indicating a four-cell high-latitude convection pattern. *Crooker* [1979] showed that the observations are also consistent with a three-cell pattern: two crescent-shaped cells driven by a viscous interaction of magnetosheath plasma within the closed field line portion of

[1] Air Force Geophysics Laboratory, Hanscom Air Force Base, Massachusetts 01731.
[2] Boston College, Chestnut Hill, Massachusetts 02167.
[3] Cornell University, Ithaca, New York 14850.

the magnetosphere and a single cell in the polar cap driven by magnetic merging on the poleward side of the dayside cusp. The side of the polar cap on which sunward and antisunward convection occurs is determined by the sign of the Y component of the IMF. Recently, *Lassen* [1979] noted similarities between the predicted convection patterns of this model and the distribution of polar cap arcs with IMF B_y. He suggested that polar cap arcs are the optical signatures of upward Birkeland currents associated with convection velocity shears derived from electric field reversals in the polar cap.

In the following section we review, briefly, the S3-2 scientific package and the satellite coordinate system in which observations are presented. The next section describes geomagnetic conditions at the time of interest, states explicitly our criteria for determining when the satellite was in the polar cap, and anticipates the kinds of variations we expect in the electric and magnetic fields in crossing polar cap arcs at nearly normal incidence. In the observations section, three dawn to dusk passes, from times near the December 1976 solstice when the IMF had a strong northward component, are studied in detail. The ionosphere was in darkness in one of the cases and was sunlit in the remaining two cases. Simultaneous electric and magnetic field deflections are compared in all three cases. In the winter hemisphere case, counting statistics alow a direct comparison of fluxes of precipitating electrons with electric and magnetic field measurements. The available evidence suggests that the primary electrons responsible for arcs have undergone a field-aligned acceleration. In most instances the upward Birkeland currents and the precipitating electrons are embedded in regions of negative space charge. Possible relationships between the observations and ionosphere/magnetosphere coupling and models for auroral arc formation are discussed in the final section.

INSTRUMENTATION

The S3-2 was launched into polar orbit during December 1975 with an intial apogee, perigee, and inclination of 1557 km, 240 km, and 96.3°, respectively. It is spin stabilized with a nominal spin period of 20 s and a spin axis that is nearly perpendicular to the orbital plane. The scientific package on S3-2 includes: (1) an electric field experiment consisting of two dipoles, (2) a triaxial flux gate magnetometer, and (3) an energetic electron spectrometer. These instruments and the methods used to reduce data are described in detail by *Burke et al.* [1980]. The coordinate system used in this paper, which is the same as that described in Figure 1 of *Smiddy et al.* [1980], has its origin at the center of mass of the satellite. X is positive in the direction of the satellite velocity; Z is positive in the radially downward direction, and Y completes the right-hand coordinate system. When the satellite trajectory is in the dawn-dusk meridian, Y is positive in the antisunward direction. One of the dipoles has a length of 29.72 m. It lies in the satellite's spin plane and measures the electric field component along the satellite's trajectory (E_x). The second dipole has a length of 11.18 m and lies close to the satellite's spin axis. Because the spin-axis-aligned dipole frequently has an unknown dc offset potential, only the spin plane data are used in this study. Potential differences between the ends of the dipoles are sampled 32 times per second. Data are usually presented (Figures 1, 8, and 9) at 5-s intervals representing 20-s (one full satellite spin) running,

least squares average values of E_x. Each point is assigned to the midpoint of the appropriate 20-s interval. To resolve small-scale structures such as polar cap arcs, all of the dipole measurements are used to infer values of E_x with a 1-s resolution.

The magnetic field was measured at a rate of 32 samples per second, with a one-bit resolution of 5 nT. Data are presented as differences between the measured and IGRF 75 model of the spin axis component (ΔB_y). The spin plane components of the magnetic field are available for reference but are not presented explicitly.

The electron spectrometer measures electrons with energies between 80 eV and 17 keV in 32 energy channels with a full spectrum compiled every second. The aperture of the instrument is mounted in the spin plane of the satellite. Because of the small geometric factor of the instrument (4.68 $\times$ 10^{-5} cm^2 sr) count rates in the polar cap are frequently at or below the one count per accumulation period (1/32 s). Results from the electron spectrometer are to be taken as semiqualitative rather than as exact, quantitative indicators of particle flux levels. For the reader's benefit, distribution function and directional, differential flux measurements are referenced to the one count per sample interval level. In the cases studied here the measurements are of sufficient clarity to bear comparison with and interpretation in the light of standard results from the ISIS [*Winningham and Heikkila*, 1974], AE-D [*Burch et al.*, 1979], and DMSP [*Hardy et al.*, this issue] satellites.

BACKGROUND, CRITERIA, AND EXPECTATIONS

Before examining the S3-2 measurements it is useful to digress briefly to discuss: (1) the background conditions at the time of the observations, (2) our criteria for determining when S3-2 was in the polar cap, and (3) our general expectations for relationships between measured quantities.

To study the characteristics of polar cap arcs, three high-latitude passes of S3-2 close to the dawn-dusk magnetic meridian were selected for analysis. The passes, one over the northern (rev. 5231N) and two over the southern (revs 5215S and 5231S) polar caps, occurred on December 7 and 8, 1976, during period of northward IMF. We have examined DMSP records and found that no visible imagery is available at the time of the winter polar cap pass. Auroral forms cannot be detected by the DMSP optical scanner under sunlit conditions. Based on the work of previous investigators, but lacking visible imagery, we believe that the IMF and orbital characteristics are optimal for encountering sun-aligned arcs in the polar cap.

The E_x measurements of December 7-8, 1976, have been discussed previously by *Burke et al.* [1979] and are illustrative of the types of large-scale electric field patterns found in the polar cap during periods of a northward IMF. Hourly averages of IMF conditions on December 7 and 8, 1976, show that at the time of rev 5231 (5215), B_x = −3.7 (3.6) nT, B_y = 3.8 (−2.8) nT and B_z = 7.4 (4.1) nT. During both rev 5231 and rev 5215 the solar wind speed was moderate (439 and 411 km/s) and the density high (10.1 and 28.4 cm^{-3}) [*King*, 1979]. December 8 was a disturbed day on which ΣKp = 26−. Rev 5231 occurred toward the end of the active period with Kp = 1. December 7 was less active throughout; Kp = 2+ for the time of rev 5215.

In order to study the characteristics of polar cap arcs it is first necessary to designate the polar cap boundaries. By the

99

term polar cap we refer to the region of open magnetic field lines at ionospheric altitudes. Recently, *Meng* [1981] has cautioned that many sun-aligned arcs, at extremely high latitudes, lie in a polewardly contracted auroral oval rather than in the polar cap. *Heelis et al.* [1980] suggest that a satellite can be known to be in the polar cap if its position is poleward of both the convection reversal and the low-latitude boundary of polar rain precipitation [*Winningham and Heikkila*, 1974]. This double condition recognizes that the ionospheric projection of the magnetospheric boundary layer (closed field lines) convects in the antisunward direction. *Smiddy et al.* [1980] have shown that near the dawn-dusk meridian both criteria are easily applied when the IMF has a southward component but not so when it has a northward component. Under northward IMF conditions the convective electric field is frequently irregular, undergoing multiple reversals across the auroral oval and polar cap. In two of the three passes studied here (revs 5231N and 5231S) the large-scale electric field is too irregular to designate the auroral boundary convection reversal. For this reason we define a structure in the high-latitude ionosphere to lie in the polar cap if it is embedded in a region of polar rain.

Discrete arcs in both the auroral oval and the polar cap result from the structured precipitation of relatively energetic electrons. This leads us to expect that polar cap arcs, just as auroral oval arcs [*Vondrak*, 1975] are electrically coupled to the magnetosphere by means of extended, field-aligned current sheets. The incoming electrons responsible for visible emissions carry a current that is directed out of the ionosphere. The so-called return current, probably carried by upward drifting, cold electrons, should lie outside of the arc. In crossing a quasi-infinite current sheet at normal incidence the Maxwell and current continuity equations reduce to the form

$$\frac{\partial}{\partial x} \{\Delta B_v - \mu_0 \Sigma_P E_x\} = 0 \qquad (1)$$

where μ_0 is the permittivity of free space and Σ_P is the height-integrated Pedersen conductivity of the ionosphere. In regions of uniform conductivity, ΔB_y and E_x should vary in the same way across quasi-infinite current sheets. Calculations by *Wallis and Budzinski* [1981] indicate that background conductivities should be ~0.1 mho in the winter (darkened) and ~5 mho in the summer (sunlit) polar cap.

Enhanced precipitation produces conductivity gradients in the vicinity of polar cap arcs. Because the responsible electrons have average energies of ~1 keV, they produce most of their ionization at altitudes ≥140 km [*Rees*, 1963]. We thus expect a greater enhancement of Σ_P rather than Σ_H (Hall conductivity) in polar cap arcs. This is consistent with empirical formulas which relate the enhancement of Σ_P and Σ_H above background to the characteristics of precipitating electrons

$$\Delta \Sigma_P(\text{mho}) = 5.2[\text{energy flux}] \qquad (2)$$

and

$$\Delta \Sigma_H(\text{mho}) = 0.55[\text{average flux}] \, \Delta \Sigma_P \qquad (3)$$

where the electron energy flux is in ergs/cm² s and the average energy is in keV [*Harel et al.*, 1981]. It is obvious too that the most severe conductivity gradients should be found near arcs in the winter polar cap. Along conductivity

gradients the relationships between ΔB_y and E_x can become rather complex. If the satellite crosses a field-aligned current sheet at an angle other than 90°, (1) is approximately valid but leads to underestimates of the field-aligned current density. Deflections also appear in the spin plane component that is normal to the main magnetic field.

It should be noted that not all deflections in the magnetic field are attributable to the satellite passing through quasi-infinite current sheets. Field-aligned currents of finite length as well as ionospheric Hall currents can produce deflections. *Langel* [1975] has shown that Hall currents flowing near the flanks of the summer polar cap produce measurable magnetic signatures at altitudes below 600 km.

OBSERVATIONS

In Figure 1. E_x, ΔB_y, the directional flux of electrons (cm² s sr)⁻¹ and electron pitch angles measured during S3-2 rev 5231N are plotted as functions of universal time (UT), invariant latitude (Λ), magnetic local time (MLT), and altitude. At this time the satellite was near apogee over the northern polar cap and on rev 5321N passed within 1° of the magnetic pole along the MLT dawn-dusk meridian. Average values of E_x at 5-s intervals are represented by a fine, solid line in the top panel of the figure. Data interruptions marked by the letter C indicate periods when the electric field experiment went through a calibration sequence. Positive values of E_x in the northern hemisphere correspond to a dusk to dawn (sunward convection) component of the electric field. The values of all ΔB_y measurements are also given in the top panel and appear as a thick line. The thickness of the line corresponds to a 5-nT (1 bit) uncertainty in the measurements. In regions where the slope of the ΔB_y curve is negative corresponding field-aligned currents are directed out of the ionosphere. Eight narrow regions of current out of the ionosphere marked in the Figure 1 are discussed in detail below.

As mentioned above, during periods of northward IMF, large-scale variations in E_x and ΔB_y are poor indicators of the auroral oval boundary. In the case of orbit 5231N, clear signatures of the region 1/region 2 current system defined by *Iijima and Potemra* [1976] are absent. We note that on the evening side there are reversals of E_x at 1956:06 UT ($\Lambda = 76°$) and at 1957:48 UT ($\Lambda = 82°$). Both reversals (events 1 and 2) are associated with currents out of the ionosphere and locally enhanced fluxes of electrons. Event 2 appears to mark a transition in both E_x and the electron flux. Equatorward of event 2 electron fluxes vary between 5×10^7 and 3×10^8 (cm² s sr)⁻¹ and are fairly isotropic over the downcoming hemisphere. Poleward of the event, the electron flux decreases abruptly to values near the lowest sensitivity of the detector, a level typical of the polar rain [*Winningham and Heikkila*, 1974]. On the morning side the last observations of polar rain fluxes are at 2003:30 UT ($\Lambda = 81.6°$). Based on the occurrence of polar rain we conservatively set the evening and morning side boundaries of the polar cap at 82° and 81.6°, respectively. On this basis, events 3 through 7, which are marked by enhanced electron fluxes and currents out of the ionosphere, lie entirely within the polar cap. The 5-s-averaged values of E_x show that all of the events, with the possible exceptions of events 3 and 6, lie in regions of negative slope in E_x. We now consider some of these events on expanded time scales.
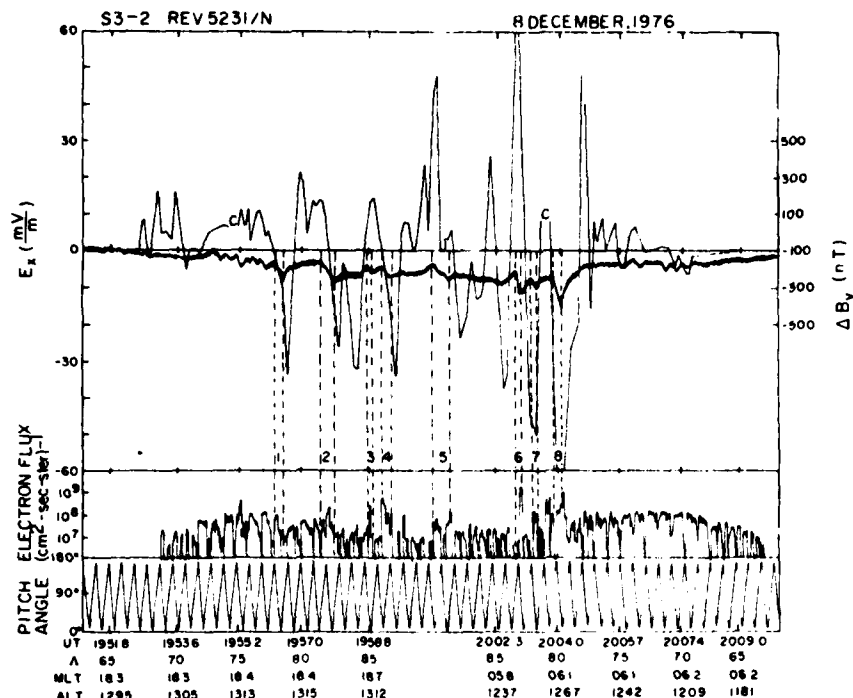
Fig. 1. Electric field, magnetic field components, the directional electron flux, and pitch angle as functions of UT, invariant latitude, magnetic local time, and altitude from S3-2 rev 5231N. Eight events marked by field-aligned currents out of the ionosphere are denoted by dashed lines. At the time of this pass the hourly averaged values of the IMF X, Y, and Z solar magnetospheric components were -3.7, 4.4, and 7.1 nT, respectively.

In Figures 2a and 2b we have plotted the potential measured between the ends of the spinning dipole between 1958:00 and 2000:30 UT (events 3 and 4) and between 2002:30 and 2005:00 UT (events 6, 7, and 8), respectively. Transverse magnetic field deflections, the electron flux, and electron pitch angle are provided for reference. Measurements from the electric field experiment have had potential difference induced by satellite motion across magnetic field lines and a constant dc bias removed. The dashed sine wave is a reference that gives the phase and amplitude of the signal that would be measured in the presence of a constant electric field of 12 mV/m that is directed from dusk to dawn and has no component along **B**. Thus when the reference and measured signals are in phase (180° out of phase), the ambient electric field has a dusk to dawn (dawn to dusk) component. The positive and negative signs at the top of the figure designate periods when the measured and reference signals are in and out of phase, respectively. We note that, despite rapid variations in the ambient electric fields, the measured and reference signals pass through zero at the same times. This indicates that there is no measurable electric field component along **B** at these times. It is possible, however, that components of **E** along **B** exist during periods away from nodal points of the reference signal.

An examination of small-scale variations in E_x in Figure 2 reveals that all of the events, including 3 and 6, lie in regions of negative slope in E_x. Twelve seconds prior to the beginning of event 3 the measured signal changes from out of phase to in phase with the reference signal. During event 3 the potential measured along the dipole decreases to zero,

then returns to a value in phase with the reference signal. Similarly, we note in Figure 2b that at the time of event 6 the measured value changed at 2002:51 UT from a high value in phase with the reference signal to a small value out of phase; i.e., event 6 is also in a region of decreasing E_x. These decreases are not seen in Figure 1 owing to the decreases ocurring on time scales significantly shorter than the 20-s interval used for the running average. Plots of 1-s average value of E_x based on the potentials measured near the times of events 3, 4, 6, and 7 (Figures 3a, 3b) clearly show that with the exception of a small deviation at the edge of event 6 (2002:58 UT) the regions of upward Birkeland currents and enhanced electron fluxes are also regions of decreasing E_x.

Sequences of electron spectra for events 3, 4, and 6 are given in Figures 4, 5, and 6, respectively. Dashed lines indicate the flux in electrons/cm^2 s sr keV that corresponds to the 1 count per sampling interval sensitivity of the detector. At the time of event 3 the integral flux increased abruptly from background to 3×10^8 (cm^2 s sr)$^{-1}$ for 2 s then returned to background. The peak directional differential flux was between 1 and 2×10^9 (cm^2 s sr keV) and appeared in <1-keV energy channels.

Since optical observations show that polar cap arcs are much longer than they are wide, it seems clear that regions of negative $\delta E_x/\delta x$ are also regions of negative space charge. If we assume that most of the electric and magnetic field variations occur along the satellite trajectory, then we can use the infinite sheet approximation to Maxwell's equations to calculate the excess space charge density (ρ) and the field-aligned current density j_{ll}. We use the spacecraft velocity of
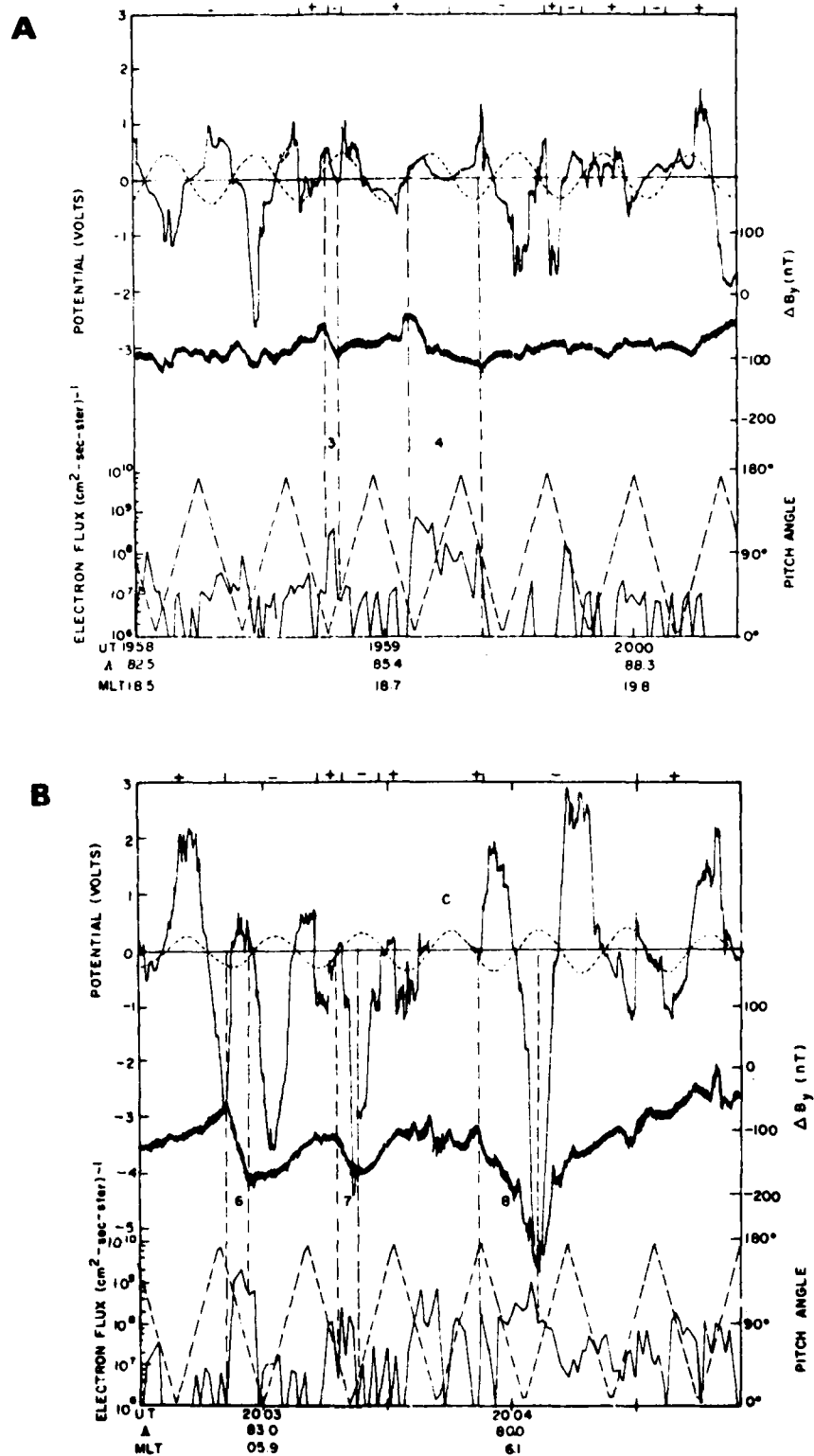
Fig. 2. Potential measured by spinning dipole (solid line) and the potential that would be measured in the presence of a constant field of 12 mV/m directed from dusk to dawn: (a) from period near events 3 and 4 and (b) from periods of events 6, 7, and 8.
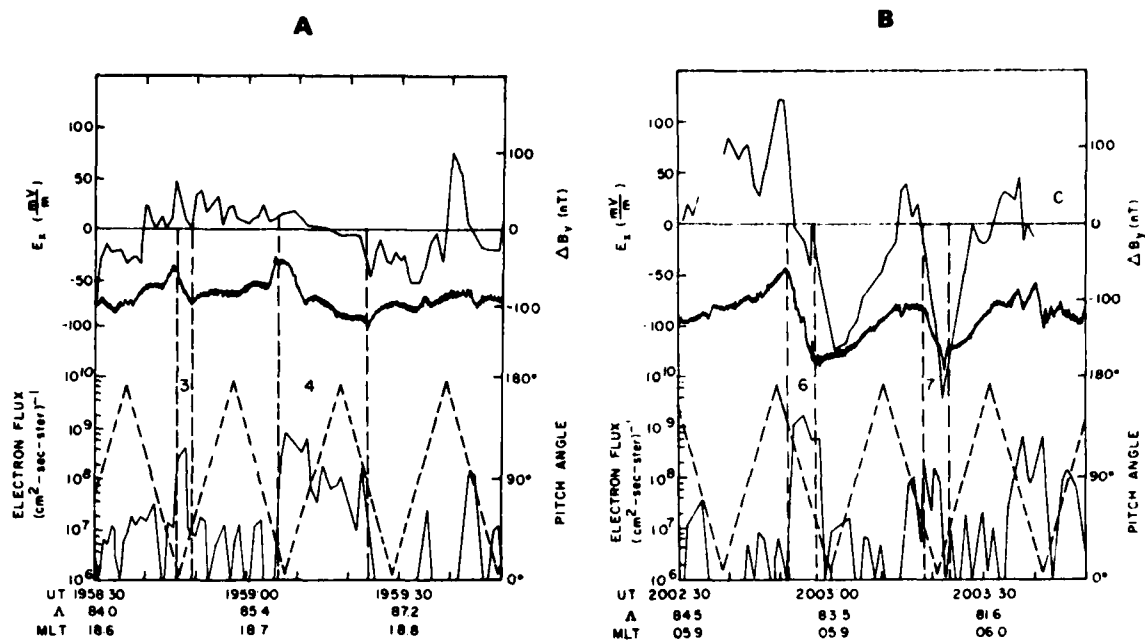
A   **B**

Fig. 3. One-second average of E_x deduced from potential measurements in Figure 2: (a) from period of events 3 and 4 and (b) from period of events 6 and 7.

7 km/s to transform into the satellite's frame of reference and express ρ in elementary charge units $(1.6 \times 10^{-19} \text{ C})$ per cm³:

$$\rho(\text{charges/cm}^3) \approx 7.9 \times 10^{-6} \frac{\partial E_x(\text{mV/m})}{\partial t(\text{s})} \quad (4)$$

and

$$j_{\parallel}(\mu\text{A/m}^2) \approx 0.113 \frac{\partial \Delta B_y(\text{nT})}{\partial t(\text{s})} \quad (5)$$

Note that if the satellite crosses charge/current sheets at angles other than 90°, (4) and (5) only provide lower-bound estimates of ρ and $j_{\parallel}$.

Between 1958:46 and 1958:49 UT, E_x and ΔB_y decreased by 50 mV/m and 47 nT, respectively. From (4) we calculate the net charge density in event 3 to be 1.3×10^{-4} el/cm³. A thermal electron probe on S3-2 [Burke, 1981] indicates that at the satellite the thermal plasma density ranged between 0.3 and 3.0×10^3 el/cm³ across the polar cap. The excess

Fig. 4. Directional, differential flux measurements during event 3. The UT and pitch angle ±9° of the electron flux. The dotted line indicates the flux from one count per accumulation period.

charge is thus about 1 part in 3 to 30 million. The current density calculated from (2) is 1.8 μA/m². This current density corresponds to an electron flux of $\sim 10^9$(cm² s)⁻¹. For this to be consistent with a measured directional flux of 3 $\times 10^8$ (cm² s sr) the electrons associated with event 3 must be nearly isotropic in their distribution over the downcoming hemisphere. Note that both the spectra were taken while the detector was looking close to the magnetic field direction. The energy flux associated with event 3 is a few tenths of an erg/cm² s sr and is probably insufficient for producing a visible, discrete arc.

During event 4, ΔB_y decreased uniformly by 50 nT between 1959:07 and 1959:09 UT. Such a decrease corresponds to a current density of 2.8 μA/m² and is consistent with the measured uniform flux of 4×10^8 (cm² s sr)⁻¹ if the electron flux is weakly field aligned. The electrons in the event have the characteristics of an inverted-V structure [Frank and Ackerson, 1971]. The peak flux appeared in the 2-keV channel at 1959:09 and in lesser energy channels at earlier and later times. A maximum directional differential flux of 10^9 (cm² s sr keV)⁻¹ was measured in the 1-keV channel when the detector was looking closest to **B**.

Between 2002:52 and 2002:57 UT (event 6), E_x and ΔB_y decreased by 160 mV/m and 127 nT indicating that $\rho = 2.5 \times 10^{-4}$ charge/cm³ and $j_{\parallel} = 2.8$ μA/m². The latter value is consistent with a measured electron flux of 1.2×10^9 (cm² s sr)⁻¹. Spectra taken at this time show peak fluxes in the 1-keV channel. We note that most of the spectra were measured while the detector was looking at relatively large angles to **B**. The energy flux during event 6 ranged between 2 and 3 ergs/cm² s sr.

Several important features of polar cap arcs may be deduced from a further consideration of event 6. In Figure 7 we have plotted in electron distribution function versus energy measured by the S3-2 detector (triangles) during
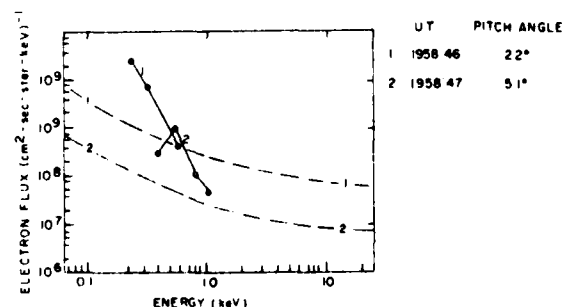
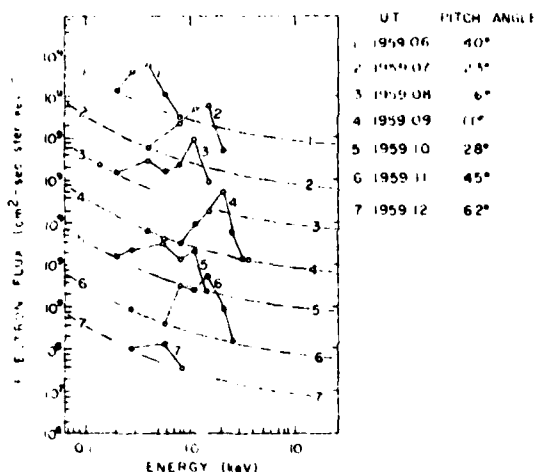| UT	PITCH ANGLE
1 1959 06	40°
2 1959 07	.°
3 1959 08	6°
4 1959 09	11°
5 1959 10	28°
6 1959 11	45°
7 1959 12	62°

Fig. 5. Directional, differential flux measurements during event 4. The format is the same as Figure 4.

event 6 and another distribution measured by a zenith-looking spectrometer on the DMSP/F2 satellite (dots) as it passed over a visible polar cap arc [Hardy et al., this issue]. The dashed line gives the S3-2 detectors one count level of sensitivity. In this semilogarithmic format a Maxwellian distribution appears as a straight line with a negative slope.

For electrons with energies >500 eV, both distributions are similar in shape having maxima near 1 keV. The flux maximum during event 6 is a factor of 5 higher than that measured over a visible arc by DMSP. This suggests that the flux associated with event 6 is also sufficient for producing a visible arc. The fact that the distributions have maxima indicates that they are made up of two populations. Electrons with energies at or greater than the maximum are primaries that have undergone a field-aligned acceleration [Burch et al., 1979]. Those with energies below the maximum are secondaries or degraded primaries [Evans, 1974]. Hardy et al. [this issue] have shown that the primary population in the DMSP event has a temperature of 350 eV and has fallen through a field-aligned potential drop of ~750 V. A least squares fit of the four data points at and beyond the maximum in the event 6 distribution function is given as a dash-dot line in Figure 7. The data are consistent with a primary population that has a temperture of ~220 eV and has been accelerated through a potential of ~1 kV. All of the primary distributions measured during events 4, 6, and 7 (not shown) have similar temperatures and accelerations.

Having established that primary electrons associated with events 4, 6, and 7 have been accelerated along field lines, two other characteristics immediately follow:

1. From Figure 3 we note that at the edges of these events the electric field intensifies. Across the events, E_x reverses direction. Consistent with observations reported by Burch et al. [1979], the electric field points toward the core of the acceleration region.

2. Despite a field-aligned acceleration the primary electron distribution does not appear to deviate significantly from isotropy over the downcoming hemisphere at ionospheric altitudes. The distribution function for primary electrons from event 6 (Figure 7), which are locally trapped, is similar to others measured in event 4 and by DMSP with

detectors looking approximately along magnetic field lines. Burch et al. [1979] have shown that at pitch angles of ~7° and 60° the distribution functions of accelerated primary electrons are almost identical. They also found field-aligned fluxes of electrons with energies well below those of the primary distribution. Such electrons are thought to be of ionospheric origin and have been accelerated through a portion of the field-aligned potential drop. Examples of such electrons are probably contained in Figure 7 at the low-energy end of the DMSP/F2 distribution. Note that these electrons would not be detected by the S3-2 spectrometer.

Figure 8 is a plot of E_x, ΔB_y, and the electron flux taken during the subsequent, southern high-latitude pass (rev 5231S). The data format is the same as Figure 1. During this pass the satellite was near perigee and reached a maximum invariant latitude of 86° on the night side of the magnetic pole. Due to the proximity of the pass in time to the solstice, the ionosphere below the trajectory was sunlit. In the southern hemisphere a positive E_x is directed from dawn to dusk (antisunward convection); negative slopes in E_x and ΔB_y again correspond to regions of negative space charge and field-aligned currents out of the ionosphere, respectively.

The electric field is highly irregular throughout the pass making it difficult to designate the boundaries between the polar cap and oval. In this summer hemisphere case, however, a well-defined region 1/region 2 current system appears in the evening but not in the morning side of the auroral oval. Using arguments similar to those employed for the northern hemisphere data, namely, the first and last appearance of polar rain, we tentatively place the poleward boundaries for the oval coincident with the E_x reversals at 2045:54 UT (Λ = 82°, MLT = 03.8) and 2050:06 UT (Λ = 78.6°, MLT = 19.4). Poleward of these invariant latitudes, E_x is irregular but basically dawn to dusk in its orientation. Like the winter polar cap data discussed above, E_x varies in an almost one-to-one fashion with ΔB, with the regions of negative slope in ΔB_y in the polar cap corresponding to negative slopes to E_x. The maximum excursions of E_x in the summer polar cap are, however, from +30 to −40 mV/m, a factor of 5 smaller than

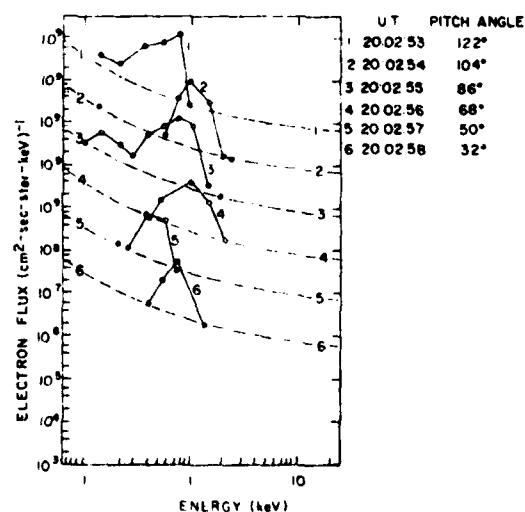| UT	PITCH ANGLE
1 20 02 53	122°
2 20 02 54	104°
3 20 02 55	86°
4 20 02 56	68°
5 20 02 57	50°
6 20 02 58	32°

Fig. 6. Directional, differential flux measurements during event 6. The format is the same as Figure 4.
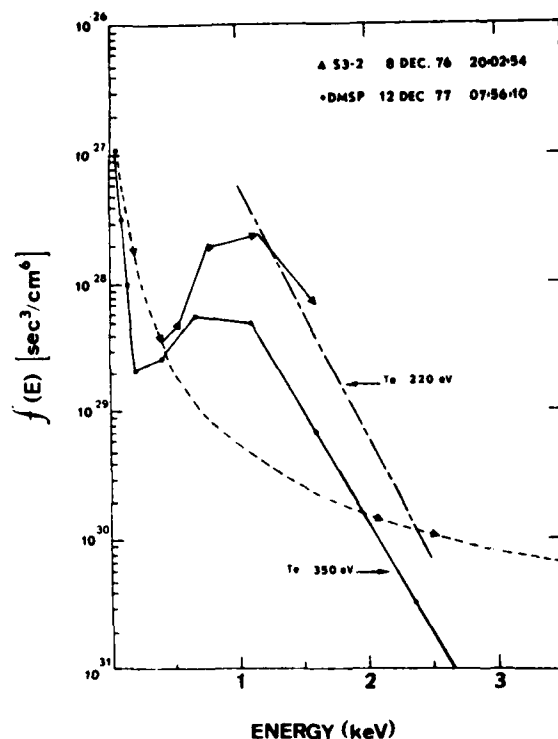
Fig. 7. Distribution functions versus energy of locally trapped electrons measured during event 6 (triangles) and of field-aligned electrons observed by means of a spectrometer on DMSP/F2 above a visible polar cap arc (dots). The dashed line gives the S3-2 detector's one-count level of sensitivity. The dash-dot line is a least squares fit of primary electrons during event 6 to a Maxwellian distribution.

the largest excursions in the winter polar cap. Conversely, the transverse magnetic variations are larger than their northern hemisphere counterparts. For example, the two prominant negative slope deflections in ΔB_y centered at 2047:55 ($\Lambda = 85.5°$) and 2048:54 ($\Lambda = 82.9°$) are of ~100-nT magnitude. The accompanying, relatively small variations in E_x during this pass reflect the basically higher Pedersen conductivity of the sunlit polar cap.

A further significant difference between this pass and the north polar pass is in the measured electron fluxes. For the south pole pass the variations in the electron flux levels measured across the polar cap were always $<10^8/(cm^2$ s sr) [1]. During the events at 2047:55 and 2049:00 UT the detector was looking earthward. The absence of variations in the particle flux may be attributed to bad luck in the look direction of the detector, degradation of the primary beam between 1300 and 250 km, or a real change in particle admittance to the cap possibly due to the sign of the component of the IMF [Burch et al., 1979].

During rev 5215S (Figure 9) the satellite was near perigee and reached a maximum invariant latitude of 84.5° on the dayside of the magnetic pole. Measurements from this pass are different in several respects from those found during rev 5231S. Attention is directed to four reversals of E_x designated by dot-dash lines. The E_x reversals at 1801:30 UT ($\Lambda = 77.1$, MLT ~ 07.3) and 1808:00 UT ($\Lambda = 16.3$) coincide with the termination of region 1 currents [Smiddy et al., 1980] and

are taken as the boundaries between the polar cap and auroral oval. Poleward of these boundaries, convection is in the antisunward direction. Between 1803:40 UT ($\Lambda = 81.7$, MLT = 08.4) and 1806:00 UT ($\Lambda = 83.3$, MLT = 14.3) in the center of the polar cap E_x is directed from dusk to dawn (sunward convection). In the region of antisunward convection along the morning flank of the polar cap ΔB_y exhibits variations at frequencies close to the 5-s resolution in E_x. These variations terminate at the reversal in E_x (1803:40 UT) where a negative slope in ΔB_y indicates that a current density of ~1.5 $\mu A/m^2$ is flowing out of the ionosphere. Such a current was predicted by Lassen [1979] for the central polar cap reversal in E_x. Unfortunately, the electron detector was looking toward local nadir, so it is not possible to determine whether the current-carrying electrons were sufficiently energetic to create an arc. Two events marked 1 ($\Lambda = 84.0$, MLT = 10.1) and 2 ($\Lambda = 84.5$, MLT = 11.7) in Figure 9 appear in the region of sunward convection and carry currents of 1.1 and 2.0 $\mu A/m^2$ out of the ionosphere. Electron fluxes during these events had maximum values of 8×10^7 and 2×10^8 $(cm^2$ s sr) [1], respectively, with maximum counting rates in the 0.8-keV channels. In both instances the detectors were looking ~90° to the magnetic field lines. The appearance of E_x remaining nearly constant across these Birkeland current structures is an artifact of the averaging process.

Along the dusk flank of the polar cap, E_x was directed from dawn to dusk and had a maximum value of 35 mV/m. Between 1806:50 UT and 1807:12 UT, ΔB_y decreased by ~300 nT accompanied by no large change in E_x. This change in ΔB_y cannot be due to the satellite crossing a quasi-infinite current sheet. An examination of the up-down and north-south components of the magnetic field (not shown) reveals significant changes simultaneous with the ΔB_y decrease. These variations in the magnetic field, in the presence of a strong, nearly uniform electric field, are consistent with the satellite having passed over an electrojet flowing along the flanks of the sunlit polar cap. Recall that the satellite was near perigee at this time. Electrojet effects have been observed under similar circumstances at satellite altitudes by means of instrumentation on OGO 6 [Langel, 1975].

The magnetic deflections marked event 3 appear only in the ΔB_y component and are probably due to two parallel, latitudinally narrow Birkeland current systems. High-time-resolution electric field measurements (not shown) exactly track the ΔB_y variations. The regions of strong negative slope during event 3 were accompanied by bursts of electrons with peak fluxes near 0.5 keV. The detector was looking at pitch angles near 90° at this time. The fluxes then decreased to background as the detector turned toward nadir.

SUMMARY AND DISCUSSION

Observations presented in the previous section represent the first report of simultaneous measurements of small-scale electric and magnetic field variations and electron fluxes in the polar cap. In the three cases studied the IMF had a significant northward component and the magnetosphere was moderately active. The satellite trajectory was close to the dawn-dusk meridian and passed to invariant latitudes $>84°$. These conditions are ideal for detecting the electromagnetic and particle characteristics of sun-aligned, polar cap arcs.

During the winter polar cap pass (rev 5231N) the dawn-dusk component of the electric field was highly irregular. Five events in the polar cap with characteristics of field-aligned currents were identified from variations of the transverse magnetic field component. A comparison with electric field measurements showed that the regions of upward Birkeland currents were embedded in regions of negative space charge. The local charge imbalar e was approximately one part in three to thirty million. Dɟring several of these events the particle detector was looking upward so that individual spectra could be examined. The electron spectra were similar to those previously reported over polar cap arcs [Whalen et al., 1971; Meng and Akasofu, 1976; Ismail et al., 1977; Hardy et al., this issue]. The primary electrons came from a population with a temperature of a few hundred eV that had been accelerated through a potential drop of ~1 kV. We are thus led to believe that the electromagnetic characteristics of the events reported here are the same as those of polar cap arcs. Comparisons of the electron flux with the measured Birkeland current densities (event 3) and with each other as a function of pitch angle (events 4 and 6) suggest that the primary electrons are nearly isotropic or only weakly field aligned over the downcoming hemisphere. This result is in agreement with the observations of Burch

[1968], Whalen et al. [1971], and Burch et al. [1979]. This implies that the potential drop responsible for the field-aligned acceleration of primary electrons either results from a double layer at great altitudes or is spread out over great distances along magnetic field lines. The magnetic mirror force could not bring the primary beam to isotropy if there were a narrow double layer at altitudes close to that of the satellite. Note that despite many reversals in the dawn to dusk electric field component there was no direct evidence for a component of E along B in the cases studied here (Figures 2a, 2b).

During periods of IMF $B_z > 0$, large-scale electric fields in the summer hemisphere can either be irregular (rev 5231S) or have dusk to dawn components in the central polar cap (rev 5215S). Transverse deflections of the magnetic field (ΔB_y) were obseved in both situations. E_x and ΔB_y correlated during rev 5231S as they had during the north polar cap pass. Observations from rev 5215S did not show such high correlations between E_x and ΔB_y. There were instances of variations in ΔB_y with little or no shift in E_x, possibly indicating the influence of ionospheric electrojets. Finally, it should be noted that regions of small-scale Birkeland currents were found in all three sections of the polar cap, i.e., embedded in regions of both sunward and antisunward convection.
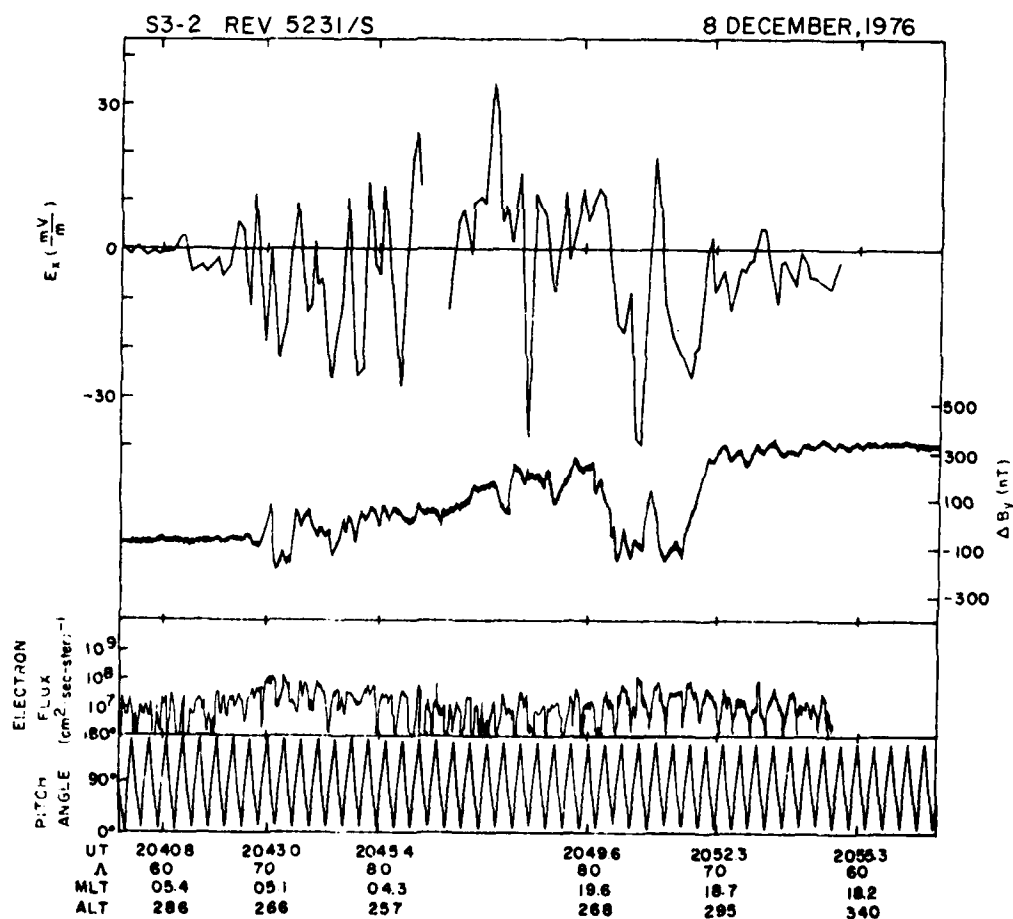

Fig. 8. Electric field, magnetic field, electron flux, and pitch angle measurements during S3-2 rev 5231S. The format is the same as for Figure 1. Hourly averaged IMF components were −3.7, 3.8, and 7.4 nT.
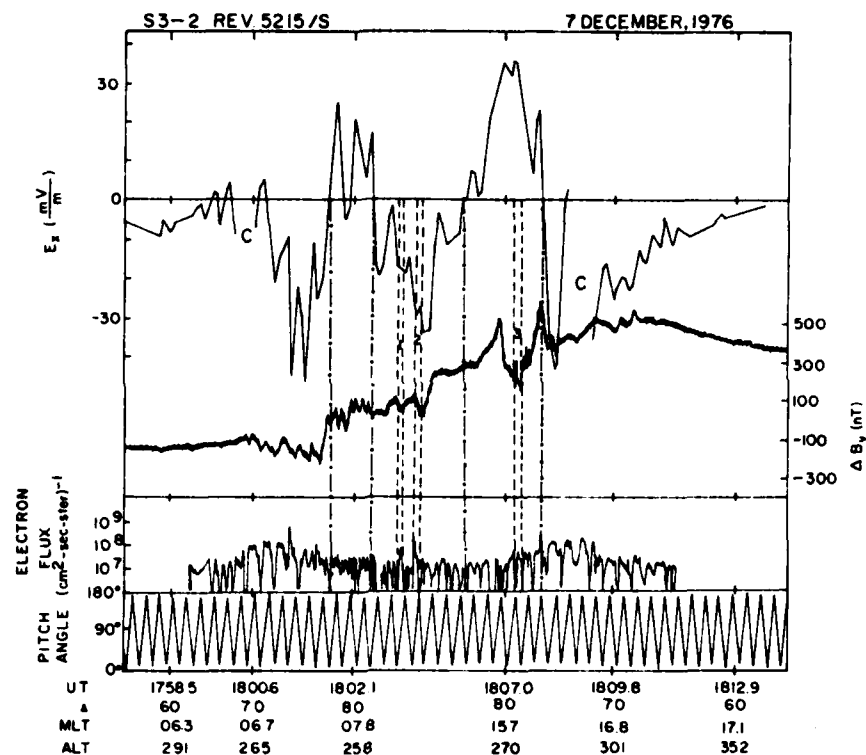
Fig. 9. Electric field, magnetic field, electron flux, and pitch angle measurements during S3-2 rev 5215S. The format is the same as for Figure 1. Hourly averaged IMF components were 3.6, −2.8, and 4.1 nT.

Electron fluxes measured during the perigee passes were not as distinctive as those measured during rev 5231N. This may reflect an IMF B_x effect as suggested by *Saflekos et al.* [1978] and *Burch et al.* [1979]. This seems unlikely to be the only explanation, since B_x had opposite polarities during the two south polar passes but the polar cap electron flux levels were comparable. The difference may also be due to an unlucky coincidence: whenever the satellite was passing through an upward Birkeland current, the spectrometer was looking earthward. The difference may also reflect apogee-perigee or summer-winter effects. Since the energy of the primary beam is frequently ≤1 keV, serious degradation of current-carrying electrons can occur between 1350 and 250 km. It is also possible that the radical differences in the ionospheric thermal plasma and conductivity between the two hemispheres affect the ionosphere-magnetosphere electrical coupling in an as yet not understood way. For example, conditions for weak field-aligned potential drops may be present when the ionosphere is almost nonconducting but not when it is highly conducting. Convection shears, evidenced by rapid variations in E_x, were stronger during rev 5231N than on either of the summer hemisphere passes. Strong E_x reversals are considered to be concomitant to field-aligned potential drops.

A detailed discussion of auroral arc theory is beyond the scope of this observational paper. However, the electric and magnetic field measurements from the polar cap do allow some comments concerning ionosphere/magnetosphere coupling and the theory of auroral arc formation.

It is generally conceded that the ionosphere and the magnetosphere are electrically coupled by field-aligned cur-

rents. Two classes of models are found in the literature which we call 'static' and 'dynamic.' In the static models, field-aligned currents close via Pedersen currents in the ionosphere [*Bostrom*, 1964; *Coroniti and Kennel*, 1972; *Lyons*, 1980, 1981; *Kan and Lee*, 1980]. Dynamic models emphasize the effects of time-varying electric fields seen by the plasma as it convects across a strip of enhanced conductivity [*Sato and Holzer*, 1973; *Maltsev et al.*, 1977; *Mallinckrodt and Carlson*, 1978]. The static model predicts that the ratio of variations of the electric field, δE_x, to those of the magnetic field, $\delta \Delta B_y$, is the height-integrated Pedersen resistivity, Σ_P^{-1}. In the dynamic model, $\delta E_x/\delta \Delta B_y$ is equal to the local intrinsic impedance of the medium (η) (cf. equation (12) of *Mallinckrodt and Carlson* [1978]). For the four events in Figure 3 (events 3, 4, 6, and 7) in the regions of upward currents the ratios give 1.34 Ω, 1.05 Ω, 1.77 Ω, and 2.94 Ω. These correspond to conductivities ranging between 0.34 and 1 mho. This is a reasonable estimate of the Pedersen conductivity in the winter polar ionosphere with soft precipitation. On the other hand, the local value of $\eta = (\mu_0 B^2/\rho_m)^{1/2}$ is in the range 3.3 to 7.4 Ω. The mass density ρ_m was estimated from the plasma density (0.3 to 3 × 10³ cm⁻³) and by assuming a dominant species of O^+. These calculations show that the S3-2 measurements are more consistent with the 'static' rather than the 'dynamic' models for the electrical coupling in polar cap arcs.

In the summer polar cap with irregular electric fields (Figure 8) the ratio of δE_x to $\delta(\Delta B_y)$ is much smaller, 0.1 to 0.3 Ω. This corresponds to a Σ_P between 3 and 10 mho. The sunlit ionosphere provided most of this conductivity without need for large precipitation fluxes.

Currently, there are two major theoretical concepts models for arc formation which invoke either an ionospheric [*Miura and Sato*, 1980] or a magnetospheric [*Lyons*, 1980, 1981; *Kan and Lee*, 1980] generator. Both models are highly developed and each, granting its initial assumptions, predicts the growth of arclike structures. There does not appear to be anything specific to these theories that makes them inapplicable to the polar cap arc situation. These theories have diametrically opposite predictions concerning the relationship between electric field and Birkeland current structures above auroral arcs. The 'ionospheric generator' mechanism (cf. Figure 1 of *Miura and Sato* [1980]) requires that arcs develop in regions of positive space charge ($\nabla \cdot \mathbf{E} > 0$). Magnetospheric generator theory makes the opposite prediction, i.e., arcs should appear in regions of negative space charge ($\nabla \cdot \mathbf{E} < 0$). The winter polar cap observations, with their clear particle signatures, show that polar cap arcs appear in regions of negative space charge, in agreement with the requirements of the magnetospheric generator model. Recently, Miura (private communication, 1982) has found that by including the effects of anomalous dissipation at attitudes of ~ 1 R_E, the feedback model predicts the phase relationship between arcs and space charge observed by S3-2.

A further argument for a magnetospheric generator may be deduced from the direction of the Poynting flux. From the cases presented in Figure 3 it is clear that the direction of the Poynting flux $\delta E_x \times \delta(\Delta B_y)$ is downward into the ionosphere. This energy would be dissipated as heat in the lower ionosphere. In the model of *Miura and Sato* [1980, cf. Figure 1] the Poynting flux is upward. *Mallinckrodt and Carlson* [1978] found an upward Poynting flux if the Alfvén waves were of ionospheric origin but downward if they were generated in the magnetosphere. In the latter case, an upward Poynting flux, associated with partially reflected waves, would be found downstream of the arc. Our analysis of the ratio $\delta E_x / \delta(\Delta B_y)$ seems to preclude this MHD wave effect in the polar cap. However, it may be very important in the auroral oval, especially near the local midnight where large zonal electric fields allow strong convection normal to east-west aligned arcs.

Due to their radically different magnetic topologies the term 'magnetospheric generator' has different meaning when applied to arcs in the auroral oval and in the polar cap. Polar cap arcs are electrically connected to the magnetopause by means of Birkeland currents flowing along open field lines rather than to the magnetospheric equatorial region. For the remainder of this paper we develop a semi-qualitative picture relating polar cap arcs to the magnetopause. The picture is based on a simplified representation of E_x and ΔB_y measurements taken in the vicinity of event 6. The infinite current sheet approximation is used.

Figure 10 gives a projection into the solar-magnetospheric Y-Z plane of a cross section of magnetic field lines connecting the polar ionosphere in the vicinity of event 6 to the magnetopause. The intersection of the field lines is assumed to take place at some unspecified distance down the magnetotail. The magnetopause is represented by a current-carrying layer of finite thickness. The current density in the magnetopause layer is j_m and flows dusk to dawn. The ionospheric structure encountered between 2002:40 and 2003:10 UT is electrically connected to the magnetopause by Birkeland currents labeled j_{in} and j_{out}. At 2002:40 and

2003:10 UT the slope of ΔB_y versus UT curve was zero and the values of $\Delta B_y \sim 100$ nT (Figure 3b), indicating that across the event the net current into the ionosphere is zero. To satisfy the requirements of current continuity the upward Birkeland current divides into two branches, labeled j_{BM}, in the magnetopause layer. At the ionospheric ends of the flux tubes, current continuity is maintained by means of converging Pedersen currents, j_P.

In both Figure 3b and our simplified representation, E_x rises to a maximum value of $+120$ mV/m (dusk to dawn) at 2002:50 UT. It reverses direction at 2002:54 UT and falls to a minimum of -125 mV/m (dawn to dusk) at 2003:00 UT. Within the central portion of the arc, E_x had an average value of -25 mV/m. A numerical integration of $-E_x dx$ shows that the potential drop on the dusk side of the electric field reversal is -6.4 kV and $+8.4$ kV on the dawn side of the reversal. A net potential drop of 2.4 kV across the region is the same as would be given by a uniform dawn to dusk $E_x = -12$ mV/m. We have already pointed out that the electrons responsible for the event 6 arc were accelerated through a potential drop of ~ 1 kV. Thus the potential drops on both sides of the reversal in E_x greatly exceed that along the field lines. This means that E_x can be mapped, albeit imperfectly,
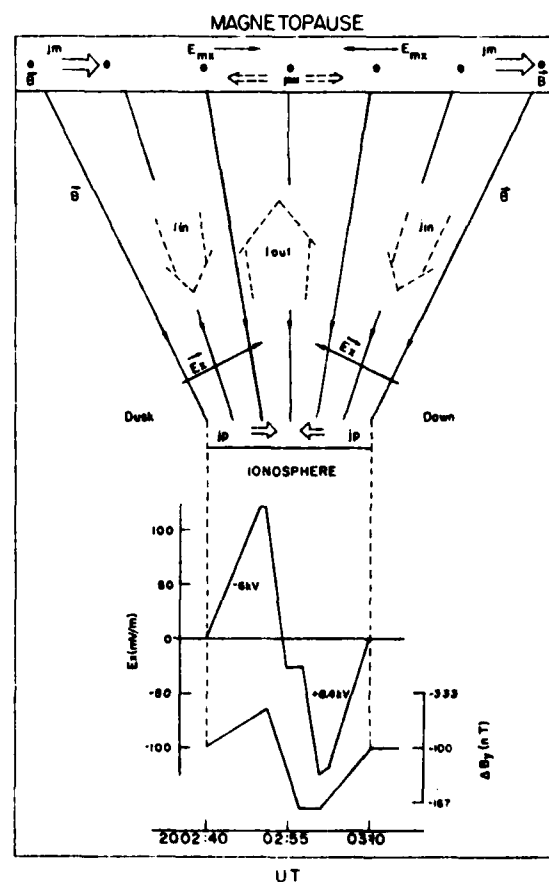

Fig. 10. A two-dimensional representation of the currents and electric fields coupling a polar cap arc to a possible magnetopause generator. The plots of E_x and ΔB_y shown in the lower portion of the figure approximate the fields measured in the vicinity of event 6 (Figure 3b).

to the magnetopause. Within the magnetopause, E_{mx} also undergoes a reversal. Because of the field-aligned potential drop the magnitude of E_{mx} is slightly greater than would be given under perfect mapping ($E \cdot B = 0$) conditions. Note that E_{mx} and j_{BM} are oppositely directed, consistent with the requirements of a magnetospheric generator.

In our emerging picture the Birkeland current system associated with polar cap arcs can be thought of as a partial diversion of the magnetopause current through the ionosphere. The diversion requirements can be estimatd from the S3-2 measurements in the ionosphere and the requirements of pressure balance at the magnetopause. The magnetic field in the high-latitude lobes of the magnetotail at lunar distance has a strength of ~10 nT. Since the magnetosheath plasma flows parallel to the magnetopause, the tail field is confined by thermal pressure. To balance a 10-nT field a pressure of 4×10^{-11} J/m^3 is required. Assuming a magnetopause thickness of 100 km (the gyroradius of a 40-eV proton in a 10-nT field), we calculate a magnetopause current density of 4×10^{-8} A/m^2. From the conservation of current and magnetic flux we know that $j_\parallel/B$ = const. The magnetic field strength in the polar ionosphere is ~40,000 nT. During event 6 the S3-2 magnetometer measured an upward Birkeland current of 2 μA/m^2. In a 10-nT magnetic field, $j_{BM} = 5 \times 10^{-10}$ A/m^2. Thus less than 1% of the magnetopause current would have to be diverted to the ionosphere to maintain the currents associated with a visible polar cap arc.

The simultaneous measurements of ΔB_y and E can be used to estimate the height-integrated conductivity in the vicinity of event 6. In Table 1 we have listed the approximate values of ΔB_y and E_x given in Figure 10 at ten points between 2002:40 and 2003:10 UT. To estimate the value of Σ_P (last column of Table 1), we use the infinite current sheet approximation and write (1) in the form

$$\Delta B_y - 1.256\Sigma_P E_x = \text{const} \qquad (6)$$

Here ΔB_y, Σ_P, and E_x are in nanoteslas, mhos, and millivolts per meter, respectively. We note that at 2002:40, 2002:54, and 2003:10 UT, $\Delta B_y = -100$ nT and $E_x = 0$ mV/m. At these points we can estimate the value of the constant in (6) as -100 nT. At points where $E_x = 0$, the value of Σ_P cannot be determined. The calculated values of Σ_P rise from ~0.3 mho at the poleward edge of the event (2002:50), reach a maximum value of 2.4 mho at 2002:58 UT, then fall to ~0.3 mho at 2003:10. The low background values away from the event are consistent with background values calculated by *Wallis and Budzinski* [1981]. The conductivity within the event is significantly less than that predicted by (2) for an energy flux

of 2–3 ergs/cm^2 s estimated from the electron spectrometer measurements. Explaining this discrepancy is beyond the scope of this report.

The picture that we have developed in Figure 10 is not a physical model of polar cap arcs. Since, to the best of our knowledge, no distinctive model of polar cap arcs exists in the literature, the picture may provide a useful first step. The fact that S3-2 cannot measure the sun-aligned component of the electric field is a serious impediment to developing such a model. Obviously, the conductivity of the winter ionosphere has severe gradient in the vicinity of polar cap arcs. The electric field component along an arc produces polarization fields [*de la Beaujardiere et al.*, 1977]. Polarizations may partially explain values of E_x which are very intense at the edges of arcs and very weak inside. It should also be recognized that in Figure 10 we have made the most naive magnetic mapping between the ionosphere and the magnetopause. In future work the consequences of tangential electric field components in the magnetopause layer must be examined. Perhaps then we may begin to understand the means by which plasma is admitted in a structured way to the polar magnetosphere.

REFERENCES

Berkey, F. T., L. L. Cogger, and S. Ismail, Evidence for a correlation between sun-aligned arcs and the interplanetary magnetic field direction, *Geophys. Res. Lett.*, *3*, 145, 1976.

Bostrom, R., A model of the auroral electrojets, *J. Geophys. Res.*, *69*, 4983, 1964.

Burch, J. L., Low-energy electron fluxes at latitudes above the auroral zone, *J. Geophys. Res.*, *73*, 3585, 1968.

Burch, J. L., S. A. Fields, and R. A. Heelis, Polar cap electron acceleration regions, *J. Geophys. Res.*, *84*, 5863, 1979.

Burke, W. J., Observations concerning the relationships between electron flux and electric field variations and thermal plasma irregularities in the polar cap, in *Proceedings of the Symposium on the Effect of the Ionosphere on Radiowave Systems*, Naval Research Laboratory, Washington, D. C., in press, 1981.

Burke, W. J., M. C. Kelley, R. C. Sagalyn, M. Smiddy, and S. T. Lai, Polar cap electric field structures with a northward interplanetary magnetic field, *Geophys. Res. Lett.*, *6*, 21, 1979.

Burke, W. J., D. A. Hardy, F. J. Rich, M. C. Kelley, M. Smiddy, B. Shuman, R. C. Sagalyn, R. P. Vancour, P. J. L. Wildman, and S. T. Lai, Electrodynamic structure of the late evening sector of the auroral zone, *J. Geophys. Res.*, *85*, 1179, 1980.

Coroniti, F. V., and C. F. Kennel, Polarization of the auroral electrojet, *J. Geophys. Res.*, *77*, 2835, 1972.

Crooker, N. U., Antiparallel merging, the half-wave rectifier responce of the magnetosphere and convection, in *Proceedings of the Magnetospheric Boundary Layers Conference, ESA-SP-148*, ESTEC, Noordwijk, The Netherlands, 1979.

de la Beaujardiere, O., R. R. Vondrak, and M. J. Baron, Radar observatons of electric fields and currents associated with auroral arcs, *J. Geophys. Res.*, *82*, 5051, 1977.

Eather, R. H., and S.-I. Akasofu, Characteristics of polar cap auroras, *J. Geophys. Res.*, *74*, 4794, 1969.

Evans, D. S., Precipitating electron fluxes formed by a magnetic-field-aligned potential difference, *J. Geophys. Res.*, *79*, 2853, 1974.

Frank, L. A., and K. L. Ackerson, Observations of charged particle

TABLE 1. Approximate Values of ΔB_y and E_x Given in Figure 10 at Ten Points Between 2002:40 and 2003:10 UT

Time, UT	ΔB_y, nT	E_x, mV/m	Σ_P
2002:40	-100	0	...
2002:50	-60	120	0.27
2002:52	-52	120	0.32
2002:54	-100	0	...
2002:55	-112	-25	0.38
2002:58	-175	-25	2.40
2003:02	-175	-125	0.48
2003:04	-156	-120	0.37
2003:09	-109	-20	0.35
2003:10	-100	0	...

precipitation in the auroral zone, *J. Geophys. Res.*, *76*, 3612, 1971.

Gussenhoven, M. S., Extremely high latitude auroras, *J. Geophys. Res.*, this issue.

Hardy, D. A., W. J. Burke, and M. S. Gussenhoven, DMSP optical and electron measurements in the vicinity of polar cap arcs, *J. Geophys. Res.*, this issue.

Harel, M., R. A. Wolf, P. H. Reiff, R. W. Spiro, W. J. Burke, J. J. Rich, and M. Smiddy, Quantitative simulation of a magnetospheric substorm, 1, Model logic and overview, *J. Geophys. Res.*, *86*, 2217, 1981.

Heelis, R. A., J. D. Winningham, W. B. Hanson, and J. L. Burch, The relationship between high-latitude convection reversals and the energetic particle morphology observed by Atmospheric Explorer, *J. Geophys. Res.*, *85*, 3315, 1980.

Hoffman, R. A., and D. S. Evans, Field-aligned electron bursts at high latitudes observed by OGO 4, *J. Geophys. Res.*, *73*, 6201, 1968.

Iijima, T., and T. A. Potemra, The amplitude distribution of field-aligned currents at northern high latitudes observed by Triad, *J. Geophys. Res.*, *81*, 2165, 1976.

Ismail, S., D. D. Wallis, and L. L. Cogger, Characteristics of polar cap sun-aligned arcs, *J. Geophys. Res.*, *82*, 4741, 1977.

Kan, J. R., and L. C. Lee, Theory of imperfect magnetosphere ionosphere coupling, *Geophys. Res. Lett.*, *7*, 633, 1980.

King, J. H., *Interplanetary Medium Data Book, Supplement 1, 1975-1978, NSSDC/WDC A-R&G-79-08*, Goddard Space Flight Center, Greenbelt, Md., 1979.

Langel, R. A., A comparison of electric and magnetic field data from the OGO 6 spacecraft, *J. Geophys. Res.*, *80*, 4661, 1975.

Lassen, K., The quiet-time pattern of auroral arcs as a consequence of magnetospheric convection, *Geophys. Res. Lett.*, *6*, 777, 1979.

Lassen, K., and C. Danielsen, Quiet time pattern of auroral arcs for different directions of the interplanetary magnetic field in the *Y-Z* plane, *J. Geophys. Res.*, *83*, 5277, 1978.

Lyons, L., Generation of large-scale regions of auroral currents, electric potentials, and precipitation by the divergence of the convection electric field, *J. Geophys. Res.*, *85*, 17, 1980.

Lyons, L. R., Discrete aurora as the direct result of an inferred high-altitude generating potential distribution, *J. Geophys. Res.*, *86*, 1, 1981.

Maezawa, K., Magnetospheric convection induced by the positive and negative *Z* components of the interplanetary magnetic field:

Quantitative analysis using polar cap magnetic records, *J. Geophys. Res.*, *81*, 2289, 1976.

Mallinckrodt, A. J., and C. W. Carlson, Relations between transverse electric fields and field-aligned currents, *J. Geophys. Res.*, *83*, 1426, 1978.

Maltsev, Y. P., W. B. Lyatsky, and A. M. Lyatskaya, Currents over the auroral arc, *Planet. Space Sci.*, *25*, 53, 1977.

Meng, C.-I., Polar cap arcs and the plasma sheet, *Geophys. Res. Lett.*, in press, 1981.

Meng, C.-I., and S.-I. Akasofu, The relationship between the polar cap auroral arc and the auroral oval arc, *J. Geophys. Res.*, *81*, 4004, 1976.

Miura, A., and T. Sato, Numerical simulation of global formation of auroral arcs, *J. Geophys. Res.*, *85*, 73, 1980.

Rees, M. H., Auroral ionization and excitation by incident energetic electrons, *Planet. Space Sci.*, *11*, 1209, 1963.

Saflekos, N. A., T. A. Potemra, and T. Iijima, Small-scale transverse magnetic disturbances in the polar regions observed by Triad, *J. Geophys. Res.*, *83*, 1493, 1978.

Sato, T., and T. E. Holzer, Quiet auroral arcs and electrodynamic coupling between the ionosphere and magnetosphere, 1, *J. Geophys. Res.*, *78*, 7314, 1973.

Smiddy, M., W. J. Burke, M. C. Kelley, N. A. Saflekos, M. S. Gussenhoven, D. A. Hardy, and F. J. Rich, Effects of high-latitude conductivity on observed convection electric fields and Birkeland currents, *J. Geophys. Res.*, *85*, 6811, 1980.

Vondrak, R. R., Model of Birkeland currents associated with an auroral arc, *J. Geophys. Res.*, *80*, 4011, 1975.

Wallis, D. D., and E. E. Budzinski, Empirical models of height-integrated conductivities, *J. Geophys. Res.*, *86*, 125, 1981.

Weber, E. J., and J. Buchau, Polar cap *F*-layer auroras, *Geophys. Res. Lett.*, *8*, 125, 1981.

Whalen, B. A., J. R. Miller, and I. B. McDiarmid, Sounding rocket observations of particle precipitation in a polar cap electron aurora, *J. Geophys. Res.*, *76*, 6847, 1971.

Winningham, J. D., and W. J. Heikkila, Polar cap auroral electron fluxes observed with ISIS 1, *J. Geophys. Res.*, *79*, 949, 1974.

110

DUAL SATELLITE OBSERVATIONS OF POLAR MAGNETIC FIELDS

IN THE

DAWN SECTOR

by

N.A. Saflekos
Boston College
Chestnut Hill, MA 02167

B.M. Shuman
Air Force Geophysics Laboratory
Hanscom AFB, MA 01731

T.A. Potemra
Johns Hopkins University, APL
Johns Hopkins Road
Laurel, MD 20810

M. Smiddy
Air Force Geophysics Laboratory
Hanscom AFB, MA 01731

ABSTRACT

DUAL SATELLITE OBSERVATIONS OF POLAR MAGNETIC FIELDS IN THE
DAWN SECTOR

S3-2 and Triad, two nearly coplanar polar orbiting satellites of similar periods, carried into orbit two sensitive fluxgate magnetometers with high spatial and temporal resolution. The two triaxial sensors frequently assumed the mother-daughter experiment configuration. Occasional close encounters inside regions of disturbance allow cross-calibration of the sensors. Random choices of varying time delays between the spacecraft in the range from 9 to 16 minutes over the dawn auroral sector show that the large scale transverse magnetic field variations are spatial in nature, extend up to a few hours in local time parallel to the auroral oval, and exhibit small motion in the north-south direction while preserving their latitudinal widths. The field-aligned current densities do not show pronounced gradients either with altitude or with longitude. The convective electric field-reversal is located at the poleward termination of regions 1 field-aligned current system or equatorward of this boundary, not deviating by more than one and a half degrees from it. Simultaneous small scale magnetic and electric field variations superimposed on the region 1 disturbance and observed at widely separated local times may correspond to discrete auroral arcs on closed as well as on open magnetic field lines. To our knowledge, except for statistical studies, these are the first reported sets of measurements suitable for making the distinction between the spatial and the temporal nature of transverse magnetic field variations.

INTRODUCTION

Over the past decade, a large number of observations made in the earth's polar regions with balloons, rockets and high altitude spacecraft have confirmed the presence of a global field-aligned current system which is closely connected with a variety of phenomena including the orientation of the IMF (interplanetary magnetic field). The field-aligned current systems surround the polar cap and are divided primarily into two regions: (a) region 1, with direction into the ionosphere on the poleward dawn-side and out of the ionosphere on the poleward dusk-side, and (b) region 2, with direction away from the ionosphere on the low-latitude dawn-side and into the ionosphere on the low-latitude dusk-side, (Iijima and Potemra, 1976a, b). The global morphology of the field-aligned currents (FAC) was first delineated by Armstrong and Zmuda, 1974. Additional FAC in the cusp region were identified with the Triad satellite (Iijima and Potemra, 1976b; Iijima et al., 1978). Relationships between cusp currents and the IMF have been presented by several authors (Potemra and Saflekos, 1979; McDiarmid et al., 1978a; McDiarmid et al., 1978b). A comprehensive review of large-scale FAC has been presented by Potemra et al., 1979.

Observations with particle detectors and electric field probes have confirmed that small scale variations in the measured quantities are associated with auroral arcs (Anderson and Vondrak, 1975). The Triad and other satellites see small scale variations in the transverse magnetic disturbances which may also be associated with polar cap auroral arcs (Saflekos et al., 1978).

In this paper we intend to study the variability of FAC using dual spacecraft observations in the configuration of the mother-daughter experiment concept. Such observations can also be used as tracers of magnetic field lines thus providing test points in validating some time varying magnetic field models (Olson and Pfitzer, 1974).

The region 1 field-aligned currents are assumed to support the electric

field reversal separating the sunward from the antisunward convection regime. The region 2 currents flow in the sunward convection regime, consistent with gradients in the electric field (Saflekos et al., 1979).

An opportunity to examine convective electric fields and field-aligned currents in relation to region and 1 region 2 current systems presented itself to the AE-C data base with the revival of an attitude magnetometer on that spacecraft (Bythrow et al., 1979). They have calculated current densities electric fields and ionospheric conductivities. They pointed out that discontinuities in the magnetic disturbance gradients $\frac{d(\Delta B)}{dx}$ associated with discontinuities in the convective electric field gradients $\frac{d(\Delta E)}{dx}$ may indicate gradients in conductivity at the base of the magnetic field lines threading the ionosphere and passing through the spacecraft observation points. Simultaneous energetic particle data are needed to confirm the positions, magnitudes and gradients of the Pedersen conductivities that they obtained. The AE-C and the S3-2 spacecraft are ideally suited for studies of the ionospheric currents causing disturbances on the ground. The height integrated Pedersen conductivities (Σ_p) calculated by Bythrow et al., 1979 ranged from 2 to 16 mhos,comparable to the Σ_p's obtained by Brekke et al., 1974, and used by Yasuhara et al., 1975 in their current system modeling. Further simultaneous observations of ground disturbances, particles, currents, electric fields, and auroral light are required to continue progress in this area (Fairfield, 1977; Greenwald et al., 1979). The field-aligned currents increase in importance as more and more plasma phenomena become closely associated with them, the latest being auroral kilometric radiation (Green et al., 1979). It is widely believed that the FAC may be the "driving mechanism" for a variety of instabilities in the auroral regions and the front side boundary layer of the magnetosphere (Haerendel et al., 1978). The precise source location of the FAC and the nature of the particle charges whose motion is responsible for these currents remain as unanswered questions at the present time.

INSTRUMENTATION

The Air Force S3-2 scientific satellite was launched into a polar orbit in December, 1975, with initial perigee of 240 km, apogee 1557 km, and inclination 96.3°. The satellite was spin stabilized with its axis maintained to within 5° of the normal to the orbit plane. Vector measurements of the real magnetic field were made using a triaxial fluxgate magnetometer mounted at the end of a 20 foot Astromast boom. The sampling rate was 32 samples/axis/sec and the digitization resolution was 5nT. The difference of the real field from the IGRF (1975) model field was found, and the transverse magnetic field perturbations were measured and transformed into the geomagnetic coordinate system (F. Rich, private communication). Other details can be found in Burke et al. (1980), and Smiddy et al. (1980).

The second set of magnetic field measurements was obtained with the triaxial magnetometer on Triad, a U.S. Navy/APL satellite. This instrument has been described in Armstrong and Zmuda (1974). Its principal features are briefly summarized below. Triad was launched in September, 1972, into a circular polar orbit of 800 km altitude. Vector magnetic measurements were made at the rate of 2.25 samples/axis/sec with resolution of 12γ. The differences of the real field from the IGRF (1965) model, extrapolated to the pertinent epoch, were found and on that signal new baselines were established through filtering. From these baselines, the transverse magnetic field perturbations were measured and transformed into the geomagnetic coordinate system. Other details can be found in Saflekos and Potemra (1979).

The electric field experiment on the S3-2 satellite consisted of three orthogonal electrostatic dipoles with one along the spin axis and two in the spin plane. Of these three, the spin axis oriented dipole was subject to time varying contact potentials and of the other two in the spin plane, one failed to deploy. Thus,

the measurements were reduced to single axis components. The properly functioning dipole consisted of two spheres with 3.81 cm radii placed at the ends of insulated cable booms extending 13.72 meters out from the spacecraft surface. The duty cycle of this experiment was 512 sec beginning with a 10 sec calibration sequence. The probe was shorted to satellite ground for 1 second beginning at 128, 256, and 384 seconds into the duty cycle. In its highest sampling rate, 64 electric field components were obtained in one second. For the purposes of the present analysis, the 32 vectors per second rate was used. These were corrected for V x B effects of satellite motion and for different contact potentials on the spheres to obtain the component of ambient electric field in the spin plane. This was projected along the satellite trajectory and averaged over one spin period with successive averages shifted by five second intervals to obtain the electric field component along the satellite trajectory. A detailed account of the method of analysis of this experiment can be found in Burke et al., 1980.

OBSERVATIONS AND ANALYSIS

Figure 1 shows the Triad observations of transverse magnetic disturbances on day 267, 1976, versus UT (Universal Time). Figure 1A depicts the magnetic measurements in the magnetometer frame of reference versus geographic coordinates and Figure 1B shows the transformed data in geomagnetic coordinates. An important fact to note is that the disturbances are oriented in the east-west direction. If one assumes that these are effects due to field-aligned current sheets, then one distinguishes three current sheets: a very intense downward current equatorward of 76.2° magnetic latitude (MLAT) identified as the region 1 current of Iijima and Potemra, 1976a, and two other currents of opposite polarity one on either side of region 1.

Figure 2A shows the Triad and the S3-2 satellite subtracks for the same day around 1555 UT. As the two spacecraft moved equatorward over the north auroral oval in the dawn sector, each encountered the region 1 current system. First, the S3-2 satellite crossed the poleward boundary of region 1 at 75.4° MLAT and 0600 magnetic local time (MLT). The convection electric field reversal as observed by the S3-2 satellite was located at 74.7° MLAT near 0600 MLT. Second, the Triad satellite (14 minutes later) crossed the region 1 poleward boundary at 76.2° MLAT and 0820 MLT. The thicknesses of the current sheets were 2.3° as deduced from the Triad measurements and 1.9° as deduced from the S3-2 measurements. These facts imply that the current sheet thicknesses do not differ by more than 17% as they extend up to at least 2.5 hours in the east-west direction. The poleward displacement (0.8°) of the region 1 boundary at later local times is consistent with the auroral oval shape in the dawn to noon local time sector.

Figure 2B and the upper panel of Figure 2C show the transverse magnetic disturbances of Triad and S3-2 respectively, plotted to the same scale but time

shifted to match the poleward boundary of the region 1 currents. There is a

remarkable similarity between the two magnetic signatures. Apparently the region 1

currents are stable for periods of up to 15 minutes. Spatially they extend 520 km

upwards from 280 to 800 km altitude and eastward they extend up to 1100 km distance

roughly lying on the same magnetic shell surface.

In order to determine the current density distribution accurately one

must know the curl of the magnetic field. Here both spacecraft show that in

the geomagnetic spherical coordinate system the meridional and the radial

components of the transverse magnetic field variations are very much smaller

than the azimuthal components therefore, we consider them to be zero. Next, we

examine the spatial dependence of the azimuthal component (positive in the

eastward direction). Figure 2B and the upper panel of Figure 2C show that ΔB_y

(positive eastward) is strongly dependent on the x (positive southward) coordinate

and weakly dependent on the y (positive eastward) and the z (positive radially

outward) coordinates. The current density then is given by the equations

$$J_x = -\frac{1}{\mu_o} \frac{\partial(\Delta B_y)}{\partial z} \quad \text{and}$$

$$J_z = \frac{1}{\mu_o} \frac{\partial(\Delta B_y)}{\partial x}$$

in the space between the two spacecraft.

The meridional component of the current density J_x (positive in the southward

direction) was found to be -0.04 $\mu A/m^2$ flowing northward. This value resulted

from using $\Delta B_y = 22$nT (1nT $= 10^{-5}$ gauss) and $\Delta z = 500$ km. The parallel currents

J_z (positive radially outward) were also calculated and found to be -1.77 $\mu A/m^2$

at the S3-2 altitude of 280 km using magnetic deflection $\Delta B = 480$ nT and -1.41 $\mu A/m^2$

at the Triad altitude of 800 km using $\Delta B_y = 512$ nT. By comparison, the meridional

current density is 2% of the parallel current density and it can easily be ignored.

If we assume uniform density in the east-west as well as the north-south direction, we find that the total parallel current sheet intensities at the two altitudes are nearly equal. In fact, the total current sheet intensity at the Triad altitude is 407 mA/m and at the S3-2 altitude is 390 mA/m. The difference is a small loss of 4% before the current reaches the lower altitude, which can also be ignored. Next we investigate the altitude dependence of the current density. It increases by 26% over a 500 km altitude decrease. This is to be compared with the magnetic flux density increase of 25% from 40000 nT to 50000 nT over the same altitude difference. The last two percentages are practically equal and they imply that there were no significant current losses between the two different sites. Thus, these results confirm the idea that the field-aligned current densities are focused by the convergence of the magnetic field lines.

The region 2 currents at the Triad altitude show greater variation than the region 2 currents at S3-2 altitude. The integrated current sheet intensity at 800 km altitude was 267 mA/m and at 280 km altitude 358 mA/m, a change of 34%. In this case, the focusing accounts for only 25% of the observed 34% increase, so it is possible that in 14 minutes the region 2 current densities changed by 9%.

By now it is well known that region 2 is more variable than region 1. Poleward of region 1 in the Triad data there is yet a third current with integrated current sheet intensity of 141 mA/m. What is interesting about this current intensity is that is constitutes the supplemental return current to region 2 needed to exactly balance the current in region 1. Thus while at S3-2 altitude the region 1 closes through southward flow in the ionosphere and back up into region 2, at Triad altitude 14 min later the region 1 closes partly via southward ionospheric current flow into region 2 and partly via northward ionospheric current flow into field lines poleward of region 1.

With regard to small scale variations (Saflekos et al., 1978), there is a V-shaped feature embedded in region 2. The midpoint of the feature is located at 69.6° MLAT as seen by S3-2 and at 72.2° MLAT as seen by Triad but 14 minutes later. If these small disturbances are due to currents associated with a discrete auroral arc, then this arc has moved 2.6° poleward in 14 minutes. The Pedersen conductivity corresponding to the downward current leg is 23.2 mhos and to the upward current leg is 34.8 mhos. The high values of the conductivity imply intense heating in the region of the discrete arc. Other small scale features at Triad altitudes did not show up at S3-2 altitudes either because they are localized or because they vary rapidly in time.

Figure 2C, bottom panel, shows the forward convective electric field. At 75° MLAT in the dawn sector, it is within 5° of being southward (positive). Thus, even though we do not have the complete vector of the convective electric field, the measured electric field is nearly perpendicular to the well-established east-west current sheets measured simultaneously. We believe that there has been no other satellite capable of making simultaneous electric and magentic field measurements with as high a temporal resolution. With this data set, we can resolve small features. For instance, at the 69.6° MLAT of S3-2, we find a sudden increase of the electric field that lasts 15 sec followed by a slower return to the baseline. This electric field variation correlates well with an opposite variation of the magnetic field. In fact, the increase of the electric field in the southward direction is consistent with the closure of these two narrow antiparallel current sheets via ionospheric Pedersen currents. As stated earlier this structure may correspond to a discrete visual auroral arc embedded in the diffuse aurora.

The dashed vertical line in Figure 2 represents the electric field reversal from northward to southward along decreasing MLAT around 0600 MLT. For the S3-2

data it is interesting to compare the height integrated Pedersen conductivity (Σ_p) of region 1 poleward of the electric field reversal to that of region 1 equatorward of the reversal and to that of region 2. We find them to be 3.0, 3.8 and 6.1 mhos in that order. (The evaluation of Σ_p from the S3-2 magnetic and electric field data has been discussed previously by Shuman et al., 1981.) This probably indicates that the particle spectra responsible for the presence of the conductivity become softer with increasing latitude. The third poleward upward current in the Triad data is similar to cusp currents but it most likely corresponds to some sun-aligned auroral arc, a class of auroral phenomena often seen in this sector.

On the dawn side, the electric field reversal is 0.7° to the equatorward side of the high latitude boundary of the region 1 currents. Thus a poleward portion of the region 1 currents flow on open field lines. The magnetic conditions during this event were moderately quiet with planetary magnetic index K_p equal to 2. The interplanetary magentic field (IMF) in geocentric solar magnetospheric (GSM) co-ordinates was (-0.6, 1.8, -0.7) nT. As usual, the positive IMF By component is associated with a stronger dawn-side region 1 current in comparison to a weaker dusk-side region 1 current. This is not surprising as the expression $\frac{\partial}{\partial x} (\Delta By - \mu_o \Sigma_p \Delta E_x) = 0$ implies a linear relationship between ΔBy and ΔEx for a well-behaved integrated Pedersen conductivity Σ_p, and as is well known, ΔEx depends on the By-component of the IMF, thus making ΔBy dependent on the IMF as well.

On the dusk side the boundaries of the poleward termination of the region 1 current and the electric field reversal do not coincide. However, the portion of region 1 flowing poleward of the electric field reversal and equatorward of the vertical line at 56560 sec GMT is much smaller than the portion of region 1 equatorward of the electric field reversal. By inspection one finds that the extension of the region 1 current into the polar cap (open magnetic field lines) carried higher current density on the dawn side in comparison to the dusk side, during this event in the northern hemisphere when the By component of the IMF was positive.

The dusk side signature of the electric and magnetic fields of Figure 2 give us the opportunity to study a phenomenon which occurs frequently in the Triad data base. That is the region 1 and region 2 currents are not adjacent to each other;instead, they are separated by a relatively broad region carrying very weak currents.

As the S3-2 satellite moves poleward, it first encounters a steep electric field gradient between 60.4° and 61.9° MLAT. The integrated Pedersen conductivity in this region is only 0.75 mhos. Between 61.9° and 64.7° MLAT we identify the dusk-side region 2 current. In it the Pedersen conductivity is 21.9 mhos. Further poleward, in the interval 64.7° to 68.6° MLAT, the electric and magnetic field plots are nearly flat. Here the Pedersen conductivity goes down to 3.3 mhos and rises again in region 1 to 4.9 mhos. The electric field around 1930 MLT is pointing to within 5° of magnetic north. At the same time the transverse magnetic field decreases in the eastward direction in region 2, and increases in region 1. Obviously there is convection in this region as the electric field remains at high values, but the slope of the electric field has flattened so much that it can no longer support a large closing Pedersen current in the ionosphere.

Figure 3 is similar to Figure 2 only for day 305, 1976 around 1200 UT. Figure 3A is a MLT-MLAT polar plot showing the satellite subtracks. The lag between the two spacecraft was nine minutes. The two tracks crossed at 80° MLAT just two degrees poleward of the region 1 currents. Both satellites crossed the current sheets at an altitude of about 850 km, separated from each other by a short angular distance of 10° (40 minutes in magnetic local time).

Figures 3B and 3C show that the poleward boundary of region 1 was first encountered by Triad at 78.1° MLAT and nine minutes later by S3-2 at 77.4° MLAT.

If it is assumed that the current sheet moved uniformly, its average southward velocity was 0.16 km/sec which is small in comparison to the satellite velocity of 7.5 km/sec. In calculating current sheet thicknesses one always assumes a stationary current sheet. Here using two spacecraft, we remove this assumption in a reasonable manner as was shown in the previous event. The thickness of the region 1 current increased from 4.3^O to 5.5^O MLAT in nine minutes as it moved equatorward. The integrated current sheet intensities of region 1 were 400 mA/m and 296 mA/m for Triad and S3-2 respectively. In region 1 the current density was 0.42 $\mu A/m^2$ and the corresponding Pedersen conductivity was 4.7 mhos as determined by S3-2. The integrated current sheet intensities differed by 26%. All the differences between the S3-2 and Triad measurements here should be explained only by temporal variations as the two spacecraft cruised on nearly identical trajectories. It is assumed that the spacecraft measure magnetic field gradients accurately. In the short time of nine minutes the region 1 current density changed by 40% because the beam spread out and got weaker. For the purpose of studying steady state large-scale field-aligned currents in this paper, we can consider the measurements at about 1200 UT as reference points for crosscalibration of the sensitivities of the two magnetometers. Of course we assume that both instruments measure rapid changes of the magnetic field with an accuracy better than 12.5 nT.

Referring to the position of the convective electric field reversal, it was found to be 1.1^O equatorward of the high latitude boundary of region 1. The counterpart difference on the dusk side was 0.7^O. The planetary magnetic index Kp during this event was 4+. The IMF vector was (-4.7, 4.4, 2.2) nT. The positive By component is consistent with the dawn-dusk asymmetry observed in the magnetic

and electric field measurements and the positive B_z component is consistent with the structured polar cap convection electric field, Burke et al., 1979.

On this day the Triad satellite happened to cross the same local time sector six times in a row. Figure 4 shows the triaxial fluxgate magnetometer records at about 1.5 hour intervals. One can clearly see that the transverse disturbances from the A and B sensors grow and decay in a time scale of five hours. During this time period the locations of the current sheets exhibit excursions reaching from a low invariant latitude of 69.4° to a high invariant latitude of 78.1°. The Kp index was near 4+ in this time interval. These temporal variations of the location and extent of the current sheets make correlative studies difficult and only quasisimultaneous observations should be used for such purposes as we are following in this paper.

In order to check the hypothesis that the current sheets execute latitudinal motion, we assumed uniform sheet velocity from one pass to the next. The most probable latitudinal velocity was 0.1 km/sec, consistent with the dual spacecraft observations described for this day. The next two examples, for a quieter period, are presented in order of increasing Kp.

Figure 5 is a third example similar to Figure 1 only for day 267, 1976, around 2240 UT. This is another good local time coincidence with a UT lag of 12.5 minutes. Figures 5B and 5C show that the poleward boundaries of region 1 were displaced by 0.8° MLAT. The trailing Triad satellite located the poleward boundary of region 1 at 73.4° MLAT. The satellite altitudes differed by about 500 km so that all of the latitudinal separation can be accounted for by the geometry of the magnetic field lines.

124

The measured widths of the region 1 current sheets were 2.25° for the high altitude and 2.4° for the low altitude. The Triad density was 2.0 $\mu A/m^2$ and the lower altitude S3-2 density was 1.5$\mu A/m^2$. Apparently a 25% difference expected from current focusing due to the convergence of the polar magnetic field did not materialize. In fact the higher altitude spacecraft measured a larger current density. Thus some of the FAC is shorted out by Pedersen currents flowing in the region between the high- and the low-altitude space-craft. Here the electric field reversal was 0.8° MLAT equatorward of the poleward boundary of the region 1 current. The current's high latitude location is consistent with quiet magnetic conditions at kp = 1+. The healthy magnetic disturbance of 500 nT on the dawn side is consistent with positive IMF By-component of 1.8 nT and negative Bz-component of -0.4 nT. It is interesting to note that the Pedersen conductivity in region 2 is 7.2 mhos whereas, in region 1 it is 9.8 mhos. Poleward of the electric field reversal we see small-scale transverse magnetic field variations. Inside the region from 75.6° to 73.4° MLAT the average Pedersen conductivity is only 2.7 mhos. Thus in this case there is a strong latitudinal conductivity gradient that inhibits the horizontal flow of current into the polar cap.

Figure 6 shows the last coincidence between Triad and S3-2 satellites to be presented. It occurred 101 minutes before the coincidence described in Figure 5. As shown in Figure 6A the two spacecraft were moving equatorward when they crossed paths at about 82° MLAT. They encountered the poleward boundary of region 1 at almost the same latitude but different altitudes and magnetic local times. Though the signatures in this and the preceding event are remarkably similar they do show variations in fine structure, location and extent. During this

event of September 23, 1976 around 1736 UT the magnetic conditions were slightly more disturbed (Kp = 2) in comparison to the event just described, and the IMF vector was (-1.3, 2.3, -0.1) nT in GSM coordinates.

Figures 6B and 6C upper panel show the magnetic field measurements with a time delay of 14 minutes. The S3-2 satellite encountered the region 1 poleward boundary at 75° MLAT, the electric field reversal at 74° MLAT, the demarcation line between region 1 and region 2 at 71.1 MLAT, and the equatorward boundary of region 2 at 66.1^o MLAT, all around 0554 MLT and 277 km altitude. The portion of region 1 that extended poleward of the electric field reversal was 1.0^o of latitude. The average integrated Pedersen conductivities in region 1 and region 2 were 2.9 and 5.4 mhos respectively. Equatorward of the electric field reversal S3-2 encountered a rapid decrease of the convection electric field, which is associated with a roughly corresponding increase of the magnetic field. This anticorrelation type of event, seen once before in a previous pass, may be the signature of a discrete auroral arc close to the electric field reversal.

The Triad satellite encountered the poleward boundary of region 1 at 76.0^o MLAT, the demarcation line between region 1 and region 2 at 73.0^o MLAT, and the equatorward boundary of region 2 at 69.0^o MLAT. The average region 1 current sheet densities at Triad and S3-2 altitudes were 0.61 $\mu A/m^2$ and 0.50 $\mu A/m^2$ respectively. Again we see that the higher altitude current densities are greater by 20%, an effect contrary to what magnetic focusing of the current would produce. On the other hand the region 2 current densities are 0.27 and 0.34 $\mu A/m^2$ for the altitudes of Triad and S3-2 respectively. In this region the lower altitude current density is greater by 21% as expected of magnetic convergence of the beam.

On the dusk-side the S3-2 satellite observed two weaker currents separated by a nearly zero current carrying disturbance region. In this same interval from 70.4° to 72.4° MLAT, not only the bottom of the magnetic disturbance signal is flat but the top of the electric field signal approaches a zero slope as well. Since the quantity $\frac{\partial}{\partial x}$ (ΔBy) is approximately zero, the assumed constant Pedersen conductivity must be nearly zero in that interval. Thus the two independent current sheets, one in the interval between 69.3° and 70.4° MLAT, and the other in the interval from 72.4° to 74.3° MLAT must close in the ionosphere via stronger heating Pedersen currents as they flow in a larger ionospheric volume with spatially varying conductivity. From what we have presented so far we see that only regions with gradients in the electric field can support field-aligned currents. The regions of zero field-aligned current embedded between region 1 and region 2 currents are probably associated with isotropic auroral particle precipitation across the diffuse aurora, or they are associated with auroral particle dropouts separating the diffuse from the discrete aurora.

DISCUSSION

1. Spatial and Temporal Variations of Birkeland Currents.

From coordinated observations between the Triad and the S3-2 satellites we found that the dawn Birkeland currents can move poleward as well as equatorward at an average speed less than .15 km/sec. The mother-daughter satellite configuration has allowed us for the first time to conclude that the Birkeland currents are spatial structures observed with a temporal resolution of nine to sixteen minutes (the satellite lag time). Previously it was known that currents persisted for at least two minutes (the satellite transit time through a current carrying region) or for as long as multiples of the satellite orbital period. From continuous coverage of a single local time sector with Triad satellite we have determined that the Birkeland currents can vanish after a period of the order of five hours. For an example of this type, see our Figure 4. On the other end of the spectrum, magnetic variations of the order of tens of seconds were observed on Triad but not as clearly on S3-2, and vice versa.

2. Spatial Extent of Birkeland Current Sheets.

This study has shown that the current sheets can extend at least up to 35° in the east-west direction and at least up to 500 km in altitude. From the two-point measurements, we determined that the current sheets do not move with latitudinal average velocities greater than 0.15 km/sec. Thus, the thicknesses previously determined by single spacecraft are reasonable approximations of the true values.

3. Current Density Gradients.

A search for large gradients in current density along longitude and altitude did not materialize. If the current continuity equation is applied, a decrease of current density with altitude is expected amounting to about 25% for an increase of altitude from 300 to 800 km. Further verification of this result is needed,as this fact is fundamental to the questions of: where are the sources and what are the sources and the charge carriers of the field-aligned currents. Many of the current models of global field-aligned currents and electric fields use the current continuity equation and the ionospheric Ohm's law to describe relationships between currents and electric fields.

4. Relationships Between Birkeland Currents Convection Electric Fields and the IMF.

Simultaneous observations inside and outside the magnetosphere have helped us to better understand the auroral phenomena described in this paper. The Triad and S3-2 magnetic disturbance measurements acquired during positive IMF B_y components were nearly identical. From the S3-2 DC electric and magnetic field measurements it was determined that during an away IMF sector ($B_y > 0$), regardless of IMF B_z direction, the dusk side currents and electric fields were weaker. In two out of three cases the currents terminated very close to the convective electric field reversal. On the dawn-side for the same IMF conditions the convective electric field reversal was about 1.5^o equatorward of the poleward termination of the field-aligned currents. From this we conclude that the greater portion of the Birkeland current regions carry current that flows on closed magnetic field lines. The small part that flows on open field lines must have its sources near the magnetopause or the mantle and the boundary layer. In the dawn sector the stronger region 1 current is downward. If it is carried by protons, these particles must come from the mantle or boundary layer having reversed their flow velocities. Furthermore,

this plasma must have passed through an electric field that separated the charges. Field-aligned downward currents flowing in limited regions in the cusp on open field lines have been observed by the high altitude Hawkeye 1 satellite (Saflekos et al., 1979). The only difference is that the cusp current for IMF $B_y > 0$ was directed upward and therefore it is different than the region 1 current flowing poleward of the electric field reversal in the dawn sector. Our present results are consistent with the correlations between the sign of IMF B_y and the mantle occurrence as well as between the sign of IMF B_y and the mantle thickness reported by Hardy et al., 1976.

5. Orientation of Birkeland Current Sheets.

The dual satellite observations have shown for the first time that, for the four cases presented here in detail, the Birkland current sheets were oriented strictly in the magnetic east-west direction, with deviations from zero to less than one degree. It is obvious that the magnetic disturbances due to current sheets lie nearly on lines parallel to convection velocity lines (Saflekos and Potemra, 1979). The S3-2 electric field measurement is effectively a one-axis measurement so it cannot contribute to the direct comparison of convective velocity direction and Birkeland current sheet orientation. One interesting observation borne out in the electric field data however, is that the extent of the convective velocity gradients, particularly on the poleward side, is wider than the extent of the magnetic disturbance gradients (for more examples see for instance Potemra et al., 1979, their Figure 14). The implications of this observation are that one cannot infer the entire convective velocity region from the magnetic disturbances. This means that there are regions with convective velocity gradients which are not associated with magnetic disturbances. Perhaps then the magnetic disturbances are not caused by altitude dependent differential convection of geomagnetic field lines producing a tilt relative to

model magnetic field lines. Rather, they are caused solely by the presence of currents flowing along magnetic field lines. At the present time the baselines of the magnetometer sensors on Triad and S3-2 are known to an accuracy of the order of 100 nT so it is possible to make statements comparable to those of McDiarmid et al., 1978a, 1978b, concerning the polar cap boundary identification using region 1 magnetic signatures alone.

CONCLUSIONS

The following are our principal findings from an analysis of four near coincident S3-2 and Triad magnetic observations in the northern polar region in the dawn sector.

1. The large scale Birkeland current sheets have features which persist for multiples of satellite periods.

2. The Birkeland current sheets move slowly with velocities less than .15 km/sec in the north-south direction.

3. The Birkeland current sheets are oriented strictly in the magnetic east-west direction.

4. The Birkeland current sheets are a few degrees thick and they extend at least up to 1100 km in longitude and at least up to 500 km in altitude.

5. The Birkeland current densities do not show systematic pronounced gradients either with altitude or with longitude. But in at least one of these cases the current was stronger at higher altitudes.

6. The convective electric field-reversal is located at the poleward termination of the Region 1 field-aligned current system or equatorward of this boundary, not deviating by more than one and a half degrees from it.

7. There are additional extended weaker current sheets, poleward of region 1, having reverse flow polarities in the dawn-side of the polar cap.

8. The portion of region 1 currents poleward of the electric field reversal and the antiparallel large scale polar cap currents most likely have their sources near the outer magnetospheric boundaries.

9. The portion of region 1 current equatorward of the electric field reversal and all of region 2 current which flow on closed field lines probably have their sources in the plasma sheet.

10. Simultaneous small scale magnetic and electric field variations superimposed on the region 1 disturbance and observed at widely separated local times on both sides of the electric field reversal may correspond to discrete auroral arcs on closed as well as on open magnetic field lines.

FIGURE CAPTIONS

Figure 1 A. Magnetic deflections observed on Day 267 of 1976 around 1600 UT. The figure shows the measured minus the model magnetic field residuals in the magnetometer frame of reference. Sensor Z points upwards, sensor A points 135° away from the velocity vector in the clockwise direction as seen from the positive Z-axis and sensor B completes the right-handed triaxial orthogonal system.

1 B. Shows polar plots of the magnitude and direction of the magnetic disturbance vectors measured by the Triad satellite over the northern polar region. Universal times (UT; hours, minutes) are marked along the satellite track. The vectors resulted from smoothing of the Figure 1A data with a three minute high-pass filter and then transforming to geomagnetic coordinates. Figure 1B shows that the field-aligned current sheets are oriented along the east-west direction.

Figure 2 A. Polar plot of the Triad and S3-2 satellite tracks in geomagnetic coordinates. Observations made on September 23, 1976 around 1600 UT. Indicated are the observed region 1 current boundaries and the simultaneously observed electric field reversal.

2 B. Represents the magnetic field disturbance due to field-aligned currents. The top trace is the magnetic north-south component and the bottom trace is the magnetic east-west component, both in geomagnetic coordinates. The data are the same as those presented in Figure 1B. The vertical lines in the figure mark the boundaries of region 1 currents and the position of the convection electric field reversal as determined by the S3-2 D.C. electric field probe.

Figure 2 C.   Upper panel shows the east-west component of the transformed
difference of the real minus the model magnetic field vectors.
Lower panel shows the component of the convective electric field
along the satellite velocity vector. Positive values below 75°
MLAT on the dawn side are pointing to within twenty degrees of
true magnetic south.

Figure 3.   The same as Figure 2 only for day 305, 1976 around 1200 UT.

Figure 4.   A sequence of successive Triad polar passes over the northern
polar region showing the latitudinal displacement of the region 1
current at dawn as a function of satellite rise time. If it is
assumed that the current sheets move uniformly, their average
velocities are about 0.1 km/sec. The currents are observed to
vanish in time scales of the order of five hours. The data were
acquired on day 305, 1976 by the Triad satellite.

Figure 5.   The same as Figure 2 only for day 267, 1976 around 2240 UT.

Figure 6.   The same as Figure 2 only for day 267, 1976 around 1740 UT.

REFERENCES

Anderson, H.R., and R.R. Vondrak, Observations of Birkeland currents at auroral latitudes, Rev. Geophys. Space Phys., 13, 243, 1975.

Armstrong, J.C., and A.J. Zmuda, The diurnal flow pattern of field-aligned currents, J. Geophys. Res., 79, 4611, 1974.

Brekke, A., J.R. Doupnik, and P.M. Banks, Incoherent scatter measurements of E region conductivities and currents in the auroral zone, J. Geophys. Res., 79, 3773, 1974.

Burke, W.J., D.A. Hardy, F.J. Rich, M.C. Kelley, M. Smiddy, B. Shuman, R.C. Sagalyn, R.P. Vancour, P.J.L. Wildman, and S.T. Lai, Electrodynamic structure of the late evening sector of the auroral zone, J. Geophys. Res., 85, 1179, 1980.

Burke, W.J., M.C. Kelley, R.C. Sagalyn, M. Smiddy, and S.T. Lai, Polar cap electric field structures with a northward interplanetary magnetic field, Geophys. Res. Lett., 6, 21, 1979.

Bythrow, P.F., R.A. Heelis, W.B. Hanson, and R.A. Power, Simultaneous observations of field-aligned currents and plasma drift velocities by Atmosphere Explorer - C, J. Geophys. Res., 85, 151, 1980.

Fairfield, D.H., Electric and magnetic fields in the high latitude magnetosphere, Rev. Geophys. Space Phys., 15, 285, 1977.

Green, J.L., N.A. Saflekos, D.A. Gurnett, and T.A. Potemra, A correlation between auroral kilometric radiation and field-aligned currents, submitted to J. Geophys. Res., 1979.

Greenwald, R.A., T.A. Potemra, and N.A. Saflekos, Stare and Triad observations of field-aligned current closure and joule heating in the vicinity of the Harang discontinuity, J. Geophys. Res., 85, 563, 1980.

Haerendel, G., G. Paschmann, N. Sckopke, H. Rosenbauer, and P.C. Hedgecock, The front side boundary layer of the magnetosphere and the problem of reconnection, J. Geophys. Res., 83, 3195, 1978.

Hardy, D.A., J.W. Freeman, and H.K. Hills, Plasma observations in the magnetotail, Magnetospheric Particles and Fields, edited by B.M. McCormac, pp. 89-98, D. Reidel, Dordrecht, Netherlands, 1976.

Iijima, T., and T.A. Potemra, The amplitude distribution of field-aligned currents at northern high latitudes, J. Geophys. Res., 81, 2165, 1976a.

Iijima, T., and T.A. Potemra, Field-aligned currents in the dayside cusp observed by Triad, J. Geophys. Res., 81, 5971, 1976b.

Iijima, T., R. Fujii, T.A. Potemra and N.A. Saflekos, Field-aligned currents in the south polar cusp and their relationship to the interplanetary magnetic field, J. Geophys. Res., 83, 5595, 1978.

McDiarmid, I.B., J.R. Burrows, and M.D. Wilson, Comparison of magnetic field perturbations at high latitudes with charged particle and IMF measurements, J. Geophys. Res., 83, 681, 1978a.

McDiarmid, I.B., J.R. Burrows, and M.D. Wilson, Magentic field perturbations in the dayside cleft and their relationship to the IMF, J. Geophys. Res., 83, 5753, 1978b.

Olson, W.P., and K.A. Pfitzer, A quantitative model of the magnetospheric field, J. Geophys. Res., 79, 3739, 1974.

Potemra, T.A., T. Iijima, and N.A. Saflekos, Large-scale characteristics of Birkeland currents, Astrophys. and Space Sci., Library Series (in press), 1979.

Potemra, T.A., and N.A. Saflekos, Birkeland currents and the interplanetary magnetic field, Proceedings of Magnetospheric Boundary Layers Conference, Alpbach, 11-15 June, 1979, (ESA SP-148, August, 1979).

Saflekos, N.A., T.A. Potemra, T. Iijima, Small-scale transverse magnetic field disturbances in the polar regions observed by Triad, J. Geophys. Res., 83, 1493, 1978.

Saflekos, N.A., T.A. Potemra, P.M. Kintner, Jr., and J.L. Green, Field-aligned currents, convection electric fields, and VLF-ELF waves in the cusp, J. Geophys. Res., 84, 1391, 1979.

Saflekos, N.A., and T.A. Potemra, The orientation of Birkeland current sheets in the dayside polar region and the IMF, J. Geophys. Res., 85, 1987, 1979.

Shuman, B.M., R.P. Vancour, M. Smiddy, N.A. Saflekos, and F.J. Rich, Field-aligned current, convective electric field, and auroral particle measurements during a major magnetic storm, J. Geophys. Res., 86, in press, 1981.

Smiddy, M., W.J. Burke, M.C. Kelley, N.A. Saflekos, M.S. Gussenhoven, D.S. Hardy, F.J. Rich, Effects of high latitude conductivity on observed convection electric fields and Birkeland currents, J. Geophys. Res., 85, 6811, 1980.

Yasuhara, F., Y. Kamide, and S.-I. Akasofu, Field-aligned and ionospheric currents, Planet. Space Sci., 23, 1355, 1975.

ACKNOWLEDGEMENTS

RESOLUTE YRDAY 1976-267 9/23/76
RISE 1555:50 UT

UT	57470	57590	57710	57830	57950
LONG	267.88	266.03	265.30	264.71	264.16
LAT	87.25	80.01	72.75	65.50	58.25

Figure 1A

139
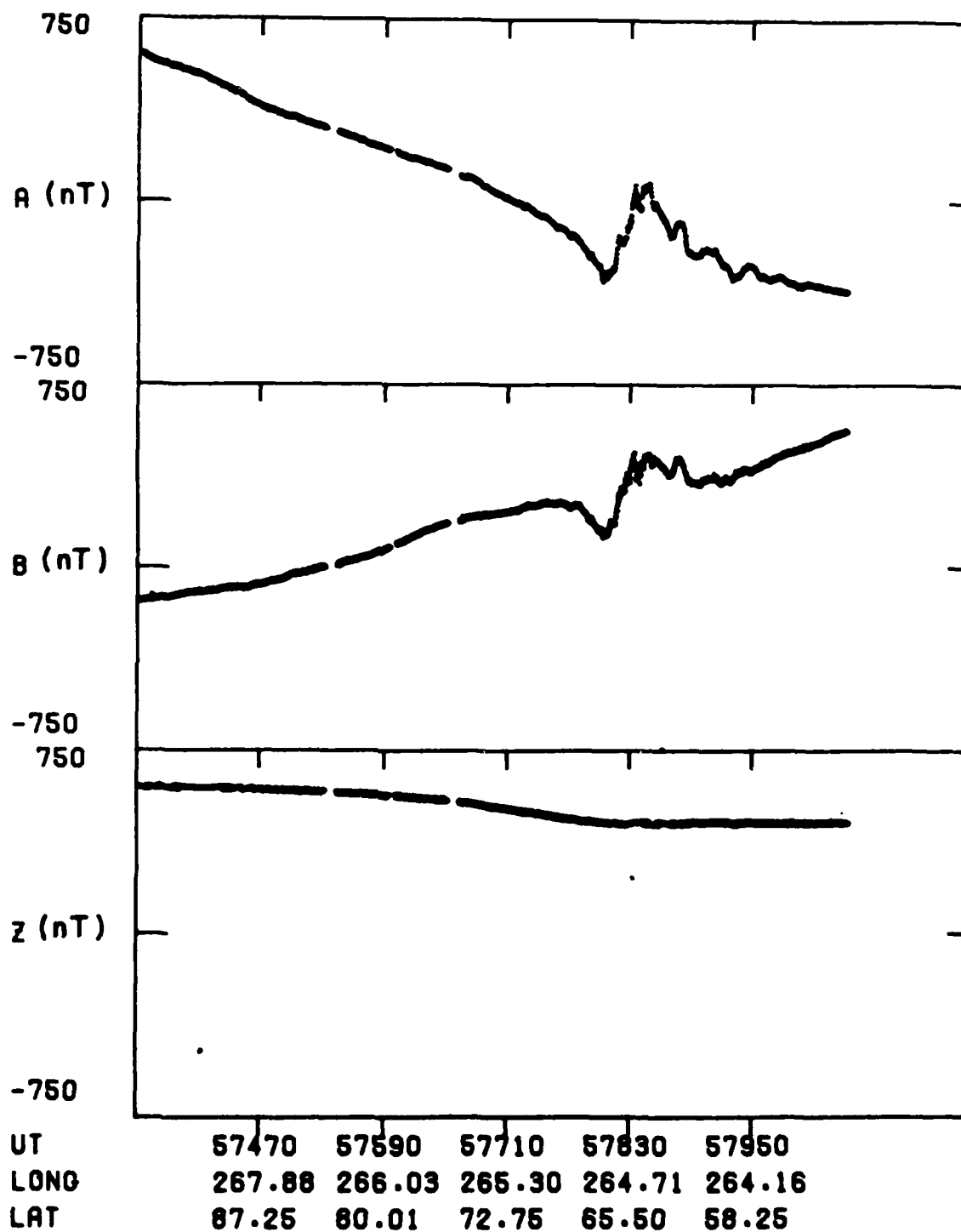
YRDAY 76 267
SEPT 23, 76
N HEMISPHERE
ALT 800 KM

12 MLT HRS

9

6

3

50° MLAT

15

18

21

24

70°

1556
1558
1600
1602
1604
1606HHMM

DB MAGNETIC
200 GAMMAS

Figure 1B
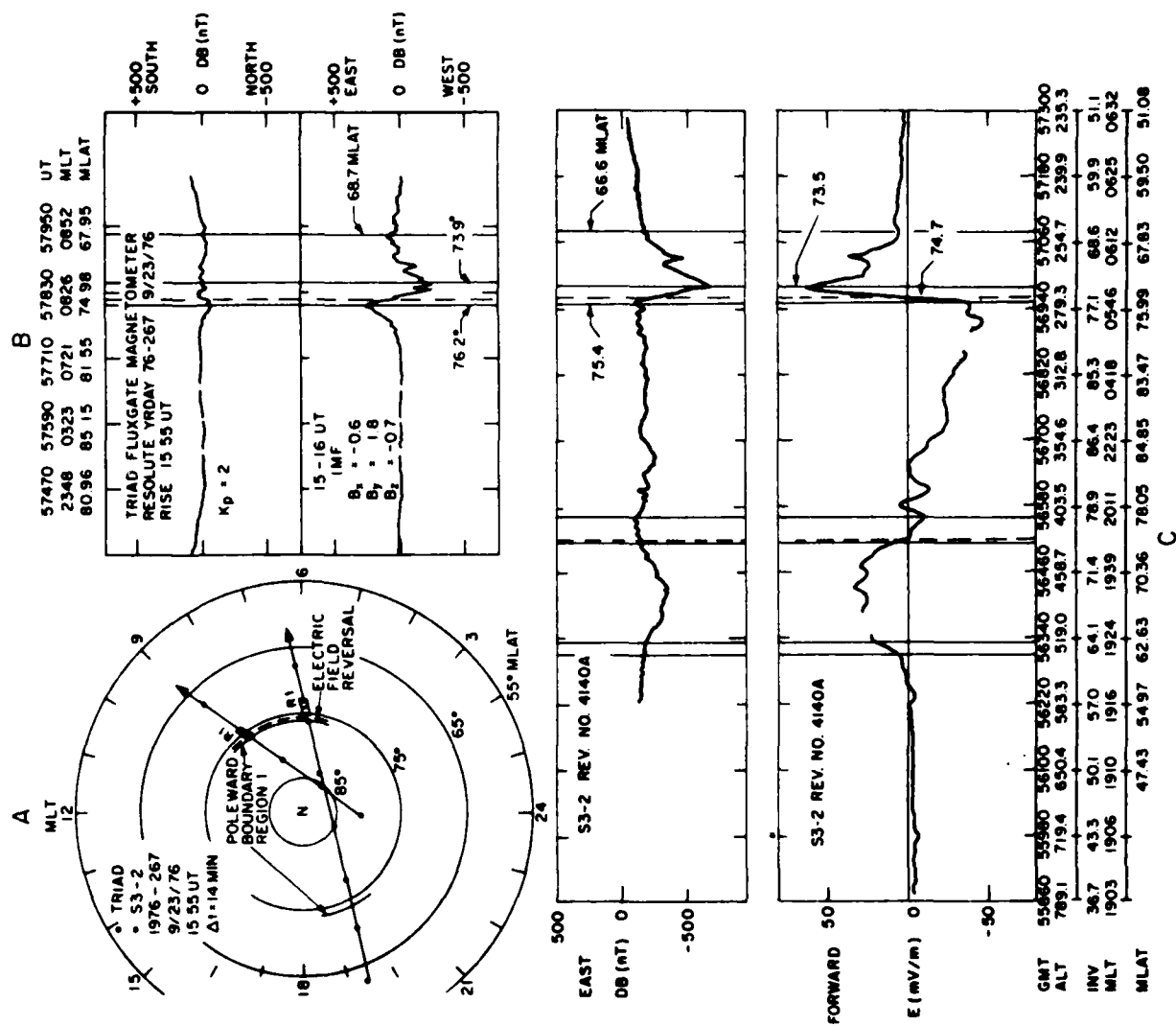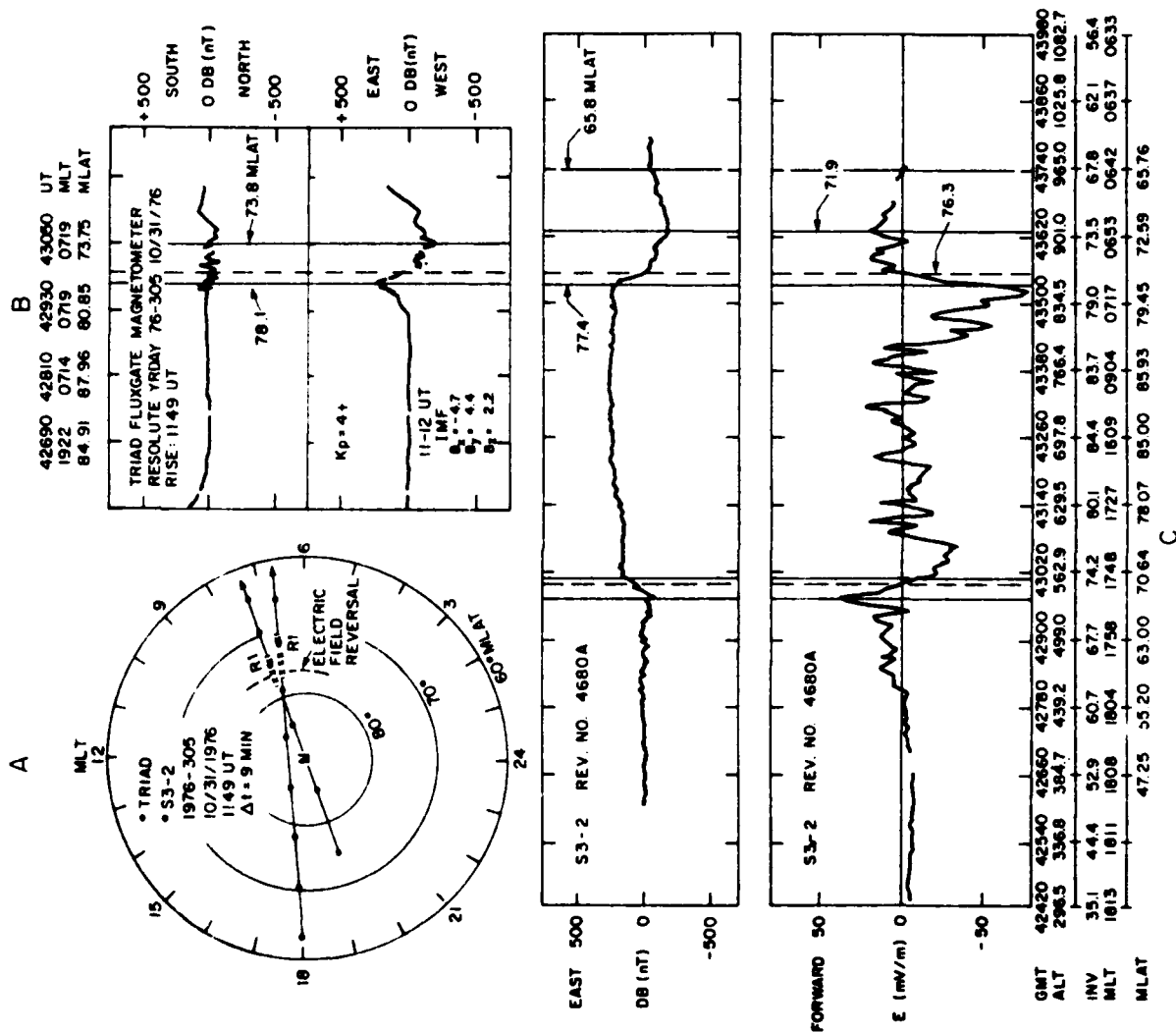
Figure 2

141
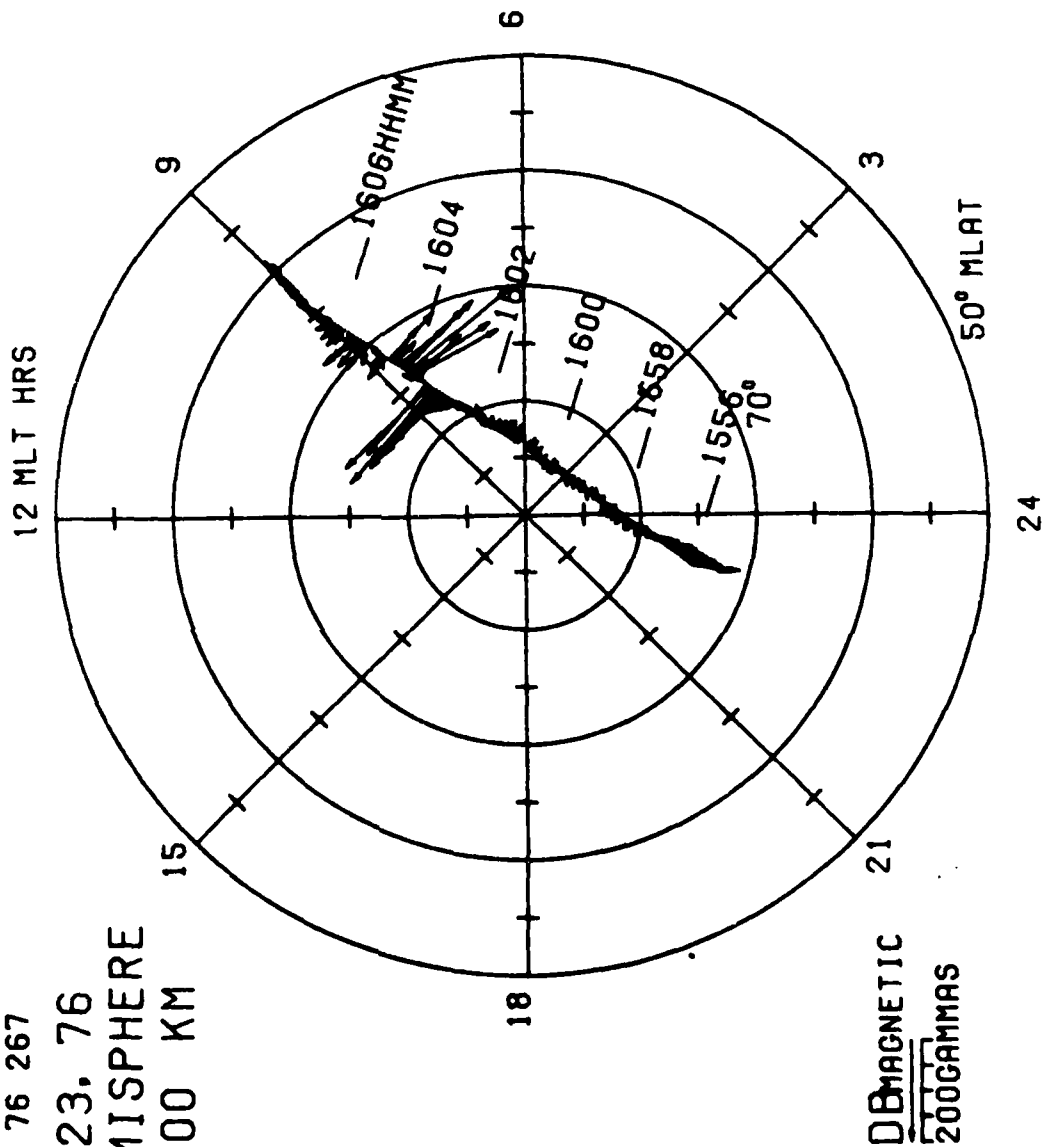
Figure 3

TRIAD FLUXGATE MAGNETOMETER
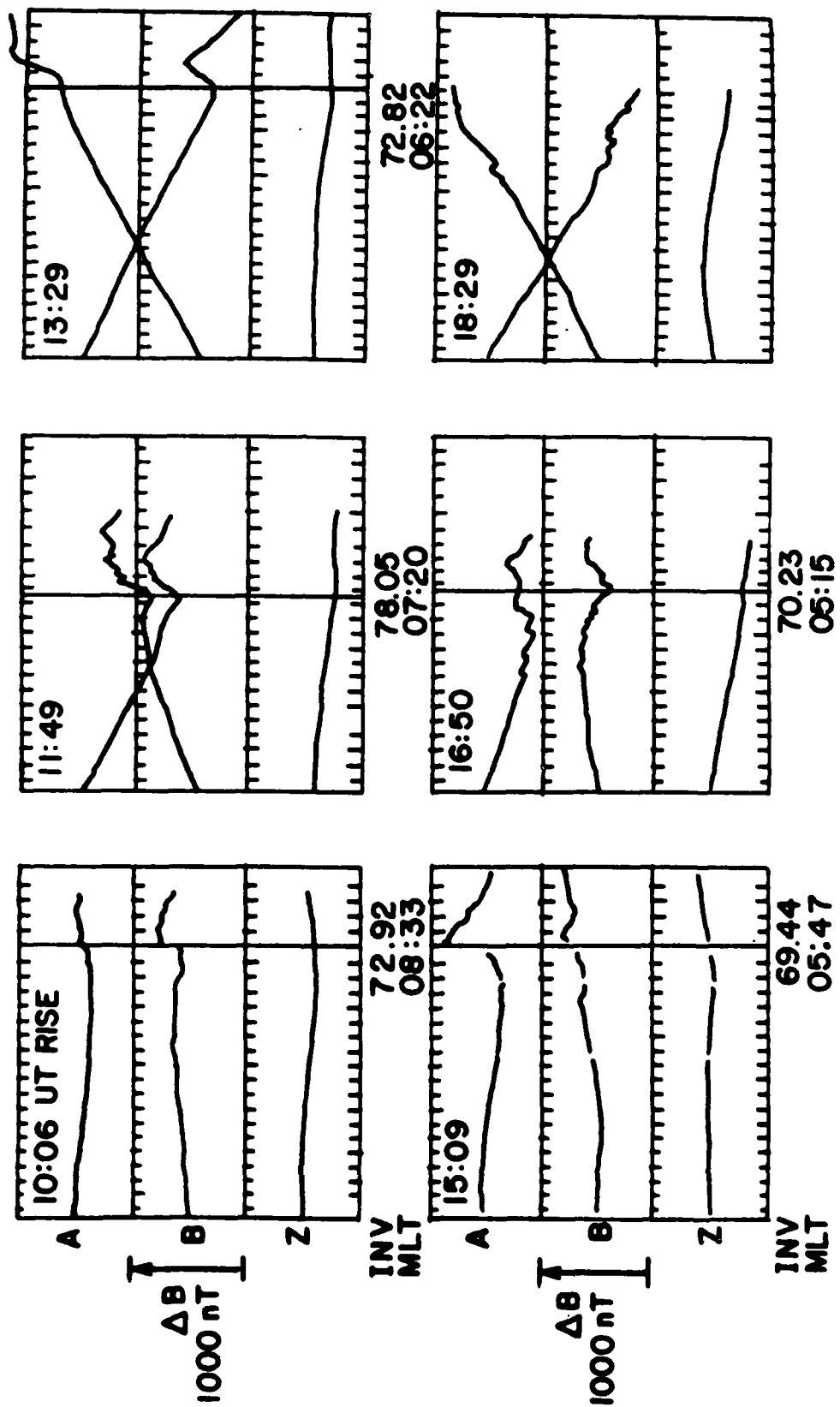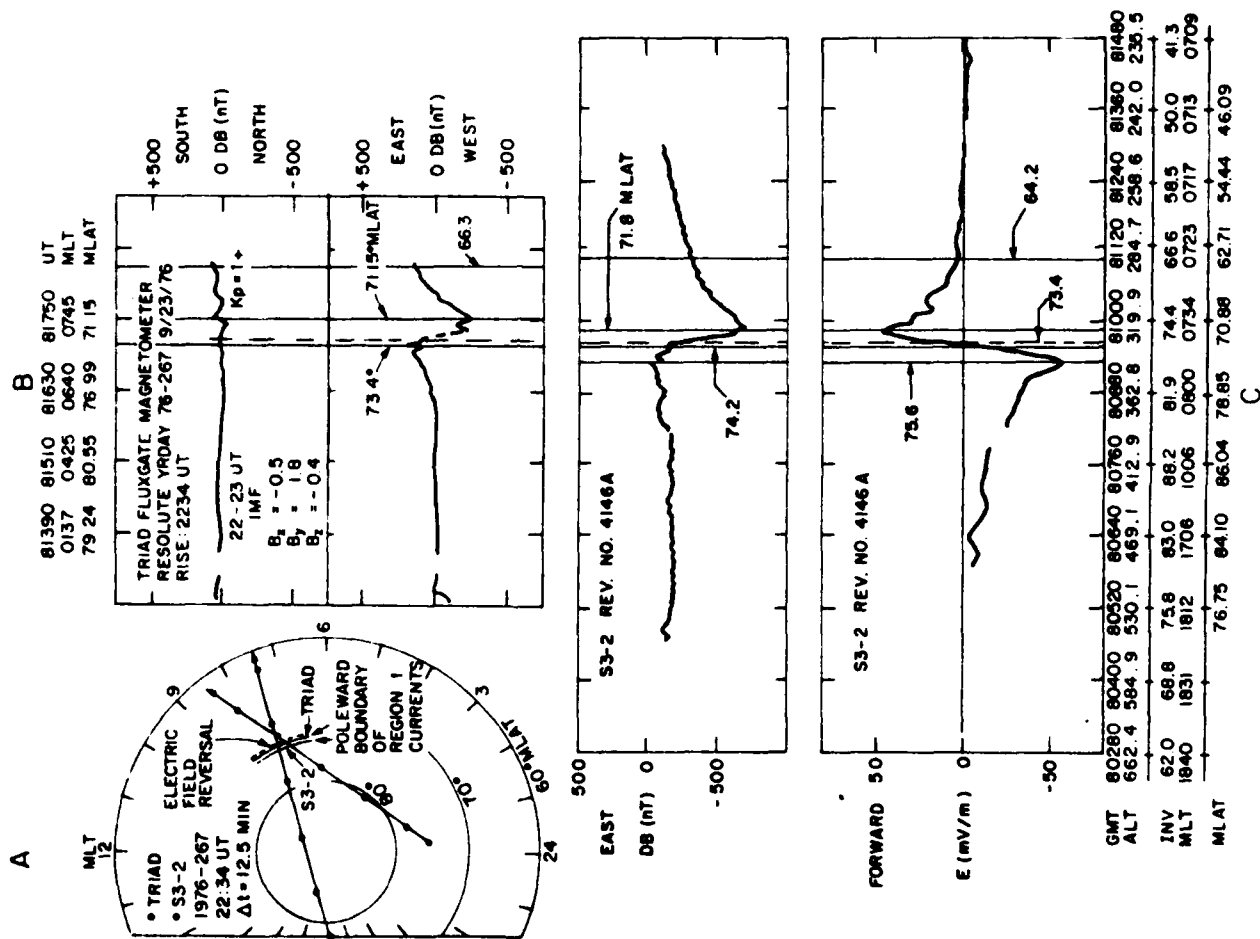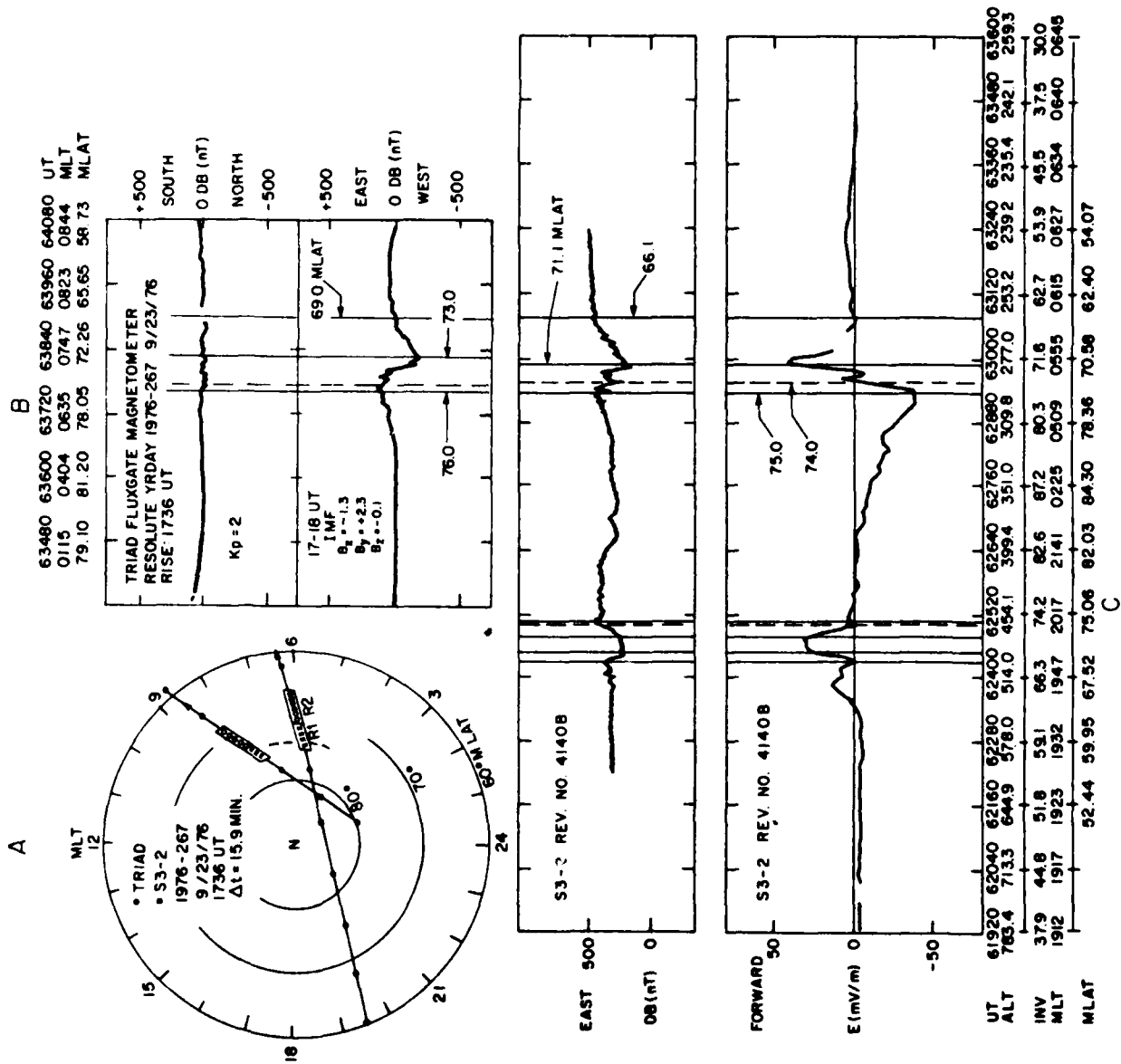RESOLUTE 1976-305 10/31/1976

Figure 4

143

Figure 5

Figure 6

145

Field-Aligned Current, Convective Electric Field, and Auroral Particle Measurements During a Major Magnetic Storm

B. M. Shuman, R. P. Vancour, and M. Smiddy

Air Force Geophysics Laboratory, Hanscom Air Force Base, Massachusetts 01731

N. A. Saflekos

Physics Department, Boston College, Chestnut Hill, Massachusetts 02167

F. J. Rich

Research Center, Regis College, Weston, Massachuse... 02193

The S3-2 polar-orbiting satellite has provided simultaneous measurements of the transverse component of the ambient magnetic field, the trajectory component of the electric field, and the auroral electron flux during the very intense substorm period of March 26, 1976. Using orbits that traversed the midnight, dawn, and noon local time sectors of the low-altitude polar magnetosphere during extremely active times, we have calculated field-aligned current densities, compared them with precipitating auroral electron fluxes, and by utilizing the direction (forward or backward) of the electric field component, identified the regions to which they map down. Our principal results from two such orbits, subject to the limitations of single-axis measurements, include the following. (1) The observed direction of the electric field component indicated closure of the major field-aligned current pattern by Pedersen current flow in the ionosphere, consistent with a magnetospheric current source. (2) Values of the height-integrated Pedersen conductivity, calculated from the gradients of the electric and magnetic field components, were typically in the range 10–30 Ω^{-1} in the current-carrying regions during active times. At such times, particle precipitation on the nightside became the major factor in controlling the magnitude of the ionospheric conductivity, outweighing the influence that sunlight has in quiet times. (3) In regions of increased fluxes of precipitating electrons in the nightside auroral oval, current densities calculated from electron fluxes in the energy range 0.08- to 17-keV accounted for up to 50% of the upward currents, increasing to better than 70% during the most intense substorm period. (4) In each of the three auroral oval crossings on the nightside, an intense upward current sheet was observed at the equatorward side of the westward electrojet, just poleward of the electric field reversal associated with the Harang discontinuity. (5) During the most intense current period, the region of field-aligned currents was compressed down to L shell values 2.2 to 5.1, within the trapping region, indicating that the equatorial source of these currents was the inner magnetospheric plasma inside the outer Van Allen radiation zone rather than the distant plasma sheet or the boundary layer.

INTRODUCTION

The concept of currents flowing along the lines of force of the earth's magnetic field connecting to the auroral zone was first proposed by *Birkeland* [1908] and was resurrected in its present form by *Bostrom* [1964] when it became apparent that dynamo winds in the ionosphere were not strong enough to power the auroral electrojets during storm times. Since then, using magnetometer data from the Triad satellite over the northern hemisphere, *Zmuda and Armstrong* [1974] determined the basic pattern of field-aligned current flow in magnetic local time (MLT) coordinates, observing current densities that varied typically from 0.3 to 4 $\mu A/m^2$. This work, from which evolved a pattern of region 1 currents (poleward) that are into the ionosphere on the postmidnight and morning side and out of the ionosphere on the afternoon and evening side, was continued by *Iijima and Potemra* [1976a, b]. For the region 2 currents, equatorward of the region 1, the current flow pattern is reversed. Further, the downward region 1 currents of the morning sector were found to extend around into the 2200–2400 MLT region overlapping along the poleward boundary of the evening region 1 upward currents. Also, cusp region field-aligned currents were observed in the midday sec-

tor at latitudes above the region 1 currents, with a flow pattern out of the ionosphere in the prenoon sector and into the ionosphere postnoon. *Sugiura and Potemra* [1976] showed from the Triad data that the poleward region 1 current generally exceeded its equatorward region 2 counterpart, leading to a net field-aligned current flow directed into the ionosphere in the morning sector and away from it in the afternoon sector. The polar-orbiting Isis 2 satellite measured electrons and positive ions in the energy range 5 eV to 15 keV as well as the east-west magnetic field component [*Klumpar et al.*, 1976]. In the morning sector, 2400–0600 MLT, the equatorward upward-flowing current was observed to coincide with nearly isotropic fluxes of precipitating kilovolt electrons. Further Isis 2 results have been reported by *McDiarmid et al.* [1978a, b]. More recently, *Iijima and Potemra* [1978] showed, on the basis of many Triad passes, that the large-scale pattern of field-aligned current flow derived from magnetically quiet times persists throughout active substorm periods. In the nighttime sector, though, and particularly in the region 2000–2400 MLT, the pattern may be complicated by the superposition of fine-structured variations.

The S3-2 satellite was equipped to measure electric and magnetic fields and particle fluxes simultaneously. Some of these results are already in the literature. *Smiddy et al.* [1977]

146

have reported on intense localized poleward-directed electric fields in the premidnight sector near the ionospheric projection of the plasmapause. *Burke et al.* [1980] correlated S3-2 observations in the late evening auroral oval with a nearly coincident auroral image from a Defense Meteorological Satellite Program (DMSP) satellite. We report here on S3-2 data taken during a major magnetic storm. Simultaneous observations of field-aligned currents, auroral particle precipitation, and convective electric fields have been reported in the literature only rarely and to date are totally missing for periods that are extremely active magnetically. The events described herein were obtained in the midnight, dawn, and noon local time sectors of the low-altitude polar magnetosphere. The nature of the measurements allows us to study current closure, Pedersen conductivity, Joule heating of the atmosphere, current charge carriers, magnetospheric topology, and acceleration mechanisms.

SATELLITE INSTRUMENTATION AND DATA ANALYSIS

The Air Force S3-2 scientific satellite was launched into a near polar orbit in December 1975 with perigee at 240-km altitude and apogee at 1557 km. Inclination was 96.28° and the orbit period 103 min. The orbit plane was nearly sun synchronous, precessing in a local time coordinate frame only −1/4° per day. The spin rate was nominally 3 rpm, and the spin axis orientation was maintained to within 5° of the normal to the orbit plane.

Magnetometer. Magnetic field components were measured with a triaxial flux gate magnetometer at a data rate of 32 points per second per axis. Full scale range on each axis was set at ±600 γ, so that the 8-bit telemetry words would allow a resolution of 5 γ in each of the field components. In order to keep the magnetometer from saturating in near-earth fields an automatic ranging current source, or range switch, was used. When necessary, this automatically provided fixed current increments, each equivalent to a 1000-γ offset field, to a separate neutralization winding about each axis of the magnetometer. One hundred twenty-eight such steps were available for each axis, allowing for a dynamic range of +63,600 to −64,600 γ in all components. The magnetometer sensor was mounted at the tip of an Astromast boom that extended it 20 feet out from the spacecraft, perpendicular to the spin axis. The boom consisted mainly of three fiberglass longerons that were stowed in the form of a tightly coiled spring (actually a triple helix). Deployment was provided by the stored strain energy in the mast.

The two magnetometer components in the spin plane, which was approximately the geographic meridional plane, were subjected to a very high rate of range switching, occurring sometimes faster than 15 times per second. This resulted in 'noisy' signals for the spin plane components. The transverse component, on the other hand, lying approximately in the east-west direction, changed at a much slower rate and produced a near noise free measurement. This was the component that was primarily used in detecting field-aligned currents.

The magnetometer coordinate frame was nearly identical to the spacecraft coordinate system, the essential difference being a 3.6° rotation about the Astromast boom axis. The magnetometer orientation varied in time as a result of a slow twisting of the boom through ±½° about its long axis owing to the alternating thermal effects of passing through sunlight/ earth shadow conditions. The International Geomagnetic Reference Field (IGRF) 1975 model field, suitably updated to the epoch of data acquisition, was calculated for the position of each data point and rotated into the magnetometer coordinate frame. The determination of spacecraft attitude used here was based on a combination of solar aspect angle and infrared horizon scanner measurements and was considered to be good to 0.5°. The quantity ΔB_y was then calculated by subtracting the model field component along the transverse magnetometer axis from the corresponding measured field component. Since the transverse magnetometer was positive to the right of the velocity vector, as seen from above, positive changes in ΔB_y indicated passage through a downward current sheet and negative changes indicated an upward current sheet.

Using the model of field-aligned currents flowing up and down in parallel infinite sheets oriented in the east-west direction, the current density j_z may be calculated from the observed changes in the transverse magnetic field residual ΔB_y as the satellite traverses the current sheet in the north-south direction x. Thus

$$\frac{4\pi}{10} j_z (\text{A/km}^2) \approx \frac{d(\Delta B_y)}{dx} (\gamma/\text{km}) \qquad (1)$$

where the x, y, z directions are positive north, east, and down, respectively. (For simplicity, the earth's magnetic field has been assumed to be vertical in the auroral and polar regions; and also the magnetic field residual along the transverse magnetometer axis (ΔB_y) has been approximated to be in the east-west direction. This latter assumption breaks down near the pole when the transverse axis actually points north-south; when the transverse axis is 45° from the east-west direction, the current density may be underestimated by a factor of two.) Also, by integrating along the north-south track, we obtain a measure of the current sheet intensity simply in terms of the change in the transverse field component.

$$\int j_z \, dx (\text{A/km}) \approx \frac{10}{4\pi} \Delta(\Delta B_y)(\gamma) \qquad (2)$$

DC electric field probe. The electric field experiment was designed to measure the three orthogonal components simultaneously by determining potential differences between pairs of 3-inch diameter carbon-coated spheres mounted at the ends of extendable booms. Two dipoles, each 90 feet long, were to be extended in the satellite spin plane at right angles to each other, and a third dipole, 36 feet long, was to be extended along the spin axis direction. Unfortunately, one set of the spin plane booms failed to deploy. Also, the spin axis data are not considered fully reliable since they exhibit the effects of time-varying contact potentials. The potential differences from the spinning electric dipole were measured at the rate of 64 times per second outside of the calibration sequences. These were corrected for the $\vec{V} \times \vec{B}$ effects of satellite motion and for different contact potentials on the spheres to obtain the component of ambient electric field in the spin plane. This was projected along the satellite trajectory and averaged over one spin period, with successive averages shifted by 5-s intervals, to obtain the electric field component E_x.

Electron detector. A parallel plate electrostatic analyzer (ESA) was used to detect electrons over the approximate energy range 0.08–17 keV, with a complete spectrum through 32 energy bins swept out in 1 s. The geometric factor was 4.68 × 10^{-3} cm² sr, and the fractional energy resolution $\Delta E/E$ was

0.0419. The instrument had a single aperture of full width 6° that was mounted in the spin plane of the spacecraft. Since the nominal spin period of the satellite was 20 s, only a limited range of pitch angles could be sampled while traversing spatially narrow features. Count rates from the ESA were directly translated to incident differential electron fluxes (el/cm² s sr keV), which were further integrated through the 32 energy bins to obtain number fluxes and energy fluxes. For selected events such as an inverted V or a possible electrostatic shock, individual spectra were obtained. Also, when a combination of conditions was favorable, such that the sensor sampled through the precipitation loss cone while the magnetometer indicated passage through an extended sheet of uniform current density, calculations of current density were made based on precipitating minus backscattered electron fluxes. Such estimates, of course, were dependent on there being no changes in the electron flux in space or time over the interval used to integrate through the different pitch angle bands. A more detailed description of the S3-2 instrumentation and data analysis has been given by *Burke et al.* [1979].

EXPERIMENTAL OBSERVATIONS

The data to be presented here were acquired on March 26, 1976, during two successive orbits, 1567 and 1568, near the peak of magnetic storm activity. The *Kp* values corresponding to these orbits were 8– and 7+, respectively. The passes traversed the entire auroral oval and the polar cap, with orbit 1567 providing data for both the north and south hemispheres and orbit 1568 for just the north. For comparison we include an example of quiet time data from the northern hemisphere, orbit 1546, which occurred 2 days earlier at a time when *Kp* was 1_0. The satellite subtracks, three north and one south, are shown in Figure 1 where they are plotted in a polar coordinate frame of magnetic dipole latitude (MLAT) and MLT. The annotations along the track are Greenwich Mean Time (GMT) in hours and minutes. The experimental results are shown in Figures 2, 3, 5, and 6, plotted versus GMT, invariant latitude Λ, altitude, and MLT. In each of these figures, panel (a) shows the residual ΔB, in gammas, where positive slope indicates a downward field-aligned current
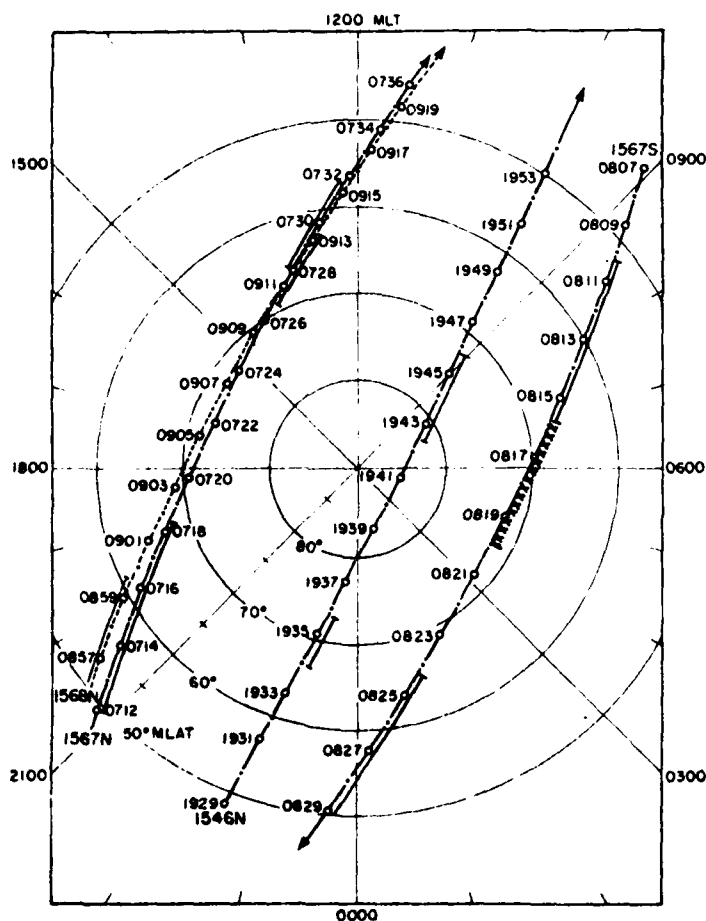

Fig. 1. Satellite trajectory over auroral and polar regions in the coordinate frame of magnetic dipole latitude (MLAT) and magnetic local time (MLT) for orbits 1546 (north), 1567 (north and south), and 1568 (north). The solid line alongside the trajectory path indicates the regions where predominately east-west field-aligned currents were detected. The x line alongside 1567S indicates a region of meridional field-aligned currents.

148

direction, panel (b) shows E_x, the trajectory component of the electric field, in mV/m, positive in the forward direction, and panel (c) shows the field-aligned current density in $\mu A/m^2$, calculated by applying (1) to the plot of ΔB_y in panel (a). Upward current flow is plotted in the positive direction. The horizontal line at the top of panel (c) indicates the region of enhanced electron fluxes as determined by the ESA. The arrows at the bottom of panel (c) indicate the forward or reverse direction of the trajectory component of electric field E_x.

The data for the quiet time pass 1546 in the northern hemisphere on March 24, 1976 are given in Figure 2. With the satellite heading poleward on the nightside near 2300 MLT, the major features in the ΔB_y plot, +230 γ and −280 γ, indicate a downward then upward current typical of regions 2 and 1, respectively. The electric field component E_x is in the forward (poleward) direction, indicating passage through the premidnight region of eastward Hall current. The direction of the electric field is also such as to provide closure of the Birkeland currents via Pedersen currents in the ionosphere. As shown in panel (c), enhanced electron fluxes were observed essentially over the region of upward current flow. In the dayside, with

S3-2 heading equatorward near 0830 MLT, the central feature of the ΔB_y plot indicates a downward then upward current typical of a region 1–region 2 dawnside encounter. In this case though, there are additional antiparallel currents bordering on both sides, as well as a pair of smaller scale currents in the middle. The shift in levels in passing through the current-carrying region indicates a net downward current at the poleward side, such as was discussed by *Sugiura and Potemra* [1976]. The electric field reversal from poleward to equatorward at 1943:48 GMT is interpreted as being due to the satellite exiting the polar cap and entering the dawnside region of sunward convective flow. The equatorward electric field is also of the correct polarity to close the major region 1–region 2 current pair in the ionosphere. The region of enhanced electron precipitation is shown with a dashed line in this case since it was not as well-defined in the dayside as in the nightside. A local peak in the precipitating flux (2.9 × 10⁸ el/cm² s sr near 0° pitch angle) was clearly observed though at 1944:16 GMT, which coincided with a narrow included band of relatively intense upward current.

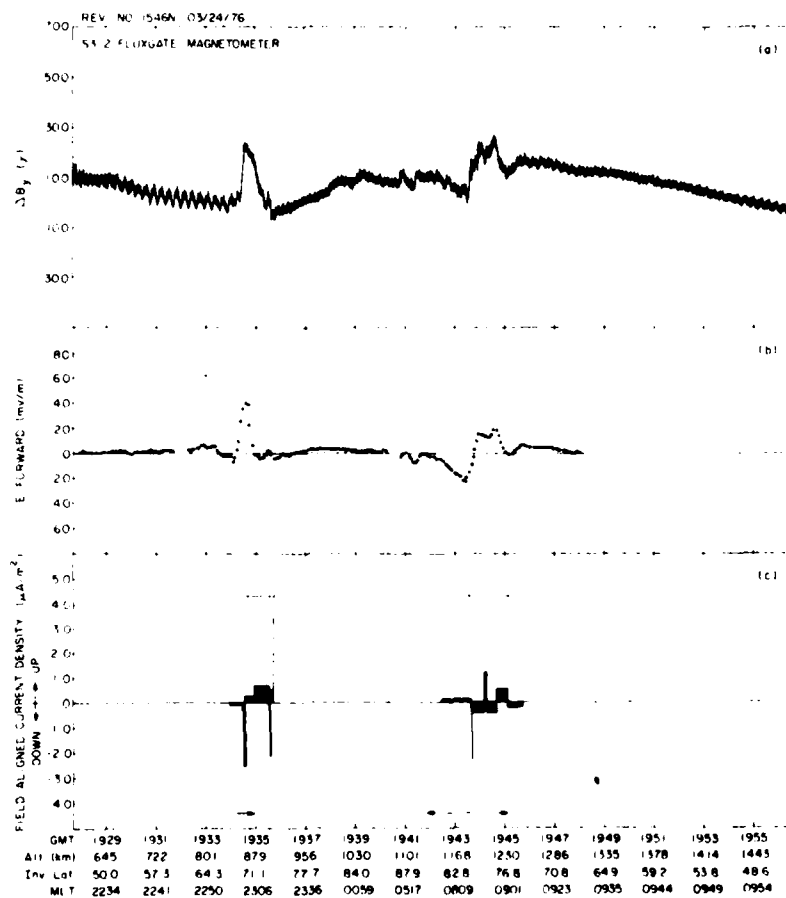Orbit 1567 occurred during the magnetic storm of March

Fig. 2. S3-2 results for orbit 1546N, above 45° invariant latitude, on March 24, 1976. Panel (a) is the nominal east-west magnetic field residual, with positive slope indicating downward field-aligned current. Panel (b) is the trajectory component of the electric field, given as positive in the forward direction. Panel (c) is the field-aligned current density, with upward flow given in the positive direction, as determined from the plot in panel (a). The line above indicates the region of enhanced electron fluxes; the arrow below indicates the direction of the trajectory component of the electric field.

149

26, 1976, in an interval when Kp was 8−. The data for the northern hemisphere portion of this orbit are shown in Figure 3. The nightside plot of ΔB_r, where the satellite was heading poleward, is morphologically similar to the nightside portion of the quiet time pass 1546, but the excursion in ΔB_r, is much larger approaching 1000 γ in the invariant latitude range 55° to 69°. Also, the poleward nightside portion of orbit 1567 shows a considerable amount of structure, with a number of sheets of high density upward current. At the equatorward side the dominant current pattern is as before, a pair of anti-parallel current sheets, downward then upward. The electric field component E_z shows a reversal from poleward to equatorward at 0716:13 GMT. We interpret this to indicate the crossing of the Harang discontinuity, even though the MLT was near 2000, two hours westward of the usual position. Thus the broad lower density, down-up sheets of current toward the equator would connect to the eastward electrojet region, and

the narrower, higher density currents would presumably connect to the westward electrojet region. The strongest current density is observed just poleward of the electric field reversal at the equatorward side of the westward electrojet. In each of the electrojet regions, the direction of the electric field component is such as to close the basic current flow pattern in the ionosphere. The region where the fluxes of precipitating electrons are greatly enhanced, by more than an order of magnitude, corresponds closely to the region of upward field-aligned currents.

The auroral electroject indices for this date, taken from *Allen et al.* [1977], are shown in Figure 4. These were compiled from seven northern hemisphere auroral zone observatories that are approximately evenly spaced in longitude. At the time the S3-2 satellite traversed the northern nightside oval during orbit 1567, at about 0715 GMT, the *AE* index, while still greater than 300 γ, was down sharply from its peak values

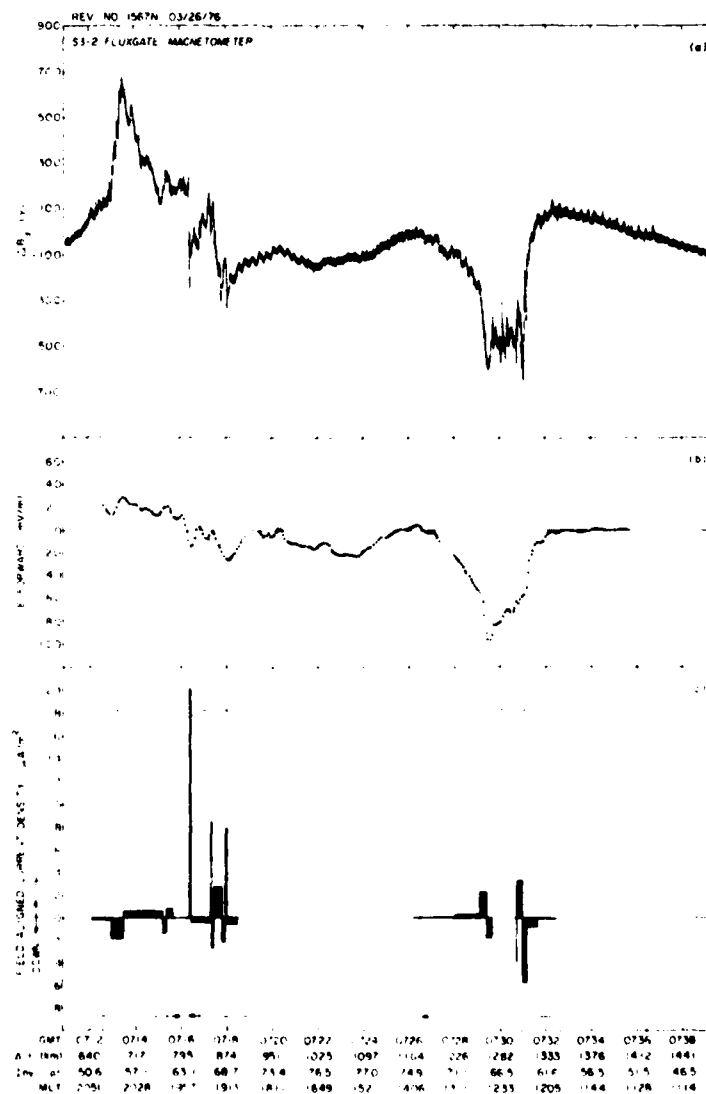

Fig 3. S3-2 results for orbit 1567N, on March 26, 1976. Panels are the same as for Figure 2.

during the storm. This may be simply a consequence of the extended equatorward movement of the auroral oval during active times. The S3-2 satellite was then close to the longitude of Barrow, one of the seven stations used in deriving the AE index, and the observed poleward field-aligned-current boundary near $\Lambda = 69°$ indicates that the current-carrying regions were predominantly to the south of that observatory, which is located at $\Lambda = 69.7°$.

The northern hemisphere dayside crossing of the auroral oval during orbit 1567, which occurred in the 1200-1300 MLT period, is shown on the right side of Figure 3. The ΔB_y plot shows a basic current pattern upward at the poleward edge and downward at the equatorward boundary, with a series of rapid variations in between. The excursions in ΔB_y were less than on the nightside, approximately 600 γ at the poleward side and 700 γ at the equatorward side. The electric field component observed in this interval reached almost 100 mV/m. It was in the poleward direction, as required in order to close the major current pattern in the ionosphere. The region of enhanced precipitating electron flux, not as sharply defined as on the nightside, is shown toward the equatorward side of the oval.

Continuing on to the southern hemisphere, the S3-2 track crossed the auroral oval on the dawnside, heading poleward. The data are shown in Figure 5. The electric field component was initially equatorward indicating a region of sunward convective flow. It reversed to poleward at 0815:50 GMT, indicating entry from the auroral oval into the polar cap at that time. The large-scale pattern of field-aligned current flow encountered in crossing the oval in the 0700-0830 MLT range can be seen from the ΔB_y plot as up-down-up-down. This pattern, combined with the equatorward direction of E_x, is again consistent with closure by Pedersen current flow in the ionosphere. The integrated current sheet intensity is quite strong, as indicated by several excursions of ΔB_y in the range of 1000 γ to 1300 γ. As shown in panel (c), increased fluxes of precipitating electrons coincide with the region of upward current flow in the auroral oval. A secondary increase in electron flux was also observed to coincide with the upward currents in the polar cap, but of lesser intensity than over the oval. These field-aligned currents in the polar cap at MLT values near

0600 appear to be oriented meridionally rather than east-west.

The southern hemisphere nightside data are shown in the right side of Figure 5 as the satellite crossed the auroral oval in the 2330-0100 MLT region heading equatorward. E_x was forward (equatorward) until 0828:42 GMT, indicating passage over a westward electrojet region until then. The large-scale current pattern observed in ΔB_y was down then up, with intense narrow current pairs superimposed. Again, this pattern, with the equatorward direction of E_x, is consistent with closure by Pedersen current flow in the ionosphere. The largest excursion in ΔB_y was approximately 1200 γ occurring in the upward current region. Also, as was noted in the northern hemisphere nightside of this orbit, the strongest current densities are found at the equatorward edge of the westward electrojet region. Beyond 0828:42 GMT where E_x is predominantly poleward, the satellite encountered the eastward electrojet region. Increased fluxes of precipitating electrons are present across the auroral oval, encompassing all of the regions of upward current flow.

Orbit 1568 followed a track similar to orbit 1567. Heading poleward on the nightside, it crossed the northern auroral oval in the MLT region 1950-2050. The experimental results are shown in Figure 6. The electric field component was poleward at first, reversing to equatorward at 0857:30 GMT. This is interpreted as marking the region of the Harang discontinuity, with the field-aligned currents observed before that time connecting to an eastward electrojet region in the ionosphere, and those encountered after that time connecting to a westward electrojet. A further reversal of E_x at 0859:24 GMT is considered to mark the satellite's exit from the auroral oval into the polar cap. (Unfortunately, the complete electric field vector is not known in these observations.) In the 103 min since the previous pass, the auroral oval has moved equatorward, and the strength of the field-aligned current has increased markedly. The ΔB_y plot bears the signature of five distinct current sheets. The largest of these, the upward sheet that spans both electrojet regions, has an excursion in ΔB_y of nearly 2100 γ, with two of the others reaching 1600 γ and 1700 γ. The largest upward current sheet is structured with intense current pairs superimposed, but the other sheets are noticeably clear of such structure. The initial downward current and a portion of the following upward current connect to the eastward electrojet region where the poleward electric field has the proper direction to provide closure by Pedersen current flow in the ionosphere. The same is true for the remaining current sheets, which connect to the westward electrojet region where the electric field is equatorward. As was also noted in two previous cases in orbit 1567, the strongest current density occurs near the equatorward edge of the westward electrojet. Increased precipitating electron fluxes, by more than two orders of magnitude, were observed to coincide with the entire region of upward current flow. Plots of integrated electron flux and integrated energy flux, along with pitch angle, are shown for this period in Figure 7. The peak value of the electron flux, 5.4×10^9 el/cm^2 s sr, was observed near 0° pitch angle at 0859:02 GMT. This was in the midst of an inverted V event where the peak energy reached 9.5 keV. An array of successive 1-s differential energy spectra depicting the event is shown in Figure 8. This event coincided with the intense upward current flow toward the poleward edge of the westward electrojet on closed field lines. At the time of this event, the subsatellite position was approximately 360 km from Cape Wellen on a true bearing of 247°. Magnetograms from Sitka,
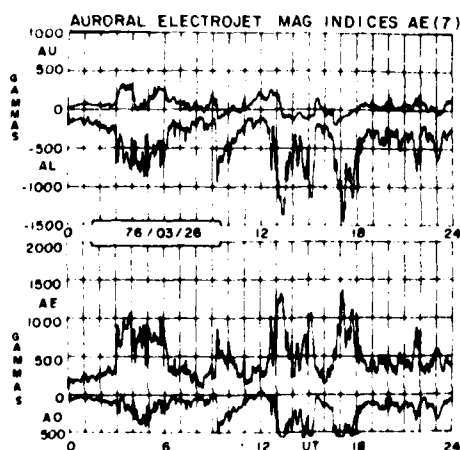
AURORAL ELECTROJET MAG INDICES AE(7)

Fig. 4. Auroral electrojet indices for March 26, 1976, from *Allen et al.* [1977].

College, ano Cape Wellen indicated the presence of a strong westward electrojet equatorward of all three stations in that period.

Continuing over the polar cap, orbit 1568 encountered the dayside oval in the postnoon MLT region 1210 to 1350, heading equatorward. The electric field component was poleward and reached almost 90 mV/m. The major field-aligned current pattern was upward then downward. This, combined with the poleward electric field, was again consistent with closure in the ionosphere by Pedersen currents. An additional narrow intense upward current sheet was observed near the equatorward boundary just before the very intense downward flow. An enhanced level in the electron flux was observed at the equatorward side of the oval, coinciding with the upward current spike and overlapping a portion of the general upward current. A local peak in the precipitating electron flux, 7×10^8 el/cm^2 s sr, was observed at 0913:11 GMT just near the boundary between the upward current sheet and the intense downward current. The enhanced flux and the intense upward current sheet coincided with a steep gradient in the electric field component E_x. The electron spectra at this time exhibited a fine structure at the higher energy levels, as shown in Figure 9. This, combined with the other factors noted, may indicate the presence of an electrostatic shock.

DISCUSSION

Before we draw any conclusions, we would like to caution the reader about the limitations of three of the experiments aboard the S3-2 satellite. The magnetometer and the dc electric field probe data utilized in this study were effectively single-axis measurements, as described in the instrumentation section. Similarly, the pitch angle information with regard to precipitating and backscattered auroral particles was obtained by a single spinning electrostatic analyzer. Thus assumptions
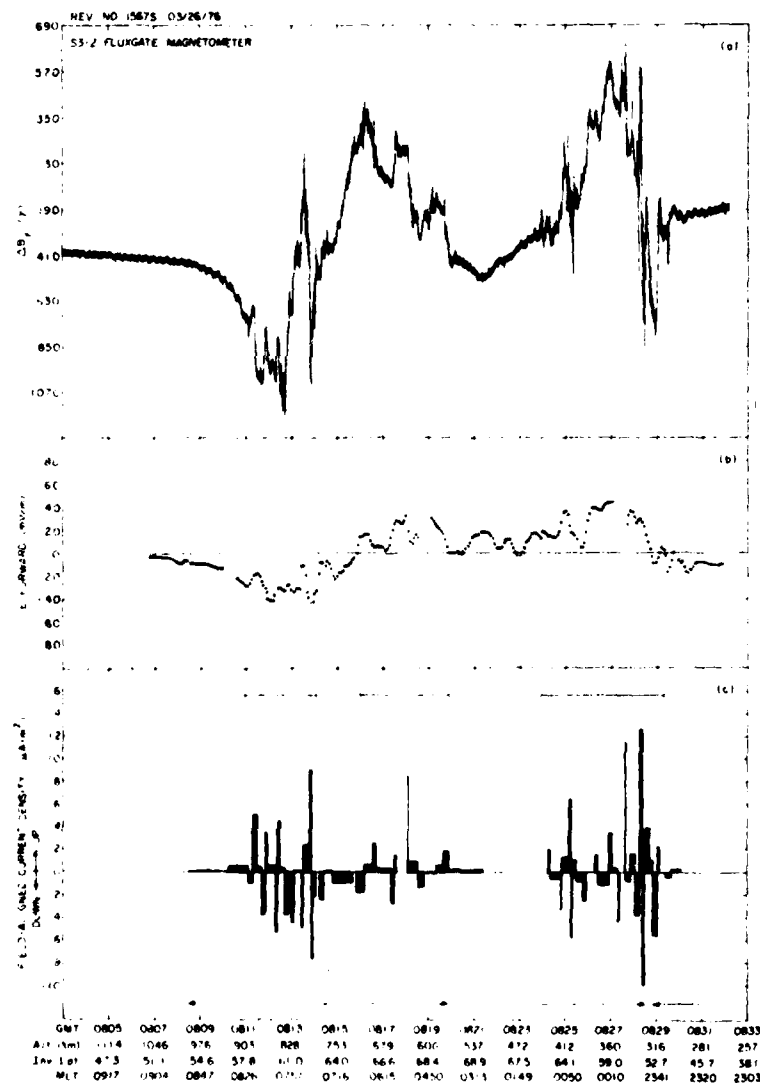

Fig. 5. S3-2 results for orbit 1567S on March 26, 1976. Panels are the same as for Figure 2.
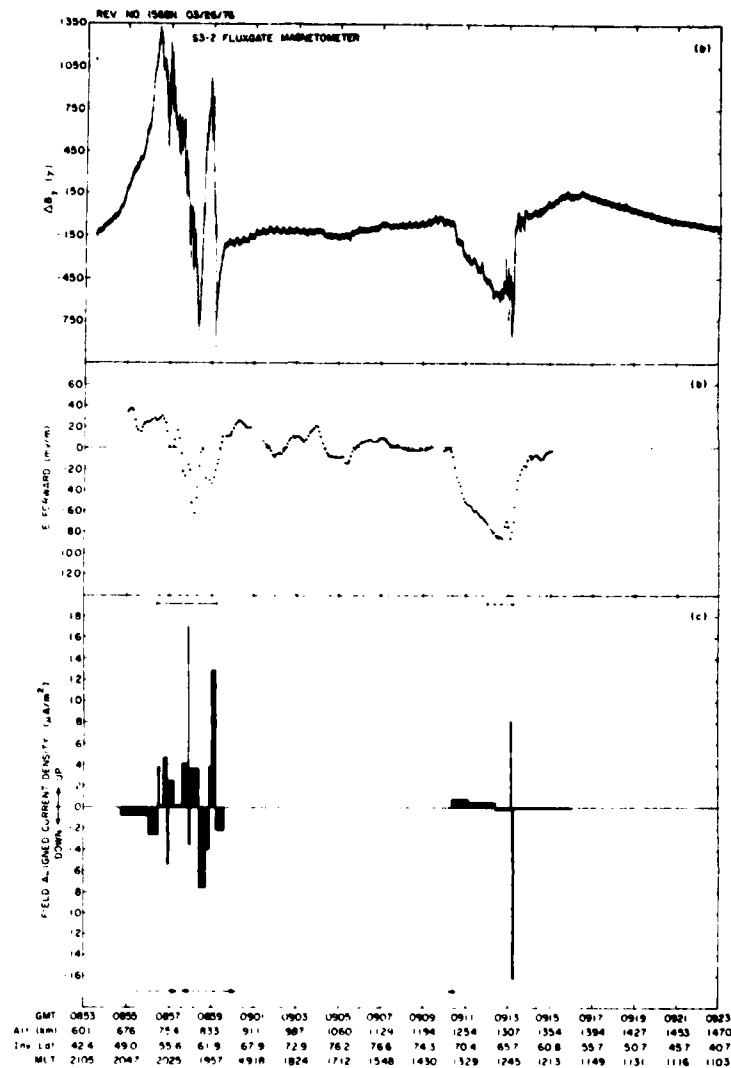
Fig. 6.   S3-2 results for orbit 1568N on March 26, 1976. Panels are the same as for Figure 2.

had to be made pertaining to the orientation of the magnetic and electric vectors, as well as to the stability of particle distributions during a loss cone scan. However, we do not believe they affect the validity of our results in a significant way.

Statistical studies have shown that the transverse magnetic disturbance vectors due to field-aligned currents are mainly oriented in the east-west direction except in the regions of the polar cusp and the Harang discontinuity where they may also assume significant meridional components [*Saflekos and Potemra*, 1980]. Similarly, studies of the dc electric field vector orientation have shown that it is oriented in the north-south direction in the auroral oval except in the regions of the polar cusp and the Harang discontinuity where it also assumes significant components along the east-west direction [*Cauffman and Gurnett*, 1971, 1972; *Maynard*, 1974].

The observations we report in the dawn sector have no difficulty with the single-axis limitation provided the satellite ve-

locity is mainly perpendicular to *L* shells. On the other hand, the orientation of the single-axis observations obtained in the regions of the cusp and the Harang discontinuity can be defended as follows. These observations are thought to constitute the major components of the magnetic disturbances and convective electric fields because they have magnitudes comparable to the largest seen by comprehensive surveys carried out by the Triad and Injun 5 satellites.

In the following, we will (1) calculate the Pedersen conductivity associated with the closure currents in the ionosphere by using the observations of ΔB_y and E_x, (2) compare the field-aligned current densities calculated from the ESA particle measurements with those determined from the gradient of ΔB_y, (3) define the location of the observed field-aligned currents relative to magnetospheric structural features, and (4) discuss briefly the fine scale variations apparent in the data.

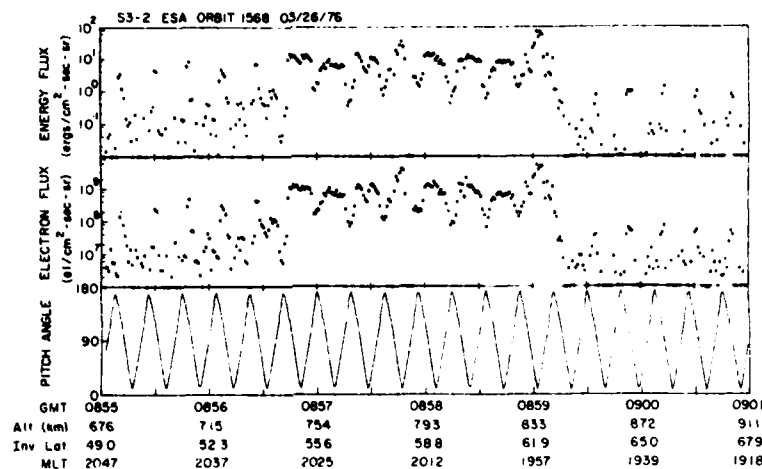*Pedersen conductivity and current closure.*   The similarity

Fig. 7.   Integrated electron flux and energy flux, with pitch angle, in the nighttime sector of orbit 1568N.

between the ΔB_y plots and the concurrent plots of E_x is striking, and suggests that a definite correlation exists between these two quantities. The height-integrated Pedersen conductivity in the auroral ionosphere, Σ_P, can be calculated from the E_x and ΔB_y measurements assuming linearity between E_x and ΔB_y, as well as a number of other simplifying assumptions. Following the method of *Kamide and Horwitz* [1978], which was used to relate the Chatanika radar measurements to a calculation of field-aligned current density, the divergence of the height-integrated horizontal current density may be taken to be balanced by the field-aligned current density. Assuming that variations in the east-west direction are small, consistent with the fact that the longitudinal extent of the auroral electrojet is much greater than its latitudinal dimension, this relation may be approximated as

$$j_z \approx \frac{dJ_x}{dx} \qquad (3)$$

where the coordinates x, y, z are north, east, and down, respectively. In the northern hemisphere the height-integrated poleward current density is given by

$$J_x = \Sigma_P E_x - \Sigma_H E_y \qquad (4)$$

where Σ_P and Σ_H are the height-integrated Pedersen and Hall conductivities respectively, and E_x and E_y are the northward and eastward electric field components, respectively. If we take the east-west component of electric field to be much less than the north-south component within the auroral oval region [*Cauffman and Gurnett*, 1971, 1972; *Maynard*, 1974], then the last term on the right may be dropped. Combining (3) and (4), and assuming that the conductivity gradient is small within an 'infinite sheet' of uniform current density, leads to the approximate relation

$$j_z \approx \Sigma_P \frac{\Delta E_x}{\Delta x} \qquad (5)$$

which can be used to determine the height-integrated Pedersen conductivity directly from the north-south gradient of the measured quantities ΔB_y (see (1)) and E_x. This technique is similar to the one described by *Greenwald et al.* [1980]

whereby field-aligned current measurements from the Triad satellite were used in conjunction with electric field measurements from the ground-based Stare auroral radar system to obtain values for the height-integrated Pedersen conductivity as well as the ionospheric Joule heating rate. Also, *Bythrow et al.* [1980] calculated values of Σ_P in similar fashion using measurements of drift velocities and magnetic fields from the AE-C satellite. This effort is extended further here.

The calculation of Σ_P was carried out only when $\Delta E_x/\Delta x$ and j_z were simultaneously matched as required by (5). It should also be noted that, owing to the averaging process in obtaining a value of E_x once every 5 s, it is not possible for $\Delta E_x/\Delta x$ to track fast variations in j_z, which were obtained from ΔB_y data taken at the rate of 32 points per second. For this reason an additional requirement, in general, was that the current density hold for at least 10 s. In some cases where j_z changed in amplitude but maintained the same direction, a weighted average density was used. No attempt was made to extrapolate j_z or E_x down to E region altitudes. Since j_z would be expected to vary with altitude roughly as $[(R_0 + 110 \text{ km})/(R_0 + h)]^3$, and $\Delta Ex/\Delta x$ as $[R_0 + 110 \text{ km})/(R_o + h)]^{3/2}$, where R_0 and h are the earth radius and the satellite altitude, respectively, such a correction would affect the calculated value of Σ_P by less than 20%. Calculated values of Σ_P in Ω^{-1} are listed in Table 1, with the less reliable values flagged with a question mark. Following *Greenwald et al.* [1980], we may approximate the Joule heating rate in the ionosphere Q_J in mW/m² due to closure of field-aligned currents by Pedersen currents as

$$Q_J \approx \Sigma_P E_x^2 \qquad (6)$$

These results are also given in Table 1 at those times for which Σ_P was calculated. During the magnetic substorm period values of Σ_P in the range 20–30 Ω^{-1} were not unusual, and one questionable value reached as high as 73 Ω^{-1}. For the quiet time orbit 1546, the averaged dayside conductivity was more than twice that on the nightside; whereas for the disturbed times, orbits 1567 and 1568, the averaged dayside conductivity was only 90% of that on the nightside. These results are in agreement with current ideas that in quiet times sunlight is the controlling factor in ionospheric conductivity, but in extremely disturbed times particle precipitation on the nightside
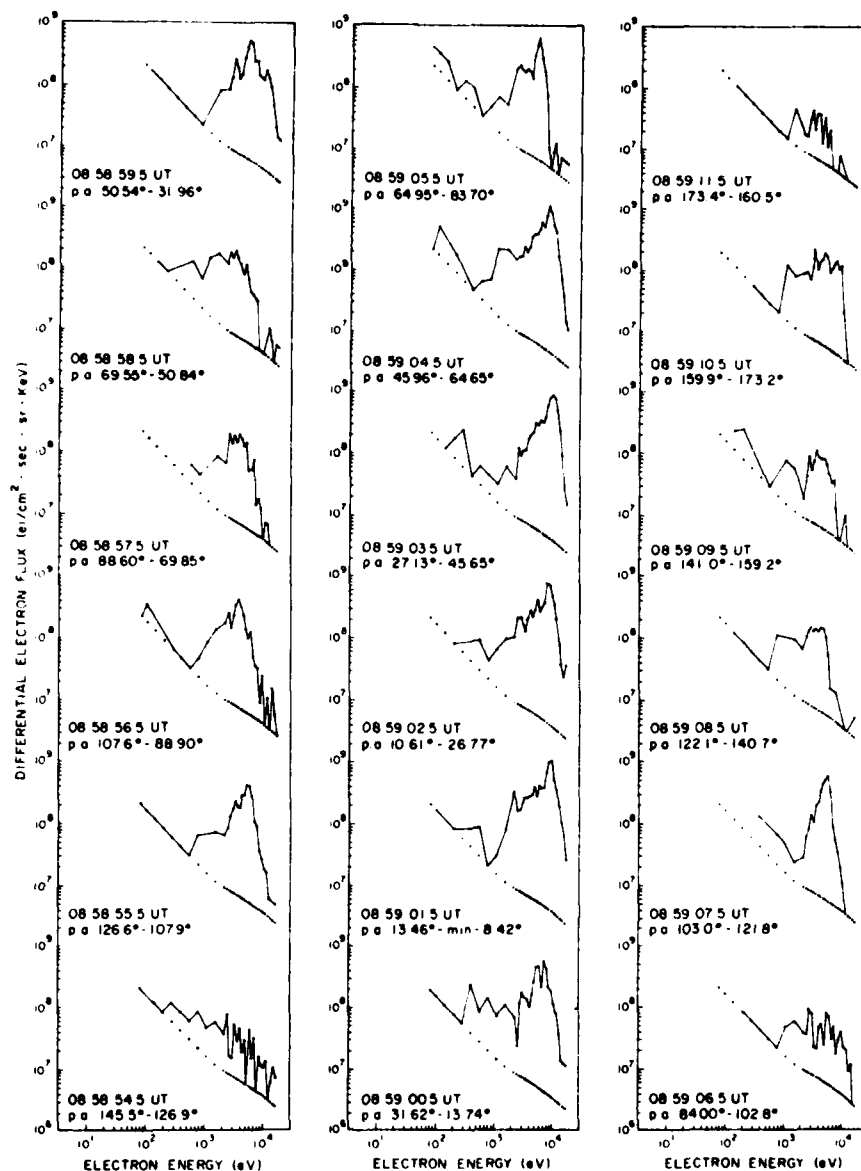
Fig. 8. Differential energy spectra obtained from the ESA in the nighttime sector of orbit 1568N. An inverted V event, with peak energy of 9.5 keV, is centered at 0859:02.

becomes the dominant factor. High values of Q_J were found mostly in the postnoon (MLT) sector where E_x was strongest. The highest value of Q_J, 164.7 mW/m^2, was found at 0913:14 GMT in the dayside of orbit 1568, in the region previously characterized by the likely presence of an electrostatic shock. However, the value of Σ_P used in this case was considered questionable since the high value of j, lasted less than 10 s and the gradient in E_x may not be valid due to smoothing. Nevertheless, if Σ_P were taken at only half its value this would still be the peak 'observation' of Q_J. The integrated energy flux was obtained from the ESA data for the time periods corresponding to each value of Q_J. Comparison showned that, away from the regions of electric field reversal, the Joule heating due to Pedersen closure currents in the ionosphere was

much greater than the energy deposited by electron precipitation in the loss cone. However, in the region of strongest upward current density (presumably auroral arcs), which were too limited in time to permit a calculation of Σ_P, the integrated energy flux obtained from the ESA was greater than the values of Q_J obtained nearby. This can be seen from the energy flux plot in Figure 7, particularly at 0857:45 and 0859:02, and is consistent with the results of *Evans et al.* [1977] and *Greenwald et al.* [1980].

We have observed in all the auroral oval crossings shown in the data figures that the direction of the trajectory component of the electric field was such as to close the major field-aligned current pattern by Pedersen current flow in the ionosphere (i.e., the ionosphere acts as a load). Also, we have observed a
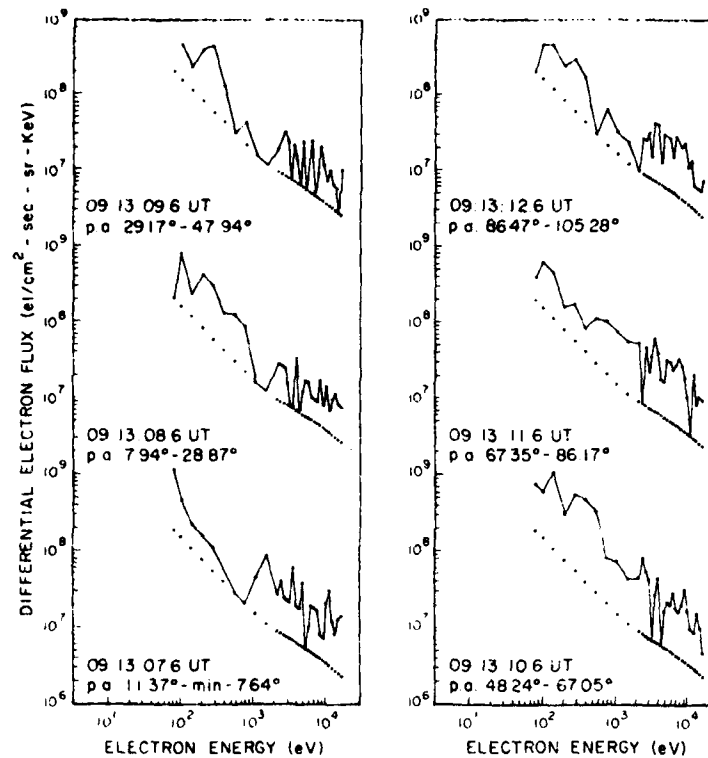
155

Fig. 9. Differential energy spectra observed on the dayside of orbit 1568N. The fine structure evident in the higher energy levels may indicate the presence of an electrostatic shock.

number of instances where the excursion in ΔB_y was greater than 1000 γ, and one even greater than 2000 γ, which would equate (see (2)) to integrated sheet current densities of 0.8 A/m and 1.6 A/m, respectively. Further, by taking the ratio of j_z to $\Delta E_z/\Delta x$, which is comparable to the ratio of the integrated sheet current density to the ionospheric electric field, we have obtained reasonable values of the height-integrated Pederson conductivities. All of these serve to confirm the results of the model of *Mallinckrodt and Carlson* [1978] for a magnetospheric rather than an ionospheric source for the observed fields and currents. For an ionospheric source their model predicts (1) integrated sheet current to ionospheric field ratios on the order of 0.2-0.5 Ω^{-1}, independent of ionospheric conductivity, (2) electric fields above the ionosphere to be essentially mapped versions of those within the ionosphere, and (3) ionospheric electric fields opposed to the direction of field-aligned current closure. For a magnetospheric source their model predicts an integrated sheet current to ionospheric electric field ratio equal to Σ_P, large-magnitude oppositely directed pairs of electric fields in the magnetosphere above auroral arcs, and an ionospheric electric field in the direction to close the field-aligned currents. Also, the model limits integrated field-aligned sheet current densities to 0.1 A/m for ionospheric polarization sources, but allows for more than 1 A/m for magnetospheric sources. Except for the large-magnitude oppositely directed pairs of electric fields in the magnetosphere, which the S3-2 satellite did not observe in these passes (but which were found by *Mozer et al.* [1977] in the altitude range 2000-8000 km with the S3-3 satellite), our results clearly support the model for a magnetospheric current source.

Our observations have not ruled out the possibility that some current sheet pairs close by polarization currents, particularly the current sheets associated with small-scale variations. For instance, interruption of a downward field-aligned current may lead to polarization charges in the electrojets that would be neutralized by field-aligned currents driven by the ionosphere. Partial choking of the downward field-aligned current can occur when the current density exceeds some critical limit causing current-driven instabilities such as anomalous resistivity [*Kindel and Kennel*, 1971].

Current charge carriers. As noted earlier, current densities were calculated from the electron differential fluxes by determining the integrated fluxes over each second (one full spectrum) and using these values with their corresponding pitch angle ranges. In general, the values of current densities calculated from electron fluxes and from $d(\Delta B_y)/dx$ agreed reasonably well. (For the purposes of these comparisons with the ESA data, the current density values calculated from the magnetometer have been corrected (upward) to account for the likely underestimate due to the transverse axis being offset from the magnetic east-west direction.) The electrons accounted for up to 50% of the upward currents in those cases where electron precipitation occurred in the nighttime auroral zone with a broad energy distribution and with increased fluxes. Whenever the fluxes were quite low, or when low energy values were below the ESA's capability to measure them, the values agreed in direction but were far apart in amplitude.

156

TABLE 1.   Height-Integrated Pedersen Conductivities and Joule Heating Rates Due to Ionospheric
Closure Current Flow

Orbit	Position	Time	Σ_P, Ω^{-1}	$\hat{E}_x$, mV/m	Q_J, mW/m^2	Hall Current Direction
1546	north-night	1934:20	3.3	9	0.3	east
1546	north-night	1934:48	1.8	20	0.7	east
1546	north-day	1943:52	2.9	4	--	west
1546	north-day	1944:30	8.5	15	1.9	west
1546	north-day	1945:00	7.1	3.5	0.1	west
1546	north-day	1945:30	6.5	3	0.1	west
1567	north-night	0713:12	26.1	22	12.6	east
1567	north-night	0714:10	25.0	20	10.0	east
1567	north-night	0715:15	34.1?	17	9.9	east
1567	north-night	0715:30	13.3	15	3.0	east
1567	north-night	0716:36	3.3?	7	0.2	west
1567	north-night	0717:36	32.3	13	5.5	west
1567	north-night	0718:12	9.6	17	2.8	west
1567	north-day	0728:30	5.6	38	8.1	east
1567	north-day	0729:15	7.8	75	43.9	east
1567	north-day	0731:06	30.0?	48	69.1	east
1567	north-day	0731:36	19.5?	7	1.0	east
1567	south-day	0810:30	20.6	21	9.1	west
1567	south-day	0811:12	17.8	23	9.4	west
1567	south-day	0811:30	33.2	30	29.9	west
1567	south-day	0813:42	18.4	26	12.4	west
1567	south-day	0814:00	25.0	25	15.6	west
1567	south-day	0815:15	22.7	12	3.3	west
1567	south-night	0824:44	7.6	25	4.8	west
1567	south-night	0825:00	18.1	26	12.2	west
1567	south-night	0825:45	10.2	22	4.9	west
1567	south-night	0826:40	30.1	40	48.2	west
1567	south-night	0827:54	16.8	30	15.1	west
1567	south-night	0828:35	29.7	16	7.6	west
1567	south-night	0829:00	73.4?	3	0.7	east
1567	south-night	0829:30	5.1	8	0.3	east
1567	south-night	0830:00	2.4	9	0.2	east
1568	north-night	0856:00	38.0?	23	20.1	east
1568	north-night	0856:50	14.5	15	3.3	east
1568	north-night	0857:40	23.5	5	0.6	west
1568	north-night	0858:06	10.7	39	16.3	west
1568	north-night	0858:30	17.7	31	17.0	west
1568	north-night	0859:20	11.7	12	1.7	west
1568	north-day	0910:40	4.3	26	2.9	east
1568	north-day	0911:40	7.1	68	32.8	east
1568	north-day	0913:14	41.5?	63	164.7	east
1568	north-day	0914:00	6.3	8	0.4	east

During the intense substorm in the nightside northern auroral zone, orbit 1568, the energy spectra shifted to higher levels and the agreement between the precipitating electron current density values and those determined by the magnetometer was very good. In the two cases of upward current flow that could be compared in this event, at 0858:20 and 0859:02 GMT, the agreement was better than 70%, indicating that, at least for the most intense upward Birkeland currents, the precipitating energetic electrons constituted the major portion of the current carriers.

Location of field-aligned currents. For the eight crossings of the auroral oval presented here, it was true in every case that the region 1 and region 2 currents, as identified by *Iijima and Potemra* [1976a, b], were located almost entirely below the electric field reversal that marked the polar cap boundary. The other reversal was taken to mark the Harang discontinuity. *Heppner et al.* [1971] proposed that a narrow upward current sheet originates from that discontinuity. We have noted intense current sheets poleward of the electric field reversal at the equatorward side of the westward electrojet in the three substorm cases studied here. *Kamide and Rostoker* [1977], us-

ing ground-based magnetometer data in conjunction with the Triad measurements, have also reported the same configuration in the evening sector—intense upward field-aligned currents immediately poleward of the eastward electrojet, presumed to coincide with the extension of the westward electrojet from the morningside. This was not as clearly observed for the quiet time orbit, 1546, where the electric field was weak inside what would be the westward electrojet region. On the ground the Harang discontinuity manifests itself as a line separating the negative from the positive horizontal magnetic perturbations. *Kamide and Akasofu* [1976] reported an absence of upward current in this narrow region.

Other types of currents, some with reverse polarities and some with smaller than usual amplitudes, were observed inside the polar cap (see dayside of Figure 5). If the polar cap field lines are open, then currents can flow on open as well as on closed magnetic field lines. Thus our combined observations indicate that the distribution of sources of currents can extend from the ionosphere to the boundary layer including the inner magnetosphere and the plasma sheet. The regions with electric fields are usually broader than the regions car-
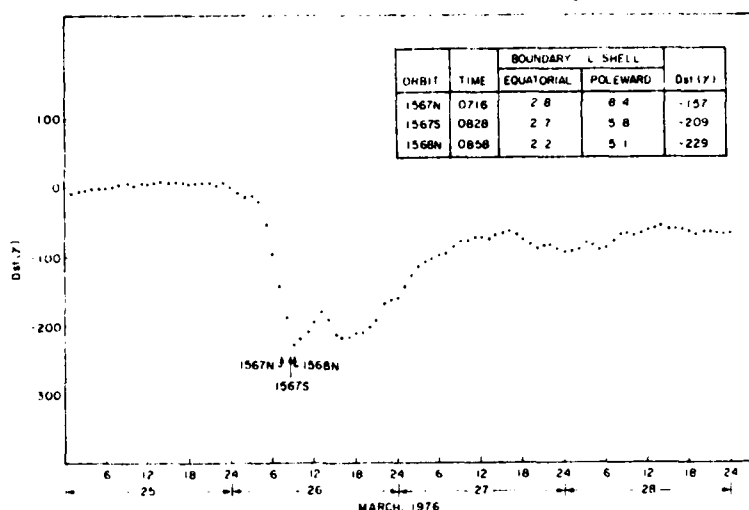
Fig. 10. *Dst* plot showing the main phase decrease in the magnetic storm of March 26, 1976. Superimposed arrows indicate the time of passage of the S3-2 satellite through the nightside auroral oval. Successive *L* shell boundaries of the nightside oval are summarized.

rying field-aligned currents. This implies that convective motion of magnetic field lines does not always produce field-aligned currents.

A plot of *Dst*, which includes the period of the March 26, 1976 magnetic storm, is shown in Figure 10. The superimposed arrows indicate the times of passage of the S3-2 satellite through the auroral oval on the nightside. These occurred toward the end of the main phase decrease, with orbit 1568 crossing the nightside oval just at the time of the maximum decrease (*Dst* = −229 γ). The *L* shell boundaries of the field-aligned current region observed in the northern nightside of orbit 1567 were 2.8 and 8.4, whereas the current distributions in the southern nightside of orbit 1567 were confined inside the region *L* = 2.7 to *L* = 5.8. The following pass, 1568N, had the currents further compressed to a region of *L* = 2.2 to *L* = 5.1 These results are summarized in Figure 10. As *Dst* decreased by 72 γ in 102 min. the outer *L* shell boundary of the current-carrying region moved earthward by an amount Δ*L* = 3.3 and the inner boundary by Δ*L* = 0.6. Thus assuming an approximately dipolar configuration of the field, which may well not be applicable during this disturbed period, the outer boundary would appear to have moved earthward five times faster than the inner boundary during the ring current buildup. Further, these observational results from the S3-2 satellite during extremely disturbed magnetic conditions support the idea that the equatorial source of these field-aligned currents is the inner magnetospheric plasma inside the outer Van Allen radiation zone and that the dawn or the dusk boundary layer and the distant plasma sheet do not play a primary role in driving these particular currents. The outer boundary of the radiation zone may be defined empirically by the trapping limit of energetic electrons. For orbit 1568, an on-board energetic electron spectrometer measurement (A. Vampola, private communication, 1980) showed that boundary to be at *L* = 4.8 for electrons of *E*, > 36 keV.

Fine-scale variations. Superimposed on the large-scale field-aligned currents, we found fine structure corresponding to large current densities. *Saflekos et al.* [1979] have observed

ULF-ELF magnetic noise and broadband electrostatic noise near structured field-aligned currents. In orbit 1568, both the magnetometer and the dc electrostatic probe observed fast variations. We present this as evidence in favor of the idea that the currents are responsible for such variations. Interpreting particle measurements taken by the S3-2 satellite during the nightside crossing of the auroral oval in orbit 1568, *Scholer et al.* [1979] postulated ion cyclotron waves in order to explain strong pitch angle scattering of energetic ions It appears that the electrostatic ion cyclotron waves were generated and amplified by current-driven instabilities [*Temerin et al.*, 1979].

Furthermore, we have studied some narrow regions of upward current characterized by steep electric and magnetic field gradients with simultaneous enhanced electron precipitation in orbit 1568. We interpret the enhanced precipitation as due to parallel electric fields above the satellite. In fact, one case is a classic example of an inverted V, as shown in Figure 8. Such parallel electric fields are usually attributed to double layers or oblique double layers [*Shawhan et al.*, 1978]. An interesting feature of some electron spectra associated with strong upward currents is the fine structure shown in Figure 9. This may be the signature of rapidly varying parallel electric fields, which can be interpreted as being due to a regenerative electrostatic shock or a rapidly firing double layer. This phenomenon, if truly observed, is of great geophysical interest [*Bostrom*, 1974].

SUMMARY AND CONCLUSIONS

The S3-2 polar-orbiting satellite has provided measurements of ambient magnetic field, electric field, and auroral electron flux during a very intense substorm period. We have used one quiet time orbit and two orbits in extremely active times to calculate field-aligned current densities, compare them with precipitating auroral electron fluxes, and by utilizing the direction of the electric field component, identify the particular regions to which they map down (i.e., eastward electrojet, westward electrojet, or polar cap). We have been

158

able to track the boundaries of the current-carrying region during the early main phase of the geomagnetic storm, and to infer the location of source regions for these currents at low L shell values in the inner magnetospheric plasma, as well as on open field lines that may extend out to the boundary layer and the tail lobes. When conditions permitted, we have calculated the height-integrated Pedersen conductivity of the ionosphere by using a number of simplifying assumptions, but without invoking models of collision frequency. For completeness, we have also calculated the ionospheric Joule heating rate due to closure of field-aligned currents by Pedersen current flow. In the most active periods, associated with intense narrow upward sheet currents and steep electric field gradients, enhanced fluxes of precipitating electrons could be identified as inverted V events or as possible electrostatic shocks.

Our principal results based on observations from the two orbits of storm time data may be summarized as follows.

1. In all the cases observed, the direction of the electric field component indicated closure of the major field-aligned current pattern by Pedersen current flow in the ionosphere. This loadlike behavior of the ionosphere was consistent with the source of the field-aligned currents being in the magnetosphere.

2. Values of the height-integrated Pedersen conductivity, calculated from the ratio of the poleward gradients of the transverse component of magnetic field to the trajectory component of electric field, were typically in the range 10–$30\ \Omega^{-1}$ in the current-carrying regions during active times. At such times, particle precipitation on the nightside became the major factor in controlling the magnitude of the ionospheric conductivity, outweighing the influence which sunlight has in quiet times.

3. High particle fluxes corresponded to regions of upward current. In regions of increased fluxes of precipitating electrons in the nightside auroral oval, the current densities calculated from electron fluxes accounted for up to 50% of the upward currents, as determined by the magnetometer. During the most intense substorm period this agreement increased to better than 70%.

4. A feature consistently observed on the nightside was the intense upward current sheet at the equatorward side of the westward electrojet, just poleward of the electric field reversal associated with the Harang discontinuity.

5. During the most intense current period, the region of field-aligned currents was compressed down to L shell values 2.2 to 5.1, within the trapping region, indicating that the equatorial source of these currents was the inner magnetospheric plasma inside the outer Van Allen radiation zone rather than the distant plasma sheet or the boundary layer.

REFERENCES

Allen, J. H., C. A. Abston, and L. R. Morris, Geomagnetic data for March 1976 [AE(7) indices and stacked magnetograms], *Rep. UAG-*

63, National Geophysical and Solar-Terrestrial Data Center, Environmental Data Service, Boulder, Colo., Sept. 1977.

Birkeland, K., *The Norwegian Aurora Polaris Expedition 1902-1903*, vol. 1, sect. 1, H. Aschehoug, Christiania, Norway, 1908.

Bostrom, R., A model of the auroral electrojets, *J. Geophys. Res.*, 69, 4983, 1964.

Bostrom, R., Ionosphere-magnetosphere coupling, in *Magnetospheric Physics*, edited by B. M. McCormac, p. 45, D. Reidel, Hingham, Mass., 1974.

Burke, W. J., D. A. Hardy, F. J. Rich, M. C. Kelley, M. Smiddy, B. Shuman, R. C. Sagalyn, R. P. Vancour, P. J. L. Wildman, S. T. Lai, and J. Bass, A case study of S3-2 observations in the late evening auroral oval, *Rep. AFGL-TR-79-0011*, Air Force Geophys. Lab., Bedford, Mass., 1979.

Burke, W. J., D. A. Hardy, F. J. Rich, M. C. Kelley, M. Smiddy, B. Shuman, R. C. Sagalyn, R. P. Vancour, P. J. L. Wildman, and S. T. Lai, Electrodynamic structure of the late evening sector of the auroral zone, *J. Geophys. Res.*, 85, 1179, 1980.

Bythrow, P. F., R. A. Heelis, W. B. Hanson, and R. A. Power, Simultaneous observations of field-aligned currents and plasma drift velocities by Atmosphere Explorer C, *J. Geophys. Res.*, 85, 151, 1980.

Cauffman, D. P., and D. A. Gurnett, Double-probe measurements of convection electric fields with the Injun 5 satellite, *J. Geophys. Res.*, 76, 6014, 1971.

Cauffman, D. P., and D. A. Gurnett, Satellite measurements of high latitude convection e ectric fields, *Space Sci. Rev.*, 13, 369, 1972.

Evans, D. S., N. C. Maynard, J. Troim, T. Jacobsen, and A. Egeland, Auroral vector field and particle comparisons, 2, Electrodynamics of an arc, *J. Geophys. Res.*, 82, 2235, 1977.

Greenwald, R. A., T. A. Potemra, and N. A. Saflekos, Stare and Triad observations of field-aligned current closure and Joule heating in the vicinity of the Harang discontinuity, *J. Geophys. Res.*, 85, 563, 1980.

Heppner, J. P., J. D. Stolarik, and E. M. Wescott, Electric-field measurements and the identification of currents causing magnetic disturbances in the polar cap, *J. Geophys. Res.*, 76, 6028, 1971.

Iijima, T., and T. A. Potemra, The amplitude distribution of field-aligned currents at northern high latitudes observed by Triad, *J. Geophys. Res.*, 81, 2165, 1976a.

Iijima, T., and T. A. Potemra, Field-aligned currents in the dayside cusp observed by Triad, *J. Geophys. Res.*, 81, 5971, 1976b.

Iijima, T., and T. A. Potemra, Large-scale characteristics of field-aligned currents associated with substorms, *J. Geophys. Res.*, 83, 599, 1978.

Kamide, Y., and S.-I. Akasofu, The auroral electrojet and field-aligned current, *Planet. Space Sci.*, 24, 203, 1976.

Kamide, Y., and J. L. Horwitz, Chatanika radar observations of ionospheric and field-aligned currents, *J. Geophys. Res.*, 83, 1063, 1978.

Kamide, Y., and G. Rostoker, The spatial relationship of field-aligned currents and auroral electrojets to the distribution of nightside auroras, *J. Geophys. Res.*, 82, 5589, 1977.

Kindel, J. M., and C. F. Kennel, Topside current instabilities, *J. Geophys. Res.*, 76, 3055, 1971.

Klumpar, D. M., J. R. Burrows, and M. D. Wilson, Simultaneous observations of field-aligned currents and particle fluxes in the post-midnight sector, *Geophys. Res. Lett.*, 3, 395, 1976.

Mallinckrodt, A. J., and C. W. Carlson, Relations between transverse electric fields and field-aligned currents, *J. Geophys. Res.*, 83, 1426, 1978.

Maynard, N. C., Electric field measurements across the Harang discontinuity, *J. Geophys. Res.*, 79, 4620, 1974.

McDiarmid, I. B., J. R. Burrows, and M. D. Wilson, Comparison of magnetic field perturbations at high latitudes with charged particle and IMF measurements, *J. Geophys. Res.*, 83, 681, 1978a.

McDiarmid, I. B., J. R. Burrows, and M. D. Wilson, Magnetic field perturbations in the dayside cleft and their relationship to the IMF, *J. Geophys. Res.*, 83, 5753, 1978b.

Mozer, F. S., C. W. Carlson, M. K. Hudson, R. B. Torbert, B. Parady, J. Yatteau, and M. C. Kelley, Observations of paired electrostatic shocks in the polar magnetosphere, *Phys. Rev. Lett.*, 38, 292, 1977.

Saflekos, N. A., and T. A. Potemra, The orientation of Birkeland current sheets in the dayside polar region and its relationship to the IMF, *J. Geophys. Res.*, 85, 1987, 1980.

Saflekos, N. A., T. A. Potemra, P. M. Kintner, and J. L. Green, Field-aligned currents, convection electric field, and ULF-ELF waves in the cusp, *J. Geophys. Res.*, 84, 1391, 1979.

Scholer, M., D. Hovestadt, G. Hartmann, J. B. Blake, J. F. Fennell,

and G. Gloeckler, Low-altitude measurements of precipitating protons, alpha particles, and heavy ions during the geomagnetic storm of March 26–27, 1976, *J. Geophys. Res.*, *84*, 79, 1979.

Shawhan, S. D., C. G. Falthammar, and L. P. Block, On the nature of large auroral zone electric fields at 1 R_E altitude, *J. Geophys. Res.*, *83*, 1049, 1978.

Smiddy, M., M. C. Kelley, W. Burke, F. Rich, R. Sagalyn, B. Shuman, R. Hays, and S. Lai, Intense poleward-directed electric fields near the ionospheric projection of the plasmapause, *Geophys. Res. Lett.*, *4*, 543, 1977.

Sugiura, M., and T. A. Potemra, Net field-aligned currents observed by Triad, *J. Geophys. Res.*, *81*, 2155, 1976.

Temerin, M., M. Woldorff, and F. S. Mozer, Nonlinear steepening of the electrostatic ion cyclotron wave, *Phys. Rev. Lett.*, *43*, 1941, 1979.

Zmuda, A. J., and J. C. Armstrong, The diurnal flow pattern of field-aligned currents, *J. Geophys. Res.*, *79*, 4611, 1974.

Electrodynamic Structure of the Late Evening Sector of the Auroral Zone

W. J. Burke,[1] D. A. Hardy,[2] F. J. Rich,[1] M. C. Kelley,[4] M. Smiddy,[2] B. Shuman,[2]
R. C. Sagalyn,[2] R. P. Vancour,[2] P. J. L. Widman,[2] and S. T. Lai[1]

Detailed observations from a late evening sector pass of S3-2 over the northern auroral zone are presented and compared with nearly simultaneous DMSP imagery. High time resolution measurements are presented from electric field, magnetic field, energetic electron (80 eV $\leq E \leq$ 17 keV), and thermal plasma detectors. The region of diffuse aurorae was characterized by nearly isotropic electron fluxes and slowly varying ($\leq$ 20 mV/m) electric fields. The Birkeland currents in this region were predominantly into the ionosphere with embedded, narrow sheets of upward currents. Simultaneous magnetometer and satellite potential fluctuations show that the upward current sheets are real and that these upward currents are probably carried by precipitating, low-energy plasma sheet electrons. Poleward of the diffuse aurorae, the covective electric field varied rapidly in magnitude, anticorrelating with the intensity of precipitating electrons. An inverted-V structure was observed above a visible arc. An intense downward current sheet ($>10 \mu A/m^2$) was found near the equatorward edge of the arc. At this place the ionospheric thermal plasma was near marginal stability for the onset of O^+ ion cyclotron turbulence. An electric field component parallel to B of ~10 mV/m was measured in this region of strong downward current. The plasma and electric field distributions in the vicinity of the arc suggest that the auroral electrojet was distributed over the region of diffuse auroral but was most intense near the equatorward boundary of the auroral arc.

INTRODUCTION

Significant progress has been made over the last decade toward an understanding of the relationship between the magnetosphere and the auroral ionosphere. A self-consistent, theoretical solution of the problem is beyond present capabilities. Thus much effort has been expended on experimental determination of various facets of the problem. This paper extends the experimental analysis by presenting a comprehensive set of measurement taken by means of instruments on board the polar-orbiting satellite S3-2. The instruments were designed to measure the ambient electric E and magnetic B fields, the thermal ion N, and electron N_e densities, the thermal ion drift velocity V_i, the thermal electron temperature T_e and the directional differential flux of electrons with energies between 80 eV and 17 keV. One pass of S3-2 over the northern auroral zone in the late evening local time sector is studied in great detail. The particular pass (S3-2 orbit 517) was chosen for analysis because of the availability of nearly simultaneous imagery data from a Defense Meteorological Satellite Program (DMSP) satellite. Emphasis is placed on the high time resolution of the measurements. This allows the identification of small-scale auroral zone features that are frequently missed by satellite-borne instruments.

Aurorae are confined to a band of relatively high geomagnetic latitudes whose instantaneous position is called the auroral oval. The dayside of the auroral oval maps into the dayside cusp, while the remainder of the oval maps into the plasma sheet portion of the magnetosphere. Within the oval, aurorae are categorized as either discrete or diffuse. Discrete auroral arcs are embedded within the diffuse aurora, generally in the poleward portion of the oval [Lui et al., 1977]. These

arcs appear to be associated with so called 'inverted -V events' [Ackerson and Frank, 1972]. Electron fluxes within inverted-V events have field-aligned components [Craven et al., 1976] and spectra that are marked by double peaks. Measurable proton fluxes are either weak or absent [Frank and Ackerson, 1971] in the vicinity of inverted-V structures.

The diffuse aurorae are characterized by electrons whose pitch angle distributions are nearly isotropic. Their energy spectra either decrease monotonically with increasing energy or have thermal, Maxwellian shapes. Proton fluxes in this region are significant. Near the equatorward boundary of this region the energy fluxes of protons and electrons are of comparable magnitude [Lui et al., 1977].

Within the auroral oval there is a complex system of electrical currents flowing both perpendicular and parallel to B. The perpendicular currents constitute the auroral electrojet and are primarily responsible for ground-based magnetometer deflections. They are driven by ionospheric electric fields and are strongest in the vicinity of discrete arcs. Broad regions of field-aligned currents into and out of the auroral oval have been identified in magnetometer measurements from polar-orbiting satellites [Zmuda et al., 1970].

To describe this large scale system, the nomenclature 're-gion 1' and 'region 2' has been introduced [Iijima and Po-temra, 1976]. Regions 1 and 2 are located in the poleward and equatorward portions of the field-aligned current region, respectively. In the evening and afternoon sectors, current flows into the ionosphere in region 2 and out of the ionosphere in region 1. The opposite current polarities are found in the post-midnight and morning local time sectors. Prior to midnight the morningside region 1 current is frequently found poleward of the evening sector region 1 current out of the ionosphere.

Small-scale, field-aligned current systems are embedded within the large-scale system detected by satellites. Numerous rocket experiments [Anderson and Vondrak, 1975, and references therein] have measured currents into and out of the ionosphere with scale lengths of 10-20 km. Current out of the ionosphere is carried by energetic electrons precipitating to form discrete arcs. Significant return currents (into the iono-

[1] Boston College, Chestnut Hill, Massachusetts 02167.
[2] Air Force Geophysical Laboratory, Hanscom Air Force Base, Massachusetts 01731.
[3] Regis College, Weston, Massachusetts 02193.
[4] Cornell University Ithaca, New York 14853.

sphere) are found at the equatorward boundaries of the arcs. Simultaneous measurements by the Triad satellite and by all-sky cameras indicate that in the evening sector, discrete arcs are found in region 1 and diffuse aurora in region 2 [Armstrong et al., 1975; Kamide and Akasofu, 1976].

A synoptic picture of large-scale electric field structures in the auroral oval has begun to develop from the measurements of polar-orbiting satellites Injun 5 [Gurnett and Frank, 1973] and Ogo 6 [Heppner, 1973; Maynard, 1974] and balloon data [Mozer and Lucht, 1974]. In the evening (morning) sector, E is principally in the poleward (equatorward) direction [cf. Heppner, 1973, Figure 3]. In the midnight sector, E rotates from poleward through westward to equatorward.

The detailed relationship between electric fields and discrete auroral arcs appears ambiguous at this time. Similar experiments flown on rockets through auroral arcs have produced conflicting results. In one case the magnitude of E strongly anticorrelated with increasing fluxes of electrons [Maynard et al., 1977], while in another case both positive and negative correlations were found in multiple arc crossings [Carlson and Kelley, 1977]. The complexity of electric field coupling between the ionosphere and magnetosphere has been further underscored by recent observations of abrupt discontinuities in E at altitudes between 4000 and 8000 km and high magnetic latitudes [Mozer et al., 1977]. These discontinuities are associated with current-driven ion cyclotron turbulence [Kinter et al., 1978], which may alter the particle distribution functions and ease the development of electrostatic shocks above the ionosphere [Hudson and Mozer, 1978]. Large parallel to B components of E exist within the shocks and have been interpreted as the source of discrete auroral arcs [Torbert and Mozer, 1978], as theoretically predicted by Swift [1975].

In the following section the S3-2 instrumentation and data reduction techniques are described. A detailed analysis of the electric field data reduction measurements from a single pass of S3-2 over the late evening auroral oval is presented in the third section. Nearly simultaneous imagery from a DMSP satellite indicates that S3-2 passed over a bright auroral arc. In the final section the measurements are discussed with relation to (1) previously reported Birkeland current measurements, (2) conditions required for anomalous resistivity along magnetic field lines, (3) relative positions of the auroral arc and the auroral electrojet, and (4) simultaneous variations in the electric fields and electron fluxes.

THE SCIENTIFIC EXPERIMENTS

The Air Force scientific satellite S3-2 was launched into polar orbit in December 1975 with an initial apogee, perigee, and inclination of 1557 km, 240 km, and 96.3°, respectively. It is spin-stabilized with a nominal spin period of 20 s and a spin axis that is nearly perpendicular to the orbital plane in a cartwheel sense. The scientific package carried by S3-2 includes (1) a dc electric field experiment, (2) a triaxial flux gate magnetometer ,(3) an energetic electron spectrometer, (4) an ion drift meter, and (5) a thermal electron probe. The various instruments and the methods by which measurements are reduced to give geophysically significant quantities are described in detail by Burke et al. [1979]. Here only a brief description of the experiments is given.

The electric field experiment on S3-2 was designed to consist of three orthogonal dipoles: two in the spin plane and one along the spin axis. Unfortunately, one of the dipoles in the

spin plane failed to deploy. The dipole in the spin plane consists of two carbon-coated spheres of 3.81-cm radius placed at the ends of 13.72-m insulated cable booms. The spin-axis-aligned dipole also consists of two spheres held at the ends of 11-m tip to tip rigid booms. It has been found that the spin-axis-aligned dipole is subject to time-varying contact potentials, which in this orientation cannot be separated from dc electric fields. For this reason the measurements are usually limited to those of a single spinning dipole with which these voltage sources are distinguishable.

The potential differences between the ends of the dipole are measured 64 times a second and are interpreted as discussed by Fahleson [1967]. A detailed description of how data from the spinning dipole are reduced is given in Appendix A. To summarize the potential differences between the ends of the dipole due to satellite motion across magnetic field lines (V, × B) and to different contact potentials (which appear as dc offsets) are subtracted from the measured potential differences to determine that due to the ambient electric field ϕ_E. This signal is then fitted to a sinusoidal function using 5 s of data. If we assume E · B = 0, this measurement yields the component of electric field in the direction of a vector in the B × (V, × B)/ $|V_s||B|^2$ direction. Differences between ϕ_E and the fitted function are examined to identify periods when E varies in spacecraft coordinates on time scales <5 s. These differences, in conjunction with other measurements, are also used to identify periods when the E · B = 0 assumption is not valid.

The magnetic field is measured by a triaxial, flux gate magnetometer mounted at the end of a 6.1-m boom in the spacecraft spin plane. The axes of the magnetometer are approximately aligned with axes of the spacecraft body. The spin-aligned magnetometer axis has been determined to be approximately 3.5° from the true spacecraft spin axis. The actual alignment of the magnetometer axis is determined from in-flight calibration to an accuracy of 0.01° [Burke et al., 1979]. The magnetic field along each axis is measured 32 times per second with an accuracy of 5 γ ($\gamma = nT$). Each measurement is made in a range of ± 600 γ. There are 128 range steps set at 1000-γ intervals for a total dynamic range of ± 64,000 γ along each axis. Each time the range step is changed, two or three data points are lost; this loss occasionally limits the measurement of the components of the magnetic field in the spin plane, but it has no noticeable effect on the spin-axis-aligned component. Owing to the orientation of the satellite the spin-axis-aligned component of the magnetic field is approximately the east-west field component, which is the one of greatest geophysical interest.

The International Geomagnetic Reference Field (IGRF) 1975, updated to the epoch of the measurement, is subtracted from the measured values of the magnetic field in the magnetometer's coordinate system Uncertainties in IGRF do not affect the analysis of the magnetic field deflections, since the error from the model is only a few times 100 γ and changes vary slowly along the path of the satellite. When the difference vector between the measured and model field is rotated out of the magnetometer coordinate system, errors are introduced because the three magnetometers are not perfectly cross calibrated and because of data losses owing to range changes.

The electron spectrometer, which has been described by Morel et al. [1975], measures electrons with energies between 80 eV and 17 keV by means of a parallel plate electrostatic analyzer. This instrument produces a 32 point spectrum once per second with $\Delta E/E = 0.0419$. The geometric factor is 4.68 ×

10^{-3} cm² sr. The aperture of the instrument is mounted in the spin plane of the satellite. Since the satellite spin period is 20 s, each spectrum corresponds to approximately an 18° sample in electron pitch angle. In their reduced form, data are available as number flux, energy flux, and average energy in the range 80 eV $\leq$ E $\leq$ 17 keV as functions of universal time, pitch angle, and other standard geophysical coordinates. Individual spectra are also available for detailed analysis of particular auroral events.

The ion drift meter experiment consists of two arrays of four passive thermal ion sensors each with a circular aperture of 6.8-cm² area. The external configurations of the two arrays are identical. They are embedded in the surface of the vehicle at diametrically opposite positions. The internal geometry of sensors 1, 2, 3, and 4 is planar. To minimize their response to solar UV, the internal geometry of sensors 5, 6, 7, and 8 are nonplanar [*Widman*, 1977]. Normal vectors to the apertures of sensors 2 (6) and 4 (8) lie in the spin plane of the satellite at relative look angles at 40°. Sensors 1 (5) and 3 (7) are coplanar with 2 (6) but look out of the spin plane by angles of 40° toward and away from the spin axis, respectively. Using precise satellite attitude information, the currents measured by sensors 2 (6) and 4 (8) can, in principle, be used to calculate the component of plasma drift in the spin plane, that is, the up-down component of plasma motion normal to the satellite velocity V_z. Currents measured by sensors 1 (5) and 3 (7) give the components along the satellite spin axis. Since the satellite motion is primarily north-south, the drift component is nearly east-west.

In addition to the plasma drift motion which requires the analysis of currents to two sensors, information about the plasma density and the dominant ion species may be gained from the measurements made by individual sensors. The latter, semiquantitative measurement, makes use of the fact that for typical ionic temperatures of ~1000°K the Mach number of the satellite is ~1 in a region of H⁺ and ~5 in an O⁺ region. Although the currents measured by a sensor, say, sensor 2, when facing toward the satellite velocity (ram direction) are comparable for H⁺ or O⁺ at a given density, the currents measured in the antiram direction are very different. The ratio of currents measured in the ram and antiram directions is much greater in the O⁺ than in H⁺ regions.

The thermal electron sensor is a gridded, spherical Langmuir probe mounted at the end of a 1.2-m boom projecting parallel to the satellite's spin axis. The probe itself consists of a solid collector of 2.54-cm radius surrounded by a concentric wire mesh grid of 3.30-cm radius and 66.4% transparency. The experiment operates in a two-mode, repetitive cycle of 32- or 16-s duration, depending on command from ground. In the first mode the grid is held for 29.5 or 13.5 s at +1.5 V relative to the satellite ground potential. The purpose of the +1.5 V bias is to offset anticipated negative satellite potentials relative to the ambient plasma. In the second mode of operation the grid is swept from +8 to −8 V in 2.5 s. The collector is always held at +50 V relative to the applied grid potential. Thus any thermal electrons passing through the wire mesh grid are accelerated to the collector, and thermal ions are repelled. The density and temperature of the ambient electrons as well as the potential of the spacecraft ground relative to the plasma are determined from the measured electron current versus applied voltage relationship. The analysis is based on standard Langmuir probe theory.

During the fixed voltage mode, electron densities are calcu-

lated from the electron currents using the electron temperature and satellite potential measured during the previous swept voltage mode period. This method of normalizing fixed voltage mode data assumes that the electron temperature and satellite potential are unchanged for the duration of the fixed voltage model. This assumption breaks down in the auroral zone, where energetic charged particles cause frequent and rapid fluctuations of the satellite potential. Changes in the electron current due to satellite potential fluctuations may be distinguished from those due to density fluctuations by referring to simultaneous measurements by the ion drift meter. Changes in the plasma density produce similar variations in the electron and ion sensor currents. Negative excursions of the satellite potentials reduce the currents to the thermal electron sensor but leave the ion sensor measurements virtually unchanged.

OBSERVATIONS

In this section, data from S3-2 are presented from a single pass of the late evening sector of the northern auroral zone. As stated above, this pass (orbit 517) was chosen for analysis because of the availability of nearly simultaneous imagery from a DMSP satellite. Structurally, this section consists of three parts. An overview of S3-2/DMSP observations is presented in the first subsection. The measurements are given as functions of universal time in seconds of the day. Observations from regions 2 and 1 [*Iijima and Potemra*, 1976] are studied in detail in the following subsections. Region 2 is subdivided according to whether the Birkeland currents are in the region of diffuse aurorae or constitute strong return currents for discrete arcs. The order for data presentation is chronological for a poleward moving satellite.

Overview

DMSP imagery taken at northern high latitudes on January 11, 1976, is given in Figure 1. The superimposed grid gives the corrected geomagnetic longitude and latitude projected to an altitude of 100 km. The trajectory of S3-2 orbit, also projected in corrected geomagnetic longitude and latitude to 100 km, is represented by the lighter dashed line. The temporal separation between the DMSP and S3-2 trajectory crossover in this coordinate system was 14 min with S3-2 measurements taken after those of DMSP. During quiet conditions, auroral forms tend to be stationery in magnetic latitude and magnetic local time. In the 14 min between the DMSP and S3-2 crossover the earth rotated under the arc ~3.5° in longitude. Thus relative to the arc, the S3-2 orbit should be moved 3.5° to the east, that is, away from the folded arc and well into the straight line arc segment. This arc is tilted by ~15° away from the magnetic east-west direction. As represented in the heavier dashed line, the S3-2 trajectory crossed the arc at an angle of ~30° away from normal incidence.

Two independent sets of measurements indicate that the auroral form remained relatively stationary during the 14 min between the DMSP and S3-2 crossovers. First, the ground-based magnetic measurements (not shown) from Dixon Island, which is marked by the symbol X in Figure 1, show that a weak $\Delta H \sim -200$ γ) substorm was in progress. This agrees with the DMSP imagery, which shows a disordered region to the east of the S3-2 track near local midnight. Although such periods normally involve large temporal variations in auroral behavior, the S3-2 orbit lies to the west of the active region. The Dixon Island magnetogram is constant in all three com-

Fig. 1. DMSP imagery for an auroral form taken ~14 min prior to S3-2 overpass (dashed line). The superimposed grid gives the geomagnetic latitude and longitude at an altitude of 100 km The position of Dixon Island is marked by the symbol X.

ponents (± 10 γ) during the 14-min period between DMSP and S3-2 overpasses. Since Dixon Island is magnetically due north of where S3-2 crossed the auroral oval, the constant magnetic field at this station is consistent with no violent changes in the auroral features. Second, as discussed below, an inverted-V structure was observed in the energetic electron measurement beginning at 60653 UT. Tracing magnetic field lines from the altitude of S3-2 to 100 km allowing for earth rotational effects, we find that this coincides (± 0.1°) with the equatorward boundary of the discrete auroral arc shown in Figure 1.

A summary of plasma and field conditions encountered during orbit 517 is given in Figures 2-4. Going from the top to bottom panels of Figure 2, we have plotted as functions of universal time, altitude, invariant latitude Λ, and magnetic local time: Figure 2a, I_2 is the current measured by the ion drift meter sensor 2; Figure 2b, N, the total ion density; Figure 2c, E is the magnitude of the spin plane component of the electric field; and Figure 2d gives the directional electron flux.

In the ion drift meter data (Figures 2a and 2b) we note several significant points. First, there is a latitudinal transition from a region of H^+ to O^+ dominance starting at Λ = 59.2° (60590 UT). This is seen as a dramatic change in the ratio of the current measured as the sensor faces the ram and antiram directions, as discussed above. Second, the ion density de-

creased from ~10^3 cm^{-3} at Λ = 51° to a trough minimum of 3 × 10^2 cm^{-3} at Λ = 55.5°. In the evening sector the trough minimum is close to the ionospheric projection of the plasmapause. Third, a local density maximum at Λ = 57.5° is followed by a significant density increase as the satellite moved poleward into the region of O^+ dominance. A second, high-latitude trough is found at ~ 60700 UT as the satellite passed from the auroral oval to the polar cap.

The electric field measurments given in Figure 2c are 5-s averages based on the fitted potentials given in the bottom panel of Figure 8 (cf. Appendix A). Smaller time scale variations are, for the time being, ignored. E is the magnitude of the projection of the total electric field into the spin plane of the satellite. The sign of E was positive prior to 060710 UT and negative thereafter. Unless explicitly stated otherwise, E is assumed to be perpendicular to B. At this time the satellite was moving ~ 15° to the west of magnetic north. Since the meridional electric field component is on the average larger than the zonal, the initial positive value of the component along the trajectory indicates that E has a meridional component in the magnetic northward direction which agrees with a variety of previous electric field measurements in this local time sector. The plasma drift caused by this component is approximately in the magnetic westward direction. The electric field rose from a level of < 2 mV /m (roughly the sensitivity
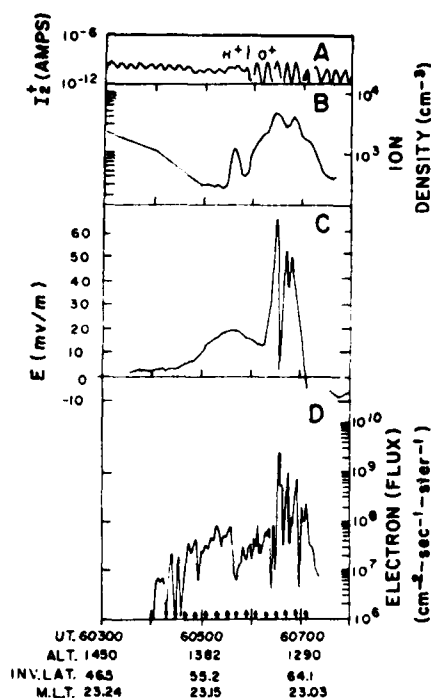
164

Fig. 2. Simultaneous measurements of (a) the current to ion sensor 2, (b) the ion density, (c) the 5-s-averaged values of the electric field, and (d) the directional electron flux (80 eV ≤ E ≤ 17 keV). The arrows at the bottom of the plot indicate times when the energetic electron spectrometer was looking upward along magnetic field lines. Data are plotted as functions of universal time in seconds of the day.

threshold) at $\Lambda = 54°$ to a first maximum of + 20 mV/m at 57°. It decreased to 14 mV/m before rising to a maximum of +66 mV/m at $\Lambda = 61.9°$. As the satellite crossed the position of the discrete arc, E decreased to an average value of 0.5 mV/m. It showed rapid variations and then reversed sign (developed a southward component) as the satellite crossed the Harang discontinuity and later passed into the polar cap.

The energetic electron flux rose above the instrument background level at approximately the same time that the electric field began to increase. This flux reached a maximum value of 8×10^7 (cm² s sr)⁻¹ at 60560 UT then decreased abruptly. The satellite then passed through a series of rapid flux variations between 7×10^7 (cm² s sr)⁻¹ and the instrument background level. These fluctuations are due to satellite-induced spin modulations and spatial-temporal variations of the electron flux. At 60653 UT the flux increased abruptly to 3×10^9 (cm² s sr)⁻¹. Several local maxima were measured up to 60720 UT, when the flux fell below the instrument background level.

Components of the magnetic field after subtraction of the model field are plotted as functions of universal time in Figures 3a and 3b in magnetometer and geomagnetic coordinates, respectively. The spin axis component is ΔB_z, in the magnetometer coordinate system. At the beginning of the data stream in Figure 3a there is a 10-γ amplitude periodic signal due to an imperfect transformation of the model field into magnetometer coordinates. Prior to 60570 UT there is a steadily increasing difference between the measured and model spin axis component. This is attributed partially to a systematic error in the model field and partially to a field-

aligned current into the ionosphere with an intensity <0.1 $\mu A/M^2$.

The magnetometer data naturally divide into three periods of contrasting behavior. In the first period, between 60570 and 60646 UT, the slope of ΔB_z is generally positive with brief periods of negative slope interspersed. In this time interval the alternating periods of negative and positive slope do not correlate with the satellite spin period. This suggests that they result from currents into and out of the ionosphere. In the second period, between 60646 and 60653 UT, ΔB_z increased rapidly to a maximum of 670 γ. This is 310 γ higher than the value at 60570 UT. The third period, after 60653 UT, is characterized by a negative slope with brief periods of positive slope embedded.

In Figure 3b the differences between the three measured and model field components in geomagnetic coordinates are given as north-south (NS), east-west (EW), and down-up (DU). The deflections are positive toward north, east, and down, respectively. There is an ~ 80-γ oscillation in the NS and DU components and a 40-γ oscillation in the EW component. These derive from uncertainties concerning the magnetometer calibration and its precise orientation in the spin plane. The increased amplitude of the EW signal results from folding spin plane information into the spin axis measurements. The main features of ΔB_z are reproduced in ΔB_{EW}. However, the maximum deflection at 60653 UT is ~ 470 γ above the component's value at 60570 UT. The mean value of the vertical component maintained, which has been displaced by 100 γ for the sake of clarity, increased at a constant rate throughout the period of study. The NS component had a
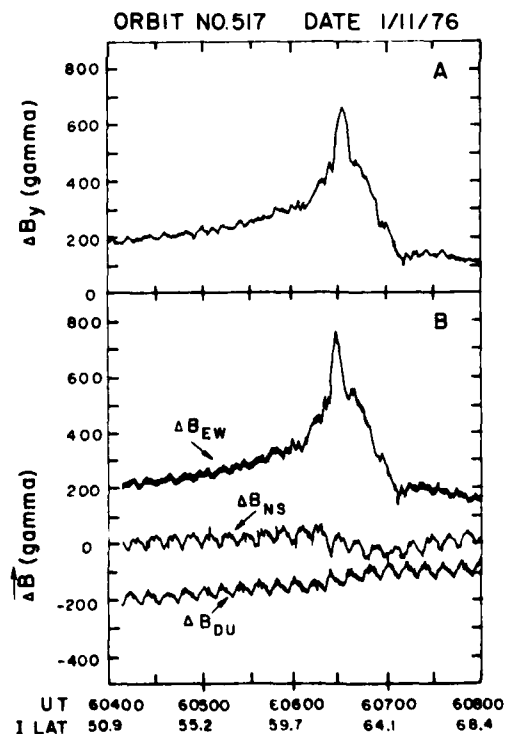

Fig. 3. Differences between measured magnetic field components and the corresponding IGRF values: (a) the spin axis component in magnetometer coordinates and (b) the north-south, east-west, and down-up components in geomagnetic coordinates.
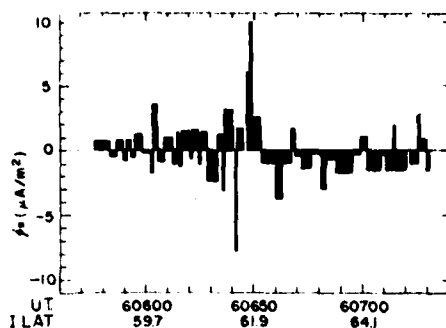
Fig. 4. Current densities calculated from variations of ΔB_y (see Figure 9a). Positive currents are parallel to B. In the northern hemisphere they are into the ionosphere.

mean value of $-25\ \gamma$ to 60640 UT, when it decreased by about $-50\ \gamma$. This component then slowly returned to its initial value. These variations suggest that deflections prior to 60640 UT were mainly in the magnetic east-west directions. In the region of the auroral arc the magnetic deflection was toward south of east. This measurement is consistent with the DMSP imagery, which shows that the arc was tilted by $\sim 15°$ away from the magnetic east-west direction. If the current sheets were parallel to the arc, a south of east total magnetic deflection should be observed.

In order to avoid ambiguities resulting from the spin-induced oscillation in the geodetic EW component we have used the spin axis data to calculate values of $j_\parallel$ given in Figure 4. The currents are positive if they are directed into (along B) the ionosphere. The current density calculations are done using the infinite current sheet approximation to Maxwell's equation, assuming that the sheets are stationary with respect to the earth and are aligned perpendicular to the satellite velocity vector,

$$ j_\parallel = \frac{1}{(\mu_0 V_\perp)}\ \frac{\partial \Delta B_y}{\partial t} \qquad (1) $$

Our use of magnetometer coordinates implies that the calculated $j_\parallel$ magnitudes, at least near the auroral arc, are lower bounds on the true values. This can be seen from the fact that the deflections between 60570 and 60653 UT were $\Delta B_y \sim 320\ \gamma$ and $\Delta B_{LW} \sim 500\ \gamma$ in spacecraft and geomagnetic coordinates, respectively. Current densities are also underestimated owing to the fact that the satellite trajectory is at an angle ζ away from normal incidence to the current sheets. For an infinite current sheet $j_\parallel = \mu_0 \partial \Delta B_{LW}/\partial x$. The measured quantity is $\partial \Delta B_{LW}/\partial s = \mu_0 j_\parallel \cos\zeta$, the variations of the Y component along the satellite trajectory. In the case of orbit 517 the DMSP imagery shows that $\zeta = 30°$. Thus the current densities reported here may be too small by as much as a factor or 2 in the vicinity of the auroral arc. However, the sign, location, and relative magnitudes of the current sheets are accurate. The net integrated downward currents in Figure 4 are within 1% of the net upward currents.

In the following three subsections we consider, in detail, the regions of predominantly downward and upward Birkeland currents. Special emphasis is placed on comparisons between the high time resolution measurements of the various instruments

Observations in Region 2

As defined by *Iijima and Potemra* [1976], in the evening sector, region 2 Birkeland currents (those which flow at the low-

est latitudes) are directed into the ionosphere. From Figure 3a it is seen that ΔB_y was predominantly increasing, which indicates that currents were predominantly into the ionosphere until 60653 UT. For the sake of clarity we subdivide this region into that of diffuse aurorae and the strong return current associated with the visible arc in region 1.

Region of diffuse aurorae. The region is encountered between $\Lambda = 54.8°$ (60490 UT) and $\Lambda = 61.7°$ (60646 UT). It extends from the ionospheric projection of the plasmapause across the region of the diffuse aurorae. The plasmapause projection and the ionospheric trough are at latitudes that are equatorward of their quiet time values ($\Lambda = 60°$). This equatorward displacement was probably not due to the ongoing minor substorm but was the result of the severe magnetic activity that marked that last 6 hours of January 10, 1976, and the first 3 hours of January 11, 1976. During these periods, K_p had values of 7, 7, and 7^+. Under such conditions it is well known that the ionospheric projection of the plasmapause and the trough move equatorward.

The region of the diffuse aurorae maps into the central portion of the plasma sheet. At ionospheric altitudes it is characterized by relatively uniform fluxes of protons and electrons that are of comparable intensity [*Lui et al.*, 1977]. In the evening sector this region is one of field-aligned currents into the ionosphere [*Iijima and Potemra*, 1976]. Data presented in Figure 3a show that in this region, ΔB_y generally has positive slope, indicating the presence of field-aligned currents into the ionosphere. There are, however, brief periods in which the slope of ΔB_y was negative. In the remainder of this subsection, high time resolution data are examined to show that these re-
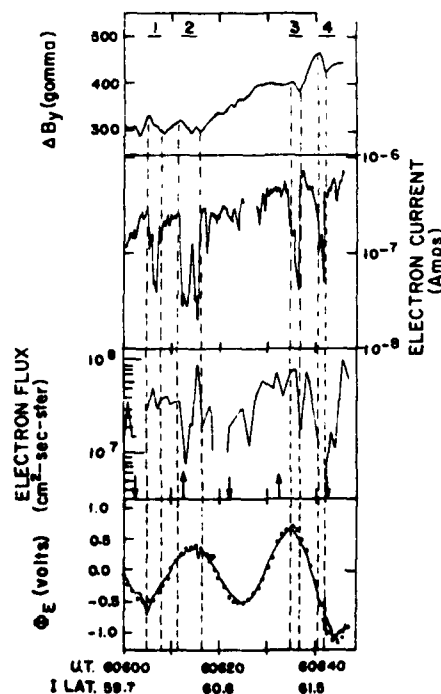

Fig. 5. High time resolution measurements of ΔB_y, the current measured by the thermal electron probe and the energetic electron directional flux. Attention is directed to four events during which ΔB_y decreased, indicating a current out of the ionosphere. The bottom panel gives the potential measured by the spinning dipole (solid line) and the function to which it was fitted (dotted line).

sult from the satellite passing through several pairs of field-aligned current sheets rather than from random fluctuations of the data.

Expanded plots of ΔB_y, the current measured by the thermal electron probe and the energetic electron flux and the potential measured by the spinning dipole, are given in Figure 5. Arrows at the bottom of the figure indicate times when the electron spectrometer was looking up or down magnetic field lines. Currents into (out of) the ionosphere are characterized by increasing (decreasing) ΔB_y. There are at least four periods, marked at the top of the figure, during which ΔB_y decreased. During each of these events the thermal electron current decreased by approximately 1 order of magnitude. Since the ion densities showed no similar fluctuations, we conclude that the thermal electron current decreased because of negative excursions of the satellite potential. Negative satellite potential fluctuations indicate a local enhancement of electron fluxes with energies above a few electron volts. The upward current indicated by the negative slope of ΔB could be carried by energetic electrons, as occurs in discrete arcs (see below). If the energy is above 100 eV or below 17 keV, it is thus expected that the electron spectrometer would observe increased (decreased) fluxes while looking up (down) magnetic field lines. During events 1 and 3 the spectrometer measured slightly increased fluxes but was a pitch angle near 90°. At the time of event 4 the flux dropped to instrument background at pitch angles near 180°. These results are consistent with the magnetometer and thermal probe measurements. However, during event 2 the spectrometer measured fluxes between approximately 0° and 90°. Here, the measured electron flux was decreasing. This result is contrary to expectations. It can be reconciled with the magnetometer and thermal proble data if the current carrying electrons had energies below the spectrometer energy threshold.

In Figure 5 we have plotted Φ_E (solid line) and Φ_{nt} (dotted line). For the 27.44-m dipole a 1-V potential difference corresponds to an electric field component of 36.4 mV/m. If $|\Phi_E| < |\Phi_{nt}|$, the instantaneous electric field has been overestimated in the 5-s averaging procedure. Throughout the 60600–60645 UT period, the fitted and measured values of Φ are very close with the largest deviations of Φ_E and Φ_{nt} found at the boundaries of the current sheets. At 60605 UT, which corresponds to the equatorward boundary of the first current sheet, the actual electric field was 6 mV/m greater than the estimated value. Deviations corresponding to electric field decreases of ~3 and ~10 mV/m are found at the poleward boundaries of the second and fourth current sheets, respectively. The electric field is consistently less than the fitted value by ~3 mV/m across the third current sheet. No consistent pattern can be found between j and E_{NS}, suggesting that their relationship is not a simple one. Note that the common mode rejection of the electric field electronics was 1 bit per 8 V. Thus vehicle potential fluctuations are suppressed in the E field measurements.

Region of intense downward current equatorward of the discrete arc. The region encountered between 60646 UT ($\Lambda = 61.7°$) and 60653 UT ($\Lambda = 62.0°$) is characterized by intense currents into the ionosphere. The position and orientation of the current sheet suggest that it constitutes the return current of the auroral arc [*Cloutier et al.*, 1973]. As shown in Figure 2, this is also a region of rapidly increasing poleward electric field component. Since the particle fluxes are relatively steady and the plasma density was increasing in the poleward direction, at least at 1400 km, it seems likely that in the E region, $\partial J_p/\partial x > 0$, where J_p is the poleward horizontal current. In a

steady state, $\nabla \cdot J = 0$ thus requires increased downward J_z in the same region, as observed.

Attention is directed to the most intense current measured between 60646 and 60648 (Figure 3a). Using (1), a lower bound on j_z has been set at 10 μA/m². The ion density was ~3 × 10³ cm⁻³. The drift meter was looking close to the ram direction and, as discussed in Appendix B, indicated that the plasma had a westward drift component but no measurable ion velocity up or down the field line. The thermal electron temperature, measured at 60628 UT was ~3150°K. The particle spectrometer measured a local maximum flux of 9 × 10⁷ (cm² s sr)⁻¹ at pitch angles near 90° (60646 UT). The electron flux fell below the instrument's sensitivity level (10⁷ cm⁻² s⁻¹ sr⁻¹) for pitch angles near 0° before rising to a value of 3 × 10⁸ (cm² s sr)⁻¹ as the satellite passed over the auroral form. A current of 10 μA/m² corresponds to a charged particle flux of 6 × 10⁹ (cm² s)⁻¹. For the most part this current must be carried by low-energy, ionospheric electrons, since the energetic ($E > 80$ eV) electron flux measured in the region of the return current was $<10^8$ (cm² s sr)⁻¹. The thermal protons showed no measurable field-aligned drift motion. Precipitating protons are generally not detected in the vicinity of inverted-V structures [*Ackerson and Frank*, 1972]. Also, plasma sheet proton fluxes are typically $<10^8$ (cm² s)⁻¹. This leaves ionospheric electrons as the only viable candidates. This conclusion is consistent with the fact that no large shift in the satellite potential was observed at this time.

We now consider the effects of such a strong current on the stability of the ionospheric plasma. If the thermal electrons are considered to be the main current carriers, it is possible to estimate the component of their drift velocity along the magnetic field via the relationship

$$V_{e\parallel} = j_\parallel/qN_e \qquad (2)$$

For $j_\parallel \approx 10$ μA/m² and $N_e = 3 \times 10^9$ m⁻³, $V_{e\parallel} > 20$ km/s. The thermal speed of the electrons is ~300 km/s. The ratio $V_{e\parallel}/a_e > 0.07$ is approximately equal to the critical value for the onset of the O⁺ cyclotron turbulence with $T_e/T_i \sim 3$ [*Kindel and Kennel*, 1971] and is well above threshold for lower T_e/T_i. This turbulence may change the effective collision frequency ν_{eff} of drifting electrons. The resistivity parallel to the field lines is then given by

$$\eta = \nu_{eff}/\omega_{pe})/\epsilon_0\omega_{pe}) \qquad (3)$$

where ω_{pe} is the electron plasma frequency. In anamolously resistive plasmas, experimentally observed values of ν_{eff}/ω_{pe} range betwen 3.3×10^{-3} and 2.5×10^{-2} [*Shawhan et al.*, 1978]. Thus η should lie between 200 and 900 ohms/m. Substitution into Ohm's law, $E_\parallel = \eta j_\parallel$ shows that $E_\parallel$ should fall between 2 and 9 mV/m. It should be noted that insofar as our calculation of $j_\parallel$ is a lower limit, so too is the possible range for $E_\parallel$.

There is evidence in the electric field measurements for the existence of a component of E parallel to B near 60647 UT. A detailed calculation is given in Appendix B. The arguments in support of this conclusion can be outlined briefly. At 60645 UT the measured potential indicates that the ambient electric was ~30 mV/m. Between 60647 and 60648 UT the measured potential across the dipole approached the value of the potential due to the motion of the satellite across magnetic field lines. This implied that either E went to zero or it was perpendicular to the instantaneous orientations of the dipole. The first hypothesis is not consistent with measurements from the ion drift meter, which indicate that the north-south electric
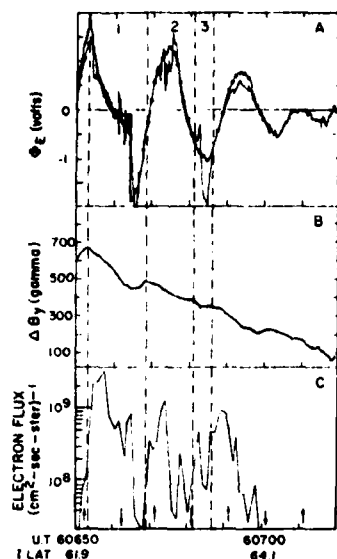
Fig. 6. Measurements in region 1 as functions of universal time and Λ, (a) gives the potential and the fitted function (dotted lines), (b) gives B_y, and (c) gives the electron directional flux.

field component decreased from 29.8 to 8.9 mV/m and then returned to 30 mV/m. Since E ≠ 0, it must be oriented perpendicularly to the dipole. Using satellite attitude information and the IGRF magnetic field, a value $E_{||}$ = 10.2 mV/m was calculated. This is slightly higher than the upper range of $E_{||}$

calculated above. However, if $j_{||}$ has been underestimated by a factor of 2, $E_{||}$ lies in the middle of the calculated range.

Observations in Region 1

In the evening sector, region 1 is characterized by currents out of the ionosphere [Iijima and Potemra, 1976]. It also corresponds to that of the auroral form, as noted in the DMSP imagery and in the electron flux dectector output beginning at 60653 UT. As mentioned above, magnetic field lines were traced from the altitude of the satellite to that of the arc. Allowing for the earth's rotation, it was found that the S3-2 position at 60653 UT agreed with that of equatorward boundary of the auroral arc.

Data relevant to an understanding of the electrodynamics of the arc are presented in Figures 6 and 7. In Figure 6 we have plotted as functions of universal time and Λ as follows: Figure 6a gives the potentials measured by the spinning dipole and the quarter-wave sine functions to which they have been fit, Figure 6b gives the spin axis component of the magnetic field, and Figure 6c gives the electron directional flux, using arrows to indicate times when the sensor was closest to looking up and down magnetic field lines. The electron spectra that were measured approximately every other second are given in Figure 7. The range of pitch angles scanned during the 1 s of measurements is indicated for reference. The dotted lines indicate the one count per accumulation period flux level. An electron flux at or above this level is indicated by a solid line. Because the satellite potential was severely depressed throughout the 60653-606700 UT time period, no information could be gained from the thermal electron probe.

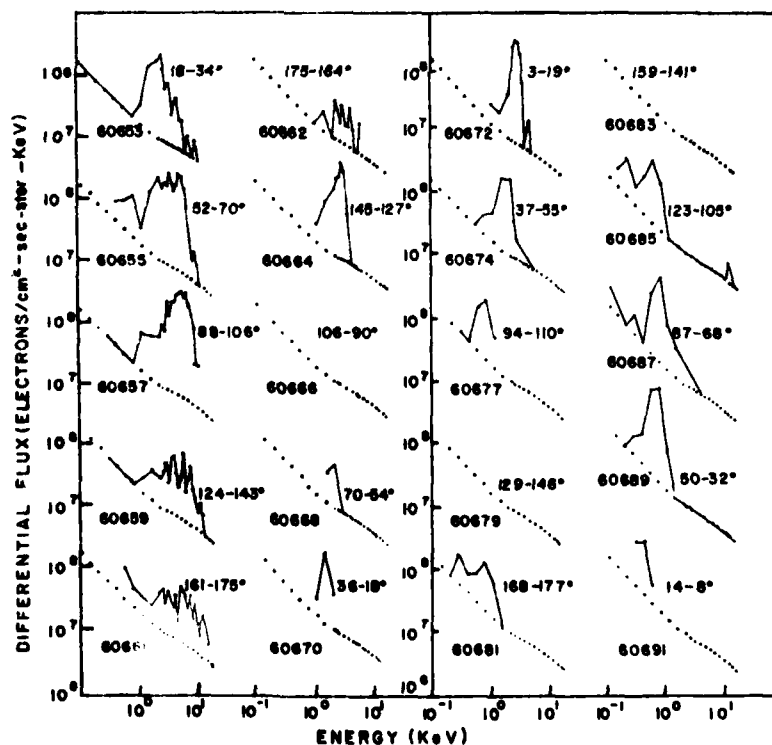Electric field values given in Figure 2c were quite variable

Fig 7. Electron spectra measured in region 1. The range of pitch angles and the universal time of the measurements are indicated.

168

in region 1. However, these values were calculated using Φ_{a_1}. Variations on time scales less than 5 s are smoothed by this procedure. Finer time scale resolution is gained by comparing values of Φ_E and Φ_{a_1}. The electric field has been underestimated (overestimated) at times when $|\Phi_E| > (<) |\Phi_{a_1}|$. Thus the value of E just prior to entering the arc was ~1/3 greater than the calculated value of 66 mV/v. The electric field strength decreased rapidly to an average value of 0.5 mV/m. By Poisson's equation this indicates a negative charge sheet at the equatorward edge of the arc and a large velocity shear, as also observed in a rocket experiment under similar conditions [*Carlson and Kelley*, 1977]. At 60665 UT the field increased abruptly to its prearc value. Note that the detector is spinning, so that the sign changes do not indicate rotations of the ambient field. Between 60671 and 60676 UT the field weakened, then increased relative to Φ_{a_1}. A third weakening-strengthening cycle is again found between 60682 and 60687 UT. After this time the north-south electric field component weakened rapidly and reversed sign at 60710 UT. The electric field sign reversal is evidenced by phase shift of ~180° in the Φ_z signal. This reversal is interpreted as the signature either of the satellite crossing the Harang discontinuity or passing from the auroral oval to the polar cap.

The three weakening-strengthening E field cycles encountered in the period immediately following 60653 UT are set off in Figure 6 by dashed lines. The first was of large enough scale to be detected in the 5-s setting routine and was roughly 100 km in extent. The others were of the order of 40 km in dimensions. When compared with the magnetometer measurements, it is found that the weakening or low E field portions of the cycles correspond to periods of relatively steep decreases in ΔB_y. Conversely, the strong E field portions of the cycles correspond to periods when ΔB_y was decreasing very slowly. During the strong E portion of the first cycle, B_y was actually increasing. That is, weak E fields occur in regions of strong currents out of the ionosphere, and strong E fields occur in the region of $j_{||} \gtrsim 0$.

The energetic electron flux began to increase at 60652 UT and reached a measured maximum value at 60655 UT, while the sensor was detecting particles with pitch angels between 52° and 70°. The electron energy distribution appears to be that of an inverted-V event. The peak energy of the spectrum shifts to higher values between 60659 and 60664 UT, while the sensor was looking down the field lines at mirroring and backscattered electrons. The observation of backscattered kilo-electron volt electrons in a region of decreasing ΔB_y indicates that the precipitating electrons were of the same or greater energies. These electrons are capable of producing visible auroral luminosity and enhanced conductivity. At 60666 UT the electron flux abruptly fell below the level of detectability and remained at a low level until 60671 UT. During the period, $\partial \Delta B_y / \partial t > 0$, and E briefly went to its highest value.

As the slope of the ΔB_y curve became negative at 60671 UT, E began to decrease, and the electron flux increased. The spectrum measured at 60672 UT is narrowly distributed in energy around 4 keV. As the detector moved away from looking up the field line, the measured flux decreased. The fact that ΔB_y and E continued to decrease until 60675 UT suggests that the current was carried by a highly monoenergetic, field-aligned beam of electrons that were perhaps accelerated by a double layer, parallel electric fields at altitudes well above 1300 km [*Torbert and Mozer*, 1978]. The beginning of the third cycle is marked by a sudden decrease in ΔB_y and a decrease in

E. The spectrometer was looking down the magnetic field line but did not detect any backscattered flux. In one case the E field increased (60675 UT) when the measured electron flux was increasing, which appears to contradict the other examples. However, the spectra at this time indicate that most of the electrons had energies less than 1 keV. Note that most of the ionization produced by these electrons is at altitudes greater than 150 km [*Rees*, 1963] and will not affect the integrated conductivity of the ionosphere as much as the higher-energy particles.

The S3-2 observations suggest a more complex situation than might be assumed from the DMSP image, which showed a single auroral arc. There are several explanations of this apparent difference.

1. Two new arcs developed in the 14 min between the DMSP and S3-2 overpasses.

2. Owing to their finite extents in altitude and latitude along slanted magnetic lines, several arcs overlapped in the DMSP image.

3. Only in cycle 1 was the precipitation sufficiently energetic and intense to produce a visual luminosity greater than the 2 kR DMSP lower limit of sensitivity.

The constancy of the Dixon Island magnetogram makes the first hypothesis seem unlikely. The low energy of the electron flux observed during the third cycle suggests that the third hypothesis may explain the third-cycle data but is a less likely explanation of the second cycle. It seems likely that S3-2 passed over these parallel auroral arcs. The most poleward may have been subvisual. Owing to the slant of the magnetic field lines the other two parallel arcs could not be resolved in the DMSP image.

SUMMARY AND DISCUSSION

In the previous section we have presented a comprehensive set of measurements taken in the late evening sector of the auroral zone. The S3-2 energetic electron fluxes showed a region of relatively constant isotropic fluxes (diffuse aurorae) followed by a region of low fluxes and an inverted-V structure on magnetic field lines above an auroral form. These observations are in agreement with previously reported results [*Lui et al.*, 1977; *Ackerson and Frank*, 1972]. The unique capability of S3-2 instrumentation comes from simultaneous, high time resolution measurements of magnetic and electric fields in conjunction with thermal and energetic plasma observations. In this section we first compare S3-2 with previously reported magnetic and electric field measurements. Some consequences of the current-field relationship in the vicinity of the visible arc are considered, and problems for future theoretical and observational study are pointed out.

Field-Aligned Currents

In the evening sector, *Iijima and Potemra* [1976] have described region 2 as a region of currents into the ionosphere. The S3-2 measurements from orbit 517 show that although the net current is into the ionosphere, there are also embedded parallel sheets of current out of the ionosphere. The positive correlation between ΔB_y and satellite potential fluctuations indicates that the current sheets are real and are carried by superthermal electrons. S3-2 passed through these current sheets on time scales < 2s. The sampling rates and resolutions of the S3-2 and Triad magnetometers are 32 and 2.25 s⁻¹ and 5 and 12 γ, respectively. Some narrow current sheets could be rejected in Triad measurements as being due to instrumental

noise. A late evening pass of Triad studied by *Armstrong et al.* [1975] showed a similarly structured system of current sheets into and out of the ionosphere. Lacking corroborative evidence showing that the east-west magnetic fluctuations did not result from remote sources, the small-scale currents were smoothed to give an average current into the ionosphere [cf. *Armstrong et al.*, 1975, Figures 7 and 8]. The vehicle potential fluctuations measured by S3-2 show that a remote source for ΔB_r fluctuations is not required. The full implications of these measurements for an understanding of the coupling between the central plasma sheet and the ionosphere are left for future study. It is important to note that the measured total currents into and out of the ionosphere were equal, provided that the transient upward currents at low latitudes are included. Thus equatorward convection of localized regions of electron precipitation may be occurring with these regions originating in the region 1 sector. Another possibility is that the current sheets are due to Alfvén waves formed in the discrete arc region, as described by *Mallinckrodt and Carlson* [1978], which have convected equatorward and been reflected from the conjugate ionosphere. This is consistent with the observed E field fluctuations associated with the current sheets and the fact that low-energy electrons carry the current.

One of the outstanding differences between previously reported measurements from rocket versus satellite-borne instruments concerns the Birkeland current structure in the vicinity of auroral arcs. Rocket measurements by the Rice University group [*Anderson and Vondrak*, 1975, and references therein] show intense currents carried by down-coming kilo electron volt electrons over visible arcs with strong return currents always found in the region contiguous with the arc. Scale lengths for these structures are typically several tens of kilometers. Such small-scale structures do not appear in published satellite measurements. The difference is usually attributed to the high speed of satellites in crossing over arcs. The upward and downward currents centered at 60653 UT in Figure 2 appear as an intense structure superimposed on the large-scale region 1-region 2 current system. Thus S3-2 data agree with both rocket and satellite measurements when proper spatial scales are taken into consideration.

Anomalous Resistivity and Parallel Electric Fields

Between 60647 and 60648 UT, S3-2 passed through a portion of the downward current sheet in which $j_\parallel > 10 \ \mu A/m^2$. Simultaneous thermal plasma measurements indicate that the ionospheric plasma was at marginal stability to the onset of O^+ ion cyclotron turbulence. Also at this time, there is evidence that the electric field had a significant component parallel to B (Appendix B). *Kindel and Kennel* [1971] suggested that if the ionospheric current exceeds a certain threshold, the electrical resistance of the plasma increases dramatically. The threshold current value depends on the plasma density, temperature, and ionic composition. At the critical current, electrostatic turbulence develops. The large amplitude waves act as scattering centers on current-carrying electrons. To maintain a constant current across the anomalously resistive region, an electric field develops along B. *Bekifi* [1966] has shown that collective mode-individual particle interactions play a role analogous to Coulomb collisions in classical runaway theory [*Dreicer*, 1959]. Thus $E_\parallel$ accelerates only electrons in the high-energy tail of the ionospheric thermal distribution. The accelerated electrons would appear in the magnetosphere

as highly field-aligned beams. In this regard we note that field-aligned fluxes of electrons are regularly observed at geosynchronous orbit, $L = 6.5$. The electrons have energies between several hundred and several thousand electron volts and last for periods of between 1 and 20 min [*Vogl et al.*, 1976]. It is interesting to speculate that these electrons may be of ionospheric origin and have been accelerated by an $E_\parallel$ similar to that measured by S3-2.

Unfortunately, no wave observations were performed on the S3-2 satellite. However, clear evidence exists for the existence of ion cyclotron waves associated with field-aligned currents in the upper ionosphere. *Kinter et al.* [1978, 1979] have shown numerous examples of hydrogen ion cyclotron waves in the altitude range from 4–8000 km studied by the S3-3 satellite. For a given field-aligned current density the electron drift velocity increases and will be unstable to hydrogen waves at high altitudes. In a rocket experiment, *Bering et al.* [1975] and *Kelley et al.* [1975] reported observations of intense oxygen ion cyclotron waves just equatorward of an auroral arc. The electrodynamic configuration of the arc in that experiment, as reported by *Carlson and Kelley* [1977], was nearly identical to the present case. A northward electric field decreased to near zero just at the arc boundary, as defined by particle detectors and all-sky cameras, and the O^+ cyclotron waves were observed simultaneously (~ 400-km altitude). *Reed et al.* [1978] have also reported radar observations of ion cyclotron waves at even lower altitudes at the poleward edge of the diffuse radar echoes, which usually trace the eastward electrojet prior to midnight. Taken together, these data make it seem likely that the region of intense downward $j_\parallel$ had associated O^+ cyclotron turbulence. *Lysak and Hudson* [1979] have performed calculations based on the H^+ cyclotron wave amplitudes detected on the S3-3 satellite and concluded that parallel electric fields of several millivolts per meter could be maintained by the anomalous resistivity owing to these waves.

However, a serious drawback exists in this or any explanation for parallel electric fields due to the magnitude of the Joule heating involved. For 10 $\mu A/m^2$ and 10 mV/m the heating rate is 10^{-7} W/m^3. Partitioned equally into ions and electrons at the observed density, this amounts to about 50 eV per particle second. Including the neutrals at 1400-km altitude only reduces this by 1 order of magnitude. Thus considerable theoretical work is necessary to explain the energy balance between thermal plasma, neutrals, and accelerated particles in regions where $\vec{J}$ and $\vec{E}$ have components parallel to $\vec{B}$.

Comparison with Low-Altitude Ionospheric Currents

The electric field and particle results presented here are in excellent agreement with the rocket measurements of *Carlson and Kelley* [1977]. They observed a rapid decrease and even reversal of the northward electric field at the equatorward edge of a discrete arc and concluded that the arc boundary separated eastward from westward electrojets. In the case presented here the reversal of the north-south electric field was measured at 60710 UT ($\Lambda = 64.2°$) near the poleward boundary of the arc system. It would thus appear that the arc system again marks the transition between eastward and westward electrojets. This is consistent with the Dixon Island magnetometer measurements, which showed negative deflections in the horizontal components. This indicates that Dixon Island, on the poleward side of the arc, was closest to a westward electrojet.

A comparison of particle and electric field measurements (Figure 2) suggests that the eastward electrojet was distributed throughout the diffuse auroral region and was most intense near the equatorward boundary of the southern-most arc. The eastward electrojet is mainly a Hall current flowing in the E region

$$I_H = -\Sigma_H (E_{NS} \times B)/B \qquad (4)$$

where Σ_H is the height integrated Hall conductivity. The presence of precipitation and significant electric fields in the diffuse auroral region indicates that the electrojet is widely distributed. That this current is strongest near the equatorward edge of the arc rather than in its center is consistent with the demands of current continuity. At 60653 UT the electric field experiment measured the strongest field (~90 mV/m), and $j_\parallel$ went through zero. Ionospheric Pedersen currents should have their maximum values at this point. If the ratio of height-integrated Pedersen and Hall currents remains constant within a factor of 10 across the arc I_H should also maximize at this point. Within the arc, E_{NS} rapidly decreased to 0.5 mV/m. For I_H to have the same value in the arc as it had at its equatorward boundary, Σ_H in the arc must exceed its value at the boundary by a factor of 180. This implies the existence of severe thermal density gradients in the E region. Cross field line diffusion and equatorward convection due to a westward electric field component would make it difficult for such gradients to be maintained in the collision-dominated E region. The steady state continuity equation for thermal plasma is

$$\nabla \cdot nV = P - L \qquad (5)$$

where P is the number of electrons produced per cubic centimeter per second owing to ionizing collisions between neutrals and energetic primary or secondary electrons. L is the loss rate due to recombination processes. The left-hand side of (5) represents the transport of plasma away from the source region. The plasma drift velocity V has components along and across B. The enhanced plasma density at 1300 km, relative to the trough background, is due to field-aligned transport, as required for pressure balance. If there were no cross field line transport, the observed density enhancement would be not found equatorward of the arc region. The cross field line component of V is primarily due to $E \times B$ drifts. This result agrees with rocket measurements reported by *Maynard et al.* [1977], who found that although Σ_H had a maximum value in the center of an evening sector, arc I_H was largest at the arc's equatorward boundary.

Relationship Between Electric Field
and Electron Precipitation Changes

If the currents out of the ionosphere are carried by precipitating, energetic (keV) electrons, then enhanced Pedersen conductivities are expected in the lower ionosphere. In a steady state condition, polarization electric fields should develop across the regions of enhanced conductivity to reduce the cross-arc electric field component. In regions of $j_\parallel > 0$, electron precipitation and ionospheric conductivity are reduced. Here the full strength of the convective electric field is observed. This could be called a steady state ionospheric feedback mechanism. This seems to be in agreement with the observations summarized earlier, in that the regions of rapid decrease in ΔB_y ($J_\parallel$ upward) corresponded to decreased meridional electric field values. However, *Mozer et al.* [1977] and *Torbert and Mozer* [1978] have shown that in the region

of discrete auroral arcs the perpendicular electric fields are largest in the altitude range of several thousand kilometers and have very large fluctuations in the north-south component. Thus the simple concept of constant electric potentials along magnetic field lines throughout the magnetosphere is not valid, and the electrodynamic structure near discrete arcs may be determined by these high-altitude processes not by the ionospheric conductivity.

Furthermore, *Mallinckrodt and Carlson* [1978] have shown that plasma convecting through these regions of varying meridional electric fields, via the zonal electric field component, will be subject to time-varying electric fields. These, in turn, will have associated perpendicular and parallel currents, which cannot be described by any steady state hypothesis. These currents will, of course, be detected by rocket and satellite magnetometers with specific relationships to the auroral arcs and interpreted as steady current systems.

CONCLUSIONS

In this paper we have presented a set of high time resolution measurements from electric field, magnetic field, energetic electron, and thermal plasma detectors aboard the S3-2 satellite. The particular late evening sector pass chosen for detailed analysis was nearly coincident in time with a DMSP satellite overpass. Optical frequency imagery from DMSP showed that S3-2 passoved over a region diffuse aurorae and a bright discrete arc. The major conclusions of this study are as follows:

1. The S3-2 magnetometer results showed the gross features of the region 1-region 2 field-aligned current system [*Iijima and Potemra*, 1976]. An intense arc-related pair of current sheets was imbedded in the large scale current system.

2. Within region 2, where the Birkeland currents were predominantly into the ionosphere, latitudinally narrow regions of negative slope in ΔB_y were found. Simultaneous measurements of the satellite potential and energetic electron fluxes indicate that the changes in ΔB_y were due to local field-aligned currents out of the ionosphere. These currents were probably carried by precipitating, low-energy (≤ 100 eV) plasma sheet electrons.

3. An intense downward return current sheet was found just equatorward of the visible arc with the current carried mostly by upmoving thermal electrons. The ionospheric plasma at this time was near marginal stability for the onset of O^+ ion cyclotron turbulence. A component of E parallel to B was measured at this time.

4. Particle and electric field measurements indicate that the eastward electrojet was distributed throughout the region of diffuse aurorae and was most intense near the equatorward boundary of the arc system.

APPENDIX A: ELECTRIC FIELD CALCULATIONS

The method used to calculate the projection of the ambient electric field into the spin plane of the satellite is illustrated in Figure 8. Here we have plotted the measured potential between the ends of the spinning dipole Φ_m (Figure 8a), the potential due to the cross magnetic field motion of the satellite Φ_v (Figure 8b), the potential due to the ambient electric field Φ_r (Figure 8c), and the function to which Φ_r is fitted, Φ_{R_t}, and its residues $\Phi_A - \Phi_{R_t}$ (Figure 8d) as functions of universal time in seconds of day and invariant latitude Λ. The data were
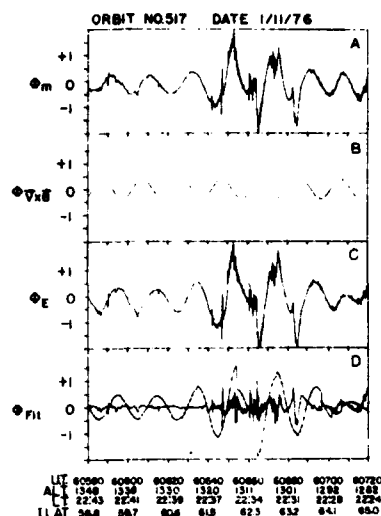
Fig. 8. Example of the way in which data from the spinning dipole are reduced: (a) gives the measured potential difference between the ends of the dipole, (b) gives the potential due to the V × B motion of the satellite, (c) gives the difference between the measured and the V × B motion, and (d) gives the faction to which Φ_c has been fit and its residues. The data were taken during S3-2 orbit 517 and are plotted as functions of universal time (seconds of the day), altitude, invariant latitude, magnetic local time, geographic latitude, and longitude.

taken during S3-2 orbit 517 as the satellite was moving poleward over the late evening sector (~2250 LT) of the northern auroral zone. The measured potential across the dipole is of the form

$$\Phi_m = \Phi_{dc} + \Psi_s + \Phi_E \qquad (A1)$$

where Φ_{dc} is the contribution due to different contact potentials of the two spheres. The Φ_{dc} is easily rejected by considering the amplitudes of the sine waves and not their dc level. The Φ_s is calculated from the International Geomagnetic Reference Field (IGRF) 1975 model updated to the epoch of measurements and precisely determined (<0.5° error) spacecraft attitude information. The Φ_s is then subtracted from Φ_m to obtain Φ_E, the potential due to the ambient electric field. In regions where the electric field varies slowly over a satellite spin period (e.g., prior to 60630 UT, Figure 2), data are fit to a function of the form

$$\Phi_{fit} = \Phi \cos (\Omega_s t - \Psi) \qquad (A2)$$

where Ω_s is the satellite's angular speed and Φ and Ψ are the amplitude and phase angle determined in the fitting procedure. In principle, both Φ and Ψ are functions of time. We must now ask to what degree is it possible to interpret S3-2 measurements if the electric field is varying in magnitude and direction on time scales shorter than the satellite spin period? At the altitudes of the S3-2 orbit the classical conductivity along magnetic field lines is high. It is assumed that in the absence of contradictory information from other instruments, $\mathbf{E} \cdot \mathbf{B} = 0$.

In order to examine the consequences of the $\mathbf{E} \cdot \mathbf{B} = 0$ assumption for the potential difference measurements of a rotating dipole we adopt a system of coordinates with origin at the satellite's center of mass (Figure 9). The spin axis of the satellite is along the $-Y$ axis of the coordinate system. The X axis

is defined as the direction of the projection of the satellite velocity into the spin plane $\mathbf{V}_p$. The Z axis is in the direction of $\hat{x} \times \hat{y}$. Thus if the orbit were circular with a 90° inclination and the spin axis were perpendicular to the orbital plane, X, Y, and Z would be positive toward north, west, and up during the portion of orbit 517 under consideration. In this appendix we use the subscript P to indicate the projection of a vector into the spin plane. This projection of an arbitrary vector A is defined by

$$\mathbf{A}_P = -\hat{y} \times (\hat{y} \times \mathbf{A})$$

The projections of the electric field, magnetic field, and $(\mathbf{V}_s \times \mathbf{B})$ near 60600 UT (arbitrary lengths) are also indicated in Figure 9.

In the spacecraft coordinate system the magnetic field can be represented as

$$\mathbf{B} = B(\sin \Theta \cos \Phi \, \hat{x} + \sin \Theta \sin \Phi \hat{y} + \cos \Theta \hat{z}) \quad (A3)$$

where the azimuth and colatitude angles are defined by $\Phi = \tan^{-1} (B_y/B_x)$ and $\Theta = \cos^{-1}(B_z/B)$, respectively. In order to study the properties of a vector perpendicular to B we define a set of orthonomal vectors $\hat{e}_1$, $\hat{e}_2$, and $\hat{e}_3$, such that $\mathbf{B} = B\hat{e}_3$. This transformation is effected by two rotations. It can easily be shown that

$$\hat{e}_1 = \cos \theta \cos \phi \hat{x} + \cos \theta \sin \phi \hat{y} - \sin \theta \hat{z}$$

$$\hat{e}_2 = -\sin \phi \hat{x} + \cos \phi \hat{y} \qquad (A4)$$

$$\hat{e}_3 = \sin \theta \cos \phi \hat{x} + \sin \theta \sin \phi \hat{y} + \cos \theta \hat{z}$$

Since $\mathbf{E} \cdot \mathbf{B} = 0$, $\mathbf{E}$ can be represented by

$$\mathbf{E} = a_1 \hat{e}_1 + a_2 \hat{e}_2 \qquad (A5)$$

Transforming to spacecraft coordinates,

$$\mathbf{E} = (a_1 \cos \theta \cos \phi - a_2 \sin \phi)x$$
$$+ (a_1 \cos \theta \sin \phi + a_2 \cos \phi)\hat{y} - a_1 \sin \theta \hat{z}$$

In regions of slowly changing electric fields, E_1 and E_2 are measured directly at times of maximum or minimum values of ϕ_E. These measured values may be used to compute a_1 and a_2:

$$a_1 = -E_1 \csc \theta$$
$$a_2 = -(E_1 \cot \theta \cot \phi + E_2 \csc \phi) \qquad (A6)$$
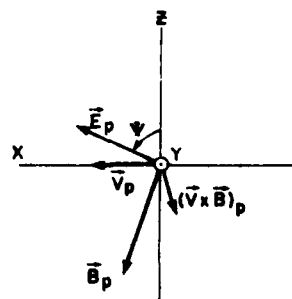

Fig. 9. Satellite coordinate system used in this paper. Vector quantities (arbitrary scale) marked with subscript P represent projections into the spin plane of the satellite. The $-Y$ axis corresponds to the satellite spin axis.

We note that unless $\phi = 0°$ or $180°$, (1) E_x and B_y are not orthogonal vectors and (2) The y component of the electric field can be computed:

$$E_y = -(E_x \cos \phi + E_z \cot \theta) \csc \phi \qquad (A7)$$

Rearranging terms in (A7), we obtain

$$E_x = -(E_z \cot \theta \sec \phi + E_y \tan \phi) \qquad (A8)$$

It is useful to define an angle $\Psi = \tan^{-1} (E_x/E_z)$ such that at the angle Ψ, Φ_E has a maximum value. Since

$$\Psi = \tan^{-1} - \cot \theta \sec \phi -(E_y/E_z) \tan \phi \qquad (A9)$$

we can examine its sensitivity to variations in the ratio E_y/E_z. A plot of ψ as a function of E_y/E_z is given in Figure 10. Magnetic conditions are those of 60600 UT on orbit 517. There are two families of solutions, depending on the sign of E_z, which, for a given E_y/E_z ratio, are separated by $180°$. To a zero-order approximation the satellite is moving in the magnetic north-south direction, and the spin axis is in the magnetic east-west direction. Because auroral forms tend to be aligned in the magnetic east-west direction, variations of physical quantities along the trajectory should be much greater than their variations in the Y direction, i.e., $\partial/\partial y \sim 0$. Since $\nabla \times \mathbf{E} = 0$ for quasi dc fields, it follows that $(\partial E_y/\partial x) \sim 0$, i.e., the Y component of the electric field should be relatively constant. In the evening sector of the northern auroral zone the electric field is generally toward the magnetic north ($E_x > 0$) and west ($E_y > 0$). From the inclination of magnetic field lines and the condition $\mathbf{E} \cdot \mathbf{B} = 0$ it can be shown that $E_z > 0$. We note that along the $E_z > 0$ curve, Ψ only changes from $72°$ to $81°$ as the ratio E_y/E_z varies from zero to 20. This implies that over a wide range of (E_y/E_z) ratios $\Psi \sim$ const. Thus variations in the electric field perpendicular to B can only produce a change in magnitude of Φ_m or a jump of $\sim 180°$ if E_x and, necessarily, E_z reverse sign.

The main features of this analysis are verified in the data given in Figure 8. The time separation between maxima and minima in ϕ_E are approximately constant prior to 60645 UT. The maximum at $\sim$60690 UT is at the appropriate time for Ψ = const. There is an abrupt shift of $180°$ in the phase of the measured signal at 60710 UT, indicating that the ambient electric field changed directions. A calibrate sequence began at 60720 UT. When the data collection resumed, the measured signal indicated that the electric field had a southwa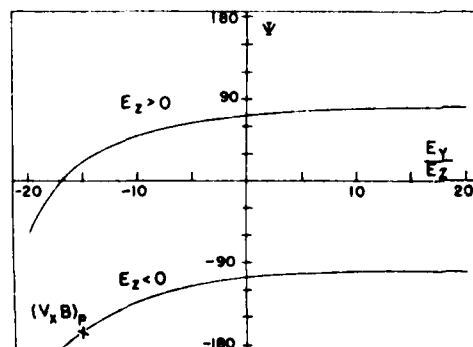rd component. The reversal at 60710 UT marks the boundary between the auroral oval and the polar cap. In the period 60645–60690 UT we assumed that Ψ had the same value that it had before and after this interval. Although, in principle, the amplitude could be fit to arbitrarily small portions of the sine waves, 5-s periods were chosen to insure that Φ_E would be near its maximum or minimum value during a portion of each fit period. Variations of E on time scales ≤ 5 s are obtained from an examination of the residues $(\Phi_E - \Phi_m)$ given in Figure 8d.

APPENDIX B: ELECTRIC FIELD COMPONENTS AT 60647 UT

In this appendix we calculate the components of the electric field at 60647 UT by using measurements by the ion drift meter to determine the component in the spin plane, that is parallel to $\mathbf{B}$. A schematic of sensors 1, 2, and 3 (Figure 11) shows that at this time sensor 2 was pointing close to the direction of the satellite's velocity vector. The currents to sensors 1 and 3 are

$$I_1 = -Nq\mathbf{V}_p \cdot \hat{n}_1$$
$$I_3 = -Nq\mathbf{V}_p \cdot \hat{n}_3 \qquad (B1)$$

where N is the plasma density, $\mathbf{V}_p$ is the total plasma velocity in the rest frame of the satellite, and $\hat{n}_1$ and $\hat{n}_3$ are unit vectors normal to the apertures of sensors 1 and 3:

$$\hat{n}_1 = \cos 40° \hat{x} - \sin 40° \hat{y}$$
$$\hat{n}_3 = \cos 40° \hat{x} + \sin 40° \hat{y} \qquad (B2)$$

In the satellite's frame of reference the plasma bulk motion has three terms.

1. The satellite motion relative to an earth-centered inertial system. At 60647 UT

$$\mathbf{V}_s = 7.05\hat{x} + 0.15\hat{y} \text{ km/s} \qquad (B3)$$

2. The corotational plasma drift

$$\mathbf{V}_c = -\Omega_{\oplus} r \sin \lambda \hat{y} = -0.5 \hat{y} \text{ km/s} \qquad (B4)$$

where $\Omega_{\oplus} = 7.3 \times 10^{-5} \text{ s}^{-1}$ is the earth angular speed, $r = 7.7 \times 10^3$ km is the satellite's distance from the earth's center, and $\lambda = 65.5°$ is the geographic latitude of the subsatellite point on the earth's surface.

3. The cross spin plane drift due to the component of E in the spin plane that is perpendicular to $B(E_{p\perp})$.

$$\mathbf{V}_E = (E_{p\perp}/B)\hat{y} \qquad (B5)$$

Substituting (B2)–(B5) into (B1) and forming the ratio $I_1/I_3 = \xi$ give

Fig. 10. Phase angle ψ as a function of E_y/E_z near 60600 UT. The projection of the $\mathbf{V} \times \mathbf{B}$ field is indicated for comparison with Figure 9
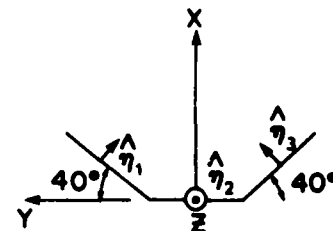

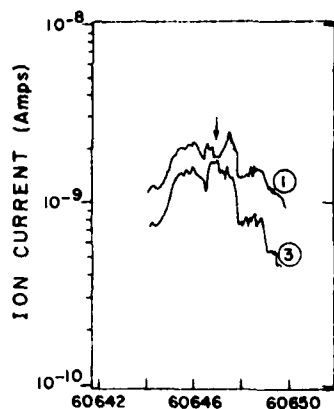Fig. 11. Schematic representation of the S3-2 ion driftmeter orientation at 60647 UT.

Fig. 12. Current measurements by the ion drift sensors 1 and 3 near 60646 UT. The fact that $I_1 > I_3$ indicates that the plasma has a westward drift component. The arrow indicates the time at which sensors 1, 2, and 3 were facing closest to the ram direction.

$$\frac{E_{p\perp}}{B} = \frac{1.09\xi - 1}{0.124(1 + \xi)} \text{ m/s} \qquad (B6)$$

At 60646 and 60647 UT, ξ had values of 1.45 and 1.05, respectively (Figure 12). The electric field at 60646 UT was 30 mV/m. Substitution of the values of ξ at 060646 and 60647 as well as E_p, at 60646 UT allows us to calculate $E_{p\perp}$ at 60647:

$$E_{p\perp}(60647 \text{ UT}) = 8.9 \text{ mV/m}$$

Having determined $E_{p\perp}$, it is now possible to estimate $E_{p\parallel}$, the component of the electric field in the spin plane that is parallel to B. To do this, we need to known the orientation of $E_{p\perp}$ and the dipole (Figure 13). The orientation of $E_{p\perp}$ is found by assuming that the value of $\psi = 75°$ calculated at 60645 UT is constant. The dipole orientation can be estimated by recognizing that the maximum excursion of ϕ_m occurred ~0.3 s after ϕ, went through a maximum. The orientation of the V × B component in the spin plane is determined from the satellite attitude and the IGRF model. The satellite spin rate is ~18°/s⁻¹ Thus the dipole has moved ~6° beyond its position at the ϕ, maximum. The angle between the dipole and the Z axis is ~34°. From simple trigonometric considerations it is seen that $E_{p\parallel} = E_{p\perp} \tan 49° = 10.2$ mV/m.
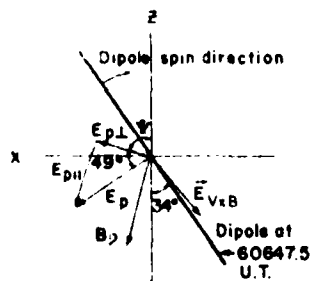

Fig. 13. Orientation of the electric field dipole at 60647.5 UT. The projections of the ambient E and B fields as well as the electric field due to the satellite motion are indicated.

REFERENCES

Ackerson, K. L., and L. A. Frank, Correlated satellite measurements of low-energy electron precipitation and ground-based observations of a visible auroral arc. J. Geophys. Res., 77, 1128, 1972.

Anderson, H. R.., and R. R. Vondrak, Observations of Birkeland currents at auroral latitudes, Rev. Geophys. Space Phys., 13, 243, 1975.

Armstrong, J. C., S.-I Akasofu, and G. Rostoker, A comparison of satellite observations of Birkeland currents with ground observations of visible aurora and ionospheric currents, J. Geophys. Res., 80, 575, 1975.

Bekifi, G., Radiation Processes in Plasmas. John Wiley, New York, 1966.

Bering, E. A., M. C. Kelley, and F. S. Mozer, Observations of an intense field-aligned thermal ion flow and associated intense narrowband electric field oscillations. J. Geophys. Res., 80, 4612, 1975.

Burke, W. J., D. A. Hardy, F. J. Rich, M. C. Kelley, M. Smiddy, B. Shuman, R. C. Sagalyn, R. P. Vancour, P. J. L. Widman, S. T. Lai, and J. Bass, A case study of S3-2 observations in the late evening auroral oval, Rep. AFGL-TR-79-0011, Air Force Geophys. Lab., Bedford, Mass., 1979.

Carlson, C. W., and M. C. Kelley, Observation and interpretation of particle and electric field measurements inside and adjacent to an active auroral arc, J. Geophys. Res., 82, 2349, 1977.

Cloutier, P. A., B. R. Sandel, H. R. Anderson, P. M. Pazick, and R J. Spiger, Measurement of auroral Birkeland currents and energetic particle fluxes, J. Geophys. Res., 78, 640, 1973.

Craven, J. D., K. L. Ackerson, and L. A. Frank, Location within inverted-V events of large anisotropies in auroral electron intensities, Eos Trans. AGU, 53, 313, 1976.

Dreicer, H., Electron and ion runaway in a fully ionized gas, I, Phys. Rev. 115, 238, 1959.

Fahleson, U. V., Theory of electric field measurements conducted in the magnetosphere with electric probes, Space Sci. Rev., 7, 283, 1967.

Frank, L. A., and K. L. Ackerson, Observations of charged particle precipitation in the auroral zone, J. Geophys. Res., 76, 3612, 1971.

Gurnett, D. A, and L. A. Frank, Observed relationship between electric fields and auroral particle precipitation, J. Geophys. Res., 78, 145, 1973.

Heppner, J. P., High-latitude electric fields and the modulations related to interplanetary magnetic field parameters, Radio Sci., 8, 933, 1973.

Hudson, M. K.., and F. S. Mozer, Electrostatic shocks, double layers, and anomalous resistivity in the magnetosphere, Geophys. Res Lett., 5, 131, 1978.

Iijima, T., and T. A. Potemra, The amplitude distribution of field-aligned currents at northern high latitudes observed by Triad, J. Geophys. Res., 81, 2165, 1976.

Kamide, Y., and S.-I. Akasofu, the location of the field-aligned currents with respect to discrete auroral arcs, J. Geophys. Res., 81, 3999, 1976.

Kelley, M. C., G. Haerendel, H. Kappler, F. S. Mozer, and U. V. Fahleson, Electric field measurements in a major magnetospheric substorm, J. Geophys. Res., 80, 3181, 1975.

Kindel, J. M., and C. F. Kennel, Topside current instabilities, J. Geophys. Res. 76, 3065, 1971.

Kinter, P. M., M. C. Kelley, and F. S. Mozer, Electrostatic hydrogen cyclotron waves near one earth radius altitude in the polar magnetosphere, Geophys. Res Lett., 5, 139, 1978.

Kinter, P. M., M. C. Kelley, R. D. Sharp, A. G. Ghielmetti, M. Temerin, C. Cattell, P. F. Mizera, and J. F. Fennell, Simultaneous observations of energetic (keV) upstreaming ions and electrostatic hydrogen cyclotron waves, J. Geophys. Res., 7201, 1979.

Lui, A. T. Y., D Venkatesan, C. D. Anger, S.-I. Akasofu, W. J. Heikkila, J. D. Winningham, and J R. Burrows, Simultaneous observations of particle precipitation and auroral emissions by the Isis 2 satellite in the 19-24 MLT sector, J. Geophys. Res., 82, 2210, 1977.

Lysak, R. L., and M. K. Hudson, Coherent anomalous resistivity in the region of electrostatic shocks, Geophys. Res. Lett., 6, 661, 1979.

Mallinckrodt, A. J., and C. W. Carlson, Relations between transverse electric fields and field-aligned currents, J. Geophys. Res., 83, 1426, 1978.

Maynard, N. C. Electric field measurements across the Harang discontinuity, *J. Geophys. Res.*, 79, 4620, 1974.

Maynard, N. C., D. S. Evans, B. Maehlum, and A. Egeland, Auroral vector electric field and particle comparisons, 1, Premidnight convection topology, *J. Geophys. Res.*, 82, 2227, 1977.

Morel, P. R., F. A. Hasuer, and B. Sellers, Design fabrication and integration of an electrostatic analyzer for a satellite payload, *Rep. AFCRI-TR-75-0017*, Air Force Geophys. Lab., Hanscom AFB, Bedford, Mass., 1975.

Mozer, F. S., and P. Lucht, The average auroral zone electric field, *J. Geophys. Res.*, 79, 1001, 1974.

Mozer, F. S., C. W. Carlson, M. K. Hudson, R. B. Torbert, B. Parady, and J. Yatteau, Observations of paired electrostatic shocks in the polar magnetosphere, *Phys. Rev. Lett.*, 38, 292, 1977.

Reed, R., W. E. Swartz, D. T. Farley, and B. G. Fejer, Radar observations of ion cyclotron waves, *Eos Trans. AGU*, 59, 1150, 1978.

Rees, M. H., Auroral ionization and excitation by incident energetic electrons *Planet. Space Sci.*, 11, 1209, 1963.

Shawhan, S. D., C. G. Falthamer, and L. P. Block, On the nature of large auroral zone electric fields at 1-R_j altitude, *J. Geophys. Res.*, 83, 1049, 1978.

Swift, D. W., On the formation of auroral arcs and acceleration of auroral electrons, *J. Geophys. Res.*, 80, 2096, 1975.

Torbert, R. B., and F. S. Mozer, Electrostatic shocks as the source of discrete auroral arcs, *Geophys. Res. Lett.*, 5, 135, 1978.

Vogl, J. L., N. L. Sanders, and S. E. DeForest, Substorm-induced spacecraft-charging currents from field-aligned and omnidirectional particles, in *Spacecraft Charging by Magnetospheric Plasmas*, edited by H. Rosen, MIT Press, Cambridge, Mass., 1976.

Widman, P. J. L., A low energy ion sensor for space measurements with reduced photo sensitivity, *Space Sci. Inst.*, 3, 363, 1977.

Zmuda, A. J., J. C. Armstrong, and F. T. Heuring, Characteristics of transverse magnetic disturbances observed at 100 km in the auroral oval, *J. Geophys. Res.*, 75, 4757, 1970.

Observations of Field-Aligned Currents in Association With Strong Convection Electric Fields at Subauroral Latitudes

FREDERICK J. RICH,[1] WILLIAM J. BURKE,[2] MICHAEL C. KELLEY,[3] AND MICHAEL SMIDDY[4]

An examination of regions of strong convection electric fields ($E > 50$ mV/m) equatorward of the auroral zone has been made on the basis of data from the S3-2 satellite in 1976. Only seven examples were found, which indicates a low occurrence rate even after accounting for the gaps in data coverage. While this phenomenon did not correlate with the magnitude of Kp or AE, it is always substorm related. The electric field and magnetic field data indicate that the electric field is generated by plasma sheet ions being driven closer to the earth than plasma sheet electrons by magnetospheric convection in the evening sector. The existence of a net field-aligned current into the ionosphere through the region indicates the presence of latitudinal conductivity gradient. The depletions of ionospheric particles near regions of strong field-aligned currents ($\geq 1~\mu A/m^2$) into the ionosphere indicate that upward moving ionospheric electrons are carrying the current. The evacuation of the E region approximately 1 min after the onset of the electric field as suggested by Banks and Yasuhara (1978) is not supported by the data, but it may occur on a time scale of ~30 min. If both the F region and E region are depleted in the strong convection region, the result may be a naturally occurring 'hole' in the ionosphere.

INTRODUCTION

Considerable interest has recently been directed toward the electrodynamics of the region near the inner edge of the ring current. In the premidnight local time period, very large poleward directed electric fields [Smiddy et al., 1977; Maynard, 1978] and corresponding large azimuthal drifts [Heelis et al., 1976] have been reported. In one case the electric field at 1500 km was 245 mV/m, which corresponds to a drift velocity of 9.8 km/s. The two events detected on the S3-2 satellite and studied by Smiddy et al. were limited to a latitude range less than 1° wide and occurred during substorm activity. The transition from a hydrogen plasma environment to an oxygen plasma also occurred quite close to the large electric field region.

In recent theoretical work, Southwood and Wolf [1978], building on a number of other studies referenced therein, showed that if ring current ions penetrate closer to the earth than do precipitating plasma sheet electrons and if the separation distance between these two boundaries is not too great, then a large meridional directed electric field will be created between them. The enhanced conductivity in the ionosphere created by these electron fluxes, which also create the diffuse aurora, plays an essential role in their analytic model. A computer simulation by Harel et al. [1980] also addresses the electrodynamics of the local time sector. They found an enhanced poleward e field at subauroral latitudes in direct association with an intense downward related current.

Two other theoretical works have relevance to these phenomena. Block and Fälthammar [1968] discussed the effect of field-aligned currents on topside plasma density when those currents are carried by thermal particles, as seems to be the case here. Banks and Yasuhara [1978] discussed the effect of

[1] Research Center, Regis College, Weston, Massachusetts 02193
[2] Physics Department, Boston College, Chestnut Hill, Massachusetts 02167
[3] School of Engineering, Cornell University, Ithaca, New York 14853
[4] Air Force Geophysics Laboratory, Hanscom Air Force Base, Massachusetts 01731

large poleward e fields on the E region ionosphere and its conductivity.

The purpose of this work is to extend the study of large subauroral electric fields by using the S3-2 satellite experiments. In addition to the electric field, we also plot the field-aligned current pattern, topside electron density, and energetic electron fluxes. Taken together, these data may shed further light on the physical processes occurring in this region of space.

DATA PRESENTATION

The data used for this report were obtained with the U.S. Air Force satellite S3-2, which was placed into a polar orbit with an initial apogee and perigee of 1556 km and 240 km, respectively. The satellite was spin stabilized in a cartwheel mode with a spin rate of ~3 rpm. The instruments used here are an electric field dipole, a triaxial flux gate magnetometer, a spherical Langmuir probe that collects thermal electrons, and an energetic electron (50 eV to 17 keV) spectrometer. The electric field experiment consists of a dipole probe in the spin plane of the satellite across which the electrostatic potential is measured 16 times/s. The electric field is determined from fitting 5 s of data to determine the component of the electric field that is perpendicular to $\vec{B}$ and is approximately in the direction of the satellite velocity. Magnetic field is measured 32 times/s with a resolution of 5 γ ($\gamma = 10^{-5}$ T). The component of the current density parallel to the magnetic field ($j_{\parallel}$) is calculated with the use of the infinite current sheet approximation to Maxwell's equations. A detailed description of the instruments and the means by which data are reduced is given by Burke et al. [1979].

The data selected were times when the convection electric field in the subauroral zone was significantly greater than the component of the induction electric field in the satellite spin plane. Thus subauroral electric fields with maximum intensities of 50 mV/m or less are not included. The result is a total of only seven examples of intense subauroral convection electric fields in 1976. This low number indicates that this feature is not a steady state feature, but the low number of observations is also caused by the satellite's data acquisition schedule. The S3-2 satellite collected data only ~15% of the time, and occasionally the subauroral passages were excluded in preference to auroral and polar cap passages. The recent re-
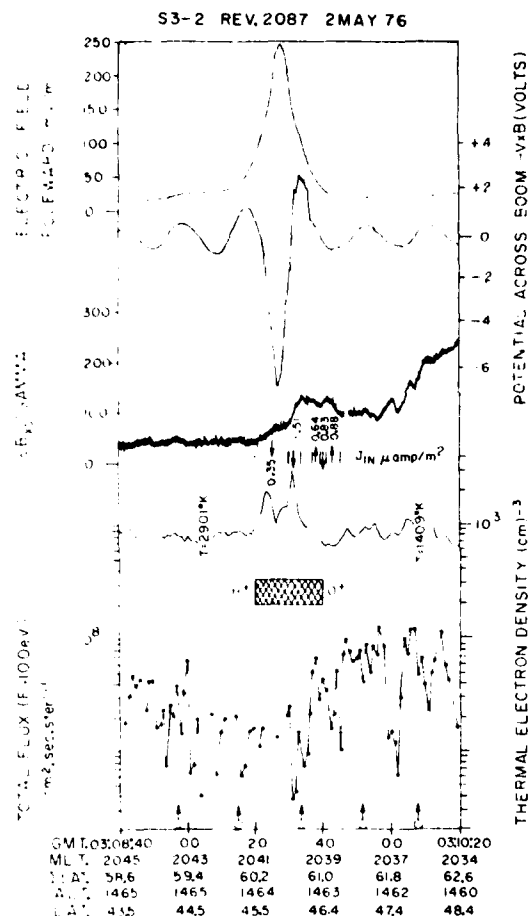
Fig. 1 Electric field, magnetic field, thermal electron, and energetic electron data obtained by S3-2 near the intense convection electric field for revolution 2087 on May 2, 1976. The potential drop across the region is ~30 kV. The transition from H$^+$ to O$^+$ (shaded region) is coincident with the strong electric field. The calculated field-aligned current (J_{IN}) is displayed under the magnetometer trace with arrows indicating current into (downward arrow) or out of (upward arrow) the ionosphere. The region over which the calculation of J_{IN} was made is denoted by vertical bars under the magnetometer trace.

less than the true values. As is presented here, regions of positive (negative) slope in the magnetic deflection correspond to field-aligned current into (out of) the ionosphere and are noted by arrows pointing down (up). The magnitude of J_{IN} is determined by the deflections from a base line established in the equatorward portion of the data set.

The fourth trace in Figure 1 gives the density of thermal electrons. This trace is broken at times when the bias voltage on the sensor grids are swept in order to measure the thermal electron temperature (T). When possible, measurements of the electron temperature are shown in the broken portion of the trace.

The shaded area below the fourth trace represents the transition zone from a hydrogen-ion-dominated region equatorward of the transition to an oxygen-ion-dominated region poleward of the zone. The average ion mass is determined from the spin modulation of ions into an ion trap. Thus the transition cannot be resolved more precisely than one spin period as in Figure 1. There are also times when the transition zone is much wider than the distanced traveled by the satellite in one spin period.

The fifth trace gives the integrated directional flux of energetic electrons sampled at a rate of one spectrum per second. This trace is broken when the flux levels fall below the in-
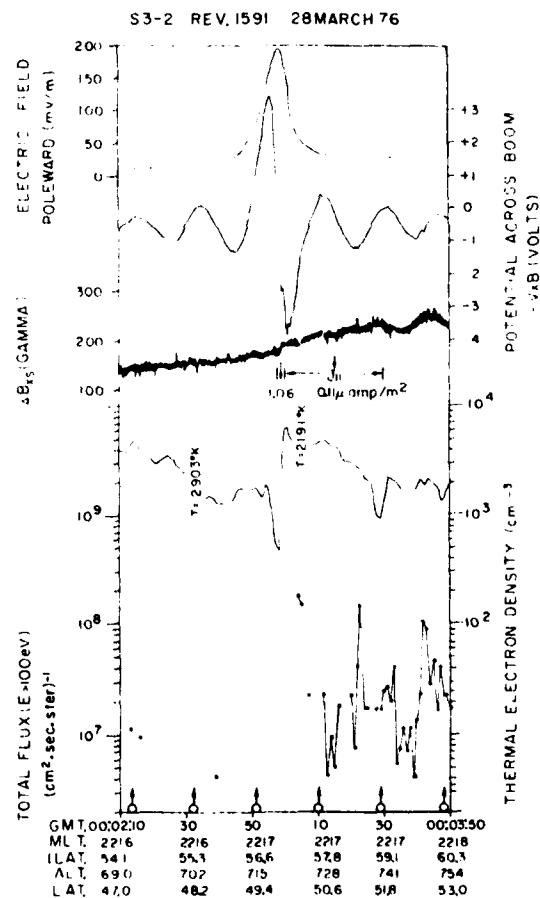

Fig. 2. S3-2 data for revolution 1591 on March 28, 1976, presented in the same format as Figure 1. The potential drop across the region is ~20 kV. Note that the satellite was in an O$^+$-dominated region throughout this data set because of the low altitude of the satellite.
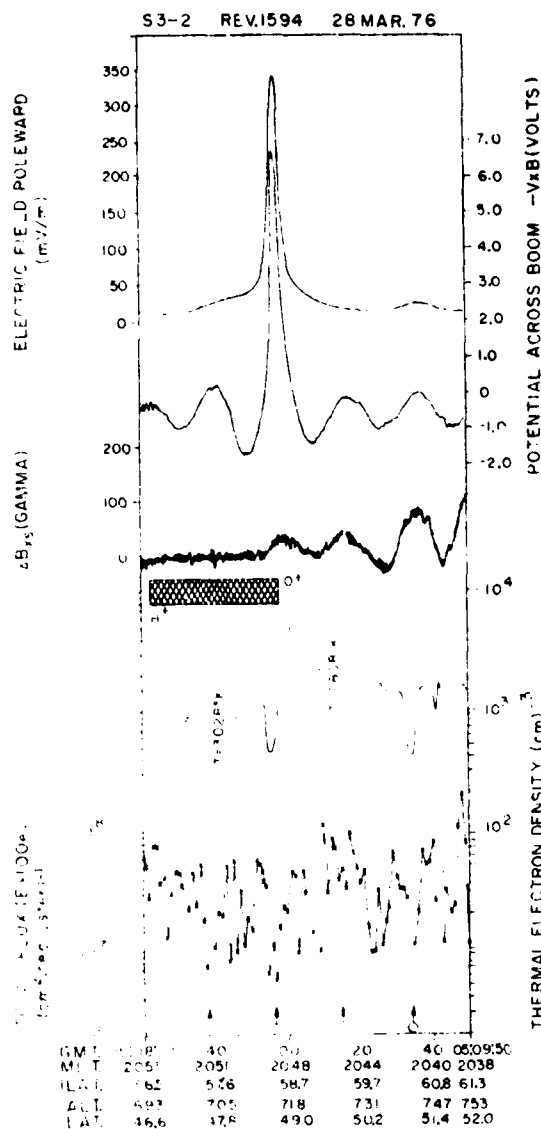
port of *Spiro et al.* [1979] includes a larger quantity of sub-auroral convection observations due to their ability to identify events easily with a maximum strength of ≤50 mV/m.

Figure 1 shows the data set that was shown in preliminary form by *Smiddy et al.* [1977]. The top trace shows the calculated electric field in the poleward direction. The smoothness of this trace is somewhat artificial because of the processing technique that eliminates variations with scales less than 5 s. The second trace gives the potential difference between the spherical electrodes after subtracting the effects of induction electric fields due to satellite motion. The result is a spin-modulated signal with amplitude proportional to the field in an earth-fixed frame.

The third trace in Figure 1 is the component of the magnetic deflection vector (measured minus model field) along the spin axis. Since the spin axis is approximately in the east-west direction, the field-aligned current can be calculated from this single component of the magnetic deflection vector. As a result of this approximation, the values of the field-aligned currents (J_{IN}) shown below the magnetometer trace are slightly

Fig. 3 S3-2 data for revolution 1594 on March 28, 1976, presented in the same format as Figure 1. The potential drop across the region is ~22 kV. This was the strongest and the narrowest region observed in 1976.

strument background level for a 1-S period. Circles with upward pointing arrows mark times when the spectrometer was collecting electrons with pitch angles near zero degrees.

As is shown in the figure, the poleward component of the convection electric field rose from a background level at 0309:15 UT to a peak value at 0309:25. The magnetic field deflection was constant with a base line value of 40 γ until 0309:28 UT, when it began to increase corresponding to a current into the ionosphere of 0.35 μA/m². Between 0309:30 and 0309:34, while the electric field was beginning to decrease, the magnetic deflection increased at its most rapid rate, indicating a current of 1.51 μA/m² into the ionosphere. Between 0309:37 and 0309:45 the slope of the magnetic deflection alternated sign with a decrease, then an increase, and then a decrease, indicating currents of 0.64 μA/m² out of the ionosphere, 0.83 μA/m² into the ionosphere, and then again out of the iono-

sphere at 0.88 μA/m². The net effect is a magnetic deflection of 60 γ, which corresponds to a net line current into the region of ~48 mA/m. A region approximately 0.5° wide in latitude was devoid of field-aligned current, but after 0309:50 the effect of the ordinary region 2 current system [Iijima and Potemra, 1976] became clear.

The thermal electron density had a nearly constant value of 8×10^2 cm⁻¹ until 0309:30 UT. It rose to a local maximum of 3×10^3 cm⁻¹ at the same place that the strong electric field was observed. A 'bite-out' in the electron density occurred where the field-aligned current maximized. Except at 0309:37, when an upward current was detected, the energetic electron flux was close to or below the detector background level. After 0309:45 UT, flux levels of ~10^8 (cm² s sr)⁻¹ were measured that indicate that the satellite had entered the region of the diffuse aurorae. As was mentioned by Smiddy et al., the strong electric field region marked the boundary between light (H⁺) and heavy (O⁺) ions in the plasma as deduced from the ratio of ram to wake currents to a spinning ion sensor.

In Figures 2 and 3 we show examples of intense electric fields that were located in a latitude range even narrower than the case shown in Figure 1. The electric field again was quite intense with values of nearly 200 mV/m for rev 1591 and al-
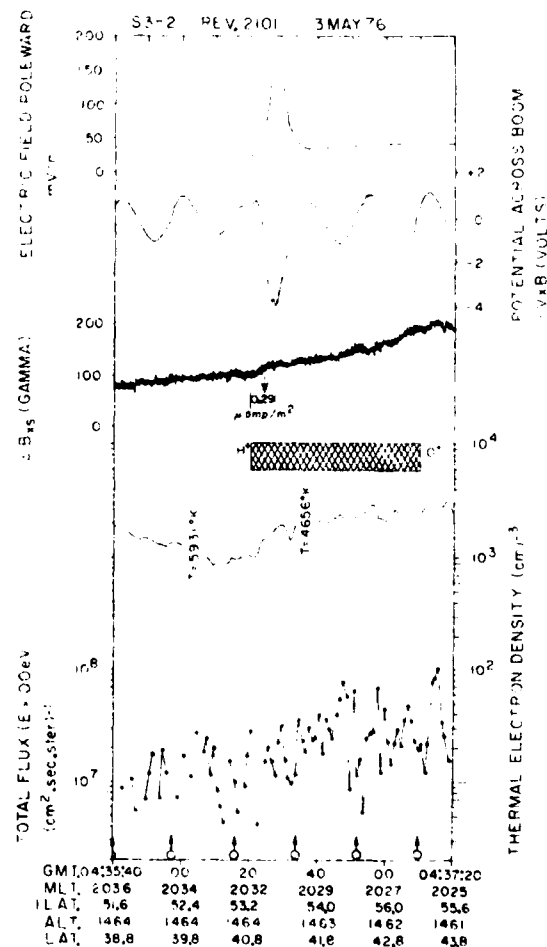

Fig. 4 S3-2 data for revolution 2101 on May 3, 1976, presented in the same format as Figure 1. The potential drop across the region is ~11 kV.
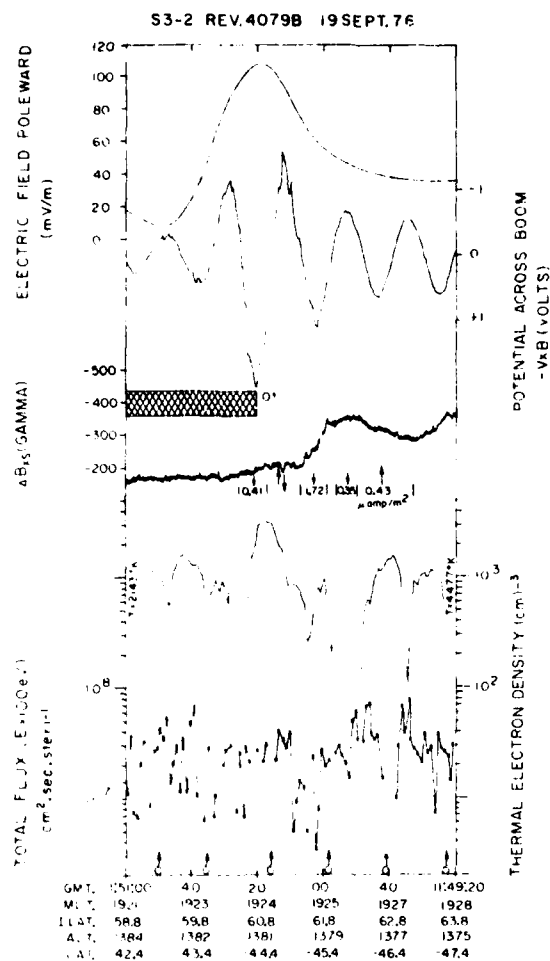
S3-2 REV. 4079B 19 SEPT. 76

Fig. 5. S3-2 data for revolution 4079B on September 19, 1976, presented in the same format as Figure 1. The time scale and magnetic deflection scale have been inverted to make it easier to compare these data with the northern hemisphere data sets. Thus the poleward direction is to the left, and downward field-aligned currents are indicated by upward magnetic deflections. The potential drop across the region is ~27 kV.

most 350 mV/m for rev 1594. Note that the latter was the most intense event studied as well as the one with the smallest spatial scale in latitude.

In Figure 2 the slope of the magnetic field deflection is basically positive (the signature of the downward region 2 currents in this local time sector) with occasional upward currents imbedded. Note the most intense downward current (~1 μA/m²) associated with the large electric field was colocated with a deep bite-out in electron density but offset poleward from the peak in the electric field. Electron flux data were sketchy on rev 1591 but indicate precipitation only poleward of the intense electric field. On rev 1591, no light/heavy ion transition was observed because of the low altitude of the satellite. On rev 1594, the light/heavy ion transition (shaded bar) was observed near and slightly equatorward of the electric field spike. The field-aligned current associated with these data is not given because the magnetometer trace has an oscillatory nature between the strong convection region and the auroral zone. Since care has been taken to remove satellite spin effects, this oscillation seems to be geophysical. However, the

period of the oscillation is within 0.2 s of the satellite spin period, which is too close to rule out an unknown satellite-induced effect.

Examples of intense fields more extended in latitude are presented in Figures 4–7. With one exception there was a general positive trend to the slope of the magnetic field, indicating region 2 downward currents. The exception is in Figure 7, in which there is no general trend.

Rev 4079B (Figure 5) is an interesting case for several reasons. (As is discussed below, this orbit has been used in a computer simulation by *Harel et al.* [1980].) Precipitating electrons were observed quite close to the *e* field peak as well as poleward of the *e* field spike. A possible local maximum in ionospheric density is also indicated in Figure 5. Just poleward of this, and in a region of decreasing electric field, an intense downward current of 1.7 μA/m² was detected, as was a decrease of electron density by an order of magnitude.

The poleward wall of the plasma trough is quite clear in Figures 6 and 7 and, slightly less evidently, in Figures 2, 3, and 4. The peak in electric field falls within the ion transition region in five of the six observations of the transition.

Figures 6 and 7 show data in both hemispheres obtained during the same orbit separated by 30 min in universal time and about 1 hour in magnetic local time. The invariant lati-
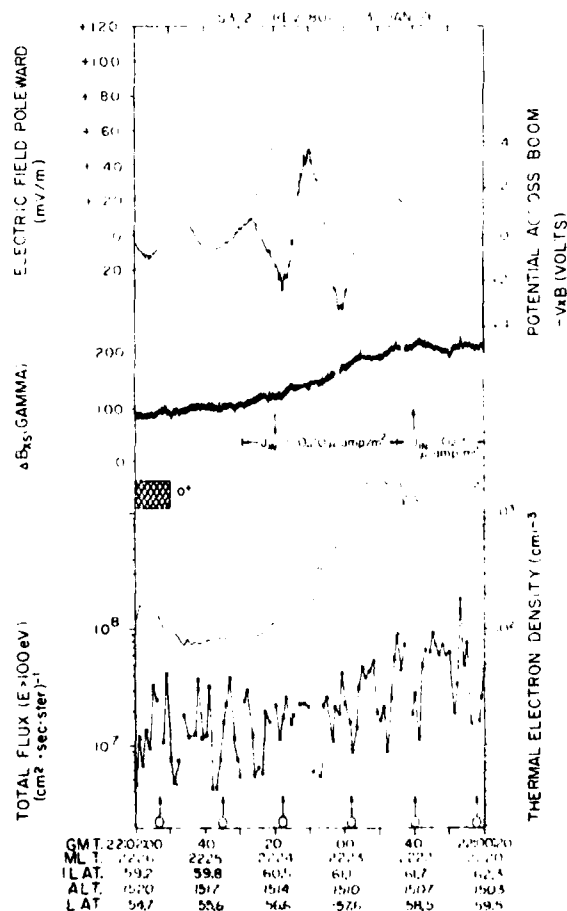

Fig. 6. S3-2 data for revolution 801 in the southern hemisphere. Like Figure 5, the time and magnetic deflection scales have been inverted to aid in comparison of the data. The potential drop across the region is ~20 kV.
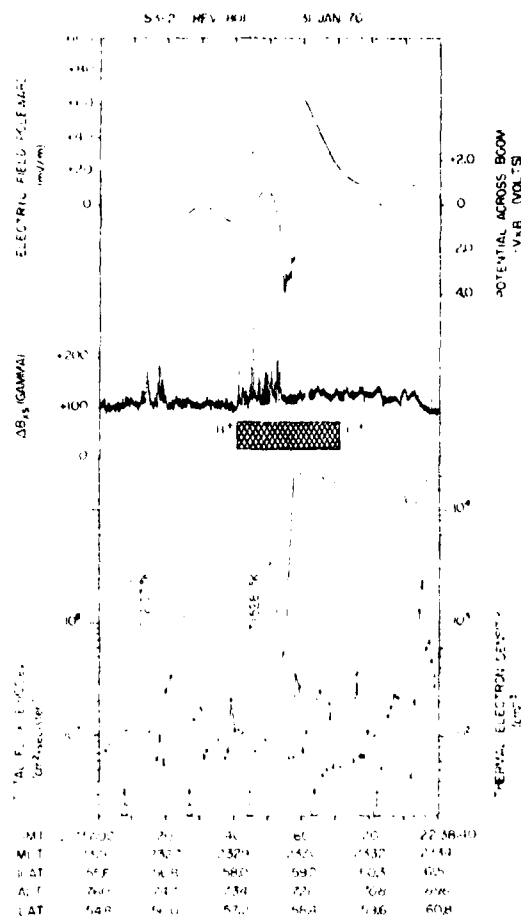
Fig. 7. S3-2 data for revolution 801 in the northern hemisphere 37 min after the data shown in Figure 6. The position and magnitude of the electric field are comparable to Figure 6, but the field-aligned current has decreased significantly.

tude of the peak was within 1° of conjugacy. The magnitude of the electric field was down only 75% at the later universal time, but the field-aligned current was considerably less.

All of these observations of intense subauroral e fields were associated with strong substorm activity, but they do not particularly correlate with the magnitude of activity indices such as AE or Kp. However, all of the observations were made in the early recovery phase of the substorm.

DISCUSSION

The simple model of magnetospheric convection of South-wood and Wolf [1978] provides an excellent source for the potential drop across subauroral L shells that is reported here. In their model the field is created by the penetration of partial ring current ions to a lower L shell than the plasma sheet electrons. They predict that the electric field will be significant for small separation (less than 3° of invariant latitude) and its magnitude will be inversely related to the latitudinal size of the region This result is in good agreement with the present data. They also predicted that the intense convection region will be on the equatorward boundary of the plasma sheet. The observations here are approximately in agreement but do not provide a clear-cut test of this prediction. For example.

Smiddy et al. mentioned that precipitating energetic electrons typical of the plasma sheet and diffuse aurora were seen 1° poleward of the intense electric field. While Figure 1 shows this boundary of precipitating electrons, it also shows a broad and complex boundary of all energetic electrons.

The computer simulation by Harel et al. [1980] was specifically designed to model self-consistently conditions during September 19, 1976, which includes S3-2 rev 4079 B, which is partly presented in Figure 5. Using the polar cap electric fields detected by the S3-2 and the position of the plasmapause, they predicted that a strong electric field should occur at sub-auroral latitudes with a peak magnitude of 95 mV/m. In this model, which included electron precipitation and enhanced conductivity, poleward of the subauroral field, all field-aligned currents below 67° latitude were downward in the evening local time sector. Because of their latitudinal step size, it was unclear whether upward currents should exist. We find that their model results are in agreement with the data presented here, since most cases show that the net currents are into the ionosphere. Such a current direction is consistent with the generally positive poleward gradient in the electric field and the resultant divergence of perpendicular current in the ionosphere (for a low-particle precipitation it seems reasonable to expect only a weak gradient in conductivity). On the poleward edge of the intense convection region the electric field decreases rapidly, and one might expect an outward field-aligned current [Smiddy et al., 1977]. This is not generally the case, however, and only in Figures 1 and 6 is there even the suggestion of a symmetrical pair of current sheets. This implies that precipitating electrons create a poleward directed conductivity gradient such that the total divergence of $\sigma_p E$ is positive. This perhaps is not surprising, since the plasma sheet precipitation is an important component of the electrodynamics of the ion and electron fluids that lead to the large poleward directed electric field.

These observations of net downward directed currents are in good agreement with the results of Klumpar [1979], who showed that on the average downward currents extend 2.4° equatorward of the electron precipitation zone. As was also discussed by Klumpar, a close comparison was found between intense field-aligned currents and topside density depletions. Figures 1, 2, 3, and 5 are particularly good examples of this effect. The currents associated with these bite-outs of density were downward and in the range of 1-2 $\mu A/m^2$. Block and Falthammar [1968] showed that currents of this magnitude could indeed cause topside density depletions for either direction of parallel current, provided that ionosphere particles carried the current, as seems to be the case here. Smiddy et al. [1977] suggested that the large electric fields may create topside density depletions via conversion of O^+ to NO^+ in the energy dependent reaction

$$N_2 + O^+ \rightarrow NO^+ + N$$

and subsequent dissociative recombination of NO^+ [Schunk et al., 1976]. This indeed should occur in the region but is inefficient for densities much below 10^5 cm^{-3}. This fact coupled with the close correlation with strong field-aligned currents reported here argues for the Block and Falthammar process for the deep depletions observed.

It is interesting to note that as the density decreases the differential drift velocity between ions and electrons that supports the current must increase. Eventually, the criterion for instability of electrostatic ion cyclotron waves will be ex-

180

ceeded, and wave-particle interactions will occur. This threshold drift is lower in an oxygen plasma than in hydrogen and hence may be located on the poleward side of the large subauroral electric field region.

Banks and Yasuhara [1978] suggested another magnetosphere-ionosphere interaction associated with the large subaurorai electric fields. They pointed out that the poleward electric field would drive E region ionization poleward, creating gradients in ionization that tend to cancel the gradients in the electric field and to lower the net divergence of perpendicular current. They predict a reduction of the field-aligned current pair to 0.01 $\mu A/m^2$ upward within 1 min of creation of the large electric field. The present data do not support this prediction. However, it should be noted that particle precipitation was not included in Banks and Yasuhara's model. Thus the effect may indeed be operating and may play an important role in the coupled electrodynamic system if the time scale is changed from 1 min to ~30 min. During rev 801 (Figure 6 and 7) the field-aligned current decreased significantly in 37 min, which implies a decrease in the height-integrated Pedersen conductivity. To be complete, computer simulations of the interaction of the intense subauroral convection electric field with the E layer should be done to assess the total meridional density gradients.

With the depletion of both the E layer as described by Banks and Yasuhara and the depletion of the F layer presented here, there may be an ionization 'hole' through the ionosphere, a region of anomalously low ionization per unit area. This hole can be useful in two ways. First, when density surveys of the auroral and subauroral ionosphere are made by ground-based incoherent radar, the intense convection region can be located and tracked as a column of depleted plasma. Second, the hole will allow lower-frequency radio frequencies to penetrate the ionosphere. Thus astrophysical radio signals that normally are blocked by the ionosphere can be observed through the hole by ground-based stations. Such holes have been artificially created but have not previously been found to occur naturally.

REFERENCES

Banks, P. M., and F. Yasuhara, Electric fields and conductivity in the nighttime E-region: A new magnetosphere-ionosphere-atmosphere coupling effect, *Geophys. Res. Lett.*, 5, 1047-1050, 1978.

Block, L. P., and C. G. Falthammar, Effects of field-aligned currents on the structure of the ionosphere, *J. Geophys. Res.*, 73, 4807-4812, 1968.

Burke, W. J., D. A. Hardy, F. J. Rich, M. C. Kelley, M. Smiddy, B. Shuman, R. C. Sagalyn, R. P. Vancour, R. J. L. Wilkman, S. T. Lai, and J. Bass, A case study of S3-2 observations in the late evening auroral oval, *Rep. TR-79-0011*, Air Force Geophys. Lab., Bedford, Mass., 1979.

Harel, M., R. A. Wolf, R. W. Spiro, P. H. Reiff, C. K. Chen, W. J. Burke, F. J. Rich, and M. Smiddy, Quantitative model of a magnetospheric substorm. 2. Comparison with observations, submitted to *J. Geophys. Res.*, 1980.

Heelis, R. A., R. W. Spiro, W. B. Hanson, and J. L. Burch, Magnetospheric ionospheric coupling in the mid-latitude trough (abstract), *Eos Trans. AGU*, 57, 990, 1976.

Iijima, T., and T. A. Potemra, The amplitude of field-aligned currents at northern high latitude observed by Triad, *J. Geophys. Res.*, 81, 2165-2174, 1976.

Klumpar, D. M., Relationships between particle distributions and magnetic field perturbations associated with field-aligned currents, *J. Geophys. Res.*, 84, 6524-6532, 1979.

Maynard, N. C., On large poleward-directed electric fields at sub-auroral latitudes, *Geophys. Res. Lett.*, 5, 617-618, 1978.

Schunk, R. W., P. M. Banks, and W. J. Raitt, Effects of electric fields and other processes upon the nighttime high-latitude F layer, *J. Geophys. Res.*, 81, 3271-3282, 1976.

Smiddy, M., M. C. Kelley, W. Burke, R. Rich, R. Sagalyn, B. Shuman, R. Hays, and S. Lai, Intense poleward-directed electric fields near the ionospheric projection of the plasmapause, *Geophys. Res. Lett.*, 4, 543-546, 1977.

Southwood, D. J., and R. A. Wolf, An assessment of the role of precipitation in magnetospheric convection, *J. Geophys. Res.*, 83, 5227-5232, 1978.

Spiro, R. W., R. A. Heelis, and W. B. Hanson, Rapid subauroral ion drifts observed by Atmospheric Explorer C, *Geophys. Res. Lett.*, 6, 657-660, 1979.

Postsunrise Refilling of the Low-Latitude Topside Ionosphere

W. J. Burke,[1] R. C. Sagalyn,[2] R. G. Rastogi,[2] M. Ahmed,[2] F. J. Rich,[2] D. E. Donatelli,[3] AND P. J. L. Wildman[2]

Plasma density measurements from a polar-orbiting Defense Meteorological Satellite Program satellite at 840 km have shown the existence of significant plasma depletions near the magnetic equator in the postsunrise hours. The phenomenon is observed regularly during magnetically quiet times near the equinoxes. The magnitude of the depletion depends upon longitude and the time elapsed since sunrise in the lower F region. It is significantly less pronounced or absent near the solstices. During magnetically active periods the low-latitude topside ionosphere is modified due to vertical $E \times B$ plasma drifts in the predawn sector. The quiet time equinox observations are interpreted in terms of a diurnal flux tube filling model. It is suggested that the observed equatorial depletions result from a pair of plasma fronts that are moving upward from conjugate ionospheres and that are associated with the early stages of the post-sunrise refilling process.

INTRODUCTION

Characteristics of plasmas in the low-latitude topside iono-sphere are subject to many variations. The most important diurnal and seasonal variations result from changes in the aspect angle of the sun. The plasmas are affected directly through local time-varying production rates and indirectly through dynamo coupling with neutral winds [Tarpley, 1970, and references therein]. Further, longitudinal variations arise because the plasma is confined by a magnetic field that is misaligned in relation to the geographic spin axis and offset from the center of the earth. Finally, the motions of equatorial plasmas are affected by latitudinally remote auroral substorms through the requirements of ionospheric current closure [Nopper and Carovillano, 1978; Rastogi, 1977] and temporal variations in the magnetospheric electric field [Kelley et al., 1979].

During the hours of sunlight, plasma is produced by solar radiations, mostly in the lower ionosphere. To satisfy the requirements of pressure balance, some of this plasma diffuses along magnetic field lines into the topside ionosphere and protonosphere [Banks et al., 1976]. The low-latitude plasma moves across magnetic field lines under the influence of dynamo and other electric fields. In the quiet time equatorial ionosphere the electric field E is directed eastward during the day and westward at night [Woodman, 1970]. During magneti-cally disturbed times, E may be reversed in direction [Fejer et al., 1976; Rastogi and Woodman, 1976]. In the postsunset sector, recombination processes deplete the E and bottomside F layers. Plasma moves earthward from the plasmasphere to maintain the nighttime ionosphere. Equatorial plasma also drifts earthward across magnetic field lines under the influence of westward E fields [Woodman, 1970]. This leads to a further depletion of the low-latitude ionosphere as plasma is con-vected down to altitudes of significant recombination. Con-versely, during periods of magnetic activity the eastward E field during the predawn hours should lead to enhanced night-time densities in the equatorial topside ionosphere.

Because the topside ionosphere is mostly made up of plasma produced at other locations, its instantaneous structure de-pends critically on the prehistory of its source regions. Signifi-cantly different prehistories are experienced in the two hemi-

spheres near the times of the solstices. Different periods of exposure to sunlight result in more plasma being produced in and more heat being added to the summer hemisphere. This leads to a considerable transfer of energy and particles along magnetic field lines from the summer to the winter ionosphere [Rishbeth et al., 1977; Bailey et al., 1978]. Near the times of the equinox the energy inputs to the conjugate ionospheres should be comparable. Thus there should be little net transfer of energy and/or particles at the equinoxes. The seasonal varia-tions of net energy transfer between the conjugate ionospheres can be expected to produce different plasma density distribu-tions in the low-latitude topside ionosphere near the solstices and equinoxes.

Models have been developed for diurnal variations of the quiet time equatorial ionosphere that include $E \times B$ drifts [Hanson and Moffett, 1966], coupling with neutral winds [Ster-ling et al., 1969], and a realistic magnetic field [Anderson, 1973a, b]. In agreement with observations these models suc-cessfully describe such F_2 region properties as the day to night density differences and the so-called equatorial anomaly. This anomaly appears as higher plasma densities near the F_2 peak at $\pm 16°$ dip latitude than at the magnetic equator [Appleton, 1946]. In local time it extends from ~0900 through the after-noon hours. Recently, a great deal of effort has also been spent in developing models to describe the dynamic coupling be-tween the ionosphere and protonosphere [Marubashi and Grebowsky, 1976; Bailey et al., 1977a, b, 1978; Murphy et al, 1976]. The model calculations were made for the $L = 3$ flux tube. Although many of the physical processes for the $L = 3$ and $L = 1.1$ (the concern of this paper) flux tubes are com-parable, the time scales for filling the flux tubes are not. The $L = 3$ tube takes several days to refill, while the $L = 1.1$ tube refills in a few hours.

The purpose of this paper is to present a set of ion density measurements taken by means of a planar probe on board the Defense Meteorological Satellite Program (DMSP) satellite F2. The satellite is in a nearly sun synchronous circular orbit at an altitude of 840 km. At the time of the 1977 autumnal equinox the orbit centered on the 0700–1900 LT meridian and was slowly precessing toward later local times. The ion detec-tor is a gridded circular aperture (2.54-cm diameter) planar sensor that is mounted on a 1.5-m boom. The sensor mounting is such that the aperture always faces the direction of satellite motion [Smiddy et al., 1978]. The primary function of this sensor is to provide plasma densities and scale heights on a continuous basis at a constant altitude near the dawn-dusk meridian.

In the following section, high–time resolution (7 measure-

[1] Physics Department, Boston College, Chestnut Hill, Massachu-setts 02167.

[2] Space Physics Division, Air Force Geophysical Laboratory, Han-scom Air Force Base, Massachusetts 01731.

[3] Regis College Research Center, Weston, Massachusetts 02193.

4201

ments/s) ion density measurements are presented from the dawn sector low-latitude ionosphere. Large density gradients, reported here for the first time, are regularly encountered in the vicinity of the magnetic equator during magnetically quiet periods at the times of the equinoxes. Modulations of this feature are found during magnetically active periods. In the discussion section it is argued, on the basis of their longitudinal characteristics, that the equatorial plasma gradients result from the satellite's passing through a diffusion front associated with dayside flux tube refilling. This process is modulated during active periods by predawn eastward electric fields that raise the height of the F layer peak and give rise to occasional spread F irregularities.

EXPERIMENTAL OBSERVATIONS

The data used in this section are presented in Figures 1, 3, and 4 and consist of ion density measurements taken within 10 min of the satellite's crossing of the magnetic equator in the dawn sector. Because the orbital period is 1.7 hours (~103 min), observations are divided into 14 universal time elements. Due to the sun synchronous nature of the orbit, this defines 14 longitudinal bins with widths between 10° and 15°.

To establish a quiet time base for the postsunrise lowlatitude topside ionosphere, we have plotted ion density measurements as functions of universal time from 42 consecutive crossings of the magnetic equator in Figure 1. Depending on the longitude the 10-min intervals correspond to between 30° and 40° magnetic latitude. The data were taken on September 4, 6, and 7, 1977, which had $\sum Kp = 6-$, 7, and 11, respectively. The universal time longitude bins were assigned according to their values as the satellite crossed the magnetic equator. The satellite was moving northward and toward earlier local times in all cases.

There are three aspects of the data in Figure 1 to which attention is directed.

1. Within any given longitude bin there is a high degree of repeatability in the macrostructure of the plasma density distribution.

2. In all instances there is a sharp density decrease near the magnetic equator.

3. If the amplitude of depletion is taken as the ratio of the interpolated density to the minimum density inside the depletion, then (a) for a given longitude bin the depletion amplitude is nearly constant, (b) for the longitude range 210°–325° the depletion amplitude is <2, and (c) for other longitudes the depletion amplitude is between 3 and 5.

An enlarged plot of density measurements between ±25° geographic latitude during orbit 1344 is given in Figure 2. This is the last orbit of September 7 (Figure 1). The data are plotted as functions of geographic latitude, geographic longitude, magnetic latitude, and magnetic local time. The density decreased slowly from 7×10^4 cm^3 at 25°S to 4×10^4 cm^3 at 8°S and then more rapidly to 9×10^3 cm^3 at 4°N. It rose quickly to 3×10^4 at 25°N. The lower terminal density in the northern hemisphere reflects the satellite's motion to earlier local times.

It is important to note that despite phenomenological similarities the equatorial depletions are not examples of the equatorial anomaly [Appleton, 1946]. The depletions presented here were found near 0700 LT, while the Appleton anomaly is found at later local times.

The density decreases near the magnetic equator are seasonally dependent phenomena. This is illustrated in Figure 3, where we have plotted measurements taken during magnetically quiet periods near the December 1977 solstice and the March 1978 equinox. No large-amplitude depletions were found near the magnetic equator in the solstice data. They were observed again with similar morphology in the March equinox data. The largest depletion amplitudes were found to occur in the same longitude bins as they did in September. However, the amplitudes were significantly smaller than they had been in September. It is important to note that between September and March the orbit precessed 24 min toward later local times. These data suggest that the phenomenon is restricted in both season and local time, and this limited occurrence probably explains why the phenomenon has not been reported previously.

The effects of severe magnetic activity on the low-latitude topside ionosphere are illustrated in Figure 4. The measurements come from two extremely disturbed days and one quieting day. A magnetic storm began at about midday on September 19, when Kp rose from 1 to 4 to 6. In the previous 18 hours, $Kp \leq 1+$. $\sum Kp$ for the days of September 19 through 25, 1977, were 30, 38+, 41+, 42+, 25+, 21+, and 19. Extremely quiet conditions did not return until September 29 and 30. Unfortunately, DMSP data were not available for these days.

Data from the disturbed days of September 21 and 22 show none of the repeating patterns found in the September 5–7 period (Figure 1). Some examples of near-equatorial density decreases can be found on these days, but with little consistency. In the 13.6–18.7 UT period of September 21 the plasma density had a highly irregular macrostructure. Most likely, these are examples of storm time spread F plasma bubbles [Fejer et al., 1976] that have moved into the topside layer [Burke et al., 1979; Burke, 1979]. As the storm abated, the density depletions reappeared as a consistent feature of the low-latitude observations. The longitudinal distribution of depletion amplitudes on September 25 (Figure 4) was quite similar to that found during the quiet period (Figure 1). It is interesting to note that at the latitudes of the plasma depletions (September 5, 6, 7, and 25) the densities were generally higher during the storm (September 21 and 22). This is prob-
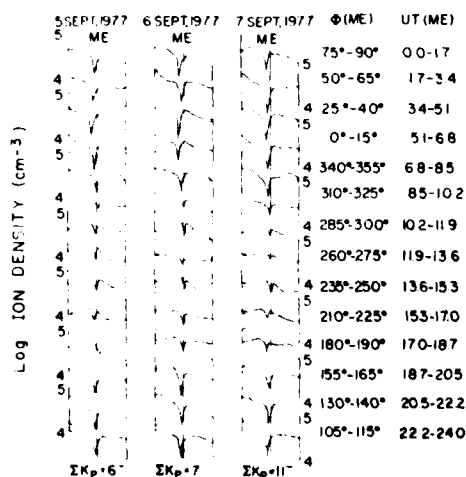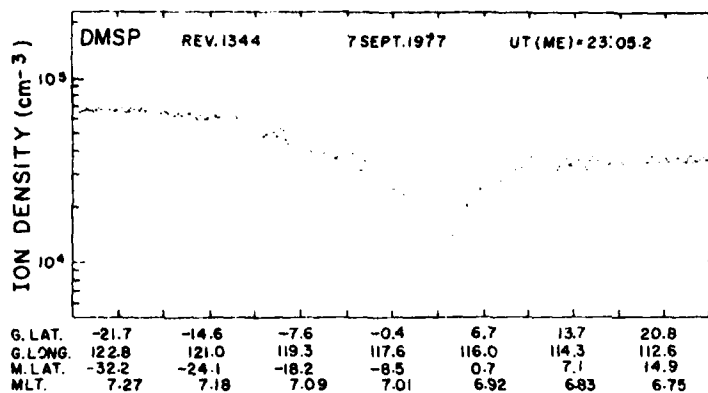

Fig. 1. Ion density as a function of universal time for three consecutive quiet days in September 1977. Twenty minutes of data centered on the dawn sector crossing of the magnetic equator (ME) are given in each instance. Each day is divided into 14 elements of 1.7-hour duration according to the universal time at which the satellite crossed the ME. Longitude bins for the ME crossing are also listed. $\sum Kp$ for each day is given at the bottom of the figure.

G. LAT.	-21.7	-14.6	-7.6	-0.4	6.7	13.7	20.8
G. LONG.	122.8	121.0	119.3	117.6	116.0	114.3	112.6
M. LAT.	-32.2	-24.1	-18.2	-8.5	0.7	7.1	14.9
MLT.	7.27	7.18	7.09	7.01	6.92	6.83	6.75

Fig. 2. Ion density as a function of geographic latitude, geographic longitude, magnetic latitude, and magnetic local time for DMSP orbit 1344. The range of geographic latitudes is 25°S to 25°N. This orbit is the last example given for September 7 in Figure 1.

ably an effect of the predawn eastward electric field, observed during magnetically disturbed periods [Fejer et al. 1976], causing the equatorial F layer to rise. Since the density decreases with altitude in the topside layer, a rising motion would increase the observed local density. At latitudes away from those of the depletions, no consistent pattern could be found.

DISCUSSION

Despite the fact that the large density decreases observed by DMSP at low latitudes have not been reported previously, their occurrence is not totally unexpected. That they have not been observed before reflects their limited range of occurrence in season, local time, and possibly altitude. Their existence and spatial-temporal characteristics are quite consistent with our current understanding of the dynamical nature of the ionosphere-protonosphere system [Banks et al., 1976]. In the present case, field lines crossing the magnetic equator at high altitudes in the topside ionosphere are analogous to those closing in the protonosphere.

The dynamical model of the ionosphere outlined in the introduction to this paper suggests that near the dawn termi-

nator the ionosphere will be in transition from a nighttime to a daytime configuration. Some of the plasma produced in the postsunrise lower ionosphere moves along magnetic field lines into the low-density nighttime ionosphere. For reasons discussed below, we treat cross-field plasma transport as being a much slower process than that along field lines. The motion of the jth ionic plasma species is governed by the continuity equation

$$\frac{\partial n_j}{\partial t} + \frac{1}{A} \frac{\partial (n_j V_j A)}{\partial s} = P_j - L_j \qquad (1)$$

and the momentum conservation equation

$$\left(\frac{\partial V_j}{\partial s} + V_j \frac{\partial V_j}{\partial s}\right) + \frac{1}{n_j m_j} \frac{\partial p_j}{\partial s} + g_{\shortparallel}$$

$$- \frac{eE}{m_j} = -\sum_k \nu_{jk}(V_j - V_k) \qquad (2)$$

where n_j, V_j, m_j, p_j, P_j, and L_j are the density, the bulk velocity along the magnetic field B, the mass, the thermal pressure, the production, and the loss rate for the jth ionic species, respec-
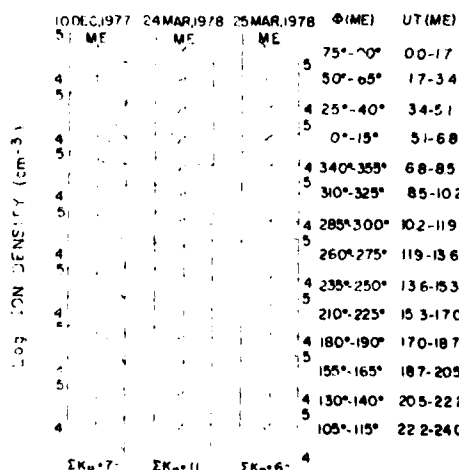

Fig. 3. Ion density measurements for quiet days near the solstice and the spring equinox. The same format as that of Figure 1 is used.
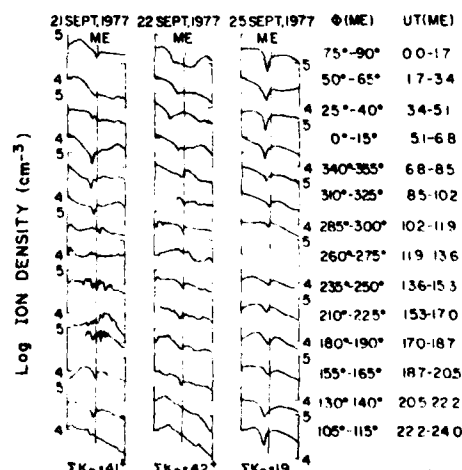

Fig. 4. Ion density measurements for two extremely disturbed days and one quieting day during a magnetic storm at the time of the autumnal equinox. The same format as that of Figure 1 is used.

tively. A is the cross-sectional area of the magnetic flux tube; g and E are the components of the gravitational acceleration and of the electric field along **B**, respectively; s is an element of length along **B**; v_{jk} is the collision frequency of the jth species with particles of the kth species; and V_k is the bulk velocity of the kth species along **B**. The momentum conservation for electrons is

$$\frac{1}{n_e}\frac{\partial p_e}{\partial s} + eE = 0 \qquad (3)$$

where n_e and p_e are the electron density and thermal pressure, respectively. This equation can be used to eliminate E from (2).

The two most important ionic species are O^+ and H^+. O^+ is mostly produced by photo-ionization, and H^+ by the charge exchange process $O^+ + H \rightleftharpoons O + H^+$. At an altitude of 840 km, production and recombination processes are negligible. Plasma observed at this altitude has been transported from below. The rate at which plasma can be transported from one region to another is limited by the finite rate at which the source region can replenish itself. The limiting flux F of O^+ out of the ionosphere is 2×10^9 cm^{-2} s^{-1}, and that of H^+ is 10^8 cm^{-2} s^{-1} [Banks and Kockarts, 1973].

Before this model is compared with the data, several reflections on the meaning of the satellite measurements are in order. The rate of change of plasma density measured along the satellite trajectory is

$$\frac{dn}{dt} = \frac{\partial n}{\partial t} + \mathbf{V}_s \cdot \nabla n \qquad (4)$$

where $\mathbf{V}_s$ is the satellite velocity and $n = \sum_j n_j$. The first term represents changes due to time variations in the local plasma density. The second term represents variations due to the satellite's motion across spatial gradients in the plasma density. Both terms contribute to the measured value of dn/dt, but the high degree of repeatability found in the data of Figure 1 indicates that the second term contributes more than the first. That is, the local plasma density is changing on a time scale that is long in comparison with the 1 to 2 min required for t' satellite to cross the depleted region.

The density gradients crossed by DMSP are three-dimensional quantities. The fact that they appear at or near the magnetic equator indicates that the gradients have significant components along **B**. Because of the circular orbit of DMSP, in the magnetic latitude range ±10 the angle between $\mathbf{V}_s$ and **B** is < 20°. If there were no large density gradients along **B**, dn/dt would not be large in this region. Except in the extremely unlikely case that there are compensating gradients in the plasma temperature, this analysis leads to the conclusion that $\partial p/\partial s \neq 0$, where $p = p_e + \sum_j p_j$. In a region where $g \simeq 0$ and v_{jk} is small, such a situation is not stable.

The equations ((1) and (2)) governing the refilling process are highly time dependent, and it is beyond the scope of this paper to provide their solutions. In solving these coupled equations, physical assumptions must be made about the way that refilling is effected. One possible simplifying assumption is that the entire field lines are close to diffusive equilibrium at all times. Diffusion speeds and density distributions for this case, which we refer to as model A, have been calculated by Banks and Kockarts [1973]. A second possibility, model B, is that refilling is accomplished by means of a conjugate pair of 'plasma fronts' of finite width moving upward along magnetic field lines. On the downstream and upstream sides of the front, conditions would be near dayside and nightside equilibrium,

respectively. How refilling is actually accomplished can only be determined on the basis of empirical measurements. The observed depletions are most easily explained by model B in the early stages of the refilling process and by model A in the later stages.

Model B predicts that for some postsunrise local times large-amplitude depletion should be observed by a satellite with a circular polar orbit in the topside ionosphere. Plasma conditions at 840 km depend on the length of time that the source region has been in sunlight. For simplicity we assume equinox conditions and that sunrise occurs along all field lines at a given longitude at approximately the same time. That is, to a first-order approximation we ignore the effects of magnetic declination. This is justified empirically by noting that ion density signatures (Figure 1) do not show a radical transition near a longitude of ~300°, where declination changes from east to west. We also assume that at some time t_0 after sunrise a sufficient amount of plasma has been produced in the F region for a front to form at some altitude h_0 and move upward with some mean velocity V_F.

Figure 5 is a sketch of a plasma front moving along two straight magnetic field lines which intersect the earth at latitudes λ_1 and λ_2, where $\lambda_1 < \lambda_2$. Also shown are the inclinations of the field lines at I_1 and I_2, with $I_2 > I_1$. The distance travelled along the field lines in a time element dt after t_0 is $V_F\,dt$. Since $ds = V_F\,dt = dh\sec I_1$, the altitude of the front near field line 2 is greater than that along line 1. For a limited period of time after sunrise a constant altitude orbit such as that of DMSP would be entirely above the front. Conversely, at much later local times the orbit would be entirely beneath the front. No steep gradients at the magnetic equator should be observed in either case. For some period of time after sunrise, however, the orbit would be below the front at high latitudes but above the front at low latitudes. In these cases the satellite would pass from a daytime to a nighttime and then to a daytime ionosphere as it moved across plasma fronts. Steep density gradients similar to those measured during September 1977 would then be observed.

The longitudinal distribution of depletion amplitudes shown in Figure 1 can be explained in terms of a moving front and the different lengths of field lines at different longitudes. Magnetic field lines crossing the magnetic equator at 840 km correspond to an invariant latitude Λ of 20°. The loci of $\Lambda = 20°$ field lines are plotted in Figure 6 as functions of geographic longitude and latitude. The solid lines represent the feet of the field lines on the surface of the earth, and the dashed lines represent the field lines at an altitude of 300 km [Evans et al., 1969]. Since the source region for the topside ionosphere is the region at or below the F peak, 300 km roughly corresponds to the value of h_0 in Figure 5. We note that magnetic field lines near 120°E are significantly longer than those near 300°E. Plasma fronts moving up magnetic field lines from the northern and southern source regions would therefore meet each other much earlier near 300°E than they would near 120°E. The greatest depletions would be observed at longitudes of the longest field lines where interpenetration of the two fronts is least.

Model B also explains why smaller depletion amplitudes were measured at the 1978 spring equinox. In March 1978 the DMSP orbit had precessed 24 min toward later local times than in September 1977. If it is assumed that other conditions in September and March were similar, then the fronts would have an additional 24 min to move closer together. This results in greater interpenetration of the plasma fronts moving from the northern and southern ends of the field lines. As the fronts

overlap more and more near the magnetic equator, conditions close to diffusive equilibrium would exist all along the field lines. Further changes in density structure along the field lines would take place at a much slower pace than was true in the early postsunrise period. This corresponds to the conditions of model A.

At the solstices the periods of time spent in sunlight at the northern and the southern end of a field line are very different. Particles and energy are transported along B from the summer to the winter hemisphere. This condition is very different from that of the equinoxes. In the local time sector sampled by DMSP the model A description seems most apt. Detailed calculations of equatorial flux tube refilling lie well beyond the scope of this paper. The observations reported here could be compared with the predictions of models such as that developed by Bailey and co-workers if the model were changed from $L = 3$ to $L = 1.1$ conditions.

It is possible to set limits on the velocity of the plasma front. Several arguments may be adduced. From the repeatability of the plasma variations shown in Figure 1 it was argued that the density changes occur on time scales less than the 1 to 2 min required for DMSP to pass through the depleted regions. From the continuity equation it can be argued that $V_s \gg V_F$. That is, V_F is significantly less than 7.55 km/s. A second estimate can be made by assuming that near the magnetic equator the plasma is expanding freely. At altitudes < 1000 km this expansion is subsonic [Banks and Kockarts, 1973]. If the main ionic species is O^+ and has a temperature of 1000°K, then $V_F \leq 1$ km/s. A third argument can be based on the concept of a limiting flux. With O^+ as the main species, $nV_F < F = 2 \times 10^9$ cm^2 s^1. The measured ion densities outside the depleted regions are several times 10^4 cm^3. This again places an upper limit of ~1 km/s on V_F. These velocities are much greater than the 20- to 50-m/s cross-field line drifts reported by Woodman [1970] in the postsunrise period. It was for this reason that cross-field line filling was ignored in this analysis.

Finally, it should be noted that fast particles in the Maxwellian tails of the plasma distributions on the downstream sides of the fronts can move along magnetic field lines at speeds significantly greater than the speed of the front. In crossing the 'nighttime' portion of the field lines, they would lose some energy and raise the temperature of the plasma on the upward sides of the front. However, they would have little
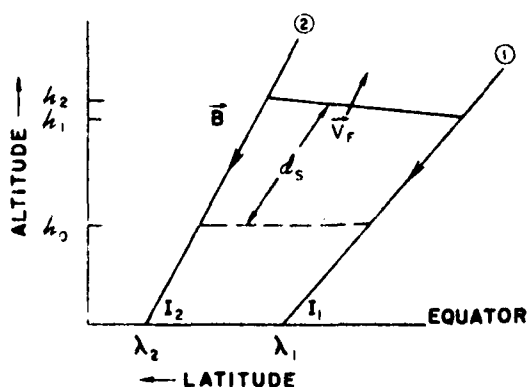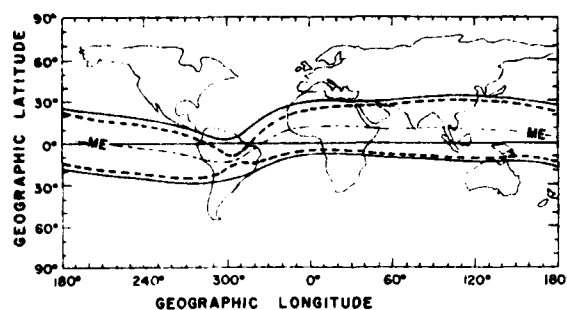

Fig. 6. Plot of loci of invariant latitude 20° field lines at altitudes of 0 km (solid line) and 300 km (dashed lines). The magnetic equator (ME) projected to the surface of the earth is given for reference.

effect on the density. There are two reasons for this: (1) The number of particles moving along the field lines with speeds significantly greater than the thermal speed is small. (2) Due to the conjugate nature of the fronts, the total net flux across the fronts is very small. For every particle crossing the front in the upward direction a particle of slightly less energy from the conjugate ionosphere crosses it in the downward direction.

SUMMARY AND CONCLUSIONS

In this paper we have reported on ion density measurements by the DMSP satellite in the postsunrise local time sector. At the time of the September 1977 equinox, significant plasma depletions were regularly observed near the magnetic equator during magnetically quiet periods. The amplitudes of the plasma depletions were longitude dependent. At the time of the March 1978 equinox the depletions were again observed but were of lesser amplitude. This was attributed to a 24-min precession of the orbit toward later local times. The equatorial depletions were not observed at the time of the solstice. During magnetically active periods the depletions were not regularly observed. This was attributed to the effects of an eastward predawn electric field raising the altitude of the F layer and occasionally inducing spread F irregularities in the topside ionosphere.

The quiet time equatorial depletions are interpreted in terms of the diurnal refilling of the topside ionosphere [Banks et al., 1976]. It is assumed that in the early stages of the refilling process, plasma recently produced in the lower ionosphere moves as a 'plasma front' into the depleted topside region. Due to different inclinations of field lines, the front reaches an altitude of 840 km at mid-latitudes before it does at the equator. The plasma depletions result from the satellite's crossing fronts that are moving upward from the northern and southern ends of the field line. The velocity of the front is estimated to be < 1 km/s. The longitudinal distribution of depletion amplitudes results from the different lengths that the fronts must travel to reach the magnetic equator.

Fig. 5. The motion of a plasma front along two magnetic field lines of different inclination. The front is assumed to start from the same altitude h at t_0 and to move a distance ds along the magnetic field lines in a time element dt.

END
DATE
FILMED

DTIC

MICROCOPY RESOLUTION TEST CHART

NATIONAL BUREAU OF STANDARDS-1963-A

REFERENCES

Anderson, D. N., A theoretical study of the ionospheric F region equatorial anomaly, I, Theory, *Planet. Space Sci.*, *21*, 409, 1973a.

Anderson, D. N., A theoretical study of the ionospheric F region equatorial anomaly, II, Results in the American and Asian sectors, *Planet. Space Sci.*, *21*, 421, 1973b.

Appleton, E. V., Two anomalies in the ionosphere, *Nature, 157*, 691, 1946.

Banks, P. M., and G. Kockarts, *Aeronomy*, vol. B, pp. 191–214, Academic, New York, 1973.

Banks, P. M., R. W. Schunk, and W. J. Raitt, The topside ionosphere: A region of dynamic transition, *Annu. Rev. Earth Planet. Sci.*, *4*, 381, 1976.

Bailey, G. J., R. J. Moffett, and J. A. Murphy, A theoretical study of nighttime field-aligned O^+ and H^+ fluxes in a mid-latitude magnetic field tube at equinox under sunspot minimum conditions, *J. Atmos. Terr. Phys.*, *39*, 105, 1977a.

Bailey, G. J., R. J. Moffett, and J. A. Murphy, Relative flow of H^+ and O^+ in the topside ionosphere at mid-latitudes, *Planet. Space Sci.*, *25*, 967, 1977b.

Bailey G. J., R. J. Moffett, and J. A. Murphy, Interhemispheric flow of thermal plasma in a closed magnetic flux tube at mid-latitudes under sunspot minimum conditions, *Planet. Space Sci.*, *26*, 753, 1978.

Burke, W. J., Plasma bubbles near the dawn terminator in the topside ionosphere, *Planet. Space Sci.*, in press, 1979.

Burke, W. J., D. E. Donatelli, R. C. Sagalyn, and M. C. Kelley, Observations of low-density regions at high altitudes in the topside equatorial ionosphere and their interpretation in terms of equatorial spread F, *Planet. Space Sci.*, in press, 1979.

Evans, J. E., L. L. Newkirk, and B. M. McCormac, North polar, south polar world maps and tables of invariant magnetic coordinates for six altitudes: 0, 100, 300, 600, 1000 and 3000 km, *DASA 2347*, Def. At. Support Agency, 1969.

Fejer, B. G., D. T. Farley, B. B. Balsley, and R. F. Woodman, Electric field coupling between high and low latitudes, *J. Geophys. Res.*, *81*, 4621, 1976.

Hanson, W. B., and R. J. Moffett, Ionization transport in the equa-

torial F region, *J. Geophys. Res.*, *71*, 5559, 1966.

Kelley, M. C., B. G. Fejer, and C. A. Gonzales, An explanation for anomalous equatorial ionospheric electric fields associated with a northward turning of the interplanetary magnetic field, *Geophys. Res. Lett.*, *6*, 301, 1979.

Marubashi, K., and J. M. Grebowsky, A model study of diurnal behavior of ionosphere and protonosphere coupling, *J. Geophys. Res.*, *81*, 1700, 1976.

Murphy, J. A., G. J. Bailey, and R. J. Moffett, Calculated daily variations of O^+ H^+ at mid-latitudes, I, Protonospheric replenishment and F region behavior at sunspot minimum, *J. Atmos. Terr. Phys.*, *38*, 351, 1976.

Nopper, R. W., and R. L. Carovillano, Polar equatorial coupling during magnetically active periods, *Geophys. Res. Lett.*, *5*, 699, 1978.

Rastogi, R. G., Coupling between equatorial and auroral ionospheres during polar substorms, *Proc. Ind. Acad. Sci.*, *86A*, 409, 1977.

Rastogi, R. G., and R. F. Woodman, Spread F in equatorial iono-grams associated with reversal of horizontal F region electric field, *Ann. Geophys.*, *34*, 31, 1978.

Rishbeth, H., T. E. Van Zandt, and W. B. Hanson, Ion temperature troughs in the equatorial topside ionosphere, *Planet. Space Sci.*, *25*, 629, 1977.

Smiddy, M., et al., The topside ionosphere plasma monitor (SSIE) for the block 5D/flight 2 DMSP satellite, *Tech. Rep. 78-0071*, Air Force Geophys. Lab., Hanscom Air Force Base, Mass., 1978.

Sterling, D. L., W. B. Hanson, R. J. Moffett, and R. G. Baxter, Influence of electromagnetic drifts and neutral air winds on some features of the F_2 region, *Radio Sci.*, *4*, 1005, 1969.

Tarpley, J. D., The ionospheric wind dynamo, 2, Solar tides, *Planet. Space Sci.*, *18*, 1091, 1970.

Woodman, R. F., Vertical drift velocities and east-west electric fields at the magnetic equator, *J. Geophys. Res.*, *75*, 6249, 1970.

The Longitudinal Distribution of Equatorial Spread *F* Plasma Bubbles in the Topside Ionosphere

WILLIAM J. BURKE

Physics Department, Boston College, Chestnut Hill, Massachusetts 02167

DELIA E. DONATELLI

Regis College, Weston, Massachusetts 02193

RITA C. SAGALYN

Air Force Geophysics Laboratory, Hanscom Air Force Base, Massachusetts 01731

Observations from a thermal ion probe on board a Defense Meteorological Satellite Program satellite have been used to study the longitudinal distribution of equatorial spread *F* occurrence in the topside ionosphere. The data were taken in the postsunrise local time sector during the September 1977 magnetic storm. In agreement with previous studies of the longitudinal variability of evening sector spread *F*, a higher frequency of occurrence was found in the American than in the Asian sector. No example of spread *F* was observed in the Atlantic-African sector. The results were interpreted using a quasi-three-dimensional model of the collisional Rayleigh-Taylor instability. It is shown that for the same initial ionospheric conditions and the same initial depletion at the magnetic equator, large plasma bubbles are more apt to reach the topside at longitudes of the American sector than at longitudes of the Asian sector.

INTRODUCTION

Recently, interest has focused on plasma density irregularities in the nighttime equatorial *F* layer. The irregularities have been studied using remote sensing and in situ measuring techniques. The remote measurements use radar backscatter [*Woodman and La Hoz*, 1976] and scintillations in radio signals. Direct measurements have been of plasma density 'biteouts' that have been found in the bottomside of the *F* layer [*Kelley et al.*, 1976], near the peak of the *F* layer [*McClure et al.*, 1977; *Basu et al.*, 1976], and in the topside region [*Dyson and Benson*, 1978; *Burke et al.*, 1979a]. The biteouts have been shown to have average vertical drift speeds of 150 m/s. These plasma biteouts, which are also referred to as spread *F* or plasma bubbles, are capable of producing observed radio scintillations [*Basu et al.*, 1976]. It is not clear that spread *F* is the only source of nighttime scintillation.

There is a growing consensus that equatorial spread *F* begins on the bottomside of the *F* layer as a collisional, Rayleigh-Taylor type instability [*Balsley et al.*, 1972]. The fact that spread *F* bubbles are found well above the peak of the *F* layer cannot be explained by the linear growth, Rayleigh-Taylor mechanism. For this reason the evolution of two-dimensional plasma depletions in the nonlinear regime have been investigated using numerical [*Scannapieco and Ossakow*, 1976; *Ossakow et al.*, 1979] and analytical [*Ott*, 1978] methods. A quasi-three-dimensional model for the linear growth of Rayleigh-Taylor waves has been developed by G. Haerendel (unpublished manuscript, 1974) using earth-centered dipolar magnetic geometry. Recent calculations by *Anderson and Haerendel* [1979] and *Ossakow et al.* [1979] have stressed the roles of the ambient electric field and the height of the *F* peak, respectively, in determining whether a bottomside depletion can rise into the topside layer. Each of these models offers valuable physical insights into various aspects of spread *F*. Yet insofar as they rely on simplifying assumptions such as

straight line or dipolar magnetic geometry, they fail to model actual physical situations. For example, none of these models, without further assumptions, could predict that bubbles would be found in the topside much more frequently in one longitudinal sector than in another.

The longitudinal variability of equatorial *F* region irregularities at altitudes of ⩾400 km were studied systematically by *Basu et al.* [1976], using measurements from the Ogo 6 satellite. Their study showed that a >60% occurrence frequency for irregularities capable for producing ⩾4.5-dB scintillations was confined to the 95°W to 20°E longitude sector. A secondary maximum with >40% occurrence frequency was found over the central Pacific Ocean. That is, large-amplitude irregularities are much more apt to be found in the American-Atlantic and the central Pacific longitude sectors than in the Asian sector. A similar longitudinal distribution of spread *F* plasma bubbles was observed by means of Isis 1 instrumentation in the topside ionosphere [*Burke et al.*, 1979a]. Simultaneous measurements by the topside sounder on Isis confirmed that the plasma depletions extended along entire tubes of magnetic flux [*Dyson and Benson*, 1978]. Both the Ogo 6 and the Isis results were obtained in the evening sector under relatively quiet magnetic conditions, during November 1969 to January 1970. The distribution of quiet time *F* region irregularities has a seasonal dependence that has been reviewed recently by *Aarons* [1977]. At Huancayo, Peru, the percentage occurrence for 137-MHz scintillation indices of >60 has a broad maximum during the summer (southern hemisphere) months. The percentage occurrence during the winter months was near zero. A similar seasonal distribution was found at Kwajalein in the central Pacific. In the Indian sector, bottomside spread *F* has been found to be largely independent of season (R. G. Rastogi, private communication, 1979).

In this brief report we present a series of measurements taken by means of a planar ion sensor on a Defense Meteorological Satellite Program (DMSP) satellite in the postsunrise local time sector at low latitudes during a magnetic storm. It is

1335

188

recognized that while evening section spread F is a quiet time phenomenon, morning sector spread F appears during disturbed periods [Bowman, 1978]. However, both varieties are associated with sharp density gradients on the bottomside of the F layer and with eastward directed electric fields in the equatorial ionosphere [Fejer et al., 1976; Rastogi and Woodman, 1978; Kelley et al., 1979]. Theoretical calculations by Burke [1979] suggest that spread F plasma bubbles that are generated in the presunrise hours and pass into the topside ionosphere should be observable for several hours after the tube of flux on which they occur passes into sunlight.

The satellite is described and the measurements are presented in the following section. The theory of spread F irregularities is reviewed briefly in the discussion section. The three-dimensional theory of Rayleigh-Taylor turbulence [G. Haerendel, 1979] is extended, in a semiquantitative way, to realistic magnetic field conditions. In agreement with observations the model predicts that topside spread F is more apt to be observed at longitudes of the American sector than at longitudes of the Asian sector.

EXPERIMENT AND OBSERVATIONS

Ion density measurements were taken by means of a planar probe on board a DMSP satellite. The satellite is in a nearly sun-synchronous circular orbit at an altitude at 840 km with an orbital inclination of 98.7°. At the time of the 1977 autumnal equinox the orbit centered on the 0700-1900 local time meridian. The ion detector is a gridded, circular aperture (2.54-cm diameter) planar sensor that is mounted on a 0.75-m boom. The sensor is mounted so that it always faces in the direction of the satellite velocity. Ion density measurements are taken at a rate of 7 per second. A complete description of the instrument and the method by which the data are reduced is given by Smiddy et al. [1978].

Ion density measurements taken near the magnetic equator, in the postsunrise sector, during 91 consecutive orbits of DMSP between September 19 and 25, 1977, have been examined for evidence of topside spread F irregularities. At this time the satellite was near the 0700 local time meridian. A plot of the hourly average of Dst presented in Figure 1 shows that the period was marked by a magnetic storm. Although Dst is a measure of the intensity of the symmetric ring current, it is the only presently available world wide index of magnetic activity other than Kp. The storm had a sudden-commencement at 1140 UT on September 19. Several ring current injections (negative slope) and recovery (positive slope) cycles are found

before a general recovery began late on September 23. The intensity and duration of the magnetic activity suggest that conditions required for the reversal of the predawn, low-latitude electric field and the onset of postmidnight equatorial spread F [Gonzales et al., 1979] were probably fulfilled during much of the September 20-23 period. The asterisks at the top of Figure 1 indicate times when large-amplitude irregularities were detected in the DMSP measurements.

Before considering an example of topside spread F irregularities some comments on selection criteria are in order. Quiet time DMSP observations at low latitude and near 0700 LT under equinox conditions have been discussed by Burke et al. [1979b]. Plasma depletions with highly repeatable variation characteristics were regularly found at or near the magnetic equator. In the Asian-Pacific longitude sector the depletions were by factors of between 3 and 5 relative to the unperturbed density. In the American-Atlantic longitude sector the depletion fractions were less than 2. These quiet time depletions are not due to spread F. Rather, they have been interpreted as resulting from the satellite passing through plasma fronts moving up magnetic field lines from the conjugate ionospheres. These fronts are associated with the diurnal process of flux tube refilling [Banks and Kockarts, 1973]. The different depletion amplitudes at different longitudes reflected the varying degree to which flux tubes were refilled. Refilling was most complete at longitudes of the American sector and least complete in the Asian sector. This diurnal process is operative to some degree independently of geomagnetic conditions and must be accounted for in looking for spread F irregularities. Thus an event was classified as a topside spread F irregularity only if several rapid amplitude fluctuations greater than a factor of 2 were observed in various longitude bins near the magnetic equator and at latitudes different from those of the quiet time depletions.

An example of topside irregularities satisfying these criteria is given in Figure 2, where ion density is plotted as a function of geographic latitude and longitude, magnetic latitude, and magnetic local time. During DMSP revolution 1523 the satellite crossed the magnetic equator (ME) at 1425.5 UT on September 20 at a longitude of 251°. Between 30°S and 12°S the density was smoothly varying with a mean value of 6×10^4 cm^{-3}. At 12°S the density decreased abruptly. A region of significant turbulence extended to 6°N, where the ion density again varied smoothly. During the period September 19-25 there were 10 cases that satisfied our selection criteria: four, four, and two cases on September 20, 21, and 22, respec-
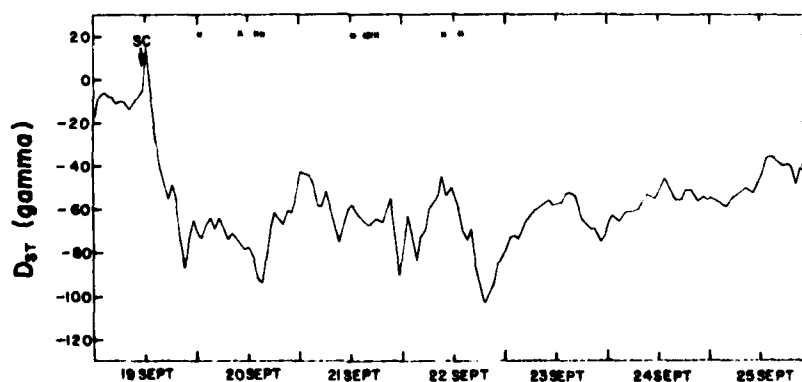

Fig. 1.   Dst for the period September 19-25. The beginning of the storm is marked SC. Asterisks at the top of the figure indicate times when spread F irregularities were observed by the DMSP satellite.

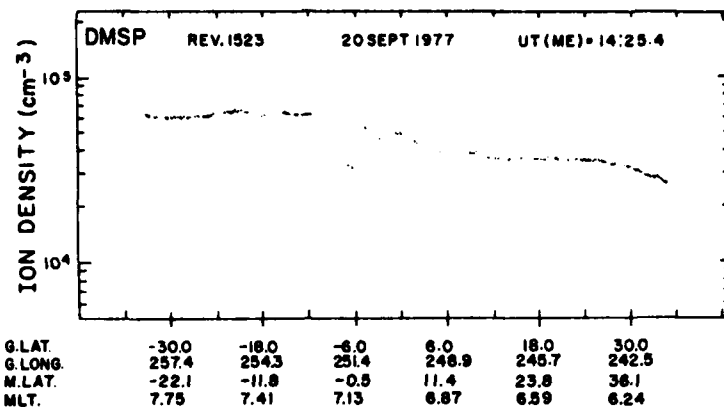| G.LAT.	-30.0	-18.0	-6.0	6.0	18.0	30.0
G.LONG.	257.4	254.3	251.4	248.9	245.7	242.5
M.LAT.	-22.1	-11.8	-0.5	11.4	23.8	36.1
MLT.	7.75	7.41	7.13	6.87	6.59	6.24

Fig. 2. An example of equatorial spread F observed near 0700 LT at 840 km. Ion density is plotted as a function of geographic latitude and longitude, magnetic latitude, and magnetic local time.

tively. In all of the orbits between the beginning of the main phase of the storm through September 23 the measured densities, at the latitude at the quiet time depletions, were raised in relation to their quiet time values [cf. *Burke et al.,* 1979b, Figure 4]. This is consistent with an eastward electric field at low latitudes during the predawn hours which causes the F layer to drift upwards. Since the density decreases with altitude in the topside ionosphere, an upward drift causes the density to increase at 840 km.

The longitudinal distribution of the 10 cases of topside irregularities is given in Figure 3. Here we have plotted the position of the magnetic equator and the longitudes at which topside spread F was observed by DMSP (crosses). Six cases come from the American sector, three from the central Pacific, and one from central Asia. The American and central Pacific sector results agree with results from Ogo 6 [*Basu et al.,* 1976]. The DMSP observations by themselves do not provide a statistical basis for demonstrating longitudinal differences in the occurrence of topside spread F. Insofar as evening and morning sector spread F arise from common physical processes, they confirm the general correctness of the previously reported distribution. There is, however, one significant difference from previous results. In both the Ogo 6 and Isis observations, evening sector, large-amplitude irregularities were frequently observed in the Atlantic-African sector. During the September 1977 magnetic storm they were not observed in this longitude sector. Since there were 12 crossings of the magnetic equator between +40° and −40° longitude between September 20 and 23, the lack of observations of topside spread F does not appear to be due merely to statistical fluctuations. We return to this point in the following section.

DISCUSSION

The theory of the development and nonlinear evolution of spread F irregularities has been studied by many investigators using analytic and numerical techniques. The current consensus is that bottomside equatorial spread F results from a collisional Rayleigh-Taylor type instability along sharp density gradients in the bottomside F layer [*Kelley,* 1979]. The equations of motion for ions and electrons in the F layer are

$$-\nabla p_i + ne(E + V \times B) + nmg - nm_i\nu Vi = 0 \qquad (1)$$

and

$$-\nabla p_e - ne(E + V_e \times B) = 0 \qquad (2)$$

where p_i, p_e, V_i, and V_e are the ion and electron pressures and drift velocities, respectively. E and B are the electric and magnetic fields; ν is the ion-neutral collision frequency and g is the acceleration due to gravity. The effects of neutral winds are ignored. The solutions of these equations are subject to the constraint that all currents are divergence free. The electric field can be expressed as

$$E = E_0 + E_i$$

where E_0 is the ionospheric electric field due to E and F layer dynamos or to equatorial closure currents from high latitudes [*Nopper and Carovillano,* 1978]. E_i is the perturbation electric field. *Ott* [1978] has shown that (1) is invariant in form under the transformation

$$g' = g - \nu(E_0 \times B)/B^2$$

and

$$V' = V - (E_0 \times B)/B^2$$

Because spread F depletion are found to be field aligned and the mathematics are more tractable, two-dimensional solutions to the transformed equation (1) are generally sought. Following standard procedures, perturbed quantities are represented as being proportional to $e^{-i(\omega+i\gamma)t}$. The linear growth rate for what we will refer to as a generalized, collisional Rayleigh-Taylor instability is

$$\gamma = \frac{1}{2}(\nu^2 + 4K \cdot g')^{1/2} - \frac{1}{2}\nu \simeq \frac{K \cdot g'}{\nu} = K \cdot \left(\frac{g}{\nu} - \frac{E_0 \times B}{B^2}\right) \qquad (3)$$
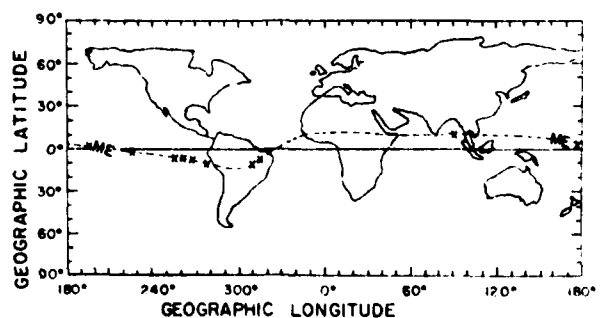

Fig. 3. The longitudes at the magnetic equator of spread F observed at 840 km during the September 1977 storm.

190

where $K = (1/n)\nabla n$. The word 'generalized' has been added to allow for the inclusion of the $E_0 \times B$ drift. On the bottomside of the nighttime F layer ∇n and g are oppositely directed and waves can grow. A zero-order electric field can also cause the growth of irregularities via the $E \times B$ instability. This may be the most important source of irregularity structure just after sunset when the F region rises most rapidly [Anderson and Haerendel, 1979]. If E_0 has an eastward (westward) component it assists (inhibits) the growth of bottomside irregularities. Thus the change of the zonal component of E_0 from west to east in the predawn local time sector during magnetically disturbed times [Fejer et al., 1976; Rastogi and Woodman, 1978; Kelley et al., 1979] is believed to be responsible for spread F at these times. If the effects of ion-neutral recombinations are included in the continuity equation, then the linear growth rate becomes

$$\gamma = K \cdot \left(\frac{g}{\nu} - \frac{E_0 \times B}{B^2}\right) - \nu_R$$

where ν_R is the ion-neutral recombination rate [Ossakow et al., 1979]. The negative sign of ν_R indicates that recombinations tend to damp linear wave growth. The dependence of the growth of bottomside disturbances on the height of the F layer peak reflects the exponential decrease of ν_R with altitude [Ossakow et al., 1979, Figure 2].

It is not entirely clear that topside spread F evolves directly from bottomside spread F. Röttger [1973] and Klostermeyer [1978] have presented experimental and theoretical evidence for the important role of gravity waves in the development of equatorial spread F. In a recent review of current research, Kelley [1979] has concluded that even if gravity waves play an important part in seeding spread F, the topside structures develop their internal electric fields through the nonlinear (generalized) Rayleigh-Taylor process. In the remainder of this brief report we are primarily concerned with the development of finite perturbations independent of their origin. It should be noted, however, that some of the seasonal effects may be explained by variations in the tropospheric and stratospheric sources of the seeding gravity waves. Also, the ionospheric dynamo-driven, quiet time postsunset eastward electric field has been found to be weakest at Jicamarca during the winter solstice period [Woodman, 1970], when spread F is most infrequently observed.

The validity of the two-dimensional analysis as a first-order approximation is confirmed by direct observation of topside plasma bubbles as being field aligned [Dyson and Benson, 1978]. The observed, nonuniform longitudinal distribution of topside plasma bubbles indicates that conditions for the growth of bottomside irregularities are more easily satisfied at some longitudes than at others. Within the context of present theory this could be explained by systematic longitudinal variations in (1) the bottomside density gradient, (2) the strength of the east-west electric field, or (3) the altitude of the F peak. Another possibility is that the longitudinal difference of topside bubble occurrence frequency is due to the offset of the earth's magnetic dipole.

G. Haerendel (unpublished manuscript, 1974) pointed out that spread F involves the interchange of entire magnetic tubes of flux. Thus a three-dimensional analysis must include field line integrated densities (N) and Pedersen conductivities (Σ) rather than the values of these quantities at the magnetic equator. Equations were derived using earth-centered dipolar geometry. The growth rate is analogous to (3), with K replaced by

$$K' = (L^3 N R_E)^{-1} \frac{\partial}{\partial L} (L^3 N) \tag{4}$$

where R_E is the radius of the earth and L is the magnetic shell parameter. The L^3 terms are required for the conservation of magnetic flux as flux tubes interchange. Recently, Anderson and Haerendel [1979] have numerically solved the three-dimensional equations. The velocities and integrated densities of plasma bubbles were calculated as functions of time after the initial perturbation. Cases involving different initial altitudes and values of E_0 were studied. A simplified representation of the current conservation equation gave the perturbation electric field as

$$E_1 = \frac{\Sigma_0 E_0}{\Sigma_1} + \frac{egL}{\Omega \Sigma_1} (N_0 - N_1) \tag{5}$$

Subscripts 0 and 1 on Σ and N are used to represent unperturbed and perturbed flux tubes, respectively. Here, g and Ω are the gravitational acceleration and ion cyclotron frequency at the equator on the surface of the earth.

The calculations of Anderson and Haerendel [1979] used an earth-centered magnetic dipole. Thus the possible effects of longitudinal variation in B were suppressed. The dipole center is at a radial distance of 436 km from the center of the earth and at 15.6°N and 150.9°E [Parkinson and Cleary, 1958]. At a given altitude along the magnetic equator, B is stronger in the Asian than in the American sector. The intensity of B as a function of longitude at an altitude of 350 km on the magnetic equator is given in Figure 4. The calculations used the Barraclough internal magnetic field model. B varies between 0.342 G at 100°E and 0.216 G at 310°E. The longitudes at which topside spread F was observed by DMSP (crosses) and Isis 1 (circles) are given for reference. Twenty-five (86%) of the 29 examples are found at longitudes where $B < 0.29$ G at an altitude of 350 km. Note that $B < 0.29$ G in only 62% of the possible 360° of longitude.

The possible effects of the longitudinal variation of B on the evolution of plasma bubbles can be understood by considering an initial depletion in N_0 and Σ_0 that is independent of longitude. After a time increment Δt the depleted flux tube will have risen a vertical distance $E_1 \Delta t / B$. At the new position N_1, Σ_1, N_0, and Σ_0 must be recalculated to determine the new value of E_1. The growth rate of the disturbance depends linearly on the value of ν_R at the new position. However, ν_R decreases exponentially with altitude. As is seen from Figure 4, a disturbance beginning at 350 km with the same initial E_1 rises a distance $E_1 \Delta t / B$ at 310°E that is 1.57 times the corresponding distance at 100°E. Bubbles thus should grow at a faster rate in the American than in the Asian sector. We do not argue that no Asian sector or all American sector disturbances reach the topside ionosphere. This has been shown to depend on the altitudes of the initial disturbance and the peak of the F layer. It also depends on the time available before the evening sector reversal of E_0 or the time before dawn in the morning sector [Burke, 1979a, b]. Rather, for the same initial disturbance and available time, plasma bubbles are more apt to reach the topside in the American than in the Asian sector.

The main features of the Ogo 6, Isis 1, and DMSP observations appear to be in agreement with the model outlined above. The lack of observations of topside spread F irregularities by DMSP in the Atlantic-African longitude sector is at variance with the Ogo 6 and Isis 1 results. It is in agreement with results reported by Koster [1972], who found that ionospheric scintillations anticorrelated with magnetic activity in
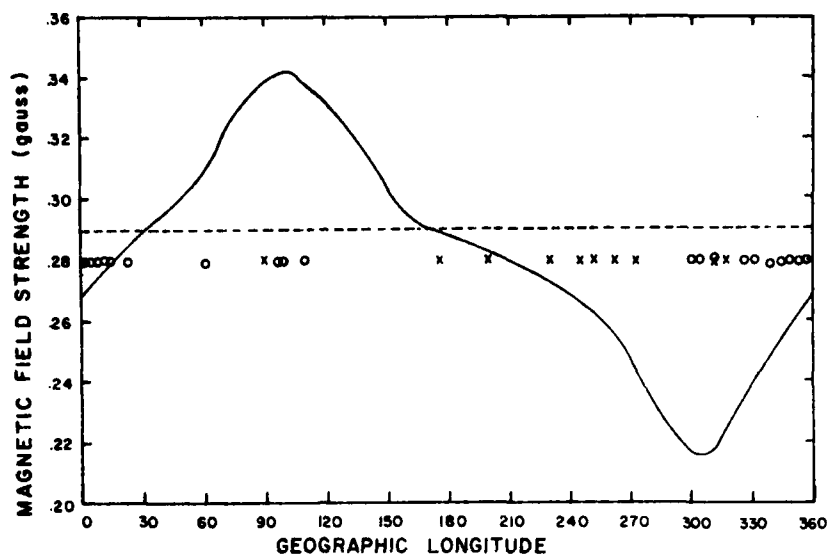
Fig. 4. Strength of the magnetic field at the magnetic equator at 350-km altitude. Crosses and circles give the longitudes at the magnetic equator of topside spread F as observed by DMSP and Isis 1, respectively.

the African sector. This was at variance with measurements taken during the same period at Huancayo, where a positive correlation was found [Aarons, 1977]. Since morningside spread F is associated with an eastward electric field in the predawn hours [Fejer et al., 1976], it may be that strong reversals in E_0 do not occur easily in the African sector. If this were so, the height of the F peak would be lower and ionic recombination would tend to slow Rayleigh-Taylor growth [Ossakow et al., 1979].

The longitudinal distribution of DMSP observations (Figure 3) considered according to the declination at the magnetic equator suggests an explanation for the lack of topside spread F in the Atlantic sector. All of the irregularities were detected at longitudes where the declination is eastward or slightly westward. The declination over the Atlantic is ~20°. At an altitude of 100 km the northern ends of these field lines cross into sunlight about 20 minutes before the southern ends in the equinox period. At sunrise the conductivity of the E region rises dramatically. This would cause E_1 to discharge through the northern ionosphere. In this case the bubble would maintain itself but would cease to rise in altitude. Bubbles formed in this longitude sector would have significantly less time to reach an altitude of 840 km than similar bubbles in the American sector. Also, a seed mechanism, such as gravity waves, is necessary to initiate the process, and the spatial resonance mechanism for gravity waves depends on magnetic declination.

SUMMARY AND CONCLUSIONS

In this brief report we have extended previous studies of the longitudinal distribution of large-scale irregularities in the equatorial topside ionosphere to include observations at 840 km in the postsunrise sector. The observations were made during a magnetic storm under equinox conditions. In agreement with previously reported results from the evening sector, topside spread F was frequently observed in the American longitude sector but not in the Asian sector. Unlike previous topside studies no examples were found in the Atlantic-African sector. It is consistent with ionospheric scintillations reported by Koster [1972]. The difference may be explained by

the nondevelopment of strong E_0 reversals in the African sector during substorms or by declination effects.

Longitudinal variations in frequency of occurrence of topside spread F could be explained by invoking longitudinally systematic variation in bottomside gradients, east-west electric fields, or the altitudes of the F peak. Here we have examined the possible effects of the offset of the earth's magnetic dipole on the linear development of equatorial spread F. For the same initial plasma conditions and perturbation electric field (E_1), plasma depletions rise more quickly in regions of weakest magnetic field. The cumulative damping effects of ionic recombination, which decreases exponentially with altitude, should be less in the American (weak field) than in the Asian (strong field) sector. There is a finite amount of time available for bubbles to reach the topside before the evening reversal of the zonal electric field or the dawn increase of ionospheric conductivity. Thus plasma bubbles are more likely to be found in the topside ionosphere of the American sector than in that of the Asian sector.

REFERENCES

Aarons, J., Equatorial scintillations: A review, IEEE Trans. Antennas Propagat., 25, 729, 1977.
Anderson, D. N., and G. Haerendel, The motion of depleted plasma regions in the equatorial ionosphere, J. Geophys. Res., 84, 4251, 1979.
Balsley, B. B., G. Haerendel, and G. Greenwald, Equatorial spread F: Recent observations and a new interpretation, J. Geophys. Res., 77, 5625, 1972.
Banks, P. M., and G. Kockarts, Aeronomy, B, pp. 191-214, Academic, New York, 1973.
Basu, S., S. Basu, and B. K. Khan, Model of equatorial scintillations from in-situ measurements, Radio Sci., 11, 821, 1976.

Bowman, G. G., A relationship between polar magnetic substorms, ionospheric height rises and the occurrence of spread F, *J. Atmos. Terr. Phys. 40*, 713, 1978.

Burke, W. J., Plasma bubbles near the dawn terminator in the topside ionosphere, *Planet. Space Sci., 27*, 1187, 1979.

Burke, W. J., D. E. Donatelli, R. C. Sagalyn, and M. C. Kelley, Observations of low density regions at high altitudes in the topside equatorial ionosphere and their interpretation in terms of equatorial spread F, *Planet. Space Sci., 27*, 593, 1979a.

Burke, W. J., R. C. Sagalyn, R. G. Rastogi, M. Ahmed, F. J. Rich, D. E. Donatelli, and P. J. L. Wildman, Postsunrise refilling of the low-latitude topside ionosphere, *J. Geophys. Res., 84*, 4201, 1979b.

Dyson, P. L., and R. R. Benson, Topside sounder observations of equatorial bubbles, *Geophys. Res. Lett., 5*, 795, 1978.

Fejer, B. G., D. T. Farley, B. B. Balsley, and R. F. Woodman, Radar studies of anomalous reversals in the equatorial ionosphere, *J. Geophys. Res., 81*, 4621, 1976.

Gonzales, C. A., M. C. Kelley, B. G. Fejer, J. Vickrey, and R. F. Woodman, Equatorial electric fields during magnetically disturbed conditions, 2, Implications of simultaneous auroral and equatorial measurements, *J. Geophys. Res., 84*, 5803, 1979.

Kelley, M. C., Equatorial spread F: A review of experimental results, in *Astrophysics and Space Science Library*, D. Reidel, Hingham, Mass., (in press) 1979.

Kelley, M. C., G. Haerendel, H. Klapper, A. Valenzuela, B. B. Balsley, C. A. Carter, W. L. Ecklund, C. W. Carlson, B. Hausler, and R. Torbert, Evidence for a Rayleigh-Taylor type instability and upwelling of depleted density regions during equatorial spread F, *Geophys. Res. Lett., 3*, 448, 1976.

Kelley, M. C., K. D. Baker, and J. C. Ulwick, Late time barium cloud striations and their possible relationship to equatorial spread F, *J. Geophys. Res., 84*, 1898, 1979.

Klostermeyer, J., Nonlinear investigation of the spatial resonance effect in nighttime equatorial F region, *J. Geophys. Res., 83*, 3753, 1978.

Koster, J. R., Equatorial scintillations, *Planet. Space Sci., 20*, 1999, 1972.

McClure, J. P., W. B. Henson, and J. F. Hoffman, Plasma bubbles and irregularities in the equatorial ionosphere, *J. Geophys. Res., 82*, 2650, 1977.

Nopper, R. W., and R. L. Carovillano, Polar-equatorial coupling during magnetically active periods, *Geophys. Res. Lett., 5*, 699, 1978.

Ossakow, S. L., S. T. Zalesak, B. E. McDonald, and P. K. Chaturvedi, Nonlinear equatorial spread F: Dependence on altitude of the F peak and bottomside background electron density gradient scale height, *J. Geophys. Res., 84*, 17, 1979.

Ott, E., Theory of Rayleigh-Taylor bubbles in the equatorial ionosphere, *J. Geophys. Res, 83*, 2066, 1978.

Parkinson, W. D., and J. Cleary, The eccentric geomagnetic dipole, *Geophys. J. 1*, 346, 1958.

Rastogi, R. G. and R. F. Woodman, Spread F in equatorial ionograms associated with reversal of horizontal F region electric fields, *Ann. Geophys., 34*, 31, 1978.

Röttger, J., Wave-like structures of equatorial spread F irregularities, *J. Atmos. Terr. Phys. 35*, 1195, 1973.

Scannapieco, A. J., and S. L. Ossakow, Nonlinear equatorial spread F, *Geophys. Res. Lett., 3*, 451, 1976.

Smiddy, M., R. C. Sagalyn, W. P. Sullivan, P. J. L. Wildman, P. Anderson, and F. Rich, The topside ionosphere plasma monitor (SSIE) for the block 5D/Flight 2 DMSP satellite, *AFGL-TR-78-0071*, Air Force Geophys. Lab., Hanscom Air Force Base, Mass., 1978.

Woodman, R. F., Vertical drift velocities and east-west electric fields at the magnetic equator, *J. Geophys. Res., 75*, 6249, 1970.

Woodman, R. F., and C. La Hoz, Radar observations of F region equatorial irregularities, *J. Geophys. Res., 81*, 5447, 1976.

COMPARISON OF SC2-3, SC5 AND SC9

Prepared by: M.S. GUSSENHOVEN, Boston College

Data provided by: E. WHIPPLE, UC, San Diego
D.A.HARDY, AFGL/PHG
J.FENNELL, Aerospace Corp

August 20, 1980

COMPARISON OF SC2-3; SC5; AND SC9

FOR TWO TIME INTERVALS ON MARCH 30, 1979 (89.4)

The time intervals chosen for comparison are:

1) the five minute interval 14:45→14:49UT (53100-53340) with special emphasis on the one minute interval 53194-53255;

2) the five minute interval 16:40→16:45UT (60000-60300) with special emphasis on the one minute interval 59965-60022.

A variety of electron beam operations (SC4) was performed in and out of eclipse on this day. The first time interval, (1), is in sunlight prior to beam operations. The second, (2), is in sunlight after beam operations.

For both time intervals the satellite was in the plasma sheet. However, for the first time interval, Alfven layers for electrons greater than 3 keV were in the process of being crossed, or had not yet been crossed.

In the three sets of instruments we compare the distribution function, f, as a function of energy, E. The energy range, position on the satellite, energy pass bands and pitch angles differ for the three instruments. The energy ranges are summarized in Table 1. The pass bands, $\Delta E/E$ are: SC2-3, .09 for electrons, and 0.14 for ions; SC5, ~1; SC9, 0.2.

SC2-3 and SC5 are mounted on the belly band (central portion) of the satellite, approximately 70° apart, with look directions radial outward from the satellite. Thus, they sample the same pitch angle distribution but with a phase difference for a given time. A complete spectrum is taken every 3 seconds by SC2-3, and every second by SC5. A second SC5 instrument is mounted to look parallel to the satellite spin axis out the forward end of the satellite. Since for the data discussed here, the two SC5 instruments agree in spectra when they sample the same pitch angle, the parallel detector will not be explicitly discussed. SC9 is mounted on the forward end of the

satellite and can be rotated independently of the satellite motion. For the data presented here, no pitch angle information was available for SC9. A full spectrum is obtained in a minimum of 16 sec. by SC9.

The SC2-3 and SC9 detectors are electrostatic analyzers; the SC5 Rapid Scan Particle Detector uses electrostatic analyzers to ~60 keV and solid state detectors for the higher energies.

The energy range covered by the three sets of particle detectors is greater than seven orders of magnitude; and the corresponding range of the distribution function, f, for a given species, is twice as great. Therefore, initial comparisons are made with a log-log plot, even though discrepancies are less obvious in this format. Figures 1 and 2 are comparisons of the distribution functions in two common time intervals, each of approximately one minute in duration (one satellite spin period), and separated by nearly two hours.

For SC9 one complete spectrum for each head (high energy and low energy) is shown for each interval. No pitch angle information was available. For SC2-3 and SC5, the range of spectra is designated for each by cross-hatching. The range of spectra is obtained by plotting the ~20 (~60) spectra of SC2-3 (SC5), which are obtained for one satellite spin period. The range results both from fluctuations and from anisotropy in pitch angle. For Figure 1, the instruments looked to within ~18° of the magnetic field direction, and in Figure 2, to within ~6°.

IONS

The ion distribution function will be discussed in two parts: A high energy range, ≥ 1.5 keV; and, A low energy range, ≤ 1.5 keV.

High energy distribution function: Comparison of the ion measurements shows
good agreement for the high energies: > 1.5 keV, by all three instruments.
A detailed study shows that the ion distribution function over the entire high
energy range is well-approximated by a Maxwellian. Over the common high energy
range (1.5 - 20 keV) the three instruments agree on the temperature of the
Maxwellian up to 20%, and on the density, by a factor of 2, with SC5 having
the higher values for both. Comparison over the entire high energy range of
SC5 and SC9, and averaging over a 5-minute interval increases agreement bet `en
the two. The results are shown in Table 2. The SC5 values for temperatur
and density are still consistently higher than those for SC9, as are the st dard
deviations. The temperatures and densities differ by 14% and 40% respecti
which is more than twice the largest standard deviation in each case.

Low energy distribution function: SC2-3 and SC9 are in good agreement for
values of f over their common low energy range, and both disagree up to an
order of magnitude with SC5. The SC5 counts in the four energy channels up
to 1.8 keV are very near those in the background channel at these times, and
all have large fluctuations. Since only positive differences between counts
in the energy channels and the background can be used to construct the
distribution function, the plasma may be over estimated under these conditions.
It is unclear whether a combination of fluctuating and subtracting background
is sufficient to account for the differences between SC5 and SC2-3, SC9.
For the ccmmon low energy range (~0.07 - 1.5 keV) the distribution function
can be only reasonable well-modelled by a Maxwellian. The temperature and
density of the Maxwellian obtained with SC2-3 and SC9 data are 180 eV and
0.05 cm^{-3}, respectively. For this range, SC5 gives a temperature twice as
high and a density higher by an order of magnitude. If the distribution

function for the low energies is modelled over the entire low energy range, the principal source of data is SC9.

From Figures 1 and 2, it appears that the SC9 data is better fit by a power law than by a Maxwellian, although care must be taken to distinguish the geometric factor effect which for energy-independent efficiencies gives a power law spectrum for single count (background) response with power equal to -2. To show this effect log f for a single count in each SC9 channel is drawn (straight line) for low energies in Figures 1 and 2. The instrument is recording near background for energies below ~10 eV, for the times shown. Thus, the validity of the power law is questionable below this energy. For a proton distribution function varying as $E^{-\alpha}$ and having a value of f_o, at E_o, the number density from E_1 to E_2 is given by:

$$n = 5.31 \cdot 10^{-7} \left(\frac{f_o}{\alpha - 3/2}\right)\left[\left(\frac{E_1}{E_o}\right)^{-\alpha + 3/2} - \left(\frac{E_2}{E_o}\right)^{-\alpha + 3/2}\right] \text{cm}^{-3} \tag{1}$$

Table 3 gives 5 minute averaged values of f_o and α for SC9 and SC5 when a power law fit is made to the data. (Corrections for the high energy Maxwellian of Table 2 were made prior to fitting the data). Also shown are the calculated values of the partial density for various energy ranges. The variation in density is ~20% for SC9 and ~40% for SC5 when densities for individual spectra are averaged. As in the case of fitting to a Maxwellian distribution the partial densities from the two instruments differ by an order of magnitude over their common energy range. Additional evidence that the SC5 is essentially at background is that the power of the distribution function is very near -2.

ELECTRONS

No correction for photoelectron background is made for low energies. Since photoelectrons can be a significant contribution to the measured plasma up to 20 eV, we only consider the energy range greater than about 50 eV in our comparison. The electron distribution function for energies greater than 50 eV appear in Figures 1 and 2 to be well-described in a piecewise manner by power laws, with one negative power applicable from ~50 eV to ~ 5 keV, and a second, larger negative power for energies greater than 5 keV. This gives the appearance of a knee in the distribution between 3 - 6 keV.

The distribution functions from each of the three instruments show the same general behavior. However, all three differ in numerical value. Generally, SC9 is about a factor of 6 higher than SC2-3 (except at the highest energies, where SC9 is more than an order of magnitude greater than SC2-3), and SC5 values lie between the values for the other two instruments, tending toward better agreement with SC2-3 for the lower range of energies; and SC9, for the higher range. Unlike the low energy ions, the electron counts for all energies considered are well above background. Therefore, the discrepancies between instruments cannot be explained by fluctuations close to background. Figure 3 shows more clearly how great the variations between instruments are. Here the log f is plotted as a function of E (linear scale). This plot also indicates how poorly a single, or even a double, Maxwellian approximates the data even over the limited energy range shown.

Low Energy distribution function

Because the differences in distribution functions for the three instruments are large and do not vary consistently with energy a detailed analysis of the data over a five minute period was not performed. Instead, we approximate

the distribution function over the low energy range with the same power law for all instruments. This, then clearly shows what will be the difference in densities between instruments, since for a given power the density is directly proportional to the value of the distribution function at the reference energy, here taken to be 1 keV. (See Eq 1 which applies to electrons when multiplied by $(m_p/m_e)^{3/2}$.) Assuming the same slope for all three instruments is poorest in the "knee" region, particularly for SC2-3 in the first time interval since the entire knee region occurs below the cut off energy of 5 keV. Table 4 shows the slopes, reference distribution function values and densities for the three instruments. The densities vary, as expected from the above comments, by a factor of 4, with SC9 having the greatest values and SC2-3 the smallest. Very little change takes place in the density in this energy range in the two hour time interval.

High Energy distribution function

The powers appropriate to describing the distribution functions over the high energy range > 5 keV are considerably greater than those for the low energy range, and because of this and the limits of integration the contribution to the density over this range is considerably less than over the low energy range. Again, for the sake of comparison we attempt to choose the same power for all three instruments for a given time. This works well for the first time interval, but for the second, SC2-3 values fall off much more rapidly than for SC5 and SC9, so an additional determination was made. For the high energy range the densities differ by less than a factor of 3. The difference in slope obscures the relationship of density values between instruments. While the densities in the low energy regime remained fairly constant over the 2 hour interval, for the high energy range the density increases by factors of 3 to 5 in SC9 and SC2-3 respectively, but stays essentially constant for SC5.
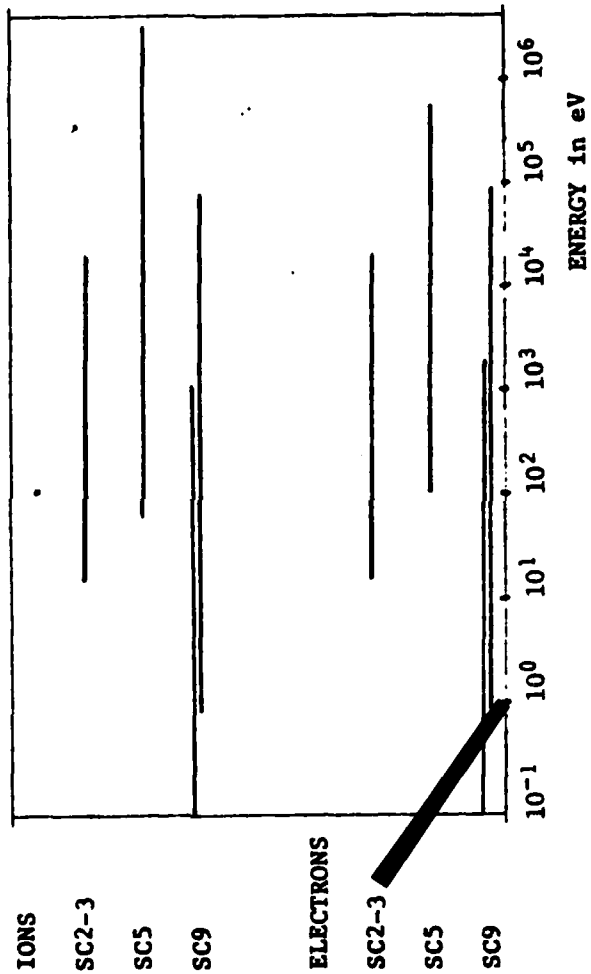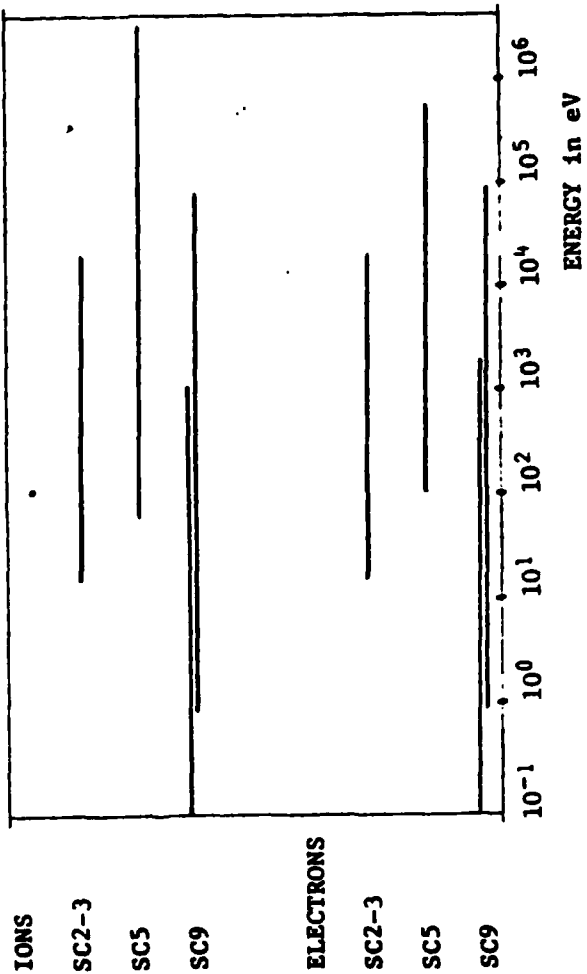
IONS

SC2-3

SC5

SC9

ELECTRONS

SC2-3

SC5

SC9

10^{-1} 10^{0} 10^{1} 10^{2} 10^{3} 10^{4} 10^{5} 10^{6}

ENERGY in eV

TABLE 1

TABLE 1

HIGH ENERGY ION DISTRIBUTION FUNCTION
MAXWELLIAN

	Range (keV)	PA	n (cm)$^{-3}$	kT (keV)
14:45-50 UT SC9	1.5-81.6	NI	.37 $\pm$ .02	14.2 $\pm$ 0.6
SC5	1.8-188	18;162° 90;180°	.62 $\pm$ .09 .59 $\pm$ .11	16.3 $\pm$ 1.1 16.2 $\pm$ 1.3
16:40-44 UT SC9	1.5-81.6	NI	.25 $\pm$ .01	12.3 $\pm$ 0.3
SC5	1.8-188	6;174° 90;180°	.22 $\pm$ .04 .35 $\pm$ .07	14.5 $\pm$ 1.4 14.0 $\pm$ 1.0

TABLE 2

LOW ENERGY ION DISTRIBUTION FUNCTION

		$f = f_o (E/E_o)^{-\alpha}$ (sec^3/km^6) E_o = 1 keV				
	α	f_o	n_1	n_2	n_3	
14:45-50 UT SC9	$-1.6 \pm .1$	$4.38 \pm .13$	.03	.07	.13 (cm)$^{-3}$	
SC5	$-2.0 \pm .4$	$5.15 \pm .32$	.32		(cm)$^{-3}$	
16:40-44 UT SC9	$-1.7 \pm .1$	$4.18 \pm .15$	.02	.06	.11 (cm)$^{-3}$	
SC5	$-2.6 \pm .6$	$4.91 \pm .50$	.20		(cm)$^{-3}$	

Limits of integration for n:

n_1: $.1 \leq E \leq$ 1keV

n_2: $.01 \leq E \leq$ 1keV

n_3: $.001 \leq E \leq$ 1keV

TABLE 3

$$f = f_o(E/E_o)^{-\alpha} \ (\text{sec}^3/\text{keV}^6)$$

$$E_o = 1 \text{ keV}$$

Low Energy Range: .05 – 5 keV			
14:47	α	f_o	n
SC9	1.25	4.37	0.75 $(\text{cm})^{-3}$
SC5	1.25	2.40	0.41
SC2–3	1.25	1.20	0.21
16:40			
SC9	1.3	4.57	0.80
SC5	1.3	2.24	0.39
SC2–3	1.3	1.20	0.20
High Energy Range: >5 keV			
14:47			
SC9	3.2	4.95	.008 $(\text{cm})^{-3}$
SC5	3.2	4.95 ,	.008
SC2–3	3.2	1.95	.003
16:40			
SC9	3.6	$3.16 \cdot 10^2$	.021
SC5	3.6	$1.41 \cdot 10^2$	.0096
SC2–3	6.25	$3.98 \cdot 10^3$	.017

TABLE 4

MARCH 30, 1979 (89.4)   14-46-34 ─→ 14-47-35 UT

ELECTRONS

IONS

SC2-3
SC-5
SC-9

ENERGY IN eV

LOG f (s³Km⁻⁶)

MARCH 30, 1979 (894)   16-39-25 → 16-40-22 UT

ENERGY IN eV

LOG f (S³Km⁻⁶)

IONS

ELECTRONS

SC2-3
SC-5
SC-9

MARCH 30, 1979 (89.4)   16-39-25 → 16-40-22 UT

SC2-3
SC-5
SC-9

IONS

ELECTRONS

LOG f $(S^3 \ Km^{-6})$

ENERGY IN KeV